University of Southampton Research Repository

Thesis: Jack Taylor (2019) "Investigation of Intracellular Compound Dynamics by Enhanced Raman Scattering Technologies", University of Southampton, Faculty of Engineering and Physical Sciences, PhD Thesis.

University of Southampton

Faculty of Engineering & Physical Sciences

School of Chemistry

Investigation of Intracellular Compound Dynamics by Enhanced Raman Scattering Technologies

by

Jack Taylor

Thesis for the degree of Doctor of Philosophy

September 2019

University of Southampton

Abstract

Faculty of Engineering & Physical Sciences

School of Chemistry

Thesis for the degree of Doctor of Philosophy

Investigation of Intracellular Compound Dynamics by Enhanced Raman Scattering Technologies

by

Jack Taylor

The highly attritional nature of drug discovery research is underpinned by a fundamental lack of knowledge regarding drug compound behaviour inside cells. At present, no single technique is capable of providing measurement of the localisation, concentration and metabolism of exogenous compounds at the subcellular level. Current platforms rely on the use of fluorescent tags, destruction of samples or are limited by poor spatial resolution. Raman spectroscopy interrogates the full vibrational fingerprint of biological samples in a label-free and non-invasive manner but is limited by inherently weak scattering intensity for intracellular studies. Signal enhancement can be achieved utilising unique optical properties possessed by plasmonic nanostructures or coherent wave mixing properties, exploited by surface-enhanced Raman scattering (SERS) and coherent Raman imaging (CRI) experimental platforms respectively. Research presented within this thesis demonstrates the ability of these technologies to perform highly sensitive intracellular measurements of exogenous molecule dynamics and actions within human cancer cell lines. The voluntary uptake of spherical gold nanoparticles (AuNPs) for use as intracellular SERS probes is established. Resulting SERS analysis subsequently evaluates molecular-level changes induced to cells following excessive AuNP internalisation with greater sensitivity than traditional biological assays. An optimised intracellular SERS methodology then performs intracellular mapping of an exogenous small molecule inside the endolysosomal pathway that is improved with application of multivariate technique principal component analysis (PCA). CRI technique coherent anti-Stokes Raman scattering (CARS) microscopy was developed for quantifiable monitoring of cytosolic lipid droplet (LD) responses to both repeated laser exposure and application of a chemotherapeutic agent in live cells. The chemical selectivity of CARS was compared with that of the second predominant CRI platform, stimulated Raman scattering (SRS) microscopy, by comparative hyperspectral imaging and statistical analysis. The research evidences capability of enhanced-Raman scattering techniques to provide valuable new pharmacological insights for drug discovery research, informing future development of label-free and industry-viable assays that would further existing knowledge and improve clinical outcomes.

Table of Contents

Table of Tables

Table of Figures

Research Thesis: Declaration of Authorship

Print name:	Jack Taylor
Title of thesis:	Investigation of Intracellular Compound Dynamics by Enhanced-Raman Scattering Technologies

I declare that this thesis and the work presented in it are my own and has been generated by me as the result of my own original research.

I confirm that:

1. This work was done wholly or mainly while in candidature for a research degree at this University;
2. Where any part of this thesis has previously been submitted for a degree or any other qualification at this University or any other institution, this has been clearly stated;
3. Where I have consulted the published work of others, this is always clearly attributed;
4. Where I have quoted from the work of others, the source is always given. With the exception of such quotations, this thesis is entirely my own work;
5. I have acknowledged all main sources of help;
6. Where the thesis is based on work done by myself jointly with others, I have made clear exactly what was done by others and what I have contributed myself;
7. Parts of this work have been published as:

J. Taylor, A. Huefner, L. Li, J. Wingfield and S. Mahajan, The Analyst, 2016, 141, 5037–5055.

J. Taylor, A. Milton, M. Willett, J. Wingfield and S. Mahajan, Faraday Discuss., 2017, 205, 409–428.

J. Taylor, A. Huefner, J. Wingfield and S. Mahajan, in Plasmonics in Biology and Chemistry, Pan Stanford, 1st edn., 2019, pp. 233–276.

Signature: Date:

Acknowledgements

My first and foremost thanks are made to my supervisor, Sumeet Mahajan, for his continued guidance, encouragement, confidence and a significant amount of patience throughout my studentship. Working for five years with both a role model and friend has been a genuine privilege, even during times when research proved challenging. I would like to offer my sincerest thanks for giving me the opportunity to develop my research career under your supervision.

Secondly, to my industrial supervisor Jonathan Wingfield, for invaluable insights in guiding this research and wider professional advice. My research placement within AZ was an unforgettable learning experience for which I have him, and everyone within AZ's Darwin site, to thank.

Completion of this thesis would not have been possible without the hard work, expertise and support offered by my lab group and wider colleagues. This is particularly true of Kostas Bourdakos, Peter Johnson and Tual Monfort for designing, building and constantly maintaining the multiphoton microscope. Similar thanks to Niall Hanrahan for his MATLAB gardening and Adam Lister for, well, something. Lastly, without the particular flavours of nonsense provided by Peter Johnson, Joshua Robertson, Krzysztof Herdzik, George Devitt and Graham Saunders, this process would have been significantly harder and I definitely wouldn't have had nearly as much fun. Or SUSU pastry. Thank you.

Enormous gratitude must be expressed beyond those directly involved in research, starting with my family. To my parents, Mark and Joanne Taylor, and Nana, Lois Whitaker, thank you for your unconditional support and encouragement throughout the last four years. I think we are all relieved that this thesis *finally* represents the end of my (at least formal) education.

Last and definitely not least, to my girlfriend, Elysia Koutrouza-Turvey, who has put every bit as much energy into supporting me as I have into this research. You have been (particularly) patient, kind and inspirational to me completing this process which wouldn't have been possible without you. I look forward to starting the next chapter of our lives together, in which I will repay the two years of housework that I certainly owe. You are my best friend and I love you more than I can comprehend.

Definitions and Abbreviations

(Au)NPs	(Gold) Nanoparticles
$[\text{AuNPs}]_{\text{Incub}}$	Incubation concentration of AuNPs
BSA	Bovine serum albumin
CCD	Charge coupled device
CRI	Coherent Raman Imaging
DMEM	Dulbecco’s modified Eagle media
DMSO	Dimethyl sulfoxide
D/RNA	(Deoxy/) ribonucleic acid
FAD	Flavin adenine dinucleotide
FBS	Foetal bovine serum
FOV	Field of view
GFP	Green fluorescent protein
ICP-MS	Inductively coupled plasma mass spectrometry
LDA	Linear discriminant analysis
LDs	Lipid droplets
LSPR	Localised surface plasmon resonance
LUT	Look-up table
4-MBA	4-mercaptobenzoic acid
NA	Numerical Aperture
OPO	Optical parametric oscillator
PBS	Phosphate buffered saline
Pen-strep	Penicillin-streptomycin antibiotic supplement
PCA	Principal Component analysis

PCC	Pearson correlation coefficient
PC	Principal Component
RME	Receptor-mediated endocytosis
ROI	Region of interest
ROS	Reactive oxygen species
SD	Standard deviation
SEM	Scanning electron microscopy
SERS	Surface-enhanced Raman scattering
SRL/G	Stimulated Raman loss/gain
SRS	Stimulated Raman scattering
TEM	Transmission electron microscopy
TPF	Two-photon fluorescence

Chapter 1 Introduction

Since 1950, the pharmaceutical industry has introduced around 1200 new FDA-approved drugs. A startling truth throughout this period is that despite vast efforts to increase new drug output, its levels have remained essentially constant while discovery costs increase exponentially[1]. In the highly attritional discovery process, sources have speculated that focussing efforts on drug candidate survival through phase two clinical trials- currently exhibiting a probability of technical success, p(TS), of 34%- provides the greatest opportunity to increase research and development (R&D) productivity[1–4]. The predominant cause for withdrawal of candidates is demonstrable lack of efficacy, accounting for 66 % of phase 3 clinical trials between 2007-2010 and 57 % of trials entered by therapeutics between 1998-2008 (with follow-up in 2015)[5–7]. This lack of efficacy identifies a large void in industry knowledge at the early discovery and preclinical stages of development, concerning the molecular dynamics of library compounds at intracellular targets. In order to reach such targets, small molecule drugs must not only be able to bypass the lipid bilayer of cell membranes but also localise to the correct target organelles. Transport through the plasma membrane is variable, with transporter molecules capable of both impeding or facilitating internalisation of the drug, whereas its own permeability also brings about very low and variable degrees of uptake[8]. In order to accurately predict the pharmacological effect of a drug species *in vivo*, determination of bioavailability is required both within cell and at target organelles[8].

The current technique of monitoring blood plasma concentrations provides an insufficient reflection of drug exposure at the critical cellular and organelle level and must be supplemented in order to improve candidate drug efficacies and clinical outcomes[2]. Concentrations of biomolecules within cells are typically of the order of nM and therefore high sensitivity is required for determining intracellular drug distributions and dynamics. No single technique is capable of providing sufficient sensitivity and resolution in a non-destructive and label-free nature for the *in situ* imaging of compound localisation inside living and intact cells.

Fluorescence imaging remains the gold-standard approach in biomedical research and benefits as an intracellular technique from large intrinsic signals, availability of a wide range of labels (including a large palette of fluorescent proteins which can be incorporated endogenously through genetic modification) and the ability to tune the response of labels to analytes or pH[9–11]. Most small molecule drugs are not fluorescent and therefore fluorophores need to be added or attached to the molecules of interest in order to study them. This labelling process, by either staining (addition of dyes) or labelling via endogenously-expressed fluorescent proteins through genetic modification, is invasive and perturbative of the natural, molecular-level progression of biological pathways being analysed. Green fluorescent protein (GFP) tags radically alter the pharmacokinetics of small molecule drugs. Such perturbation from normal activity reduces the validity of exposure models of compounds to natural or healthy cell models[8,10]. The intracellular distribution of cationic amphiphilic drug (CAD) azidobupramine has successfully been observed using fluorescent labelling of both drug compound and target organelles following immobilisation of drug accumulation inside cells before staining[12]. Other CADs (amiodarone, chloroquine, clofazimine and quiancerine) possess intrinsic fluorescence to offer label-free contrast[12,13], but such specific cases do not offer a ubiquitous solution. A further limitation of fluorescence imaging is observed when multiplexed data, for wider investigation of numerous species within a sample, is required. Only a finite number of dyes may be simultaneously employed for probing the desired environment due to spectral overlap of comparatively broad emission peaks. Photobleaching effects are also limiting by the apparent fading of emitted fluorescent light and can be a rapid phenomenon[10,14].

Mass spectrometry (MS) provides an alternative approach for pharmacological analysis. Advantages include rich chemical information from samples, non-targeted specificity and multiplexed detection[15,16]. MS has become of increasing use within pharmaceutical research, owing the richness of information available in the modern ‘omics’ era. The MS imaging platforms used in bioanalysis are generally secondary ion mass spectrometry (SIMS) and matrix assisted laser desorption ionisation mass spectrometry (MALDI-MS). SIMS utilises a primary ion beam to ablate successive layers from the surface of a sample by destruction of covalent bonds and a secondary, lower energy beam for ionisation of fragments[8,15]. Along with the obvious drawback that this technique is destructive to samples by its very nature, sensitivity in biological samples is also limiting as detection limits rise from 5 nM in physical samples to 200 nM in organics. Sensitivity issues can be a recurrent problem throughout MS platforms as efforts to increase the resolution of ionisation beams result in reduction of the amount of material available for detection[17].

The limitation of insufficient spatial resolution possessed by MS platforms for intracellular study is being addressed but remains. SIMS offers the highest spatial resolution of MS imaging platforms and has been utilised to produce 2D and 3D images of single cells[15]. Time-of-flight SIMS (ToF-SIMS) imaging has yielded 3D metabolic imaging of amiodarone in rat macrophages with a spatial resolution of 2 µm for biomolecules and 200 nm for inorganic species[18]. By utilising a soft ionisation method to gather high, intact molecular ion yields, MALDI-MS provides an imaging platform with larger observable mass range and is routinely used for analyte detection in tissues[15,19]. However, unlike SIMS, resolution (micron range) is currently a limiting factor. Developments in MALDI-MS imaging are addressing the need to expand topographic aspect ratios to counteract the existing trade-off between spatial resolution and 3D sectioning capability, providing lateral resolution of 10 µm in 3D samples[20]. A requirement of rare and inorganic elements to be present in analytes for detection amid a vast array of present organic fragments[8] also exists in the utility of MALDI-MS to investigate compound localisation inside individual cells.

Research presented in this thesis informs how existing shortcomings in sub-cellular imaging of compound localisation and action can be addressed using Raman scattering-based techniques. Spontaneous Raman spectroscopy is widely applied in bioanalytical fields and offers non-destructive and label-free interrogation of the full molecular signature of samples at high, subcellular resolutions. However, it suffers the limitation of weak signals, precluding studies that require continuous and rapid monitoring or visualisation.

Surface-enhanced Raman spectroscopy (SERS) utilises the unique optical properties of plasmonic metal (usually gold, Au, and silver, Ag) nanostructures to achieve significant enhancement (factors 10^6-10^{10})[21,22] of spontaneous Raman signals, potentiating intracellular study[11]. It retains the advantages of allowing fine spectral details to be observed without interference from the broad vibrational peaks of H_2O (observed in IR spectroscopy) and increased depth of penetration by NIR radiation. Sensitivity can be comparable to or greater than fluorescence for biological assays[23,24], with single molecule detection reported in optimal cases[25–27]. SERS nanoparticles (NPs) are internalised into living cells to serve as ideal nano-antennas for interrogation of the intracellular matrix. Combination of SERS datasets with statistical analysis techniques forms a powerful investigative tool for intracellular analysis[11,28]. Coherent Raman imaging (CRI) techniques, predominantly coherent anti-Stokes Raman scattering (CARS) and stimulated Raman scattering (SRS) microscopy, utilise spatially and temporally overlapped laser pulses that can be tuned to stimulate desired molecular vibrations for selective observation of enhanced Raman intensities. CRI platforms hold significant advantages of high resolution and low acquisition times for cellular imaging[29–31].

1.1 Aims

Research presented in this thesis builds towards development of a Raman-based assay platform for investigating the intracellular dynamics of exogenous molecules in drug discovery. Such a platform is required to be label-free, so as not to perturb the natural state of cells outside applied drug effects, in addition to meeting the requirement for low acquisition times, richness of data and high throughput capabilities demanded by modern pharmaceutical research. SERS enhancement is a short-range phenomenon and therefore holds potential as a novel assay-based detection technology of nanometre-scale resolution to meet a crucial pharmaceutical requirement. A SERS-based approach localises gold nanoparticles (AuNPs) to target organelles, performing highly sensitive interrogation of molecular-level changes in a chemical environment's response to the arrival of exogenous molecules inside cells. CRI is utilised to visualise vibrational modes of specific chemical bonds of endogenous cell biomolecules for visualisation of drug actions without the use of fluorescent tags or internalised AuNPs. Knowledge gained may be extended to develop targeted intracellular localisation assays and further apply CRI to realise a potentially more advanced and industry-friendly platform for chemically-selective imaging with minimal sample preparation.

Specific aims of the presented research were to:

1. Develop an understanding of enhanced Raman-based experimental procedures and their utilisation for cellular study
2. Investigate the uptake of SERS-NPs into cells, optimising administration conditions for non-toxic and non-perturbative use as intracellular SERS probes
3. Establish a SERS-based methodology for intracellular detection of exogenous molecule localisation
4. Explore capabilities of CRI for intracellular drug and biomolecule visualisation
5. Evaluate investigated experimental platforms to inform development of an industry-applicable assay for Raman delineation of intracellular drug candidate dynamics

This thesis firstly discusses the theoretical nature of Raman spectroscopy, along with mechanisms of the signal enhancement achieved through optical properties of SERS NPs and CRI modalities. A comprehensive review of existing literature concerning enhanced-Raman based capabilities for intracellular and related studies is presented. Research provides a fundamental examination of complex NP-cell interactions and their effect upon SERS spectra towards optimisation of NP administration parameters to perform sensitive and non-perturbative intracellular measurements. This essential knowledge was then applied in development of a SERS-based intracellular drug mapping platform that is demonstrated for a selected exogenous molecule's localisation within lysosomes. The label-free ability of CRI platforms for visualising drug actions inside cancer cells was demonstrated by optimisation of CARS microscopy for live cell imaging of a chemotherapy agent on cytosolic lipid droplets. The chemical selectivity of CRI platforms (CARS and SRS) is evaluated in the context of imaging and discriminating cell biomolecules as drug targets within the 2800-3000 cm^{-1} region of the Raman spectrum. The potential for progressing research outcomes into the development of an industry-optimised cellular assay is critically evaluated, identifying feasible contributions that can be made to drug pharmacodynamic knowledge and improvements required.

Chapter 2 Theoretical Basis

2.1 Light-Matter Interactions

Light-matter interactions are fundamental to our understanding of the universe and form the basis of spectroscopy and imaging tools in scientific research. Key interactions occurring between incident radiation (modelled as either a propagating oscillating dipole or a photon by the wave-particle duality respectively) and energy states of a material (atoms, molecules, substances) produce various energetic transitions (Figure 2.1). These energetic states in a molecule comprise of electronic, vibrational and rotational states that are quantised to discrete energies. In the following explanation it must be noted that the Born-Oppenheimer approximation is applied, assuming that atomic nuclei and electrons may be treated individually to simplify the model by disregarding vibronic coupling between their vibrational motions.

The quantised energy levels of largest energetic separation are electronic states, incrementally increasing in energy from the electronic ground, most stable, electronic state to the first and subsequent excited states (S_0, S_1, S_2 ...). Energetic sublevels arise from the vibrational state of a chemical bond, again increasing in energy with incremental levels (v_0, v_1, v_2 …). These variations in energy arise from the periodic movement of electrons relative to the much heavier atomic nuclei that are therefore considered as stationary. Transition between states may occur through absorption of energy (Figure 2.1A), supplied to the molecule following interaction with incident radiation of energy corresponding to the separation between states. These interactions give rise to a number of well-established spectroscopy techniques that are commonly utilised in analytical chemistry. In UV-Vis spectroscopy, high energy radiation is applied to induce excitation of chemical bonds to higher electronic states for investigation of molecular electronic structure. Transitions between vibrational levels (within the ground electronic state) are probed by IR spectroscopy, achieved by irradiating samples with lower energy excitation fields. Rotational levels (usually denoted j_o, j_1, j_2 …) exhibit the smallest energetic separations and are mostly relevant for gaseous molecules and rotational spectroscopy, which are not discussed any further.

Emission processes present an opposite result to absorption, whereby molecules existing in excited energetic states relax back to those lower in energy, achieved by emission of a photon possessing energy corresponding to the gap between travelled states (Figure 2.1 A). Emission processes may be either spontaneous or require stimulation by radiation. Fluorescence (Figure 2.1 B) microscopy is a current standard technique applied in biological research, which relies on detection of photons emitted from fluorescent organic molecules (fluorophores) attached to

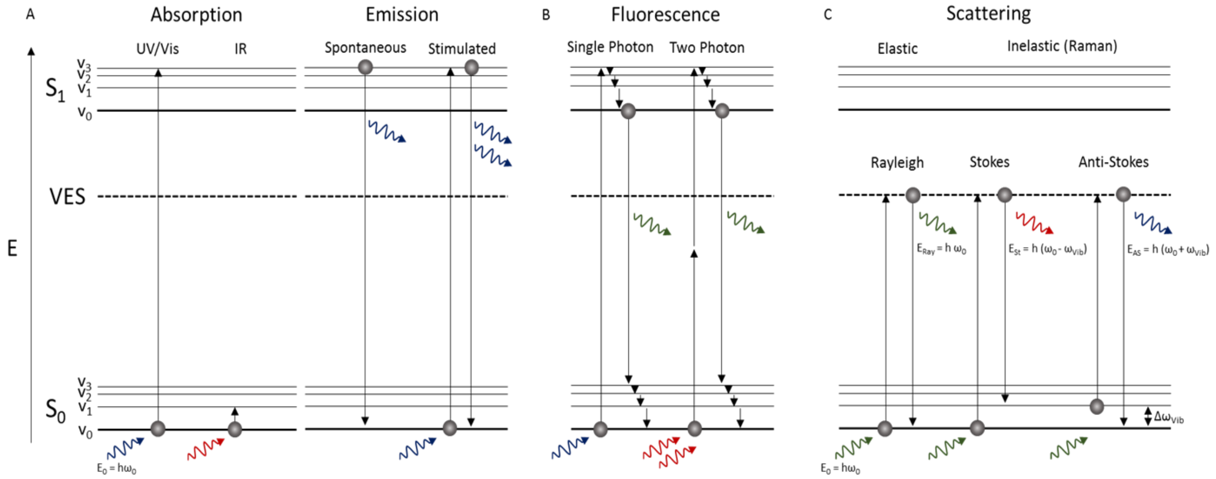

Figure 2.1 Key energetic transitions arising from light-matter interactions in molecules. From left to right: absorption of energy from molecule-photon interactions produces molecular excitation in vibrational (v_n) or electronic states (S_n) depending on incident photon energy (IR or UV/Vis respectively); emission processes may be spontaneous or stimulated to achieve relaxation back to ground electronic states through the emission of a photon possessing the excess energy for removal; scattering processes following excitation to a 'virtual' excited state (VES) and instantaneous relaxation either without net energy change (elastic, Rayleigh scattering), with gain of vibrational energy from interaction with the incident photon (inelastic, Stokes scattering) or loss of vibrational energy from the interaction (inelastic, anti-Stokes scattering).

biomolecules of interest. The emitted radiation is of slightly lower energy (longer wavelength) than the excitation field due to non-radiative decay processes between vibrational levels within electronic states. Excitation can be achieved by absorption of either a single (single photon fluorescence, SPF) or multiple low-energy photons (multiphoton fluorescence). In two-photon fluorescence (TPF), two incident photons of lower energy than the desired emission are absorbed by samples, subsequently producing a single photon of energy equal to the sum of that possessed by the incident photons ($2\ \omega_0 = \omega_{TPF}$). Advantages of multiphoton excitation include reduced photodamage effects and increased sample penetration depth afforded by NIR radiation.

Unlike absorption and emission process, scattering events (Figure 2.1 C) occur with no discernible intermediate excited state. Interaction with radiation (of insufficient energy for electronic excitation) polarises the molecule's electron cloud, exciting it to higher energy and causing temporary adoption of a new electronic geometry. This 'virtual' excited state (VES) exists at intermediate energy between the ground and first electronic state. It is an unstable configuration that instantaneously decays back to the energetically-favourable ground state with molecular relaxation. Therefore, scattering processes are considered as sequential and instantaneous occurrence of absorption and emission steps.

Scattering processes may be elastic or inelastic in nature, referring to either conservation or change in molecular energy respectively, following the scattering process. Rayleigh scattering is an elastic process, terminating with the molecule existing in the same vibrational energy state from which it was initially excited. Therefore, no energy change is produced between incident and scattered photons ($E_{Ray} = E_0 = h\nu_0$). The effect is caused by the incredibly short-lived duration (ps order) of the VES, which is highly unlikely to allow sufficient time for nuclear movement during the existence of its temporary, newly-adopted electron geometry. Conversely, inelastic or Raman scattering produces energy transfer between incident radiation and vibrational levels in a molecule that can arise from small degrees of nuclear movement during the VES's existence. Probability dictates that elastic scattering is by far the predominant mechanism of photon scattering, with just 1 in 1 x 10^6 photons experiencing a change of energy. This renders Raman scattering a very weak phenomenon. Stokes Raman scattering occurs when a molecule existing in a low vibrational state gains energy from interaction with an incident photon and returns to a higher vibrational state. The energy lost by scattered photons (compared to those incident) is equal to the energy gap between the initial and final vibrational energy states. Conversely, anti-Stokes scattering results in loss of vibrational energy in the molecule that is gained by the scattered photon, such that photon energy $E_{AS} = E_0 + E_{Vib}$. Thus, a requirement of the molecule to pre-exist in a vibrationally excited state is essential for anti-stokes Raman scattering to occur. The intensity of anti-Stokes Raman scattering is therefore weak compared to Stokes scattering at room temperature. This effect is accounted for by consideration of the Boltzmann distribution, a mathematical representation of the relative occupancy of energetic states:

$$\frac{N_n}{N_m} = \frac{g_n}{g_m}\, e^{(\frac{-\Delta E}{kT})} \qquad 2.1.1$$

Where N represents the population of (vibrational in this case) states n and m by electrons, g denotes the degeneracy of each state, ΔE the energy difference $E_n - E_m$, T represents temperature and k the Boltzmann constant. When m represents the ground state, this population ratio $E_n > E_m$ tends towards zero with increasing E_n values (progressively higher energy states) under normal conditions. Concurrently, elevation of T to infinity achieves a maximal population of excited-state photons that remains limited to the ratio $N_n = N_m$. Thus, the ground vibronic state is more populous than excited states, meaning more electrons are available for Stokes than anti-Stokes scattering to occur and increasing the relative intensity of the transitions.

2.1.1 Raman Scattering

Vibrational spectroscopies are widely applied across analytical and biochemical research and retain the selection rule that a change of 1 quantum in vibrational energy is required for a vibrational mode to be observed. This describes the gross selection rule ($\Delta v = \pm 1$) of vibrational spectroscopies. However, precise selection rules for IR and Raman activity of a mode differ from one another upon irradiation with plane polarised light. While IR activity requires a change in the dipole moment (μ) of the electron cloud for activity, Raman activity arises from a change in its polarizability (α). Polarizability is defined as the ease of distortion of the electron cloud of an atom or molecule in the presence of an electric field. The polarizability of a molecule contributes to its induced dipole moment such that:

$$\mu_{ind} = E\,\alpha \qquad 2.1.2$$

E represents the strength of the electric field into which the molecule is placed. Dipoles are induced by the placing of molecules into electric fields and subsequent displacement of electrons and nuclei according to their respective charges. Herein, a classical approach is adopted to model light as an electromagnetic wave of field strength (E_0) to derive the requirement of a change in polarizability for observation of Raman scattering[32]. Scattering of radiation is isotropic.

The electric field strength (E) of incident radiation fluctuates as a function of time (t) at frequency (v) and maintains a maximum possible amplitude (E_0).

$$E = E_0 \sin(2\pi\nu t) \qquad 2.1.3$$

As previously described, this oscillating electric field causes a distortion of the electronic field about a molecule, inducing a dipole moment (μ_{ind}) such that:

$$\mu_{ind} = \alpha\, E_0 \sin(2\pi\nu t) \qquad 2.1.4$$

Assuming that the molecule examined already possessed a permanent dipole moment before application of the electric field (μ), its total dipole moment becomes a combination of the existing and induced:

$$\mu_{Tot} = \mu + \mu_{ind} \qquad 2.1.5$$

From this point, a degree of nuclear displacement occurring during the interaction must be considered, causing changes to both internuclear distances and electronic conformation. For a simple diatomic molecule, this displacement (*dQ*) of the nucleus from equilibrium position fluctuates with a mode's vibrational frequency (v_m) and its maximum possible coordinate (Q_o) as:

$$dQ = Q_0 \sin(2\pi v_m t) \qquad 2.1.6$$

Modelling of both polarizability and the dipole moment can be achieved by Taylor series expansion, with each new term in the series making an incrementally smaller contribution to the total:

$$\alpha = \alpha_0 + \frac{\delta\alpha}{\delta Q}\, dQ + \frac{1}{2}\frac{\delta^2\alpha}{\delta Q^2}\,(dQ)^2 + \cdots \qquad 2.1.7$$

$$\mu = \mu_0 + \frac{\delta\mu}{\delta Q}\, dQ + \frac{1}{2}\frac{\delta^2\mu}{\delta Q^2}\,(dQ)^2 + \cdots \qquad 2.1.8$$

Where α_0 and μ_0 denote equilibrium position values of the polarizability and permanent dipole respectively. Assuming very small degrees of nuclear displacement, second order (and above) terms can be neglected such that the polarizability and induced dipole moment become:

$$\alpha = \alpha_0 + \frac{\delta\alpha}{\delta Q}\, Q_0 \, \sin(2\pi v_m t) \qquad 2.1.9$$

$$\mu = \mu_0 + \frac{\delta\mu}{\delta Q}\, Q_0 \, \sin(2\pi v_m t) \qquad 2.1.10$$

2.1.10

Recalling $\mu ind = \alpha\, E_0 \sin(2\pi v t)$ 2.1.4 and $\mu_{Tot} = \mu + \mu_{ind}$ 2.1.5, the induced dipole moment therefore becomes:

$$\mu_{ind} = E_0 \sin(2\pi v t)\left[\alpha_0 + \frac{\delta\alpha}{\delta Q}\, Q_0 \, \sin(2\pi v_m t)\right] \qquad 2.1.11$$

Finally, combination of the induced and permanent dipole moments yields the equation of the total dipole moment:

$$\mu_{Tot} = \mu_0 + \frac{\delta\mu}{\delta Q} Q_0 \sin(2\pi v_m t) + \alpha_0 E_0 \sin(2\pi v t) + \left(\frac{\delta\alpha}{\delta Q}\frac{Q_0 E_0}{2}\right)\{\cos[2\pi(v - v_m)t] - \cos[2\pi(v + v_m)t]\}$$

2.1.12

In this expression, the first term represents the permanent dipole of the diatomic molecule and the second shows contribution to a change in dipole moment with nuclear displacement, wherein $\frac{\delta\mu}{\delta Q} \neq 0$ produces IR activity. Subsequent terms relate to scattering interactions of the induced dipole with the incident radiation, the first of which contains the incident frequency and is thus representative of Rayleigh scattering. The final two terms describe Stokes and anti-Stokes interactions with the induced dipole of the molecule respectively, comprising of terms with lower

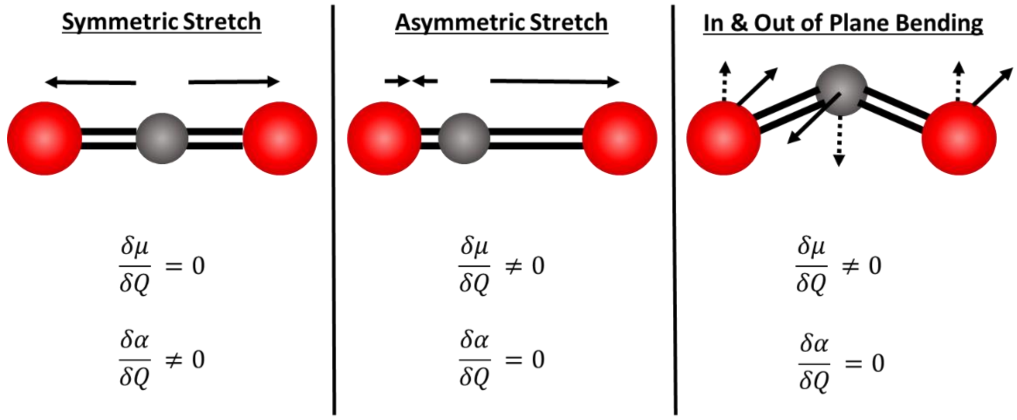

Figure 2.2 Mutual exclusivity of vibrational modes in carbon dioxide between IR and Raman activity. CO_2 possesses (3N – 5 =) four degrees of vibrational freedom, consisting of symmetric and asymmetric stretching and in/out of plane bending vibrational modes. A symmetric stretch produces no change in dipole moment (μ) but does induce a change in polarizability (α) of the electron cloud, thus is IR inactive and Raman active. For centrosymmetric molecules IR and Raman activity are mutually exclusively, with the asymmetric stretch and bending modes of CO_2 presenting only IR activity.

($v - v_m$) and higher ($v + v_m$) frequencies than the wave itself. The equation also demonstrates that in order to probe the vibrational frequency of a bond (v_m) by an incident frequency (v), a non-zero value of the change in polarizability with nuclear displacement is required such that $\frac{\delta\alpha}{\delta Q} \neq 0$. Thus, the selection rules of vibrational spectroscopies are presented.

Applying the derived selection rules to a molecular example, the vibrational modes of centrosymmetric molecule carbon dioxide (CO_2) are examined. The number of vibrational degrees of freedom a molecule possesses depends upon its symmetry, producing *[3N-5]* or *[3N-6]* vibrational modes for linear and non-linear molecules respectively where *N* is the number of atoms. This yields four vibrational modes from a total of nine (*3N*) degrees of freedom. A principle of mutual exclusivity exists between IR and Raman activity in centrosymmetric molecules, such as CO_2, stating that a single vibrational mode may only bring about a change in the dipole moment or polarizability singly and thus is only observable by one of the vibrational techniques. This exclusivity is demonstrated for the four vibrational modes of CO_2 (Figure 2.2). Only its symmetrical stretching mode induces a deformation to the electron cloud without altering its dipole moment, thus presenting Raman activity. In non-centrosymmetric molecules, intensity in the respective techniques still varies with modes being more strongly observable in one than the other. Therefore, IR and Raman spectroscopy are often employed as complementary techniques, acquiring comprehensive vibrational signatures of a given sample. This is particularly advantageous in biological samples, containing water as a major constituent that presents broad signals of O-H stretching vibrations and has a masking effect on less intense IR peaks. Meanwhile, the molecule's high polarity renders it negligibly Raman-active.

Raman spectroscopy benefits from a label-free, non-invasive nature with minimal preparation required to collect full molecular signatures of given biological samples. Despite this, the predominant limitation of the technique exists in the inefficiency of Raman scattering, which gives rise to previously mentioned weak intensities that may be lost within fluorescent backgrounds during measurements. Collection of appropriate spectra can also require the use of excessive laser exposure (through high laser power, acquisition time, spectral averaging) as well as high analyte concentrations which may be unsuitable for use on live or delicate biological samples. Therefore, modern techniques have been developed which deliver enhancement of otherwise weak Raman scattering to circumvent these issues. Surface-enhanced Raman spectroscopy (SERS) utilises the unique optical properties of nano-scale structures in noble metals and more commonly nanoparticles (NPs) to provide enhancement factors of 10^6-10^{10} [21,33,34]. Coherent Raman imaging (CRI) techniques such as stimulated Raman scattering (SRS) and coherent ant-Stokes Raman scattering (CARS) provide enhancement of specific vibrational modes by tuning of laser excitation to stimulate desired vibrations, affording specific enhancement across large sample areas for chemically-selective imaging in high resolution with low acquisition times. The next section discusses the theoretical basis of enhanced Raman scattering techniques, focussing on mechanisms by which spherical NP plasmon frequencies provide SERS enhancement in individual and multi-particle arrangements, in addition to description of coherent wave-mixing processes involved in the CRI enhancement mechanisms which are employed for imaging in this body of research.

2.2 Enhancing Raman Scattering Intensity

2.2.1 Nanoparticles and Surface Plasmon Resonance

Spherical AuNPs are the simplest and remain the most commonly employed morphology in biologically-relevant SERS studies. As a conductive metal, electrons exist within a conduction band and are modelled as a freely-moving, incompressible and charged 'plasma', about a fixed lattice of positively charged atomic nuclei (which makes up the bulk metal). Under plane wave excitation of a spherical NP, the negatively-charged electron plasma becomes displaced from atomic nuclei, creating polarisation of the metal particle which oscillates, due to restoring coulombic attraction, with the incoming light about the nuclear coordinate (Figure 2.3). This collective, harmonic

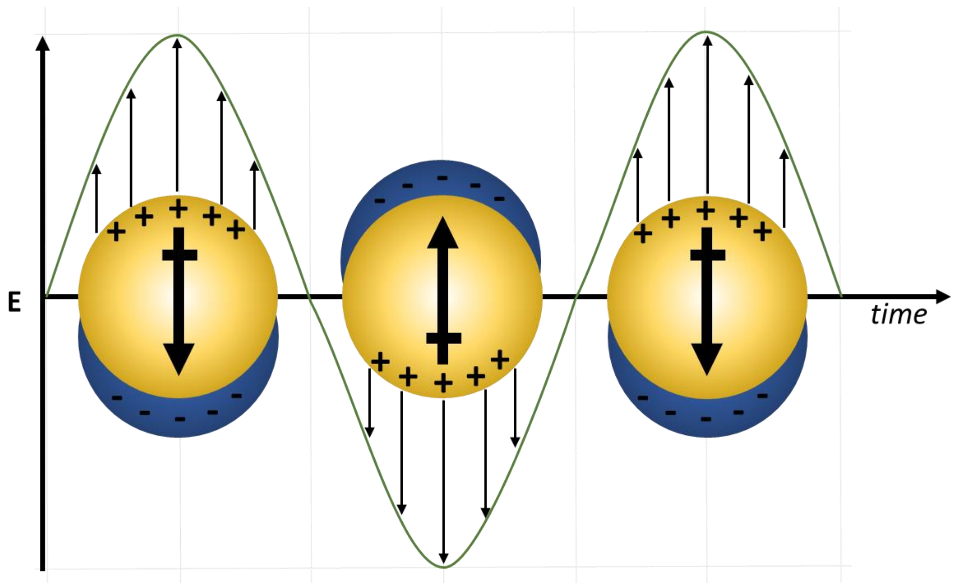

Figure 2.3 Representation of oscillating displacement of negatively charged ‘electron plasma’ from nuclei about the surface of noble metal NPs, induced by the oscillating field of incident radiation. Time-dependent charge density fluctuations are represented by induced dipole arrows.

oscillation of surface charge density is referred to as a *surface plasmon*, and represents a non-uniform and time-dependent polarisation of the NP with motion that comprises of multiple orders. The frequency of this plasmon resonance is dependent upon electron density, the effective mass of unbound electrons and the size and shape of the charge distribution[35]. Under the Drude model, the response of bulk metal to an applied external field may be described using the dielectric functions of both the NP (ϵ) and its surrounding medium (ϵ_m). This section will model such responses in spherical AuNPs, firstly for single NPs and followed by discussion of more complex systems such as interaction within NP dimers and aggregated clusters, those most commonly observed when employing NPs as intracellular SERS sensors. The *surface plasmon resonance* (SPR) of NPs is discussed with respect to enhancing Raman scattering intensities and the mechanisms by which this occurs.

2.2.1.1 Single NPs

The dominant contribution to electronic oscillations of NPs is made by dipolar motion. Higher order multipole polarisations arise when portions of the electronic ‘plasma’ are oriented parallel and antiparallel to the applied field, providing more complex electrostatic interactions that are neglected in this model. For a spherical NP much smaller than the incident wavelength ($r << \lambda$), high order modes can be neglected and a quasi-static approach becomes applicable. This allows the electric field, *E*, to be treated as constant across the NP volume, such that interactions are governed only by electrostatics without electrodynamic contributions which account for dampening effects observed in larger NPs. The response of free conductance electrons is described using the metal dielectric function, expressed by the Drude model:

$$\epsilon_{Dru} = 1 - \frac{\omega_P{}^2}{\omega_0{}^2 - i\gamma\omega_0} = \left(1 - \frac{\omega_P{}^2}{\omega_0{}^2 - \gamma^2}\right) + i\left[\frac{\omega_P{}^2\gamma}{\omega_0(\omega_0{}^2 - \gamma^2)}\right] = \epsilon_1(\omega_0) + i\epsilon_2(\omega_0) \qquad 2.2.1$$

The Drude dielectric function is dependent upon the frequency of both the incident wave (ω_0) and of the bulk electron plasma (ω_P) as well as a damping constant (Υ). The dielectric function consists of real (*Re*) and imaginary (*Im*) parts. The imaginary part incorporates broadening effects and absorptive dissipation of resonance by damping and dephasing while the real part governs the frequency position of the oscillation resonance. The plasma frequency is determined by the number of unbound electrons (*N*), their effective mass (m_e) and charge (*e*), as well as the vacuum permittivity (ε_0):

$$\omega_P = \sqrt{\frac{Ne^2}{\varepsilon_0 m_e}} \qquad 2.2.2$$

The Drude model does not consider contribution of bound electrons to the dielectric function (ϵ_∞). This must be included for real metals to account for interactions such as inter-band electronic transitions from valence to conduction bands[36]:

$$\epsilon = \epsilon_\infty - \frac{\omega_P{}^2}{\omega_0{}^2 + i\gamma\omega_0} \qquad 2.2.3$$

The dipolar polarizability (α) describes the collective response of the electrons in a small spherical NP to the applied electromagnetic field:

$$\alpha = (1 + \kappa)\epsilon_0 V\left(\frac{\epsilon - \epsilon_m}{\epsilon + \kappa\epsilon_m}\right) \qquad 2.2.4$$

The volume of the spherical NP is denoted by *V* and κ is a shape factor that incorporates the dependence of the polarizability on the geometry of the surface defining the electronic oscillations. For a simple spherical NP, $\kappa = 2$ but increases for more complex NP morphologies. As indicated by the denominator of the equation, polarizability (thus local field strength) maximises when the real part satisfies the resonance condition:

$$Re(\epsilon) = -\kappa\epsilon_m \qquad 2.2.5$$

Given that the dielectric constant of medium is usually equal to 1, the polarizability becomes greatest as $|\epsilon(\omega_P) + 2\epsilon_m|$ tends towards zero (i.e. $\epsilon = -2\epsilon_m$). The localised surface plasmon frequency (ω_{SP}) is, in general, described by the expression:

$$\omega_{SP} = \sqrt{\frac{Ne^2}{\varepsilon_0 m_e(\epsilon_\infty + \kappa\epsilon_m)}} \qquad 2.2.6$$

This resonance frequency lies within the visible region for small, spherical, noble metal NPs. A value of around 520 nm is calculated for a spherical AuNP of diameter 10-20 nm in water. Thus, the dielectric function of the metal is key to the enhancement of local electric fields by surface plasmon resonance and is dependent on the incident radiation frequency in this quasi-static model, which is time dependent and spatially independent.

The single spherical model is complicated by increasing NP size when $a \approx \lambda/2\pi$ and retardation effects contribute to the dielectric function through non-radiative damping. The Drude-Somerfield model states that a plasmon is a superposition of many independent electron oscillations[37]. These oscillations can become de-phased through scattering events with other particles such as phonons, lattice ions, other electrons, the metal surface and impurities, giving rise to population decay known as *damping*. Damping may be radiative (emitting a scattered photon) or non-radiative, which produces an electron-hole pair by electronic excitations. Pauli exclusion means that electrons can only be promoted into empty states within the conduction band, which may occur from the *d*-band or conduction band itself giving rise to inter- and intra-band damping respectively. To account for these damping effects, correction of the quasi-static approach is required to include finite wavelength effects using the Modified Long Wavelength Approximation (MLWA) and introducing electrodynamic considerations[35]. As previously, the dipole moment is the product of the electric field strength and the polarizability. The polarizability of a spheroid is now approximated as:

$$\alpha = \left(\frac{\epsilon-\epsilon_m}{\epsilon+\gamma\epsilon_m}\right)\frac{b^3(1+\gamma){\xi_0}^2+1}{3{\xi_0}^2} \qquad 2.2.7$$

Υ and ξ are governed by the spheroid geometry:

$$\gamma = -1-2\left[{\xi_0}^2-\frac{\xi_0({\xi_0}^2+1)}{2}\cos^{-1}\left(\frac{{\xi_0}^2-1}{{\xi_0}^2+1}\right)\right]^{-1} \qquad 2.2.8$$

$$\xi_0 = \left(\frac{b^2}{a^2}-1\right)^{-\frac{1}{2}} \qquad 2.2.9$$

Note the polarizability contains the denominator $(\epsilon + \gamma\epsilon_m)$ and is still heavily dependent on the metal dielectric function, such that $\epsilon = -\gamma\epsilon_m$ would now satisfy the resonance condition. The equations demonstrate that the damping constant increases with the ratio of the major to minor axis (b^2/a^2), with increased damping causing a red-shift in the plasmon resonance. Red-shift of the plasmon resonance means that lower energy is required to excite the plasmon mode and enhance the local electronic field. For modelling of damping mechanisms that are now relevant due to larger NP diameters, electrodynamic considerations are included in the induced dipole model, accounting for the radiative correction field, E_{Rad}:

$$P = \alpha[E + E_{Rad}] \qquad 2.2.10$$

$$E_{Rad} = \frac{2}{3}ik^3P + \frac{k^2}{b}P \qquad 2.2.11$$

Where $k = 2\pi/\lambda$. The terms which form the radiative correction field account for radiative and dynamic damping mechanisms in order of appearance. Radiative damping arises from spontaneous emission by the induced dipole, which increases with NP size. It reduces the size of the induced dipole and increases the plasmon linewidth. Dynamic damping originates from the finite ratio of NP size to the radiation wavelength and represents a depolarisation term. It also reduces the strength of the induced dipole moment with increased NP size. The result of these terms is inclusion of expression F in the dipole moment equation ($P = \alpha E$):

$$F = \left(1 - \frac{2}{3}ik^3\alpha - \frac{k^2}{b}\alpha\right)^{-1} \qquad 2.2.12$$

Importantly, the term relating to radiative damping is proportional to αk^3 and the term relating to dynamic damping is proportional to $(\alpha/b)k^2$. Recalling that $k = 2\pi/\lambda$, it is evident that the radiative and dynamic damping terms unite in order of magnitude when the particle radius nears $\lambda/2\pi$. Indeed, for an incident wavelength of λ = 600 nm, the NP radius is calculated as b = 100 nm and represents a large diameter NP[35].

It is demonstrated that single NPs each possess a localised surface plasmon for which resonance conditions are only satisfied by a particular wavelength range and that it is highly dependent upon the metallic dielectric function. Existence of single particles is a rare occurrence in intracellular SERS experiments using spherical NPs, given their preference for aggregation when incubated with cells for voluntary internalisation. Therefore, interaction between the plasmon resonances of multiple NPs, each experiencing the electric fields of its near neighbours, must be modelled to provide a more valid explanation of SERS enhancement mechanisms.

2.2.1.2 NP Dimers and Plasmon Hybridisation

The picture of interacting plasmon resonances between adjacent particles is now considered. Conductance electrons are only loosely held about a nucleus and may thus couple with others such that the observed plasmon resonance is actually that of numerous NPs. The electric field of one LSPR forms a constituent of its neighbours' surrounding media when considering the relative dielectric constants. The coupling of plasmonic properties gives rise to very strong electronic field enhancement, localised to the junction between plasmon structures known as *plasmonic hotspots*. Molecules located within plasmonic hotspots are subjected to enormous enhancement of Raman signals, albeit heterogeneously, which is utilised to experimental advantage[11].

By considering first the simplified case of an isolated dimer and then adapting for a cluster of NPs, as is more likely observed in intracellular SERS investigations, the associated plasmonic properties using existing theories are herein described[36,38–41].

In a NP dimer of inter-particle separation *d*, the electronic field experienced by NPs is now a superposition of the fields arising from incident radiation (E_0) and that of its neighbouring NP (E_N):

$$E_{Dim} = E_0 + E_N = E_0 + \frac{\xi \mu_N}{4\pi\epsilon_m\varepsilon_0 d^3} \qquad 2.2.13$$

For $\mu_N = \epsilon_m \alpha_{NP} E_0$ and $\xi = 3\cos(\phi_i)\cos(\phi_j) - \cos(\phi_{(i-j)})$

E_N holds dependence on the dipole moment of the neighbouring NP (μ_N), the dielectric constant of the embedded medium (ϵ_m), and an orientation parameter (ξ). Angles ϕ_i and ϕ_j represent those of the dipole of NPs *i* and *j* with respect to the dimer axis, while $\phi_{i\text{-}j}$ is the orientation between them. There are two relevant in-phase modes contributing to the field strength of E_N (and hence E_{Dim}), which may occur either parallel or perpendicular to the dimer axis, representing longitudal (with $\xi = 2$) or transverse ($\xi = -1$) modes respectively. The total polarizability of the dimer is given by:

$$\alpha_{Dim} = \frac{\alpha_{NP}}{1 - \frac{\xi \alpha_{NP}}{4\pi\varepsilon_0 d^3}} \qquad 2.2.14$$

The polarizability of a single spherical NP, α_{NP} becomes maximal and thus gives the largest field for the resonance condition:

$$\epsilon_1 = -\epsilon_m \frac{2+\xi\left(\frac{r}{d}\right)^3}{1-\xi\left(\frac{r}{d}\right)^3} \qquad 2.2.15$$

Thus, as the interparticle distance in a dimer increases towards infinity ($d \rightarrow \infty$), the expression satisfies the previously described resonance condition of a single particle ($|\epsilon_1 = -2\epsilon_m|$) and coupling is no longer observed. The field enhancement also exhibits a decrease with increasing interparticle distance due to the term $(r/d)^3$, while the coupling of plasmons produces a red-shift in the plasmon resonance frequency when radiation is longitudal to the plane of polarisation[42].

Additionally, the interaction between plasmons of neighbouring spherical NPs has been calculated to be analogous to the hybridisation interactions observed in atomic orbitals (AOs) with higher order angular momentum AOs during the formation of molecular orbitals (MOs) in chemical bonding models, as presented by Nordlander *et al*[38]. Plasmon modes are hybridised when two nanostructures approach one another, producing new plasmon modes which are lower (bonding) and higher (antibonding*) in energy than the single modes. The Aufbau principle then dictates that the low energy, bonding plasmon resonance is filled by electrons and resonance is achieved with lower energy.

In order to most simply demonstrate the hybridisation of plasmons, the dielectric effects of the media and the polarisation of ion cores are neglected, although the method has been applied to accurately determine plasmon energies when including these factors[38,40]. NPs are also considered small such that previously discussed retardation effects may be neglected. The coulombic interaction between surface charges as a function of internuclear separation (*V(d)*) is expressed by:

$$V(d) = \int {r_1}^2 d\beta_1 \int {r_2}^2 d\beta_2 \frac{\sigma_1(\beta_1)\sigma_2(\beta_2)}{|\vec{r_1} - \vec{r_2}|} \qquad 2.2.16$$

Where $\sigma(\beta)$ denotes the surface charge as a function of the solid angle. Selecting the polar axis along the dimer axis, this interaction is diagonal in magnetic quantum number *m* which gives decoupling of plasmon modes possessing different *m* values[38]. Non- and interacting plasmon modes are denoted with *i* and *j* respectively, possess energy *ω* and angular momentum *l* on sphere *N* of radius *r*. The coulombic interaction of plasmons possessing the same *m* is zero if *i* and *j* are on the same sphere and its distance dependence is modelled as:

$$ {V_{ij}}^{(m)}(d) = 4\pi \sqrt{l_i l_j {r_i}^{2l_i+1}} r_j \int d\theta_j \sin\theta_j \frac{P_{l_i}^{m}(\cos\phi_i(\theta_j))}{(2l+1)x_i(\theta_j)^{l_i+1}} P_{l_j}^{m}(\cos\theta_j) \qquad 2.2.17$$

This equation describes the interaction of separate spheres of relative geometries depicted in Figure 2.4. Distance x_i is that between the centre of sphere N_i and a point on the surface of neighbouring sphere N_j polarised to angle ϑ_j. Angle Φ_i is the corresponding polar angle in the coordinate system of sphere N_i. Importantly, the interaction between two plasmonic modes of orbital angular momenta *l* and *l'* vanishes with a minimum speed of $d^{-(l+l'+l)}$.

The coulombic interactions of the two plasmons are symmetric such that $V_{ij} = V_{ji}$, with these terms describing the hybridisation between plasmonic modes *i* and *j* which amount to separation-dependent dimer plasmon energies. Calculations performed by the group demonstrated that for $m = 0$ (polarisation parallel to dimer axis), large separations give weak interactions and dimer plasmons are analogous to bonding and anti-bonding combinations of plasmons with equal orbital angular momentum *l*. The lowest dimer plasmons ($l = 1$) showed energy dependence with $d^{-(l+l'+l)} = d^{-3}$, which is symmetrical at high *d* values. However, as the interparticle distance is decreased, the symmetry of energy dependence between the symmetrical bonding and asymmetrical anti-bonding plasmon was lost due to the antibonding plasmon gaining in energy at a rate slower than expected (d^{-3}). This effect was due to coupling of the $l = 1$ plasmons with those of higher order angular momentum. The same effect was observed in calculation for plasmons of $m = \pm1$,

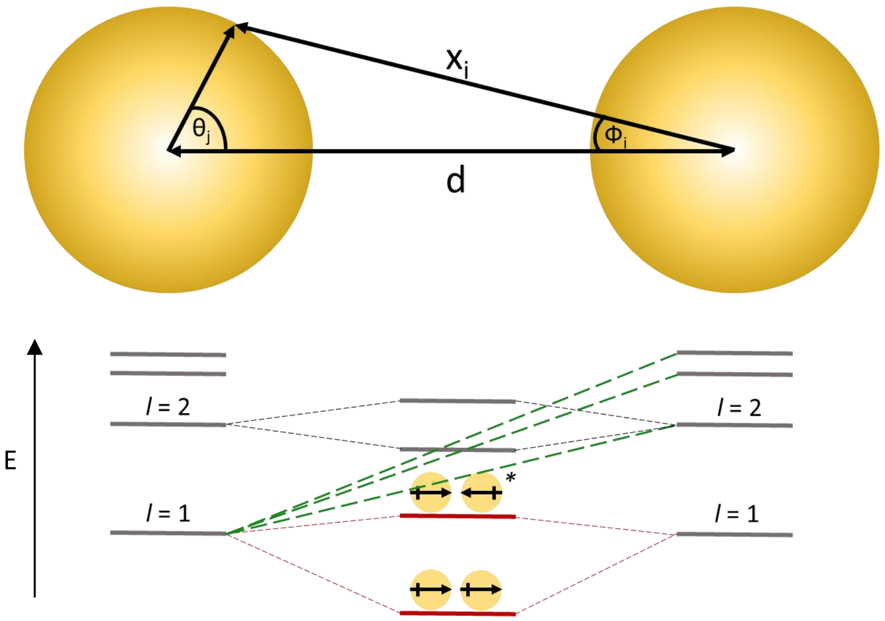

Figure 2.4 Visual representation of hybridisation of NP surface plasmons within a NP dimer, separating by distance *d*. Distance x_i is between the centre of a sphere and a point of the surface of that neighbouring which is polarised to angle *ϑj*. Plasmon hybridisation is analogous to the formation of molecular orbitals (MOs) from atomic orbitals (AOs). Combination of the lowest angular momentum plasmons (*l = 1*) parallel to the dimer axis (*m = 0*) produces high and low energy dimer resonances, stabilised by mixing with higher order (*l >1*) plasmon modes, akin to the formation of bonding and antibonding (*) MOs. In this case the antisymmetric plasmon mode is more stable due to attractive orientation of the sphere dipoles.

perpendicular to the dimer axis, although in this case the symmetric plasmons are labelled as antibonding and those asymmetric were bond due to the opposing sign. This hybridisation effect is depicted in Figure 2.4 for plasmons of *l* = 1 to reveal the stabilisation of 'anti-bonding' dimer plasmons through plasmonic hybridisation.

2.2.1.3 Higher Nanoparticle Assemblies

Having described models of plasmon resonance within single and dimer-arranged spherical and the interactions between plasmon modes of neighbouring NPs, the case of higher order NP arrangements is now examined. For spherical AuNPs, close proximity of neighbouring NPs to produce plasmonic hotspots is afforded by aggregation that arises as a response to their surrounding environment (discussed within chapter 'NP-cell interactions'). Thus, this model is most relevant to intracellular SERS investigations given the uncontrollable nature of unmodified spherical AuNPs within biological systems. As previously discussed, red-shift is produced in aggregate plasmon resonances due to coupling of plasmon modes from proximal NPs.

Consider a one-dimensional chain, effectively an extended dimer, of *n* NPs at a constant separation *d*. Again, the orientation of the applied electronic field with respect to the chain axis is significant to the resonance achieved. When perpendicular, NPs are polarised perpendicular to the chain axis which induces weak coupling effects and the plasmon resonance is similar to that observed for a single NP (such that $\lambda_{Chain} \approx \lambda_{NP}$). In contrast, longitudal coupling of NP plasmons is achieved when incident radiation is parallel with the chain primary axis and depolarisation occurs within interparticle gaps (assuming *d* is sufficiently small). Thus, a significant red-shift of plasmon resonance frequency is induced to greater extent than within dimers ($\lambda_{Chain} > \lambda_{Dimer} > \lambda_{NP}$). The extent of plasmon resonance energy red-shift was demonstrated by Schatz *et al* to depend on *n*, with longer plasmon resonance excitation wavelengths recorded as more NPs are added to the chain[43] and reach a saturation value. A distance dependence has also been evidenced which displays greater coupling at shorter interparticle distances[36,43,44] and has been proposed as *1/d*, consistent with the short-range van der Waal attraction between two spheres[45].The far-field resonance of super-radiant modes in AuNP chains has been shifted by up to 250 nm and 100 nm through variation of *n* between *n* = 1 and 7 and of *d* between 0.37 nm and 1.08 nm respectively[46]. The red-shift of plasmon resonances in 1D chains is saturable, as demonstrated for AuNPs (50 nm, *d* = 1 nm) by shifts of ≈ 200 nm compared to single NPs, which saturated at *n* = 3.5. Interestingly, a larger shift of ≈ 1200 nm was observed in flat-faceted AuNPs with saturation at *n* = 11.8 particles[47]. Thus, it is concluded that plasmon resonances of 1D chains depend upon morphology as well as number of chain NPs and gap distance.

The coupling of plasmon resonances through 1D chains is significant for modelling the response of NP aggregates using the single composite dipole model (CDM)[48]. The model states that the longitudal plasmon mode of the longest embedded chain within a NP aggregate of fixed sub-nm gap (*d*) accounts for both the long wavelength peak and spectral line width of the cluster. The characteristics of the dominant lower energy resonance are robustly inferred by chain modes through spectral extinction coefficient of the aggregate (A_{agg}), given by:

$$A_{agg} = \frac{V_{agg}}{c} \omega \, Im \left[\frac{\epsilon_{NP} - \epsilon_m}{\epsilon_m + L_{agg}(\epsilon_{NP} - \epsilon_m)} \right] \qquad 2.2.18$$

V_{agg} represents the active volume of the plasmonic system, ω is the angular frequency, ϵ_{NP} and ϵ_{m} are dielectric constants of the AuNP and the embedding medium, c is the speed of light in the medium and L_{agg} denotes a depolarisation factor (1/3 for a perfect Drude sphere, 0.23 with 90% ellipsoidal eccentricity). Taking the imaginary part, combining this expression with the Drude model (thus assuming a quasi-static interaction) and accounting for multipolar and retardation terms by careful selection of parameters[48] yields the extinction maximum of a nanoaggregate:

$$A_{agg}^{m} = \frac{\pi d^3 n_{ch} N_P g_{(N_P)}}{6 c f_{agg}} \qquad 2.2.19$$

Where $g(N_p)$ relates the active plasmonic volume to the physical volume of the dominant chains (V_{agg}'):

$$V_{agg} = g(N_P) V_{agg}' = g(N_P) \frac{n_{ch} N_P \pi d^3}{6} \qquad 2.2.20$$

The fraction of NPs existing within the optically active chain is represented by n_{ch}, N_p is the effective number of spheres in the chain (determined by matching experimental aggregate plasmon resonance frequency with equivalent 1D chain simulations). f_{agg} depends upon the squared damping constant (assumed to be the same as in single NPs) and the inverse of the total active chain length ($f_{agg} = \gamma^2 a^{-1}$). The effective proportion of NPs responsible for the dominant low energy response (η) can then be extracted from the experimental aggregate extinction peak and straight chain simulations, with the notation '*sp*' denoting properties of single particles:

$$\eta = \frac{N_P n_{ch}}{n_{sp}} = \frac{g(1)}{g(N_P)} \frac{A_{agg}^{m}}{A_{sp}^{m}} \frac{f_{agg}}{f_{sp}} \qquad 2.2.21$$

Of particular interest for SERS experiments is the ability to design an aggregate structure with optimal optical properties (plasmon resonance frequency) for a given incident frequency, in order to achieve maximum electronic field enhancements and thus higher SERS sensitivities. This is particularly pertinent in the context of single-molecule detection. Surface plasmon resonance interactions localised to hotspots are essential to the enhancing weak Raman signals achieved in SERS experimentation as the fluctuating surface charge density enhances the strength of the local electric field. The discussed LSPRs of NP arrangements enhance the strength of electronic fields in the immediate vicinity of analytes, providing highly sensitive measurements. The mechanisms by which this is achieved that are summarised in the next section.

2.2.2 SERS Enhancement: Two Predominant Mechanisms

2.2.2.1 Electromagnetic Enhancement

It is the enhancement of local electric field strength, achieved by excitation of NP LSPRs, interacting with both incident and scattered radiation which gives rise to the predominant and most widely accepted electromagnetic mechanism of SERS enhancement.

Enhancing local electric fields around molecule(s) of interest is essential for enhancing the intensity of inelastically scattered photons. Neglecting the complex interactions between LSPRs of NPs, key properties of electric field enhancement are summarised by a simplification of electric field (at distance *r*, E_r) strength that is induced by interaction of single-sphere LSPR with an incident, oscillating electromagnetic wave (E_0):

$$E_r = E_0 \cos\theta + g\left(\frac{a^3}{r^3}\right) E_0 \cos\theta \qquad g = \left(\frac{\epsilon_{NP}(\nu_0)-\epsilon_m}{\epsilon_{NP}(\nu_0)+2\epsilon_m}\right) \qquad 2.2.22$$

The local electric field strength is dependent upon the energy of the incoming wave (ν_0); the relative angle of radiation and NP polarisation (θ, representing longitudinal or transverse plasmonic modes); NP radius (*a*); distance dependence of $\frac{1}{r^3}$ (rendering SERS enhancement a short-range phenomenon); and crucially matching of dielectric constants of the metal and media to resonance conditions (such that $\epsilon_{NP} = -2\epsilon_m$). Optimisation of these parameters for a desired system gives rise to huge enhancement factors, particularly within plasmonic hotspots between plasmon-coupled neighbouring NPs.

Herein, the dependence of the electric field enhancement about an NP following interaction with incident and inelastically scattered electromagnetic radiation is described, as originally developed by Moskovits[33]. When incident light is resonant with a dipolar surface plasmon, the metal surface radiates light that is characteristic of dipolar radiation and coherent with the exciting field. This may be described as a spatial distribution of electric field magnitudes. The electric field enhancement averaged over the surface of an NP (*g*) relates the average electric field magnitude radiated by the NP (E_S) to that of the incident field (E_o):

$$E_S = gE_0 \qquad 2.2.23$$

The field strength of Raman scattered light (E_R) is dependent upon the NP-radiated field strength and a Raman tensor (α_R) of the scatterer. Therefore, it varies with the field strength of the incident radiation and the average field enhancement such that:

$$E_R \propto \alpha_R E_S \propto \alpha_R g E_0 \qquad 2.2.24$$

The NP-radiated field interacts with and enhances both the incident electric field, as well as Raman scattered radiation from the analyte. The enhancement factor *g′* is introduced to describe factors affecting the amplitude of the SERS scattered electric field, E_{SERS}:

$$E_{SERS} \propto \alpha_R g g' E_0 \qquad 2.2.25$$

The average SERS intensity, I_{SERS}, is then proportional to the square modulus of the SERS scattered field:

$$I_{SERS} \propto |\alpha_R|^2 |gg'|^2 I_0 \qquad 2.2.26$$

For low wavenumber, lower energy bands (such that *g = g′*) the SERS intensity becomes enhanced by a factor proportional to the fourth power of the local incident near field enhancement, E_L:

$$|E_L|^4 = |g|^4 \qquad 2.2.27$$

The ratio of SERS signal intensity in the presence of NP-radiated electric fields compared to spontaneous Raman scattering intensities is represented by the SERS enhancement factor (*G*). It's value depends on relative polarizabilities of the molecule (α_{Ra}) and of the SERS scatterer (α_R):

$$G = \left|\frac{\alpha_{Ra}}{\alpha_R}\right| |gg'|^2 \qquad 2.2.28$$

Thus, it is observed that the major contribution to SERS scattering actually comes from plasmonic NPs rather than molecules themselves, whose inelastically scattered radiation becomes enhanced. It is important to note that SERS is a linear optical effect (varying with I_0), enhancing spontaneous Raman signal which is linearly dependent on the Raman susceptibility tensor (Section 2.2.3.1) despite its fourth power dependence upon the local incident near-field enhancement. The near-field nature of enhancement arises from the field comprising of spatial elements which decay more rapidly with distance than the far-field spatial variation, which has a structure on the order of the wavelength. This may give rise to relaxation of dipolar selection rules, allowing detection of vibrationally forbidden modes. Lastly, the polarizability of the scatterer may differ from that of the pure molecule in the absence of plasmonic NPs because it includes contributions from the metal surface in addition to the adsorbed analyte[33]. This is of particular relevance to systems which involve the secondary mechanism of SERS enhancement, namely 'chemical enhancement', whereby charge transfer can occur between metal and molecule.

2.2.2.2 Chemical Enhancement

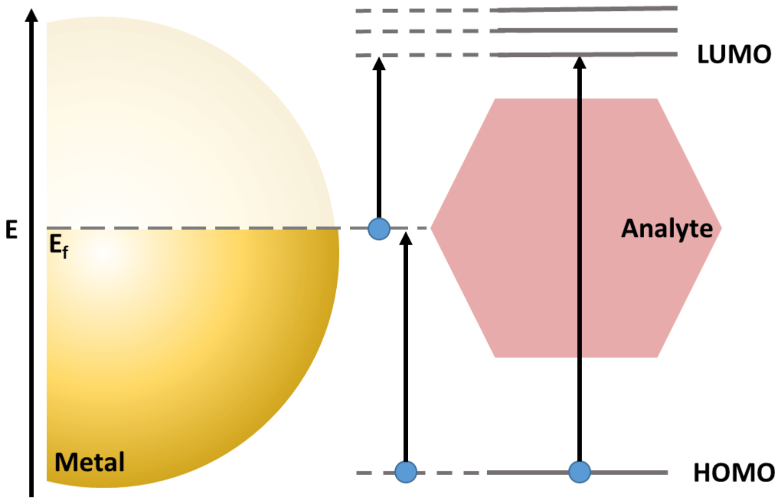

Figure 2.5 Depiction of energetic transitions between analyte and NP in the charge transfer mechanism of SERS enhancement. The metal Fermi level (E_f) acts as an intermediate, allowing for transitions from analyte HOMO to NP; and NP to analyte LUMO at lower energies than would be required for electronic transitions within the analyte.

While electromagnetic enhancement through surface plasmon interaction provides non-discriminant enhancement of local fields, certain vibrational modes are always found to be selectively enhanced in SERS[49]. Chemical enhancement of Raman signal occurs via interaction between the analyte and noble metal surface, in an interaction assumed as weak covalent bonding (weak chemisorption).

The charge transfer (CT) is such an interaction that is considered a resonance Raman process between the electronic ground state and the new excited levels of the molecule-metal complex. This is achievable in cases where the metal and the lowest occupied and highest unoccupied molecular orbitals (HOMO and LUMO respectively) of the analyte are symmetrical in energy with respect to the fermi level (total chemical potential) of the metal's electrons. New excited levels of the metal-molecule complex are formed as a result, which act as resonant intermediates[50]. These metal-molecule levels are of intermediate energy between the analyte's intrinsic electronic states, thus potentiating electronic excitation at lower energies (Figure 2.5). CT may occur from molecule to metal or *vice versa*.

Visualisation of CT mechanisms is challenging and usually performed using electrochemical and computational methods such as charge density difference (CDD) and density functional theory (DFT). The ease by which modelling of precise adsorption sites on analytes is achieved varies between molecules. For instance, adsorption is demonstrated between the nitrogen atom on pyridine and AgNPs[51,52] whereas other molecules such as rhodamine and amino acids are more complex.

Chemical and electromagnetic enhancement systems are thought to operate independently from one another. However, they are highly difficult to observe individually and provide additive enhancement that renders SERS an incredibly sensitive technique when the experimental platform is optimised. Their relative contributions to signal enhancement are inhomogenous across SERS systems and across the same nanostructured surface. Small structural variations in a set of polymethine dyes on Ag nanoaggregates have been shown to vary in SERS intensity within an order of magnitude as a function of chemical substitution[53]. Indeed, with the exception of CT resonance cases, chemical enhancement should only be considered as a small, analyte-specific perturbation of electromagnetic enhancement factors[54].

2.2.3 Coherent Raman Scattering Techniques

Coherent Raman processes offer an alternative route to enhance the inherently weak intensities of inelastically scattered photons. Predominant techniques are coherent anti-Stokes Raman scattering (CARS) and stimulated Raman scattering (SRS), increasingly used in tissue and cellular imaging. The combination of optical wave physics with microscopy has been of wide utility in biochemical and biological research, with fluorescence microscopy affording highly spatially resolved images in two and three dimensional modes through confocal fluorescence microscopy.

CARS provides enhancement of Raman scattering by orders of magnitude (typically 10^4)[30], permitting video-rate imaging at moderate excitation powers and its non-linear nature potentiates three dimensional sectioning[55]. Furthermore, CARS scattered photons are blue-shifted from those incident (in direct contrast with SERS) which allows for easy detection amid (single photon) fluorescence backgrounds with the use of appropriate optical filters. However, limitations requiring circumvention include the need for sophisticated laser systems with high peak (pulsed ps or fs sources) and moderate average powers (order of mW), owing to weak intrinsic non-linear polarizability of molecules. As will be explained in this section, it is also not free from background signal contributions which may limit contrast and selectivity, requiring suppression.

CARS is a four-wave mixing process which relies upon temporally and spatially overlapped pulses of radiation that are tight-focussed into samples to give a small excitation volume (< 1 μm^3)[31]. Pump ($E_{Pu}(\omega_{Pu})$), Stokes ($E_{St}(\omega_{St})$) and probe ($E_{Pr}(\omega_{Pr})$) electric fields interact with the sample to generate an anti-Stokes ($E_{AS}(\omega_{AS})$) field, such that $\omega_{AS} = \omega_{Pu} - \omega_{St} + \omega_{Pr}$. Thus, a molecular vibrational coherence is created, the decay of which is recorded as directionally-radiated CARS signal. Samples are excited by pump and Stokes beams for interrogation by the probe, however it is common practice to use degenerate pump and probe fields such that $\omega_{Pr} = \omega_{Pu}$ and $\omega_{AS} = 2\omega_{Pu} - \omega_{St}$. In this system, the pump laser also provides the probe field (thus, both are denoted by frequency ω_P). When the frequency difference $\omega_P - \omega_{AS}$ corresponds to the energy difference between vibrational energy levels in the sample that, when on resonance, produces strongly enhanced CARS signals are produced (Figure 2.6). Thus, CARS is a chemically-selective process.

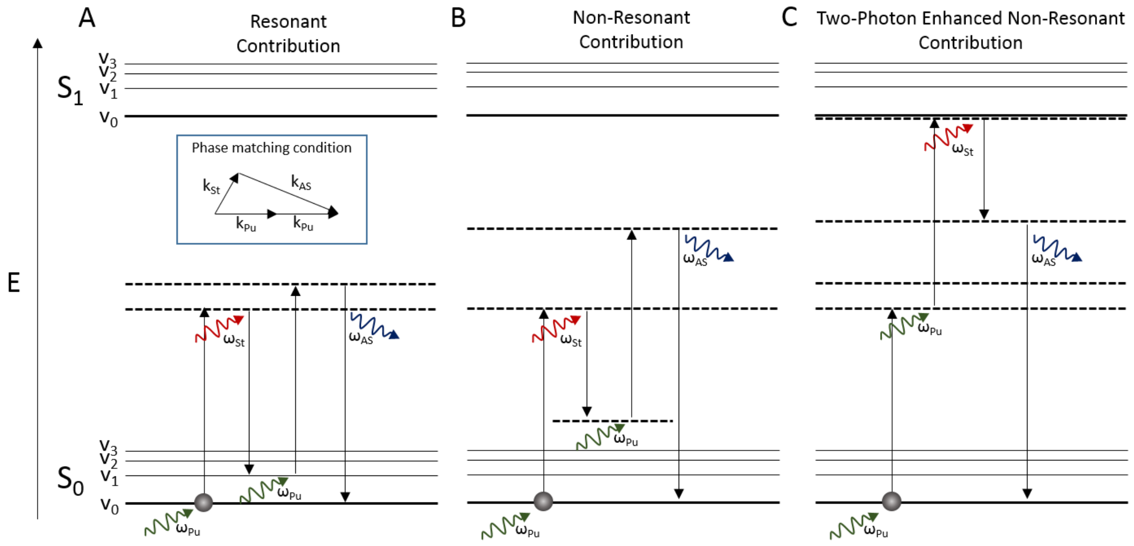

Figure 2.6 Jablonski diagrams depicting the major contributions to signal observed in CARS microscopy. (A) Resonance CARS occurs when the Stokes beam is tuned to be resonant with a specific vibrational mode such that energy $\omega_{AS} - \omega_{St}$ is exactly equal to that of the difference between vibrational levels. Inset shows the phase-matching condition of wave vectors in each field ($k_{Pu/St/AS}$). (B) Non-resonant CARS contributes to background through vibrations which are out of resonance with the Stokes tuning, so the second pump pulse excites the bond from an intermediate state between the ground and virtual excited state. Contribution from (C) two-photon contributions occur through a different combination of the incident fields, exciting molecules to a higher virtual state, (closer to the first excited electronic state) by additive absorption of photons and emission of one higher energy photon by fluorescence.

2.2.3.1 Macroscopic Polarisation

Theoretical description[30] of coherent Raman scattering begins with macroscopic polarisation ($\vec{P}$). At rest, this is equivalent to the sum of all electric dipoles present in the sample:

$$P(t) = N\,\mu(t) \qquad 2.2.29$$

$$\mu(t) = -e\,.\,r(t) \qquad 2.2.30$$

Where *N* represents the number of dipoles per unit volume and μ the magnitude of the electric dipole which depends upon electron charge, *e*, and its displacement, *r*. However, scattering interactions require application of an electric field, the linear response to which is observed in the macroscopic polarisation as:

$$P(t) = \epsilon_0\,\chi\,E(t) \qquad 2.2.31$$

The linear response is dependent upon both the electric permittivity (ϵ_0) and susceptibility tensor (χ), in addition to the strength of the applied electrostatic field ($E(t)$). However, this does not represent the full response of the sample to the applied field. Non-linear optical processes exhibit a quadratic or higher order relationship in their intensity with incident radiation and also take place upon sample irradiation, contributing to the macroscopic polarisation such that:

$$P(t) = \epsilon_0\,[\chi^1 E(t) + \chi^2 E(t)^2 + \chi^3 E(t)^3 + \cdots] \qquad 2.2.32$$

The first term in the expression represents the linear component of the polarisation, due to linear proportionality to the susceptibility tensor and therefore spontaneous Raman scattering. Since $\chi^1 >> \chi^3$, non-linear components are intrinsically weak and therefore require intense radiation of at least 10 nJ order[30]. Coherence is a property of optical processes in which the waves emitted by dipole emitters throughout the sample possess a well-defined phase relationship between one another, such that the total field is non-vanishing. When the phases of emitters are random, this total field becomes equal to zero and the process is described as incoherent. While its build-up can also allow observation of linear processes, coherence is a property that is common to all non-linear Raman scattering responses. Symmetry requirements of coherence mean that χ^2 is close to zero, rendering χ^3 the dominant non-linear contribution to the macroscopic polarisation.

2.2.3.2 Coherent Raman Scattering

The mechanism of coherent Raman scattering will now be described by a two-step process using a classical model. The description is simplified by assuming there is a single harmonic oscillator mode per molecule.

(1) Firstly, the interaction of two incoming fields (fundamentals) induces electron cloud oscillation along the vibrational degree of freedom in order to drive nuclear vibrational modes (a local oscillator).

(2) The second step is spatially-coherent modulation of the sample's refractive properties by the driven nuclear motion, acting upon a third field as it propagates through the sample in order to develop side-bands. The amplitude of the field that is scattered into these shifted side-bands provides the basis of frequency-shifted coherent Raman signal.

2.2.3.2.1 Driving of the Nuclear Vibrational Mode

Incident light fields are modelled as plane waves of field strength $E_i(t)$, with *i* representing field 1 or 2, of amplitude A_i and frequency ω_i:

$$E_i(t) = A_i\, e^{-i(\omega_v)t} + c.c. \qquad 2.2.33$$

An assumption that the vibrational frequency, ω_v, is significantly smaller than either incident frequency ($\omega_{1/2} \gg \omega_v$) is applied so that neither can individually drive the nuclear oscillation. The incident fields differ in energy ($\omega_1 > \omega_2$) and non-linear electron motions may occur at combination frequencies ($\Omega = \omega_1 - \omega_2$). The force exerted on a vibrational oscillator is then described in the case that the changing polarisability with nuclear coordinate is non-zero:

$$F(t) = \left(\frac{\delta\alpha}{\delta Q}\right)_0 \left[A_1 A_2^* e^{-i\Omega t} + c.c.\right] \qquad 2.2.34$$

The time-varying oscillatory force is produced by the modulated electron cloud at the difference frequency $\Omega = \omega_1 - \omega_2$, which causes displacement expressed by an equation of nuclear motion:

$$\frac{d^2 Q(t)}{dt^2} + 2\gamma \frac{dQ(t)}{dt} + \omega_v Q(t) = \frac{F(t)}{m} \qquad 2.2.35$$

In the above equation, Υ represents the damping constant, ω_v the resonance frequency of the harmonic nuclear mode and *m* is the reduced mass of the nuclear oscillator. The nuclear displacement can be modelled as a function of time ($Q(t)$) which oscillates at the combination frequency (Ω) with amplitude $Q(\omega_v)$.

$$Q(t) = Q(\Omega) e^{-i\Omega t} + c.c. \qquad 2.2.36$$

$$Q(\omega_v) = \frac{1}{m} \left(\frac{\delta\alpha}{\delta Q}\right)_0 \frac{A_1 A_2^*}{\omega_v^2 - \Omega^2 - 2i\Omega_\gamma} \qquad 2.2.37$$

The nuclear mode is observed to be driven by simultaneous action of two applied fields, the amplitude of which is subject to the incident field amplitudes and the coupling between the nuclear coordinate to the electronic polarisability. The extent of its vibration depends on the difference between the frequencies of driving difference field and the oscillator's resonance. The denominator in (Eqn $Q(\omega_v) = \frac{1}{m} \left(\frac{\delta\alpha}{\delta Q}\right)_0 \frac{A_1 A_2^*}{\omega_v^2 - \Omega^2 - 2i\Omega_\gamma}$ 2.2.37) shows that the amplitude of the nuclear mode oscillation is greatest when the driving difference frequency is equal to the oscillatory resonance frequency.

2.2.3.2.2 Generation of Coherent Raman Signal

The second step of the coherent Raman scattering process is modulation of the sample's refractive properties by the driven nuclear motion. This produces altered electronic polarisability that is experienced by incident fields E_1 and E_2 propagating through the material. To understand this, the macroscopic polarisation (recalling Eq $P(t) = N\,\mu(t)$

2.2.29) is modified to show the two incident fields involved:

$$P(t) = N \left[\alpha_0 + \left(\frac{\delta\alpha}{\delta Q}\right)_0\right] \{E_1(t) + E_2(t)\} \qquad 2.2.38$$

Terms of $P(t) = N\left[\alpha_0 + \left(\frac{\delta\alpha}{\delta Q}\right)_0\right]\{E_1(t) + E_2(t)\}$ 2.2.38 that are proportional to α_0 and $(\delta\alpha/\delta Q)_0$ relate to the linear and third-order polarisation of the material respectively. The non-linear contributions to the macroscopic polarisation (P_{NL}) can be described:

$$P_{NL}(t) = P(\omega_{CS})e^{-i\omega_{CS}t} + P(\omega_2)e^{-i\omega_2 t} + P(\omega_1)e^{-i\omega_1 t} + P(\omega_{AS})e^{-i\omega_{AS}t} + c.c. \tag{2.2.39}$$

Frequencies ω_{CS} and ω_{AS} refer to coherent Stokes ($\omega_{CS} = 2\omega_2 - \omega_1$) and anti-Stokes ($\omega_{AS} = 2\omega_1 - \omega_2$) frequencies respectively. The equation describes all contributions to the non-linear polarisability, including those of the fundamental fields 1 and 2, in addition to combination fields oscillating at frequencies ω_{CS} and ω_{AS}.

During the coherent Raman scattering process, the fields ω_1 and ω_2, separated by energy Ω, develop side bands (caused by the changing polarisability throughout the sample) that are located at shifts of $\pm\, \Omega$. Therefore, fundamental field ω_1 produces bands at frequencies equal to ω_2 and ω_{AS} whereas ω_2 produces bands equivalent to ω_1 and ω_{CS}. Four fields, of homogenous energy separation Ω, are therefore passing through the sample.

Examining the amplitude of the polarisation at the anti-Stokes frequency, $P(\omega_{AS})$.

$$P(\omega_{AS}) = \frac{N}{m}\left(\frac{\delta\alpha}{\delta Q}\right)_0^2\left(\frac{1}{\omega_v^2 - \Omega^2 - 2i\Omega Y}\right)A_1^2 A_2^* = 6\epsilon_0 \chi_{NL} \Omega A_1^2 A_2^*$$

Where $\chi_{NL}(\Omega) = \frac{N}{6m\epsilon_0}\left(\frac{\delta\alpha}{\delta Q}\right)_0^2 \frac{1}{\omega_v^2 - \Omega^2 - 2i\Omega Y}$ 2.2.40

The non-linear susceptibility (χ_{NL}), at oscillatory frequency Ω, simplifies the expression to demonstrate the observed non-linear polarisation at the anti-Stokes frequency and describe the effect of coherent anti-Stokes Raman scattering. Similar examination of the non-linear polarisation amplitudes in the remaining fields describe the remaining lowest order Raman effects, all of which depend on the magnitude of the same susceptibility χ_{NL}.

$P(\omega_{CS}) = 6\epsilon_0 \chi_{NL}^* \Omega A_2^2 A_1^*$ Coherent Stokes 2.2.41

$P(\omega_2) = 6\epsilon_0 \chi_{NL}^* \Omega |A_1|^2 A_2$ Stimulated Raman Gain 2.2.42

$P(\omega_1) = 6\epsilon_0 \chi_{NL} \Omega |A_2|^2 A_1$ Stimulated Raman Loss 2.2.43

Driven by the same nuclear motion, the polarisations in each field are of similar magnitudes but can differ in experimentally-detected signal. This is due to energy flow in the coherent Raman process, which may occur through either dissipative or parametric processes. Dissipative processes involve energy transfer from fundamental fields to the material, such that the total energy of the fields is reduced and that of the material is raised. In contrast, parametric optical processes generate new fields without requirement for energetic exchange with the material. Energy is added or subtracted from the input fields to generate new fields while conserving the total combined field energy.

The new fields generated in the coherent scattering process are those of the anti-Stokes and coherent Stokes frequencies. The non-linear anti-Stokes field (E_{AS}^{3}) and its intensity (*I*) can be described by the following equations:

$$E_{AS}^{3}(t) = A_{AS}e^{-i\omega_{AS}t} + c.c. \qquad 2.2.44$$

$$I(\omega_{AS}) = \frac{\epsilon_0 c}{2}|A_{AS}|^2 \qquad 2.2.45$$

Considering only the lowest order coherent Raman interactions, the non-linear polarisation oscillating at ω_{AS} is the only source for the anti-Stokes field. The magnitude of this field is therefore proportional to the magnitude of the nonlinear polarisation:

$$I(\omega_{AS}) \propto |\chi_{NL}|^2 I_1^2 I_2 \qquad 2.2.46$$

Similarly, the intensity of the coherent Stokes contribution to the nonlinear polarisation is also dependent upon the intensities (I_1, I_2) of the fundamentals (ω_1, ω_2):

$$I(\omega_{CS}) \propto |\chi_{NL}|^2 I_2^2 I_1 \qquad 2.2.47$$

The homodyne-detected signal intensity is shown to be directly proportional to the square modulus of the nonlinear polarisation. The process is described as parametric since the energy of these fields is taken from the fundamental fields without exchange with the sample material. In the presence of a local oscillator (an additional field applied at either ω_1 or ω_2), an additional source of radiation at the signal frequency is present and the detected intensity of the anti-Stokes frequency is altered:

$$\begin{aligned} I(\omega_{AS}) &= \frac{\epsilon_0 c}{2}\left|E_{AS}^{(3)} + E_{AS}^{LO}\right|^2 \\ &\propto \left|E_{AS}^{(3)}\right|^2 + \left|E_{AS}^{LO}\right|^2 + \left[\left\{E_{AS}^{(3)}\right\}^* E_{AS}^{LO} + \left\{E_{AS}^{LO}\right\}^* E_{AS}^{(3)}\right] \end{aligned} \qquad 2.2.48$$

The introduction of terms on the right hand side of the equation describe new heterodyne mixing interaction between the anti-Stokes field and the local oscillator field, at the anti-Stokes frequency (E_{AS}^{LO}). The heterodyne contribution to the signal intensity becomes:

$$I^{Het}(\omega_{AS}) = 2A_{AS}^{LO}\left[Re\left\{E_{AS}^{(3)}\right\}cos\phi + Im\left\{E_{AS}^{(3)}\right\}sin\phi\right]$$
$$= 2\alpha\ [Re\{\chi_{NL}\}cos(\phi - \phi_P) + Im\{\chi_{NL}\}sin(\phi - \phi_P)]$$

Where $\alpha = \left|A_{AS}^{LO}A_1^2A_2\right|$ 2.2.49

A_{AS}^{LO} is the local oscillator amplitude, φ represents the phase difference between $E_{AS}^{(3)}$ and (real) E_{AS}^{LO} field. The phase difference between the radiated field $E_{AS}^{(3)}$ and the induced polarisation $P(\omega_{AS})$ is denoted by ϕ_P.

In the case that the local oscillator is driven at the vibrational resonance frequency ($\Omega = \omega_v$), the non-linear susceptibility (χ_{NL}) becomes purely imaginary and non-resonant contributions are ignored. Total detectable signal intensity in the anti-Stokes channel becomes:

$$I(\omega_{AS}) \propto \left|E_{AS}^{(3)}\right|^2 + \left|E_{AS}^{LO}\right|^2 + 2\alpha Im\{\chi_{NL}\}sin(\phi - \phi_P) \qquad 2.2.50$$

It is therefore demonstrated that the phase difference between the induced field and local oscillator ($\Delta\phi = \phi - \phi_P$) is crucial to the detected intensity in this simplified model that ignores the effect of propagation factors on the geometric phase difference. When the phases are matched ($\Delta\phi = 0$) the heterodyne contribution is eradicated and the detected signal is purely a combination of the homodyne anti-Stokes contribution and the local oscillator intensity. Conversely, if ($\Delta\phi = -\pi/2$) the heterodyne term becomes negative and the total detected intensity becomes less than the sum of the homodyne contributions, introducing a dissipative nature to the CARS process. Here, modulation techniques may be used to selectively detect the dissipative part of the interaction which is directly proportional to the imaginary part of the nonlinear susceptibility. For stimulated Raman processes (SRG/SRL), the ability of a phase-coherent local oscillator to modify signal intensities of probed parametric and dissipative processes is key to explaining their relative sensitivities. Stimulated Raman loss is detected in ω_1, where the source of the nonlinear field $E_1^{(3)}$ is the polarisation of the fundamental field, $P(\omega_1)$. The similarity of the frequencies of the nonlinear radiation and the fundamental ω_1 gives rise to interference such that the field E_1 acts as a local oscillator and the detected intensity of the fundamental field becomes:

$$I(\omega_1) = \frac{\epsilon_0 c}{2}\left|E_1^{(3)} + E_1\right|^2 \propto \left|E_1^{(3)}\right|^2 + |E_1|^2 + 2\beta[Re\{\chi_{NL}\}cos\Delta\phi + Im\{\chi_{NL}\}sin\Delta\phi]$$

Where $\beta = I_1I_2$ 2.2.51

Therefore, the case of $\Delta\phi = -\pi/2$ now implies that the real part of the material response is retarded by $\pi/2$ compared to E_1 and the imaginary part is out-of-phase with E_1. The detected signal intensity of fundamental field ω_1 becomes:

$$I(\omega_1) \propto \left|E_1^{(3)}\right|^2 + |E_1|^2 - 2\beta[\,Im\{\chi_{NL}\}] \qquad 2.2.52$$

The equation describes destructive interference between the induced and fundamental fields as ω_1 is attenuated by the presence of a driven local oscillator and the process becomes dissipative. In contrast, examination of the second fundamental field, ω_2, at $\Delta\phi = \pi/2$ reveals constructive interference between the driven oscillation and the applied field that gives rise to stimulated Raman gain:

$$I(\omega_2) \propto \left|E_2^{(3)}\right|^2 + |E_2|^2 + 2\beta[\,Im\{\chi_{NL}\}] \qquad 2.2.53$$

The increase in intensity in ω_2 is directly proportional to the dissipative part of the coherent Raman interaction and matches the energy lost during the SRL interaction observed in ω_1. Therefore, this heterodyne portion of the signal may be separated for detection to provide optical contrast. Stimulated coherent Raman processes SRL and SRG suffer from increased complexity of practical implementation compared to CARS microscopy due to the requirement for beam modulation in order to detect the weak energy change in the fundamental field. However, the techniques hold advantage in bearing closer resemblance to spontaneous Raman peak positions and more straightforward quantification since signal is significantly less susceptible to the background contributions arising from excitation of undesired optical phenomena in CARS microscopy, described in the next section.

2.2.3.3 Background Contributions in CARS Microscopy

Despite its blue-shift and commonly-implemented homodyne detection, a common challenge exists in the detection of CARS signal in an isolated, background-free nature. Significant background is observed in CARS experimentation, resulting from excitation of undesired optical phenomena by the applied fields. These non-linear processes directly contribute to the third-order susceptibility tensor (χ^3) and can therefore dominate non-linear contributions to the $t=\epsilon 0\chi 1Et+\chi 2Et2+\chi 3Et3+\ldots$ 2.2.32). The third order susceptibility[31] is composed of contributions from resonant (*R*), non-resonant (*nr*) and resonantly enhanced two-photon excitations (*2p*), accounting for the first, second and third term in Equation 2.2.54 respectively:

$$\chi^{(3)} = \frac{A_R}{\omega_{Vib}-(\omega_P-\omega_{St})-i\Gamma_R} + {\chi_{nr}}^{(3)} + \frac{A_{2p}}{\omega_{2p}-2\omega_P-i\Gamma_{2p}} \qquad 2.2.54$$

In this equation, ω_{vib} is the vibrational mode frequency, $\Gamma_{R/t}$ represents the half-width at half maximum (HWHM) of the Raman line and two-photon electronic transition and $A_{R/t}$ constants describing Raman and two-photon cross sections. Resonant CARS signal represents excitation of the intended vibrational mode, since the frequency of the applied fields are tuned such that the energy difference between them matches its resonance frequency. Further contributions of the third-order susceptibility are therefore non-specific and referred to as the *non-resonant background* (Figure 2.6 B-C). Non-resonant contributions arise through excitation of vibrational modes differing in vibrational frequency to the desired mode, such that the energy difference between the applied fundamentals does not match the resonance energy of the non-resonant modes. This means that interaction with the Stokes field yields relaxation into a lower intermediate state (rather than the first vibrational state in the resonance case), giving rise to an anti-stokes shifted emission from a higher energetic state than the resonance mode following excitation of the molecule by the second pump pulse. Although anti-Stokes shifted, the frequency of this emitted wave (ω_{nr}) does not match that of the resonance-driven vibration (ω_{AS}). Two-photon excitatory background arises from additive summation of two pump pulses to an intermediate energetic state close to the first excited electronic state. A high-energy fluorescence emission (ω_{2p}) results following interaction with the Stokes pulse.

Signal intensity relies upon constructive interference of CARS, occurring when the phase matching condition of field-sample interaction length (l) being less than the coherent length (l_c) is fulfilled:

$$l < l_C = \pi|\Delta k| = \frac{\pi}{|k_{AS}-(2k_P-k_{St})|} = \frac{\pi}{|k_{AS}-2(k_P+\Delta k_{P,G})+(k_{St}+\Delta k_{St,G})|} \qquad 2.2.55$$

The wave vector of each component is represented by *k* and the wave-vector mismatch as *Δk*. The final iteration of the equation accounts for the negative Gouy phase shift (hence a phase delay ($\Delta k_{P/St,\,G}$) around the central foci of excitation fields incurred upon application of the tight focussing condition (TFC)[31]. The TFC affords relaxation of the previously described phase matching condition within a collinear geometry. This is because of the high numerical aperture of the objective lens employed, supplying irradiation from a larger range of angles to compensate for the wave-vector mismatch occurring within dispersive media (as opposed to in a vacuum). The use of collinear geometry allows increased spatial resolution and aids suppression of non-resonant background. As a coherent method, CARS imaging differs from fluorescence and spontaneous Raman microscopy in that the induced polarisation assumes a well-defined phase relation with the excitation fields. Image intensity is thus the squared modulus of coherently superimposed radiation fields from different constituents within the tight focal volume and signal is calculated as coherent addition of these fields from induced dipoles[31,55]. This coherent summation of CARS fields provides large and directional signal, allowing use of low power and short acquisition times to achieve chemically-selective enhancement of Raman-active vibrational modes at high resolution. Although enhancement is not as high as that achieved in SERS, CRI lends itself as a powerful imaging tool that reduces sample preparation time and circumvents need for introducing of inorganic matter into cells, albeit at the expense of applying higher laser powers.

2.3 Enhanced Raman Scattering in Cells

2.3.1 Cell Interactions with SERS-NPs

For successful cellular investigation by SERS, selection of suitable NPs is essential. Systems must overcome barriers of NP internalisation and toxicity while maintaining desired optical properties. For *in cellulo* studies, particle diameter must be small enough to penetrate the intracellular matrix yet larger than 15 nm to achieve sufficient SERS enhancement[56]. Spherical AgNPs exhibit stronger plasmonic fields than those of Au, especially in the visible region of the electromagnetic spectrum owing to the partial Au plasmon band overlap with its inter-band electronic transitions. NP material also affects SERS detection sensitivity by variability of molecules that can adsorb onto their surface[57]. Notwithstanding this, AuNPs are more widely applied in biological studies due to their well-established and controlled methods of synthesis along with good biocompatibility and chemical stability[58]. The ability to track and detect plasmonic NPs using various analytical tools is an added advantage, especially via synthetic tuning of LSPR bands into the near-infrared region (the optical transparency window for biological tissues). Facile surface chemistry allows for easy surface functionalisation, affording not only the binding of specific delivery peptides, but other ligands such as artificial antibodies with binding affinities precisely tuned by varying the density of surface bound ligands. The ability to shield unstable drugs or poorly soluble imaging contrast agents to facilitate their delivery to the otherwise inaccessible cells and tissues of the body is augmented by AuNPs' multivalent nature[59].

From the above it can be seen that the type of NPs, choice of their surface chemistry and consequent interaction with cells (uptake, toxicity) can be critical to their utilisation for intracellular SERS. Within this section, scientific literature concerning all aspects of intracellular SERS sensing and imaging is reviewed. The journey of NPs from internalisation to intracellular SERS reporting is followed; focussing on (but not limited to) spherical AuNPs as the most widely used and understood SERS probes. The crucial roles of NP-cell interactions are discussed, including physical and diffusive routes of internalisation, biocompatibility factors such as tunability of surface properties to assist uptake and resulting toxicity. Two prevalent methodologies, the SERS-reporter and reporter-free approaches, to intracellular study are then presented. Significant and state-of-the-art studies are reported that portray the potential of intracellular SERS for numerous applications in life sciences, therapeutics and drug discovery.

2.3.1.1 Nanoparticle Internalisation Methods

The key to successful utilisation of NPs inside cells for SERS and other measurements is understanding and manipulating their uptake and distribution. Internalisation methods are generally categorised as involuntary delivery by physical methods, passive diffusion and active (voluntary) uptake.

Physical insertion methods apply a force to in order to create localised membrane pores and increase cell permeability to NPs. Electroporation and microinjection achieve this by application of electrical and physical force respectively[60]. Microinjection has been of particular interest in single cell studies, providing tight control of dosage and timing of delivery, but is highly sensitive and inappropriate use (injection location or pressure) can easily damage cellular components. Despite the tight control offered, the complexity of both procedure and instrumentation limits the technique, which is also confined to delivering only large diameter NPs[61]. Electroporation has been compared with diffusive approaches of TATHA2 peptide functionalised and citrate-capped AgNPs for facilitated and passive uptake by endocytosis respectively. Although yeast cells can tolerate high electroporation doses, severe damage was observed when used to deliver AgNPs. Free diffusion of AgNPs resulted in poor uptake which improved with TATHA2-AgNPs. A uniform intracellular distribution was also observed through passive uptake which is a requirement for detection of ubiquitously distributive molecules in cell-based biosensors[60].

Voluntary uptake of particles via endocytosis presents the most commonly employed internalisation strategy, whereby metallic species are taken up by the cell’s intrinsic machinery. This is owing to the method’s experimental simplicity, as well as allowing targeting through surface modification[10]. Successful endocytosis of SERS nanoprobes is dependent upon a number of NP and cellular parameters which directly impact interaction of the inorganic cargo with the cell, discussed herein.

2.3.1.2 The Endocytotic Pathway

Endocytosis is the active mechanism by which cargos too large to diffuse across the cell plasma membrane are internalised into endosomes from extracellular fluid. It is heavily involved in cellular uptake of macromolecules and proteins but also provides the predominant mechanism of the NP internalisation required for intracellular SERS investigations. Cellular uptake pathways are generally categorised as phagocytosis, micropinocytosis, pinocytosis and endocytosis[62–64]. Their general progression follows distortion of the plasma membrane to invaginate extracellular cargo, forming a transport vesicle containing ingested material inside the cytosol (Figure 2.7). More specifically, phagocytosis (i) is an actin-mediated process, limited to specialised cells such as macrophages and neutrophils, for engulfing large particulate matter (> 0.5 µm) or microorganisms in a non-specific manner via cup-shaped protrusion of the plasma membrane into the extracellular matrix[63,64]. Similarly actin mediated, macropinocytosis (ii) is ubiquitous to eukaryotic cells and yields engulfment of fluids and particles into large vesicles (0.2-5 µm), known as macropinosomes[62,64]. The wrapping of the plasma membrane is achieved by a ruffling action over the cargo for internalisation[63]. Pinocytosis is an endocytic process which is likened to cell 'drinking' as fluids are continuously removed from the plasma membrane into small (≈ 100 nm) vesicles[62,63]. Finally, endocytosis (iii) ingests macromolecules by invagination and pit formation into early endosomes, which may be non-specific or receptor-mediated (RME) in nature. Specificity is determined by the nature of cargo ligand-receptor binding, the free energy of which drives internalisation[62,63]. The character of such enclosed membrane species is entirely defined by

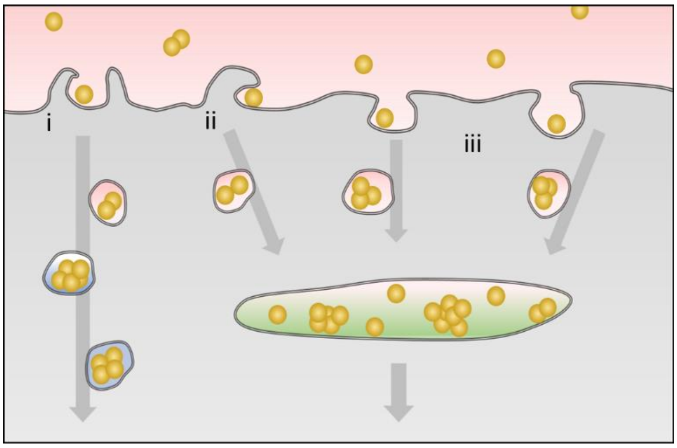

Figure 2.7 Mechanisms of solid material ingestion by cells following wrapping of the plasma membrane around cargoes that can generally be categorised into (i) phagocytosis, (ii) micropinocytosis or (iii) endocytosis pathways.

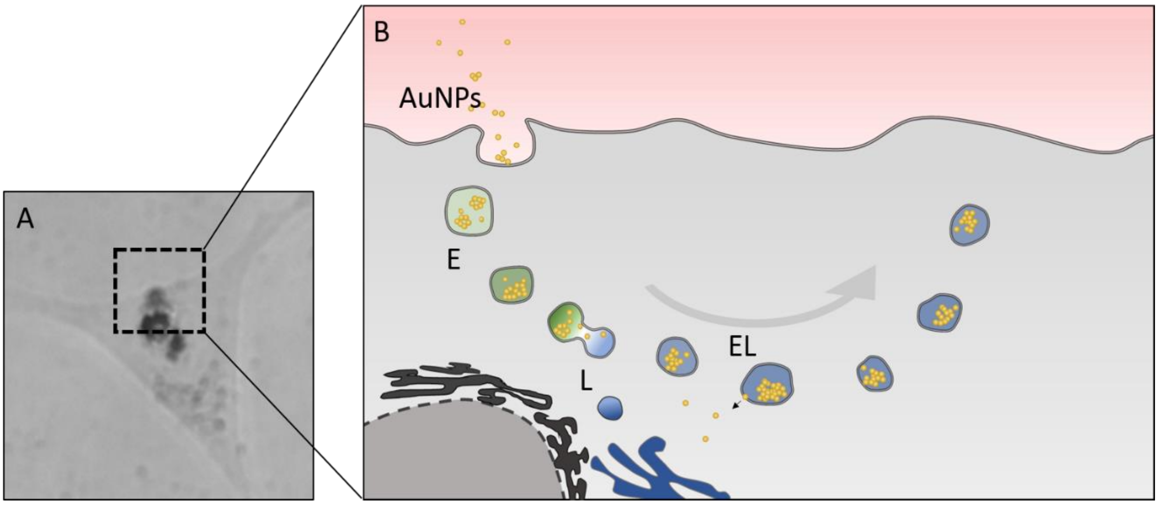

Figure 2.8 Brightfield imaging of AuNPs resident within a SH-SY5Y cell (A, dark grey), internalised following endolysosomal uptake (B) and progression from AuNP invagination of the cell membrane to endosomal formation (E, green), combination with cellular lysosomes (L, blue) and maturation into endolysosomes (EL).

the combination of molecular markers on their cytosolic surface which serve as guidance cues for vesicle transport and fusion[62].

Proteins clathrin and caveolae are responsible for RME and coat the cytosolic surface of early endosomes. Clathrin coats vesicles that mediate cargo from the plasma membrane and Golgi apparatus and adopts a three-legged structure known as a triskelion. Clathrin triskelions assemble into a basket-like network, forming coated pits on the cytosolic side of the plasma membrane and can self-assemble to produce polyhedral cages. Aided by membrane bending proteins to induce deformation, the process provides the driving force of vesicle formation. Mediating receptors are internalised with their corresponding ligands for recycling, rendering the internalisation process saturable. Incoming transport vesicles fuse to early endosomes, compartments that patrol the outer cell along microtubules to capture vesicles and sort cargoes. The duration of vesicle receipt is typically ≈ 10 mins, during which contents such as membrane and fluids are recycled with the cytoplasm while others accumulate. The structure of early endosomes comprises of vacuolar and tubular domains, containing the majority storage volume and plasma membrane surface respectively.

Early endosomes undergo maturation processes (Figure 2.8), involving the shrinkage and disappearance of their tubular domains to alter morphology as they migrate to the cell interior. A 'molecular makeover' of the cytosolic surface changes vesicle functional characteristics as it becomes a mature endosome (Figure 2.8, E). Protons are pumped inside the vesicle from the cytosol, increasing vesicle acidity (pH 4.0-5.0) to activate acid hydrolase enzymes, delivered from the trans-golgi network for macromolecule digestion[62,65]. Residency of cargos within maturing endosomes, rather than cytosolic exchange, increasingly commits them to degradation. Once at the perinuclear region, late endosomes and phagosomes fuse with primary lysosomes (Figure 2.8, L) from the golgi apparatus to form endolysosomes (EL) that contain interior cargos of both fusion partners[62,65]. Endolysosomes represent the major site of molecular digestion and degradation cells, with recycling of digested material or commitment of non-digestible components to removal from cells by exocytosis[66–68].

The exact internalisation pathway experienced by plasmonic NPs depends on their structural and physical properties, as well as the cell line involved. However, they have been shown to enter by RME[69]. To achieve prolonged residence times inside cells, NPs must avoid exocytosis through escape from endolysosomal transport vesicles. Release into the free cytosol may be achieved, along with specific organelle targeting by attachment of localisation peptides.

Uptake of plasmonic NPs by endocytosis is experimentally simple, typically following incubation of cells with NPs suspended in culture medium before washing away for extracellular NPs. Tunability is afforded by careful altering NP properties (size, shape, surface coating) and incubation parameters (concentration, time, media composition) that can be manipulated to localise SERS nanoprobes to desired cellular locations as well as to access or escape specific pathways and transport vesicles.

2.3.1.3 Manipulating Interactions

It is of great importance to understand intracellular behaviour of AuNPs for SERS probing of desired cell compartments. Extensive studies have shown that factors including size, shape, surface coating, concentration and aggregation state of NPs, cell line and exposure conditions play important roles in determining uptake and localisation[64,70]. With innovations in nanotechnology, a library of fit-for-purpose AuNPs with different physicochemical properties has been established[21,71–78].

Several factors contribute to identifying the optimal NP diameter for use. AuNPs larger than 15 nm possess sufficient plasmonic properties for electric field enhancement of scattering intensity while providing information on their localisation[79]. Additionally, NPs must also be efficiently internalised into cells. Optimal diameters for endocytotic uptake of AuNPs has been reported as ≤ 50 nm[70,80]; although this depends on a wealth of other system variables. Size dependence of uptake is attributed to ‘wrapping time’, the numerically determined time required for elevation of membrane receptor density for complete invagination of the total NP surface area[81]. Wrapping is affected by factors including adhesion ratio, membrane stretching and bending. Optimal values of wrapping time have been calculated as 2-58 s for three dimensional NPs of diameters 54-60 nm[80]. Practically, AuNPs of 50 nm diameter have been shown exhibit greatest uptake in HeLa and MCF-7 cells under normal and hypoxic conditions compared to sizes ranging 14-100 nm, showing agreement with theoretical simulations[69,82]. AuNPs of 55 nm diameter were calculated to have the fastest wrapping time, with RME receptor binding of NPs producing sufficient free energy to drive internalisation. This energy value is reduced in NPs of diameters < 50 nm, which are therefore required to cluster together for overcoming the energy barrier for uptake. Conversely, wrapping times of large NPs increase because more RME receptors are required to bind their larger surface area and generate sufficient free energy for uptake. Consequently, the number of AuNPs entering the cell in transport vesicles is reduced; with uptake rate limited by the speed of diffusion of extra receptors to the site of invagination[80,81]. Henceforth, most intracellular SERS studies conducted utilise AuNPs in the diameter range 40-60 nm.

Particle morphology can also play a key role in determining cellular interactions. The size dependence of cellular uptake has been shown to exhibit opposing trends with NP size in triangular and spherical AuNPs, alongside 20-fold increase for 72 nm triangles relative to 66 nm spheres despite possessing the same surface area[83]. Larger degrees of internalisation by healthy endothelial cells was reported in spherical AuNPs and gold nanorods (NRs) than hollow AuNPs and silicon/gold core/shell structures of matching monocarboxy-hexaethyleneglycol coatings[84]. Particle morphology is also altered in order to benefit SERS measurements (discussed later), thus presenting a trade off in shape as well as size for intracellular SERS experiments.

Cellular uptake via endocytotic pathways may be aided by applying surface modifications to NPs, facilitating their diffusion. A common requirement for surface stabilisation exists to prevent further growth or aggregation of NPs. Charged ligands such as citrate are often utilised for this purpose, with coulombic repulsion serving to keep NPs separate. However, the negative charge possessed by citrate and other ligands may produce unfavourable interactions with the similarly negatively charged cell membranes upon contact. On the other hand, small, uncharged cargos are favourable for uptake. Under biological conditions, environmental macromolecules such as serum proteins adhere to the surface of NPs, forming a coating known as ‘protein corona’[85–89]. This conjugation is observed with a red-shift of NP LSPR, decreased surface charge and increase of hydrodynamic radius[86]. The corona about NPs adopts a double-layered structure (Figure 2.9), consisting of a ‘hard’ (H), strong and directly bound, layer that displaces a ‘soft’ (S), weakly bound layer maintained by intermolecular attraction between proteins following exposure to biological media[89]. Thus, the composition and thickness of the protein corona is subject to dynamic changes with its environment that potentiates exchange of proteins by relative affinities.

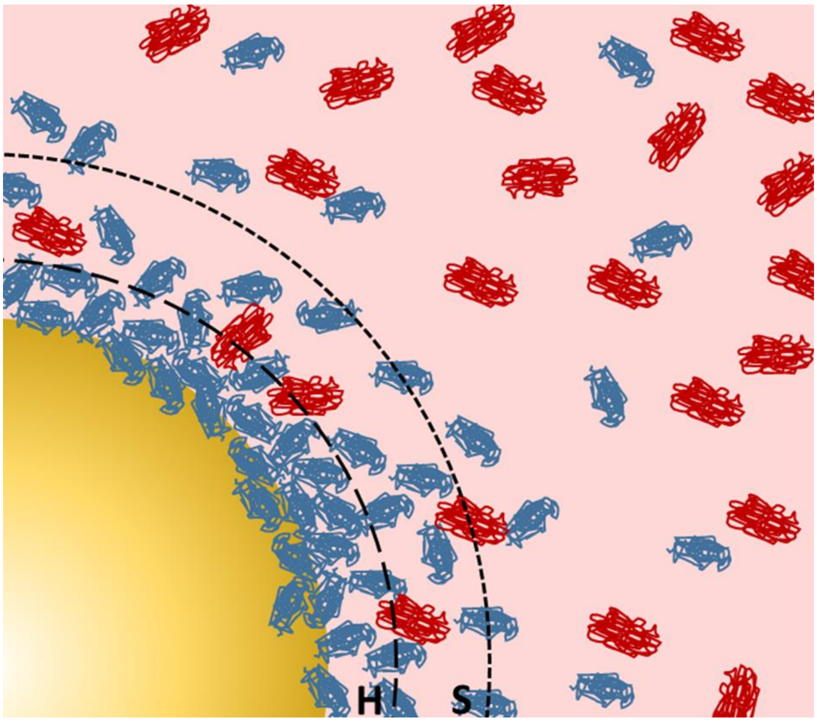

Figure 2.9 Schematic of protein corona dynamics around the surface of a spherical AuNP within changing biological media. Pre-existent proteins (blue tangles) form a hard, strongly and directly adsorbed inner layer (H) and an indirectly bound, 'softly' adsorbed outer layer (S) maintained by protein-protein interactions. The protein corona is subject to dynamic compositional changes by exchange with media proteins (red tangles) subject to concentration gradients and relative binding affinities.

The nature of the protein corona defines the biochemical identity of NPs as experienced by the cell and so plays a crucial role in NP-cell interactions. An 'adsorbome' cataloguing the plasma proteins detected at NP surfaces has been created for prediction of NP-cell interactions from analysis of their corona composition[90,91]. In biological media containing 10% foetal bovine serum (FBS), the most prevalent protein in the corona was identified as albumin, giving rise to the enhanced biocompatibility observed on its formation[86]. Protein corona of human plasma protein has been shown to reduce oxidative stress events following uptake of AuNPs of varied size and surface-charged ligands in hepatocytes compared to coronas of human serum albumin or bare particles[92]. However, decreased cellular uptake of NPs following corona formation has been reported, shown to obstruct NP recognition by scavenger receptors but promote clathrin-mediated endocytosis with dependence upon NP physicochemical properties and cell line[88,92]. Research presented in this thesis (Chapter 4) utilises ICP-MS to quantify the effect of media-protein compositions upon AuNP internalisation by SH-SY5Y cells[28].

Easy modification of the protein corona by simple media replacement offers huge advantage in tailoring of NP properties. Environmental changes such as enzymatic presence or pH are only experienced by the outer corona layers, allowing the use of organic molecules as SERS reporter molecules (discussed later) or fluorescent tags protected within. A SERS NP probe must escape the endolysosomal pathway for targeted study of the cytoplasm or organelles other than endolysosomal vesicles.

Permeability of the lipid bilayers is achieved through NP-functionalisation with cationic molecules that disrupt membranes to form NP-permeable nanopores. The choice of molecules spans cationic molecules[93–97], cell penetrating peptides (CPPs)[95,96,98–101,102], ligands[103–105], amine-containing polymers[106–108] and cationic liposomes[109–111]. The traditional method of NP functionalisation with peptide sequences involves covalent Au-S bonding between NP and cysteine residue linkers placed at the sequence C-terminus[95]. CPPs have been widely applied to target specific intracellular organelles. Many peptide sequences have been derived from natural systems used by viruses, such as the TAT peptide derived from the HIV-1 virus which potentiates cytoplasmic localisation of NPs[99,112–114]. TAT is thought to mediate cellular import via multiple routes including direct membrane passage[113,115] and intake through endocytosis[114,116]. Meanwhile, triphenylphosphonium (TPP) is a delocalised lipophilic cation commonly used to functionalise NPs for mitochondrial localisation, inducing accumulation in response to high membrane potential[95,117,118]. Localisation peptide sequences remain a key functionalisation for organelle targeting and have been designed for nuclear, mitochondrial, peroxisomal and cell membrane localisation[95–97,119,120].

2.3.1.4 Toxicity

A vital consideration to the intracellular SERS experiment is the effect of administered NPs on the host. That is, any changes or decline in key cellular processes induced by NP-cell interactions which decrease the validity of the experimental system as a representative model of the natural state. Cytotoxicity of NPs is generally attributed to the size of both single particles and clusters thereof, surface modifications, NP concentration and composition of the protein corona in addition to the cell type[121–126].

Size determines the translocation of NPs across lipid membranes into various subcellular structures possessing size exclusive pores such as nucleopores in the nuclear membrane. Nuclear pore complex structures are of around 9 nm in diameter[62,95] and NPs sufficiently small to achieve passive transport are generally considered toxic. Confinement of larger NPs within cellular vesicles may also still present toxicity, when local concentration of noble metals far exceed known LD_{50} (the concentration at which a molecule dose is fatally toxic to 50% of a population) values. Surface area to volume ratios increase with decreasing NP size, therefore increasing interactions between smaller size NPs and their environment. As such, single particles of diameters less than 2 nm induce damaging effects on cells[121,127–129].

In addition to size-based effects, homeostatic processes are also disrupted by the presence of NPs within the cell. Oxidative stress results from the production of reactive oxidative species (ROS) upon cellular recognition of ‘foreign’ inorganic material and is usually compensated for by homeostatic defence mechanisms[130]. However, at extreme metal concentrations these mechanisms are unable to maintain normal cell function, therefore causing toxicity and cell death[128]. NP internalisation is reported to induce oxidative stress in cells through a variety of pathways[125,126,130].

NP surface molecules also impact interactions and healthy cellular function. AuNPs coated with CTAB, a shape-directing agent utilised in their synthesis, present toxicity to cells (at concentrations ≥ 10 nM) through interaction of the molecule’s strong positive charge with the plasma membrane[122,129,131]. However, reduction of toxicity can be achieved by surface modification with capping agents, such as PEG[132], PAA[133], PAH[133] and polystyrene sulfonate[134]. Oxidative stress induced by exposure of HeLa cells to 1.4 nm diameter AuNPs was reduced following their pre-treatment with reducing agents/antioxidants N-acetylcysteine, glutathione, and triphenylphosphine monosulfate[128]. For this reason, ligand chemistry is defined as a critical parameter for biocompatibility and toxicity of AuNP SERS probes, alongside the earlier discussed size dependence.

In spite of numerous studies, a fundamental requirement for standardisation of investigative procedure remains before an acceptable consensus on AuNP toxicity can be reached[125,135]. For instance, the aforementioned toxicity of CTAB has also been attributed to its presence as an unbound molecule in AuNP solutions, raising the need for tight supernatant control steps to be taken for valid NP toxicity evaluation[122,133]. Two predominant causes are attributed to current ambiguity, the first being the complex governance of the phenomenon by a large number of both chemical and physical properties of the NP, along with cell type and degree of NP internalisation. The second then arises from the lack of standardisation in experimental design, execution of procedure and data treatment[125,135].

To illustrate the latter point, Fratoddi *et al*. gathered existing data from published studies conducting MTT (cell proliferation) assays of HeLa cells exposed to differently functionalised AuNPs, for analysis by metric numerical particle concentration as opposed to mass concentration or particle size[135]. This produced a simplified view of how parameters such as NP size, concentration and surface coating impact individual cell viability, concluding that size dependence is much less important than the number of particles present per unit volume (cellular concentration). Differently functionalised AuNPs behaved similarly, with NP surface coatings defining the range of particle concentrations at which toxic effects commence. Thus, there is a need for the standardisation of NP internalisation protocols and data treatment for advancing SERS as a standardised tool for intracellular study, however promising steps are being taken to achieve this[125,135].

Finally, it is important to consider the threshold at which perturbation of natural cellular processes as induced by NP exposure becomes defined as toxic. For the intracellular SERS experimentation, toxicity must be defined at the point of SERS spectral deviation from the 'normal' or minimally stressed cell states, forming a central paradigm to research presented in this thesis[28].

2.3.2 Approaches to Intracellular SERS

The first application of SERS inside cells was carried out in 1991 when Nabiev *et al*. detected the presence of antitumor drugs doxorubicin (dox) and 4’0-tetrahydropyranyl-adriamycin (THP-ADM) in the nucleus and cytoplasm of living cancer cells using AgNPs[136]. Since then, SERS has been successfully applied for detection of a vast array of biological markers and metabolites in turn, for sensing and tracking environmental changes through cellular pathways and processes. These include monitoring cellular functions[105,137–139], dynamics[140,141], enzyme kinetics[142–144], stress response[145], apoptosis[146] and cell death[147,148], probing specific compartments such as the mitochondria[118,149] and tracking of drugs released into the cytoplasm by NP carriers[104,150–154].

The cell-based SERS experiment generally adopts one of the following two methodologies: the SERS-reporter (SERS-label) approach or the reporter-free (label-free) SERS approach, key features of both approaches are summarised in Table 2.1[11,155,156]. While the SERS-reporter approach has been historically prevalent, the merits of the label-free approach have begun to emerge with concomitant advancements in computational approaches[156]. The following section will proceed to explain the fundamental concepts and review research developments in each of these two approaches.

2.3.2.1 Intracellular SERS-Reporter Research

The SERS-Reporter approach, whereby NPs are functionalised with covalently bound, strongly Raman-active, organic molecules, is the most developed intracellular SERS approach. Analyte detection is facilitated by induced changes to the reporter molecule’s SERS spectrum following changes in its immediate chemical environment. The reporter itself, or an additional recognition element, may also serve to provide binding specificity to a target for detection. The generated SERS spectrum then reveals the defined signature of the label to facilitate indirect and highly sensitive detection of the target molecule for Raman sensing applications. Examples of this include sensing of reactive oxygen species (ROS), hydrogen peroxide and hypochlorite[157]; and antioxidant glutathione (GSH)[158,159] in living cells, achieved ratiometrically by comparison of reporter spectral peaks in the presence/absence of target molecules.

The Raman-active molecule 4-mercaptobenzoic acid (4-MBA) is commonly functionalised to NPs as a SERS reporter of cellular pH, which is sensitive to changes between pH 6-8 within the cellular environment[160,161]. This is owed to spectral differences between the protonated and deprotonated forms of the molecule, which thus serves as a sensor of proton abundance for pH measurement[160]. Intracellular pH imaging has been performed throughout the cell cycle in live

SERS-Reporter Approach	Reporter-Free Approach
SERS Probe: 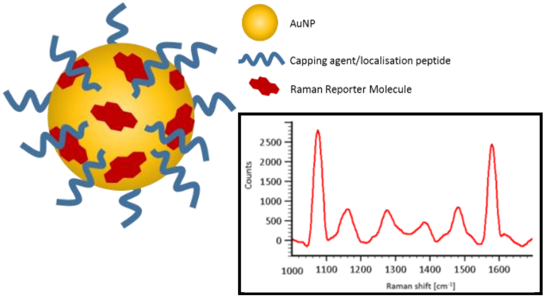 	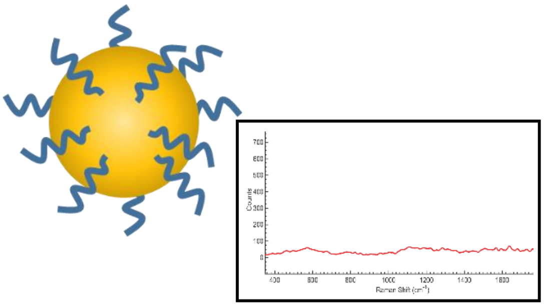
Intracellular SERS: 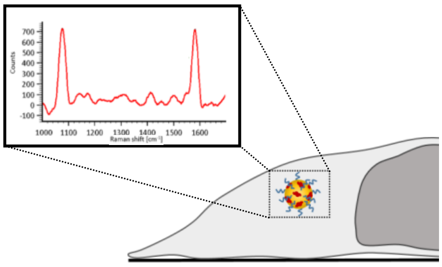 	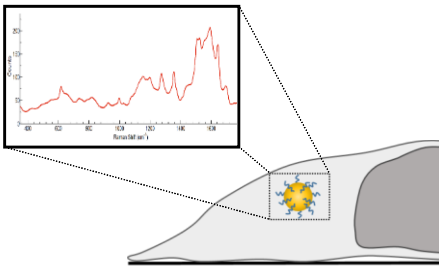
Detects changes to Raman shift/intensities of the reporter molecule spectrum- detection is inferred and specific	Samples the NP's immediate biochemical environment- detection is unspecific, direct and highly localised
Targeted sensing- simple data analysis	Datasets are rich and complex- requires careful analysis
Typically applied for specific sensing applications- cellular environmental factors (eg. pH), abundance and mapping of biomolecules/markers	More explorative nature- characterising molecular pathways and dynamics, interrogating unknowns
SERS nm-range and narrow band widths give greater spatial and spectral resolution than fluorescence for multiplexed sensing	Wealth of extractable molecular-level information available surpasses that from fluorescence
Increased functionalisation of NPs may complicate cellular interactions, producing toxicity or limiting transport by increased size	Uncontrollable aggregation of spherical NPs *in cellulo* if no capping agent is used- implications for homogeneity of SERS enhancement and reproducibility

Table 2.1 Key characteristics of SERS-reporter and reporter-free SERS approaches to intracellular experimentation. Pure and intracellular SERS-reporter spectra were obtained using reporter molecule 4-mercaptobenzoic acid (4-MBA).

human cervical carcinoma cells using a 4-mercaptopyridine Raman reporter conjugated to 40 nm AuNPs[101]. The technique also has been multiplexed with simultaneous measurement of redox potential in live EAhy926 cells. Cluster analysis permitted quantitative analysis of redox potential dysregulation, a common indicator for the progressive pathology in neurodegeneration, cardiovascular diseases and cancer[161]. Such application of multivariate data analysis techniques, particularly principal component analysis (PCA), is an incredibly powerful tool for the analysis of both SERS-reporter and reporter-free SERS sensing and diagnostic applications. PCA has been applied to improve pH sensing by para-MBA SERS reporter NPs in macrophage cells, producing a more robust model than previous ratiometric approaches[162].

The density of SERS labels on the surface of the plasmonic NP can be adjusted to experimental needs. For instance, the co-adsorption of other, undesired molecules causing spectral interference can be avoided by complete coverage of the NP's surface with the label. Additionally, physical and chemical protection of the probes can be achieved by encapsulation with a silica layer[97,163]. Tian and co-workers synthesised ultrathin silica shells[73,164,165], thus causing minimal loss of SERS signal which decreases with distance from the NP surface. Hollow AuNPs can also be protected by PEG capping, offering stabilisation and red shifting of their SPR from 700 nm to allow optimal excitation by 785 and 1064 nm irradiation[166]. Many SERS reporter molecules have been developed since the technique was established including enzymes, dyes, peptides and DNA which allow for multiplexed detection of numerous molecules using only a single laser wavelength. Multiplexing of SERS reporter functionalised nanoprobes allows simultaneous interrogation of a greater number of analytes than fluorescence microscopy, due to increased spectral resolution of Raman peaks (< 2 nm), enabling access to 10-100 unique optical signatures as provided by varying reporter molecules[167].

SERS reporter experiments benefit from the specificity of attaching a specific organic molecule to the NP and detecting its known SERS signature, suitable for various intracellular sensing applications. Stevenson *et al.* presented the first use of SERS reporter methodology to monitor intracellular activities of specific enzymes, a tool which could possibly be implemented to detect dysfunction underlying many diseases[168]. SERS signals from 40 nm AuNP-bound palladacycle reporter ligands are sensitive to carbonylation by carbon monoxide inside cells, achieving sensitivity to carbon monoxide releasing molecules of 0.5 µM in HeLa cells[169] and offering palladacycle-based SERS reporters as an analytical technique for determining pathophysiological events involved with carbon monoxide.

Due to high specificity and developed understanding, SERS-reporter methodologies have been developed for similar therapeutic applications, of particular interest in oncology. Much work has gone into the detection of biomarkers using the technique in conjunction with microfluidics[170–174], however this is mostly conducted at the cellular level. In diagnostic terms, cancer cells can be detected by the specific binding of SERS probes, functionalised with tumour cell antibodies and Raman reporter molecules at the Au surface[175,176]. Circulating tumour cells were detected in blood plasma by labelling of Ag-Au nanorods with a mixture of four SERS dyes, an 'antibody rainbow cocktail' of four breast cancer antibodies and a specific leukocyte CD-45 marker to achieve highly sensitive (1 in $7x10^6$ blood cells) detection when applied with multicolour and photothermal imaging[175]. Similarly, multicore SERS-reporter labels functionalised with epithelial cell adhesion molecule antibodies bind to MCF-7 tumour cell membranes without cellular uptake following just 25 ms exposure time, offering potential enumeration and sorting of tumour cells on microfluidic chips[174]. Identification of cancer cell lysates has also been demonstrated, utilising a 2-pyridyldithio ethylamine reporter (functionalised onto AgNPs@Si wafers) to detect changes in its SERS fingerprint induced by a thiol-disulfide exchange reaction with characteristic elevation in levels of glutathione[159].

SERS reporter methodology may be used to visualise distributions of endogenous molecules within intact cells through careful selection of NP-conjugated ligands. Gregas *et al*. targeted 4-MBA-AgNP probes to cell nuclei with HIV-1 protein-derived TAT sequence to characterise their location and produce two dimensional SERS images of PC-3 human prostate cells[177]. However, uncontrolled aggregation of spherical NPs not only causes locally heterogeneous enhancement of Raman signal by variable SERS hotspot generation, but also may prevent their internalisation or disturb cell function due to the size of agglomerates.

The heterogeneity of SERS enhancement inside cells can be circumvented with the synthesis of alternative plasmonic nanostructures. Novel morphologies offer increased homogeneity of local field enhancement through controlled or limited aggregation and self-contained intra-particle hotspots. Such morphologies include nanostars, nanoshells (Au/Si/polymer cores with plasmonic outer shells), nanorods, nanocages and nanoflowers[178]. Nanostructures, such as domes of constant diameter and separation, may also be printed onto SERS microchips[77] and tip-enhanced Raman spectroscopy involves scanning of a plasmonic tip across the analyte surface to record spectra. Au nanostars of 60-70 nm diameter, labelled with toluidine blue and encapsulated in a 30 nm coating of silica have been employed for probing of the intracellular matrix, exhibiting no aggregation tendencies but also diminished uptake compared to smaller, spherical NPs[179]. Nanoclusters formed of 2-6 AgNPs, offering controlled inter-NP gaps, have been tagged with biorthogonal alkyne ligands and conjugated dopamine molecules to yield maps of the biomolecules within single cells[180]. Similarly, study of receptor-mediated endocytosis, important in intracellular SERS experimentation, has been offered by conjugation of reporter-tagged bridgegaps enhanced Raman tags that were coated with PEG and decorated with transferrin receptor ligands for selective tracking of the pathway in live HeLa cells[105]. Depositing plasmonic NPs onto larger super-structures such that interparticle distances are controlled and relatively constant also increases enhancement reproducibility. Dox-bound AuNPs assembled around a silica nanocarrier were tracked through cancer cells by mapping of peaks of 4-MBA used as the Raman reporter, demonstrating enhanced sensitivity of SERS compared to fluorescence[181].

Improvements in reproducibility of SERS enhancement factors have led to SERS now being widely considered as a semi-quantitative technique[156]. Detection of protein cytochrome C release following in induction of apoptosis was performed with a detection limit of 0.02 µM in living human hepatoma cells[182]. The measurement was performed using dual-modality loss of SERS intensity following the protein's binding to its Au nanotriangle-conjugated aptamer, with simultaneously removal of fluorescence quenching by release of the analyte-aptamer complex.

Achieving traceable intracellular delivery of therapeutics is a key aim in SERS research and is often inferred by loss of SERS intensity of a Raman reporter molecule following payload release from the NP. Gemcitabine, used to treat breast and pancreatic cancer, was immobilised onto AuNPs by pH-sensitive amide bonds for release inside cancer cells by observing intensity loss of 4-MBA and p-aminothiophenol reporter SERS intensities[153]. AgNP-loaded, graphene oxide reporter-based nano platforms have been employed by Huang *et al.* to provide pH-dependent delivery of anti-tumour drug dox into live cells, but also to monitor its release by SERS[183]. Song *et al.* also performed successful delivery and monitoring of dox in live SKBR-3 cells using hollow, amphiphilic SERS-reporter aggregates which lose plasmon resonance enhancement of BLGA reporter molecule following pH-dependent disintegration and hence drug release in endosomes[184]. In contrast, imaging of cellular micro RNA (miRNA) expression following treatment with mir1246 has been performed using an 'off-to-on' SERS detection motif[185]. Core-satellite nanosensors consisted of an Au nanodumbell cores and AuNP satellites, which detected SERS-reporter enhancement of a conjugated miRNA-induced catalytic hairpin assembly exhibiting intensity at 1501 cm^{-1}.

The probing of intracellular chemical environments is very much a key application for SERS given its high resolution and non-destructive nature. The ability to sensitively detect, map, monitor and quantify the localisation of both endogenous and extraneous molecules at the sub-cellular level would unlock a world of new information regarding the molecular changes undertaken by live cells during a range of cellular processes. The SERS reporter methods presented here offer promising steps towards visualisation and quantification of targeted molecules across individual cells. However, the vast abundance and variety of biomolecules surrounding nanosensors go unaccounted for, disregarding detailed information available as molecular events unfold for single parameter measurement. Despite the ability to multiplex a greater number of Raman reporter molecules than fluorophores, a limitation of the technique is manifested when requiring full molecular characterisation of cellular pathways or unknown responses to cellular drug actions. The approach may also lack spectral resolution in some applications where characteristic reporter bands (such as the phenyl ring modes of 4-MBA) only exhibit small wavenumber shifts (few cm^{-1}) as a function of bound substituents[186–189].

2.3.2.1 Reporter-free Intracellular SERS

In reporter-free SERS approaches, employed NPs probe the entirety of their direct chemical vicinity, measuring the full complexity molecules present in cellular components. In reality, the affinity of molecules for NP surface chemistry (charge) will determine the composition of environments measurable by SERS. Nevertheless, a more holistic intracellular view can be obtained compared to the SERS-reporter approach, playing to the multiplex advantage of SERS and generating rich datasets that are increasingly valued in –omics styled-studies[156]. Molecules near or adsorbed onto NP surfaces/protein corona determine the measured SERS spectrum and allow for (bio)chemical sensing and characterisation, tracking cellular processes such as differentiation by DNA/RNA ratios[120]. As previously described, bonds vibrating within inter-NP hotspots experience greater SERS enhancements and consequently provide larger contributions to measured SERS spectra in a non-uniform manner, as their aggregation is largely uncontrolled inside cells. This phenomenon presents difficulty in quantifying both SERS reporter (unless the reporter is isolated within a shell) and reporter-free SERS data, however it does allow for qualitative and highly-sensitive detection of molecular compositions inside cells[190]. While developing NPs which do not require aggregation for enhancing SERS signals is an active area of research, most current work uses spherical AuNPs which become aggregated to produce high SERS signals.

Despite the simple preparation of reporter-free SERS NPs, selectively identifying molecular changes resulting from cellular processes in large and multidimensional data sets (arising from the large variety of biochemical molecules detected) can be challenging. Moreover, a lack of simple tools for extracting useful information has so far limited characterisation of fundamental cellular processes. However, when applied effectively, access to a vast wealth of chemical information within biological samples such as cells is afforded[28,120,139].

Reporter-free SERS studies have been guided towards tracking and characterisation applications. The Kneipp group carried out an early study characterising cellular compartments by reporter-free SERS in living macrophages and endothelial cells[56]. The tendency of internalised AuNPs to uncontrollably aggregate in changing chemical environments was also revealed by TEM, with dimer and trimer formation leading to increased enhancement of the Raman signal compared to individual particles[56]. Thus, controlling or even preventing NP aggregation inside cells, in order to eliminate spectral heterogeneity from hotspots, remains one of the key challenges to reporter-free SERS.

A key component of reporter-free intracellular SERS characterisation approaches is the careful application of statistical analysis methods such as PCA to reduce dimensionality in complex data matrices and unambiguously extract key information. ‘Exo-SERS’ performed using colloidal AuNPs has identified of Raman phenotypes between exosomes derived from normal and cancerous cells in a platform that utilised PCA-LDA to differentiate between 8 different cell types[191]. Au@AgNP nanoshells have also discriminated between exosomes of melanoma cells and erythrocytes, preventing distortion of SERS signatures by NP-stabilising ligands[192]. Within cells, multivariate analysis of reporter-free SERS data has demonstrated discernment of closely-related cell phenotypes in progenitor and differentiated cells, citing changes in nuclear content (DNA/RNA ratio) and increased expression and variety of proteins during morphological and structural development[120,193]. The same group combined chemometric analysis with tailored sample preparation to achieve detailed hyperspectral characterisation of endocytotic transport vesicles in SH-SY5Y cells[139]. A pulse-chase AuNP incubation approach[56,66,194], allowed SERS monitoring of molecular processes during endolysosomal maturation using PCA-LDA, including breakdown of proteins and lipids, progressively increasing acidity and degradation of DNA/RNA in lysosomes[139]. Furthermore, pseudo colour mapping of LD scores clearly depicted the identity and localisation of endosomes and lysosomes in a single cell[139].

The lack of uniformity in SERS signal enhancements must be addressed for quantitative analysis by reporter-free SERS techniques. Considerable efforts have been made in counteracting the uncontrollable aggregation of internalised AuNPs by adaptation and modification of the reporter-free NP structure. Gold lace nanoshells generate SERS hotspots between branch-like structures without aggregation, offering delivery and monitoring of hydrophobic drugs[75] with tight synthetic control of diameter relative to thermosensitive polymer gold cages[75,78] and liposome-gold nanocontainers[76]. Au-coated microchips imprinted with uniformly-spaced nano-domes have detected extraneous molecule rhodamine 6G (R6G, 1365 cm^{-1}) in human fibroblast cells, overcoming the apparent barrier of reaching reproducibly-enhancing plasmonic hotspots that were protected by rich protein corona[77].

Combinative SERS-reporter and reporter-free sensing platforms combine advantages offered by each approach. Endosomal uptake of Au nanobridged-nanogap particles was tracked in live HeLa cells using a 4, 4’-dipyridyl Raman tag, characteristic SERS peaks from which provided locational information while biochemical changes inside cargo vesicles were monitored using the full SERS spectral range[154,190]. Chen *et al.* simultaneously imaged the nucleus and plasma membrane of single HeLa cells in three dimensions by confocal SERS microscopy[167]. Nuclear characterisation and tracking of time-dependent changes in molecular compositions during apoptosis was achieved using NLS-functionalised, reporter-free AuNPs while Raman tags 4-MBA, Crystal Violet and Cresyl Violet acetate monitored localisation and detachment of specific hormone receptors in real time[167].

Along with characterisation of cellular structure and events, utilising reporter-free SERS to monitor the release and intracellular dynamics of drugs is emerging as a key application area. This is particularly relevant for delivering Raman-active, small molecule therapeutics which have a distinctive signature. While relevant to many diseases, most current examples are in oncology and often exploit the pH-sensitive nature of NP-drug binding. Inherent drug fluorescence offers dual mode monitoring intracellular drug delivery.

AuNPs functionalised with hyper-branched polymer and pH-sensitive Schiff-base bound doxorubicin (dox) have offered strongly enhanced SERS-signals while drug fluorescence intensity remained quenched by the AuNP[195]. Upon intracellular drug release from the NP, fluorescence quenching was removed that accompanied loss of SERS drug detection for complementary inference of delivery[195]. Presenting both Raman activity and inherent fluorescence, dox is often used to demonstrate SERS monitoring of drug delivery. Dox-coated bio-hybrid AuNPs functionalised with anti-HER2 antibody and cell-penetrating TAT peptide have allowed mapping of the drug-NP complex across cells by quantifiable loss of dox SERS detection following release[196]. Au nanorods functionalised with dox-conjugated aptamers have been targeted to nuclei of HepG2 cells, similarly indicating release by fluorescence while monitoring subsequent protein and DNA damage within nuclei by reporter-free SERS nature[104]. 6-mercaptopurine (6-MP, leukaemia therapeutic) has been conjugated to the Au surface of asymmetric Janus particles for pH-dependent drug release into lysosomes, also containing a silica-bound dox/CMR FRET pair that allowed fluorescence imaging of dox following displacement at FRET donor CMR by cellular glutathione[197]. Delivery of anticancer agent mitoxantrane (MTX) has also been achieved using Au nanostars for combined detection by SERS, FTIR and confocal microscopy, while AuNP dimers encapsulated in silica microtubules performed *in vivo* MTX detection in murine models that was accompanied by 4-MBA SERS reporter pH sensing[198,97]. AuNPs are of interest as novel drug carriers even in absence of SERS measurements, owing to inert nature and reportedly increased efficacy and bioavailability of drug payloads[97,195–198]. Therefore, the opportunity to simultaneously monitor drug localisation and effects could be of great utility in pharmaceutical discovery.

While inference of drug release by SERS intensity loss is highly useful, the major advantages of intracellular SERS are not fully utilised. That is, increased spatial and molecular resolution accompanying the richness of molecular information provided by single experiments. Moreover, most drug molecules are not fluorescent in the visible range, precluding ubiquitous use of multimodal SERS-fluorescence platforms. An alternative approach is offered in interrogation of intracellular drug dynamics by reporter-free SERS independently in an assay-based platform. Pre-incubation of cells with SERS NPs holds potential for characterisation of cellular response to subsequently administered drugs for which mechanisms of action are poorly understood, as well as directly detecting drug localisation and metabolism at intended intracellular targets.

A recent application has characterised varying biomolecular changes accompanying both photothermally and chemically-induced apoptosis in live cells using mitochondria-targeting TPP-modified AuNPs[118]. Induced variation of SERS spectra included decreased intensity of disulphide bond stretches, increased beta-sheet protein vibrations and detection of cytochrome C released following treatment with a pyruvate dehydrogenase kinase inhibitor. Furthermore, the apoptotic response of HeLa cells to treatment with cordycepin (an antimetabolite and antibiotic with suspected antineoplastic activity) was similar observed by SERS using 64 nm AgNPs[148]. Different stages of apoptosis were categorised using PCA, while significant decreases of RNA mode intensities suggested that the poorly-understood mechanism of drug action involved interference of RNA production that could be caused by restraining translation of RNA-encoding ribosomal proteins. As such, intracellular SERS is demonstrated as a useful tool for delineating drug action mechanisms in anticancer screening applications.

Zhang *et al.* has demonstrated microfluidic delivery and immobilisation of single cells for characterisation of cellular compartments and chemical changes during ionomycin-evoked Ca^{2+} flux response, used to stimulate cellular production of proteins[199,200]. Thus, *in situ* SERS monitoring of protein expression dynamics is offered in a continuous flow format of increased throughput of sequential measurements that are required in modern industrial research[199].

Reporter-free SERS has been employed to directly observe the dynamics of non-fluorescent drug molecules 6-MP and methimazole (MMI) inside living HeLa cells using AgNPs[201]. The internalisation and distribution of 6-MP and MMI was confirmed by recognition of vibrational modes at 862 and 1360 cm^{-1} respectively, achieving a lower detection limit of 1 nM for 6-MP and determining that 6-MP was metabolised faster than MMI by ratiometric comparison of the disappearance of the drugs' respective vibrations[201]. Albeit using AgNPs and drug structures with known affinity for silver adsorption, the study provides an excellent example of the direct drug detection power possessed by reporter-free intracellular SERS. In an assay-based format, this approach holds enormous potential to provide insights into drug delivery and cellular dynamics. This new knowledge in live, intact cells regarding compound bioavailability, localisation and metabolism would prove invaluable to pharmaceutical industry, elucidating the pharmacodynamic properties of drug candidates to improve efficacy and clinical outcomes.

2.3.2.2 Intracellular SERS: Conclusions and Outlook

As a non-destructive, highly sensitive technique capable of sub-micron imaging resolutions, SERS provides a useful tool for interrogation of the intracellular environment across biomedical research. Acquisition times can be optimised down to the sub-millisecond range, sufficient for even single molecule detection[25,27,202]. Under appropriate laser powers, absence of signal deterioration effects such as photo-bleaching also potentiates live cell investigations over prolonged durations. Despite a requirement for standardisation of toxicity studies[135], the employed nanostructures - particularly those of gold - appear not to significantly reduce the viability of live cells. Intracellular SERS remains a versatile and fast-paced field attracting high levels of interest with an ever-growing body of research. Advances in nanotechnology have led to an increasingly varied library of SERS active structures, tailored to addressing the difficulties of *in cellulo* experiments such as cellular entry, pH dependent aggregation and targeting of specific compartments.

It is clear that the choice of intracellular SERS technique employed is highly dependent on not only the experimental system but also the data required. SERS reporter studies benefit from simplicity of data analysis, high specificity and high spectral resolution to allow multiplexing of large numbers of unique optical signatures. The discussed studies offer reporter-based SERS as an effective tool for the imaging of molecules and proteins with known vibrational signatures, as well as relatively simple quantification of cell characteristics[160,161,169]. The approach has matured to therapeutic application with multipurpose nanostructures, which not only detect and monitor but deliver hydrophobic drug cargos into intracellular compartments[184].

Reporter-free SERS has been less widely developed and is more suited as a powerful means of probing complex cellular processes due to the enhanced wealth of information extractable from single measurements. The opportunity cost of simple nanosensor design lies in requirement for careful processing and analysis of experimental data that is necessary for accurate and unambiguous molecular-level process characterisation. Such characterisation has however been demonstrated of endocytosis and apoptosis[139,203]. Combination of label-free and SERS reporter techniques has yielded comprehensive findings that encompass advantages of both formats.

Future developments in intracellular SERS will be of particular interest to the pharmaceutical industry, for elucidating new drug targets in both healthy and pathogenic cells. Applications can be developed in both characterisation of unknown mechanisms of drug action, in addition to meeting requirement for direct intracellular drug distribution measurements. Microfluidics will also play a major role in providing tightly controlled, reproducible and ultimately higher throughput cell diagnosis by SERS, while continual development of increasingly-sophisticated data analysis algorithms will increase both throughput and scope of reporter-free SERS experiments. These avenues should for both development and implementation of highly powerful intracellular SERS techniques for drug discovery and wider life science applications.

2.3.3 Coherent Raman Microscopy in Bioimaging

2.3.3.1 Intracellular CRI Microscopy

Non-linear imaging is a growing tool in biomedical research, with CRI technologies often employed in multimodal approaches with two-photon fluorescence (TPF) or second-harmonic generation (SHG) imaging. The approach benefits from fast acquisition times, large sampling areas, chemical selectivity and high spatial resolution. Biomolecules regularly imaged by CRI include lipids (CH_2, 2845-50 cm^{-1}) proteins (CH_3, 2930-50 cm^{-1}) and DNA (CH, 2965-75 cm^{-1}, PO_2-, 1095 cm^{-1})[204]. Imaging is often performed in the C-H stretching region (2700-3100 cm^{-1}) of the cell Raman spectrum due to strong signal intensities and discrimination of protein and lipid content[205]. Considered with the ease of sample preparation from biopsy, CRI has rapidly become an established tool for tissue imaging. A large number of applications have arisen in detection and diagnosis of cancer within human and murine models, including measuring glioblastoma infiltration using quantifiable image-derived parameters such as tissue cellularity, axonal density and protein/lipid content ratios[204,206–210]. The quantitative nature of SRS, possessing a linear relationship of signal intensity to analyte concentration, has also permitted multiplexed measurement of chemical concentrations of blood, lipids and protein in *ex vivo* skin tissues[211]. In addition to tissue imaging, *in vivo* microscopy of *C. elegans* has been established with particular focus paid to abundance and dynamics of lipid density[212–214]. However, subcellular study forms the focus of this thesis, studies of which are summarised in the following discussion with reference to possible applications in pharmaceutical research.

Early CARS imaging of internal cellular structure was performed by the Xie group, observing DNA backbones during live, unstained fibroblast cell metaphase and aliphatic CH vibrational modes during interphase and apoptosis. Forward detected (F-CARS) was used to observe features similar or larger than the excitation wavelength, while epi-detection revealed smaller features with high contrast[215]. The same group also achieved polarisation-sensitive CARS imaging in live cells and tracked the dynamic changes occurring in lipid-droplet (LD) distribution during cellular differentiation[216,217]. This early work demonstrated the non-perturbative-nature of CARS imaging as a key advantage in observing realistic cellular dynamics, with LD aggregation found to be induced by the use of Oil Red-O fluorescent LD stain[217]. Using laser exposures optimised to avoid photodamage to cells, LD transport was also characterised by CARS while simultaneous TPF imaging suggested that interaction between LDs and mitochondria may be facilitated by high LD motility[218]. The imaging of lipid structures, particularly LDs, represents a major functionality of intracellular CARS imaging owing to the high optical contrast offered by aliphatic CH vibrational modes in the region ≈2850 cm^{-1}. As a result, study of adipocytes using the technique has been intensive. Adipogenesis is the differentiation of pre-adipocytes into adipocytes, a process which has been interrogated by CARS to observe responses to various conditions and quantitative parameters of LD dynamics[219–222]. Similar contributions to stem cell differentiation and tissue engineering have been made by monitoring calcium hydroxyapatite (PO_4^{3-}, 959 cm^{-1}) during osteogenic differentiation[223]. Lipid imaging by CARS has also quantified variation in lipid content of mammalian oocytes between species and developmental stages[224].

SRS microscopy offers reduced background interference compared to CARS by avoidance of non-resonant background contributions. As such, a more diverse range of chemical vibrations may be successfully probed. SRS has allowed observation of mitotic chromosomal dynamics using the C-H vibration of deoxyribose (2967 cm^{-1}) in synchronised MCF-7 cells, developed to perform mitotic counting in proliferating mouse tumour tissue[225]. Utilising the quantitative nature of SRS microscopy, measurement of the local concentrations of neurotransmitter molecule acetylcholine has been achieved at the neuromuscular junctions of *cutaneous pectoris muscle* in a frog model[226]. The C-N symmetrical stretch (720 cm^{-1}) arising at the molecule's quaternary ammonium group was imaged using frequency-modulated and spectrally-focussed SRS to obtain readings of 12.9 and 5.7 mM before and after electrical stimulation of the junctions.

A useful tool in CRI investigation of cell metabolism is labelling of biomolecules, in order to provide distinctive Raman vibrational modes that deviate from innate cellular compositions. Approaches involve either incorporation of isotopically-substituted moieties to shift vibrational frequencies or labelling of compounds with spectroscopically biorthogonal alkyne or cyano- tags.

As such, SRS microscopy of D_2O incorporation has allowed imaging of lipogenesis and protein biosynthesis imaging inside cells, *C. elegans*, zebrafish embryo and mouse tissue xenografts[214]. At the intracellular level, changes in anabolic metabolism of amino acids, glucose, fatty acids and choline have been observed following epithelial-mesenchymal transition of MCF-7 cells by SRS following incorporation of deuterium and alkyne Raman labels[227].

Stimulated Raman microscopy has been utilised to achieve ratiometric imaging of proteome degradation in living HeLa cells using a ^{13}C phenylalanine isotope to measure intensity decay ratio between original and nascent proteomes[228]. Similarly, incorporation of a glucose-d7 isotope, has afforded measurement of lipogenesis in pancreatic cancer cells and D_2O has potentiated measuring of metabolic activity in biofilms following treatment with antibacterial agent ciprofloxacin[229,230]. Alkyne tagging, meanwhile, of mitochondrial probes has been utilised to perform ratiometric SRS imaging of H_2S within live cells, while a tagged-thymidine analogue has been employed to visualise DNA synthesis[231,232]. Significantly, phenyl-diyne tagging was combined with the quantitative nature of SRS microscopy to afford monitoring of cholesterol storage in living CHO cells, achieving 31 µM sensitivity and visualising redistribution of cholesterol from lysosomal accumulation to storage within lipid droplets following chemical intervention[233].

SRS has been presented as capable of replacing fluorescence staining in a number of traditional biological applications. The optical colour boundary of fluorescence microscopy can be overcome with modern synthesis of Raman-active dye libraries for super-multiplex imaging using electronic pre-resonance SRS microscopy[205,234]. Label-free cell flow cytometry has also been demonstrated at high speed (140 cells s^{-1}) to identify circulating tumour and blood cancer cells from whole blood and peripheral blood mononuclear cells in mixed samples[235].

2.3.3.2 CRI in Drug Discovery

In terms of pharmaceutical development and screening applications, intracellular CRI microscopy remains in its infancy, predominantly owing to its recent development. Combination of CRI techniques with other non-linear imaging modalities has proved useful in imaging of cellular interactions with exogenous molecules. Study of MCF-7 breast cancer cells has demonstrated lipid (membrane) and DNA (nucleus) structures by probing wavenumbers 2845 and 1095 cm^{-1} respectively, the former of which was combined with doxorubicin's TPF signal to observe differences in intracellular drug distribution between chemi-sensitive and -resistant cells[222,236]. Combined non-linear optical microscopies also find utility in assessment of novel drug delivery systems. Poorly understood cell interactions with drug micro-/nanocrystals were imaged using combined F-CARS imaging of macrophage cellular structure (2845 cm^{-1}) and TPF of prodrug paliperidone palmitate crystals in three dimensions[237]. The crystals (large in relation to excitation wavelength) were observed both adsorbed to the cell surface and internalised into cytoplasm by phagocytosis, providing insights into subcellular drug dynamics if not directly detected by CARS itself. Similarly, polymeric mesoporous silica NPs, which perform pH- and photo-activated drug delivery, have been shown to internalise into MCF-7 cells using CARS imaging of intracellular structure and TPF of drug-mimic rhodamine B[238]. The technique has also been used to image TiO_2 and Au nanomaterials inside cells to assess uptake and associated toxicity effects of such drug-delivery materials[239].

Applied in isolation, tag-free CRI remains mostly limited to visualisation of biomolecular response to drug administration. As such, LD abundance remains a key measurement in CARS microscopy. Quantified increase in LD abundance with incubation time has characterised intestinal epithelial cell monolayers that are cultured upon membrane inserts for use in intestinal drug permeation testing (Caco-2 cell permeability assay)[240]. Increasing cytosolic LD abundances have also been identified as a marker of MCF-7 cell stress and apoptosis in response to chemotherapy drugs etoposide, camptothecin and kinase inhibitor staurosporine[241]. The parameter has similarly afforded RNAi screening for fat regulatory genes in *C. elegans* models, representing a mature platform with direct pharmaceutical application[213].

As with metabolic studies, isotopic substitution or Raman-reporter functionalisation of exogenous molecules have demonstrated strong ability to simplify CRI experiments by providing unique vibrational signatures. Deuterium-labelling of polymeric drug carriers (0.6-1.4 µm) has allowed their visualisation by E-CARS within mouse liver sections, distributed in the intercellular space between hepatocytes but within the cytoplasm of Kupffer cells, informing understanding of drug carrier biodegradation and clearance pathways[242]. Quantitative concentrations of accumulated, deuterated surfactant molecules have been measured inside lung cells, revealing that induced cell lysis occurred prior to surfactant adsorption to cell plasma membrane and trafficking into the cytoplasm[243]. Similarly, SRS has been employed to visualise the distribution of polymeric NPs labelled with deuterium, alkyne and cyano- tags within HeLa cells and absorption of MoS_2 nanosheets into live cells[205,244,245]. Thus, development of CRI technologies can delineate interactions between cell and inorganic material, for development of platforms that are complementary to improving drug payload delivery by novel nanoparticle assemblies.

The low number of studies reporting direct intracellular compound localisation using CARS arises from poor sensitivity, limited by non-resonant background contributions. Therefore, isotopic substitution or Raman-reporter tagging offer routes for CRI assessment of drug uptake and localisation inside cells. Even then, CARS study of deuterated anti-malarial naphthylisoquinoline was reported to only achieve detection at 50-100 mM in DMSO[246] which is insufficient for the µ-nM ranges observed within cellular environments.

SRS-based studies have, however, proved more successful. Deuterium-labelled docosanol (topical treatment for *Herpes labialis*) was visualised to accumulate within the cell membrane periphery in keratinocytes and in dense, punctate regions of fibroblast cell cytoplasm by fibre supercontinuum-based SRS microscopy (2000-2500 cm^{-1}) following a 24 h incubation period[247]. Tagging of ferrostatins with a diyne-reporter moiety has also provided new insights into their relatively-unknown molecular mechanism of ferroptosis suppression by SRS microscopy, revealing accumulation within HT-1080 cell lysosomes, mitochondria and endoplasmic reticulum[248]. The same study concluded that neither lysosomes nor mitochondria bear functional relevance to the suppression mechanism, thus unveiling off-target localisation of drug compound that could prove a valuable capability in drug-candidate screening. While these studies demonstrate the capability of SRS microscopy to perform intracellular imaging of compound localisation, they are not free of pre-requisites that selected molecules require either structural sites for isotopic substitution or addition of molecular tags that may still impact compound properties, despite being of smaller size than fluorescent labels.

Tyrosine kinase inhibitors (TKIs) remain a key drug class in treatment of chronic myelogenous leukaemia. SRS has previously demonstrated visualisation of leukaemia cell model proliferation, characterised by accumulations of cholesteryl esters, following co-administration of TKI Imatinib and cholesterol esterification inhibitor avasimibe[249]. The most significant measure of intracellular compound dynamics by CRI was performed in observation of TKIs Imatinib and Nilotinib (20 µM) administered to murine BaF3 cells using hyperspectral SRS microscopy[250]. The region 1200-1600 cm^{-1} was imaged, observing 1000x concentration enrichment (> 20 mM) of drug within cell lysosomes which was reduced in Imatinib following co-administration of the compound with chloroquine. Cells were imaged at durations of 1, 2, 4 and 8 h, with quantification achieved by subtraction of control lysosomal signal intensities and comparison against calibration solutions. The significance of this study is found in its sole existence as a demonstration of quantitative drug concentration mapping inside cells by CRI without use of secondary techniques, isotopic substitution or fluorescent or Raman-active labels. Development of the system would require enhanced spectra resolution (20-30 cm^{-1} was achieved) and performance upon the same live cells throughout the time-course for tracking of intracellular uptake, distribution and clearance.

In summary, evaluation of existing literature presents CRI approaches as a tool with high potential for label-free interrogation of the intracellular environment that is still to be fully realised. The vast majority of articles discussed were published after the commencement of the presented research studentship, verifying the rapidly-growing nature of the field. As a result, the lack of commercially-available coherent Raman microscopes means that research produced between groups is highly variable in terms of developmental maturity. Furthermore, establishment of fundamental parameters such as tolerance of live cells (and their homeostatic mechanisms) to the high laser powers required must be standardised across the field to verify experimental validity.

Despite this, common themes are presented in the requirement for CARS microscopy to be developed in ways that overcome reduced sensitivity brought about by non-resonant background contributions, while the observation of specific exogenous compound dynamics inside cells is still largely reliant upon some degree of labelling. Despite this, potential to qualitatively measure intracellular drug concentrations in a direct, label-free manner is demonstrated by a very small number of studies, the most significant of which being presented by Fu *et al*[250]. Similarly, monitoring the response of biomolecules to drug treatments should not be overlooked and can offer significant new insights for drug discovery processes, exemplified by CARS microscopy of lipid droplet dynamics. Thus, CRI is presented as a tool that can offer not only visualisation of intracellular compound concentrations but a diverse range of quantifiable measures that can be tailored to specific research requirements.

Chapter 3 Methodologies

Methodologies related to study-specific experiments are detailed within relevant manuscript-styled chapters provided in this thesis. Thus, the following section will provide an overview of the central techniques used to establish the enhanced-Raman platforms investigated. General cell culture and AuNP administration (in the case of SERS) protocols are described, along with detail of the employed commercial Raman microscope, home-built CARS multiphoton microscope and adaptations made to perform SRS microscopy. Data processing and associated chemometrics are explained. Lastly, fundamental investigations that informed establishment of the intracellular SERS experimental platform applied in this thesis are presented and discussed.

3.1 Cell Culture

Within this thesis, stable human cancer cell lines SH-SY5Y (neuroblastoma) and MCF-7 (epithelial, breast cancer) were selected for study owing to their ability to voluntarily internalise AuNPs and healthy-state presentation of cytosolic LDs respectively[120,251,252]. Thus, SH-SY5Y cells were studied by SERS while MCF-7 cells were investigated using CRI microscopy. Both cell lines represent clinically-relevant human cancer models, with oncology remaining the predominant research area in small molecule drug discovery.

Both cell lines were cultured in Dulbecco's modified Eagle's medium (DMEM, Gibco), supplemented with foetal bovine serum (FBS, 10 % v/v, Gibco) and penicillin-streptomycin antibiotic mixture (Pen-strep, 1 % v/v, Gibco) and incubated at 37 ^{o}C in an atmosphere containing 5% CO_2. Cell cultures were passaged every 3-4 days, routinely tested for mycoplasma infection and were discarded at high passage numbers (> 20). General sample preparation involved seeding of cells onto poly-d-lysine coated coverslips (ϕ = 16 mm) or experiment-specific plastic/glassware. Following 24 h incubation to allow cell attachment (Figure 3.1 A), SH-SY5Y cells were differentiated using retinoic acid (RA, 10-20 µM) in low-serum (1-5 % FBS) media for a minimum of 72 h. The purpose of the differentiation step was primarily to limit cell proliferation such that cell numbers did not drastically increase during AuNP incubations (see next), maintaining a stable AuNP concentration per cell. RA treatment of SH-SY5Y cells yields morphological N-type differentiation to grow neuronal-like processes extended for the cell body (Figure 3.1 B) and has also been shown to increased resistance to toxin-mediated cell death than the undifferentiated form[251,253]. Attached MCF-7 cells (Figure 3.1 E) were either dosed as per specific experiment or imaged as either live or fixed samples (Figure 3.1 F).

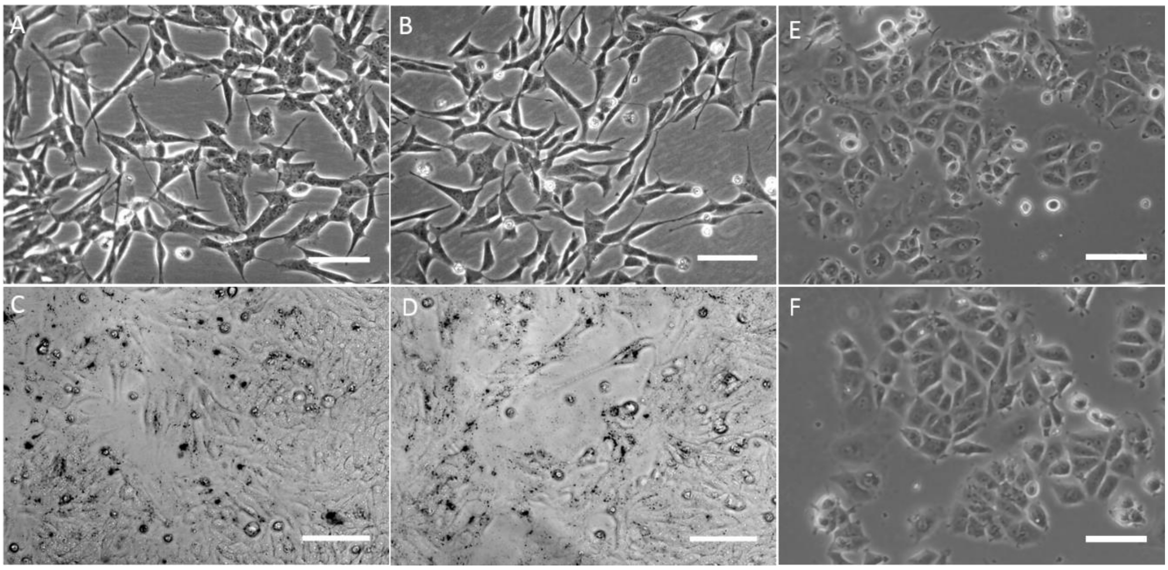

Figure 3.1 Cell appearance of cultured (A-D) SH-SY5Y and (E-F) MCF-7 cells. SH-SY5Y cells were (A) seeded and allowed to surface-adhere for 24 h before (B) RA differentiation for 72 h, (C) internalisation of AuNPs and (D) fixation by paraformaldehyde. MCF-7 cells were (E) seeded and allowed to attach to substrate before (F) fixation. Phase contrast images (A, B, E, F) allowed clear morphological discernment of cells, scale bar = 40 µm. (C, D) Simple brightfield images of AuNP-treated SH-SY5Y emphasised visualisation of internalised AuNP aggregates (dark spots), scale bar = 100 µm.

3.1.1 AuNP Administration

Literature review has emphasised that the nature of AuNP uptake into cells is highly variable with altering a number of NP, cell and incubation protocol parameters. The effect of incubation parameters upon both AuNP uptake and subsequent SERS measurements is investigated in Chapter 4 of this thesis. Typical AuNP incubation protocol involved washing and resuspension of colloidal AuNPs (ϕ = 60 nm, BBI international) into phosphate buffered-saline (PBS) solution and then fresh DMEM, containing a decided amount of FBS (1-10 % v/v), at the desired concentration ($[\mathrm{AuNP}]_{\mathrm{Incub}}$). Previous differentiation medium was removed from SH-SY5Y cells, which were washed in PBS solution before addition of the AuNP-doped media and returning to incubation for a desired duration for uptake. On completion of the AuNP treatment (Figure 3.1 C), cells were either fixed (Figure 3.1 D) or advanced to the next stage of the experiment (e.g. application of analyte or fluorescence staining).

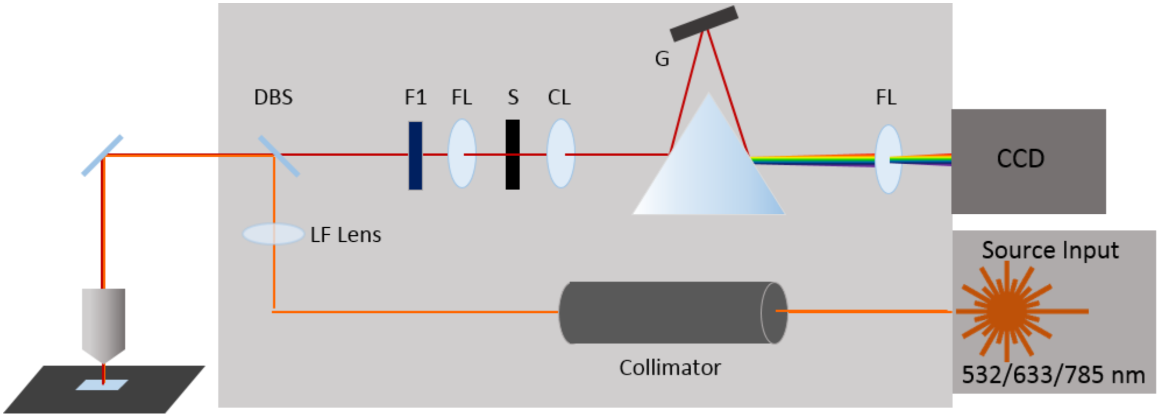

Figure 3.2 Schematic of the Raman spectrometer used to perform spontaneous Raman and SERS experiments. Monochromatic radiation (532, 633 or 785 nm) was expanded and collimated before being focussed onto samples using an upright microscope. A line focussing (LF) lens was employed for Streamline® mapping acquisitions. Scattered light was collected in the epi-direction, transmitted by a dichroic beam splitter (DBS, long pass, varied with excitation wavelength) and filter (F1, LP) to exclude Rayleigh and anti-Stokes scattered photons for separation into its constituent wavelengths by a diffraction grating (G, 1200 l/mm) focussing by a lens (FL) onto a CCD camera detector.

Fixation of both SH-SY5Y and MCF-7 cell lines was performed using paraformaldehyde (4 % in PBS, 15 mins) before washing and storage (5 ° C) in PBS for analysis. Paraformaldehyde was selected for fixation owing to minimal perturbation of Raman spectra collected from cells[254].

3.2 Raman Scattering Microscopes

3.2.1 Raman Microspectroscopy

A practical advantage of the intracellular SERS platform is that introduction of SERS nanosensors into cells is performed as part of the sample preparation process, such that no expensive SERS-specific instrumentation is required and measurements are acquired on a commercially available Raman microscope.

Raman and SERS measurements presented in this thesis were performed on a Renishaw InVia Raman microscope system (Renishaw plc, Wotton-under-Edge, UK), fitted with an upright Leica DM 2500-M brightfield microscope. The system was equipped with three laser input lines, of wavelengths 532, 633 and 785 nm. Laser radiation (Figure 3.2**,** orange path) enters the system for beam collimation and expansion before reflection by an excitation-appropriate dichroic beam splitter and focussing incident onto the sample by an objective (varied by experiment). Radiation scattered in the epi-direction (red path) was collected by the same objective, with red-shifted photons (> 100 cm^{-1}) transmitted by a long pass edge filter to exclude Rayleigh and anti-Stokes shifted radiation. A diffraction grating (1200 lines/mm, 1.7 cm^{-1} spectral resolution) dispersed Stokes-shifted photons into their constituent wavelengths and onto a master Renishaw Peltier cooled charge coupled detector (CCD, 1024 pixel x 256 pixel). Renishaw Wire (version 3.4) software was used to control acquisition parameters, microscope settings and a Renishaw automated x-y-z stage. An internal silicon wafer (Raman shift 520 cm^{-1}) was measured as a reference to calibrate system performance between experiments.

Measurement formats include single point static and extended scans, conducted over short wavenumber range about a midpoint or a larger, limit-defined range respectively. Point map scans are static scans performed at points of defined separation within a defined area, whereas Streamline mapping scans disperse incident radiation into a line-shaped area using a focussing lens employed between the collimator and dichroic beam splitter. Larger sample areas are illuminated with division of intensity and recording multiple spectra within, before moving to the next defined spatial interval is beneficial in performing continuous mapping of large sample areas. Streamline mapping achieves high scan speed but with lower average intensity, since laser power is spread over a larger area than in single point scans. Acquired spectra were saved in Renishaw's Wire data file (.wdf) format and converted to text (.txt) files for subsequent cross-software processing and analysis steps.

3.2.2 Coherent Raman Scattering Microscopy

The multiphoton imaging system employed in this thesis (Figure 3.3) was built in-house, customised to research requirements with two-channel photomultiplier tube (PMT) detection. A fibre laser source (Emerald Engine, APE, 1032 nm, 2 ps, 80 MHz) produced two fundamental pulse beams, one directly providing Stokes beam excitation. The second output beam was frequency-doubled to 516 nm to provide the Pump field for tuning with an optical parametric oscillator (OPO, Levante Emerald, APE, 650-950 nm). The Stokes beam passed through a half wave plate for transmitting only light of desired polarisation with subsequent dumping of excess by a polarisation beam splitter (PoBS). A delay stage tuned the Stokes path length for achieving temporal overlap of Stokes pulses with the desired pump wavelength at the sample. The frequency-doubled, 516 nm pulse drove the OPO to obtain tunable pulse wavelengths (usually 650-1000 nm) for probing of specific molecular vibrations (matching $\omega_{AS} = 2\omega_{Pu} - 1032$ nm). Following similar dumping of incorrectly polarised radiation, the pump beam was filtered (LP, F1) and combined with the Stokes beam by a dichroic beam combiner (DBC, SP, 970 nm). The combined, spatially and temporally overlapped radiation was collinearly directed, via a

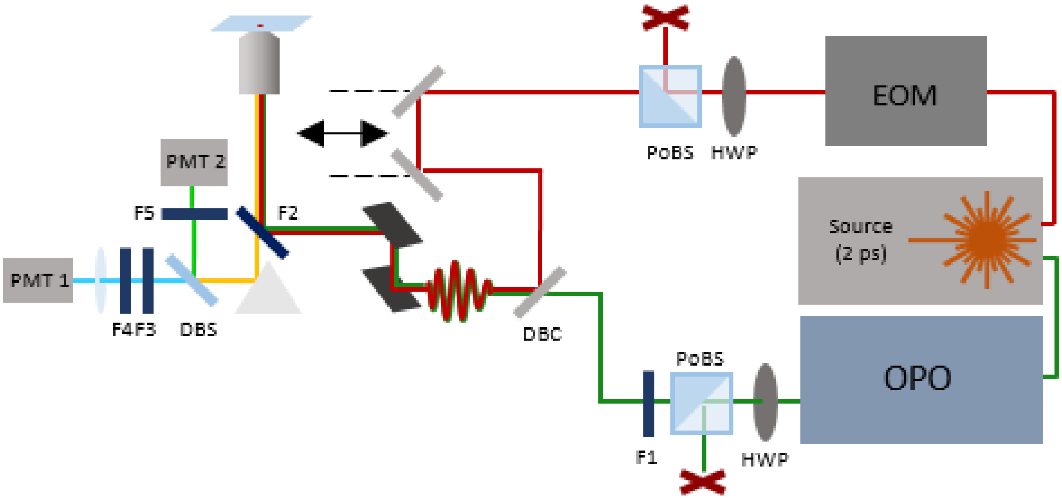

Figure 3.3 Schematic of the custom-built developmental multiphoton imaging system used to perform CRI experiments in this thesis. In the configuration shown, the system is capable of CARS (PMT 1) and SHG or TPF (PMT 2) imaging, along with SRL microscopy following photodiode detection in the forward direction.

galvanometric scanner, into a microscope stand (Nikon Eclipse Ti) and focussed onto samples in an inverted configuration with epi-detection. Phase-matching was achieved by using a high numerical aperture objective (40x water immersion, NA = 1.2) for tight focussing. Scattered radiation was transmitted through an excitation filter (SP, 750 nm, F2) for separation of imaging channels by a dichroic beam splitter (DBS, SP, 594 nm). CARS signal was isolated by cascaded short (775 nm, F3) and band (643/20 nm, F4) pass filters for lens-focussed detection by a photomultiplier tube detector (PMT 1). For CARS detection of the 2845 cm^{-1} CH_2 stretching vibration in polystyrene and lipids, pump excitation was tuned to a wavelength of 797.2 nm, producing CARS scattered radiation at 649.4 nm that could be detected using the filters described. The second imaging channel, detected by PMT 2, was adapted for second harmonic generation (SHG) or two-photon fluorescence (TPF) imaging as required. Within this thesis, only TPF was utilised to observe autofluorescence from cells at 520 nm. Therefore, following reflection by the DBS (LP, 594 nm), signal was isolated using a single (BP, 520 ± 20 nm, F5) filter. Samples were mounted onto an automated x-y-z stage, controlled (along with collection parameters) using MATLAB toolbox ScanImage (Vidrio Technologies)[255]. Tuning of pump laser wavelength was controlled on a separate PC using APE's software interface.

For SRS microscopy, the multiphoton imaging system was adapted to detect SRL in the pump field. Detection was performed in the forward direction, with Kohler illumination employed to ensure matching of 63x (glycerol immersion, NA = 1.3) collection and 40x (water immersion, NA = 1.15) excitation objective focal planes. Scattered radiation was detected using a silicon photodiode following removal of Stokes intensity by two consecutive and identical filters (SP, 900 nm) and imaging of the beam into the detector by a telescope. Detector sensitivity was increased by application of reverse bias (120 V) to the photodiode and filtering of low-frequency electrical noise. Signal from the photodiode was demodulated using a lock-in amplifier for phase-sensitive detection of loss in the Pump field relative to the 20 MHz modulation of the Stokes beam applied by an electro-optical modulator. The system was capable of simultaneous CARS and SRL microscopy with simple scan-phase adjustment between acquisitions.

3.3 Raman Spectral Processing and Chemometrics

Raw spectra acquired from spontaneous Raman, SERS or hyperspectral CRI measurements require sensitive processing steps in order to accurately display and extract the rich chemical information obtained. Pre-processing steps are taken to improve the quality of spectra and have been performed in iRootLab toolbox[256] for MATLAB (Mathsworks). Baseline subtraction removes broad background signals, such as fluorescence, upon which acquired Raman spectra are superimposed. Polynomial (order typically ≥ 5) background subtraction is an iterative partial least squares process whereby a polynomial curve is produced which matches the spectral baseline for subsequent subtraction, revealing the ‘pure’ Raman peaks. Wavelet de-noising is a regularly applied technique which reconstructs smoothed signals with the effect of noise reduction. Normalisation of data removes multiplicative effects by division of each variable (wavenumber) value by a normalisation constant, allowing comparison of peak:noise ratio between spectra which possess different base intensities. Vector normalisation uses a normalisation factor equal to the square root of the calculated sum of squared intensity values of the spectra at each variable. Alternatively, spectra may be normalised to the intensity of a specific peak which is known to be constant between different samples or treatment groups.

Enhanced-Raman measurements, particularly hyperspectral maps, produce large and highly complex data matrices which require reduction of dimensionality while preserving as much variability for extraction of useful spectral characteristics and thus chemical information[257]. Principal component analysis (PCA) is an unsupervised, multivariate analysis technique that is widely used for this purpose. New variables, principal components (PCs), are calculated that are linear, orthogonal functions of the original data generated to iteratively maximise data variation without bearing correlation to one another. Consider an original data matrix (X) of I rows (containing objects $i_1, i_2, \dots, i_I$) and J columns (of variables $j_1, j_2, \dots, j_J$) where, in the case of SERS data, objects refer to individual spectra and variables refer to Raman shift (wavenumbers). Each shift intensity value thus populates the matrix. The columns of X are all vectors in the I dimensional space and can be linearly combined as:

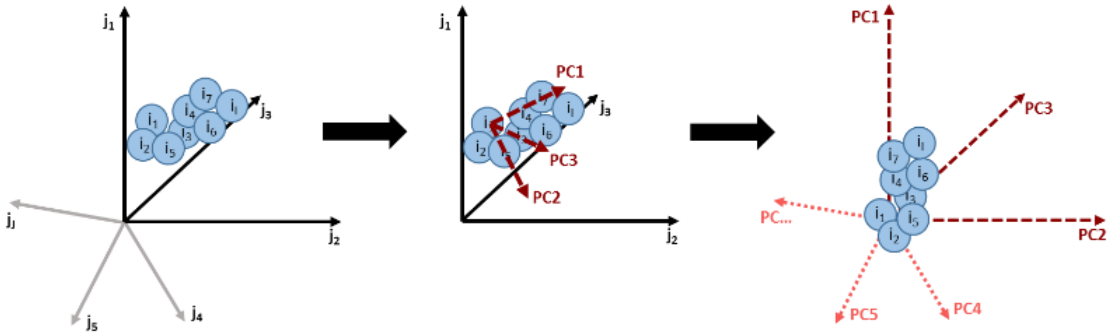

Figure 3.4 PCA can be geometrically visualised as a replotting of an original data matrix (*i* events, *j* variables) into a new coordinate system, PC space, which reduces dimensionality and accounts for the maximum amount of variance within the dataset, clustering spectra (*i*) with most similar characteristics together in the case of Raman experimentation.

$$T = w_1 \times x_1 + \cdots + w_J \times x_J \qquad \text{or} \qquad T = Xw$$

T is a newly generated vector that is a linear combination of *X* variables (plotted within the same space) and *w* is the vector of elements w_j ($j = 1,\ldots, J$). The amount of variation in *T* is measured by its variance *var(T)* and can serve as a good summary of the *X* variables as only a single variable, reducing dimensionality. The optimal weights w_j ($j = 1, \ldots, J$) require normalisation such that their sum of squared values is one ($||w||^2 = 1$), achieved by mean centring of *X* in pre-processing steps. The capability of summarising *X* by vector *T* is achieved by projecting the columns of *X* onto *T* and calculating the residuals of the projection, by using an ordinary regression equation:

$$X = TP^T + E = \hat{X} + E$$

E is the matrix of residuals and *P* is the vector of regression coefficients and is equal to *w*. PCA may be visualised as a remodelling activity (Figure 3.4) of data within new PC space. As such, matrix *X* is modelled by term TP^T where vector *T* is a fixed regressor and vector *P* is a coefficient to be determined. In chemometrics, *P* is normalised to equal 1 and is called the PC loadings vector, while *T* is the PC scores vector. In SERS measurements, residual noise factors are accounted for by *E*, which is not included in the PC model but may be used in judgement of the quality of summarisation achieved of *X* by *T*, given by the percentage of explained variation of *T* ($\%EV_t$):

$$\%EV_t = \frac{\|X\|^2 - \|E\|^2}{\|X\|^2}\,100\%$$

The variance accounted for by generated PCs becomes iteratively decreased with each new axis. PC scores are visualised by the plotting of each object (acquired spectrum) into axes defined by selected PCs (PC space) as a single data point, so that spectra containing similar spectral features (elements of variables) will be assigned similar PC scores and thus cluster together in PC space. Plotted objects (spectra) which do not share many characteristics have dissimilar PC scores and will be separated in PC space. PC loadings are coefficients which describe the weighted contribution of each original X variable (wavenumber value) to the generated PCs and are thus visualised as a spectrum in loadings plots with the X variables for a given PC. Within each PC, loadings plots can therefore be used to identify the original variables which most significantly account for most of the dataset representation. These variables directly correspond to values of Raman shift and thus reveal the chemical bonds responsible for the projection.

Application of PCA to vibrational spectroscopic data is predominantly used for characterisation, be that in tissue diagnoses[258], cell type identification[120,175] or characterisation of intracellular compartments[259]. The careful extraction of molecularly-relevant information from large and complex SERS datasets has proven to be a powerful tool which uses statistics to combat the effects of heterogeneous SERS enhancements given sufficiently large sample sizes. It is often paired with linear-discriminant analysis (LDA), a supervised and more powerful approach which actively seeks to maximise observed variance between spectral characteristics of defined classes. Within this thesis, back projection of PC scores has been utilised to provide pseudo-colour maps of intracellular environments in both SERS and CRI experimentation, coloured by associated loading coefficient to provide statistically-weighted mapping of chemical compositions within samples.

3.4 Establishing Intracellular SERS Methodology

As discussed in Section 2.2.1, enhancement of weak spontaneous Raman signal by plasmonic NPs is dependent upon excitation of LSPR by incident electromagnetic radiation of appropriate wavelength. In order to establish a SERS platform that would allow sensitive SERS interrogation of the intracellular matrix, a number of parameters require optimisation for achieving strong SERS enhancements. Herein, with selection of spherical AuNPs as the most commonly employed morphology for SERS experimentation, development of the intracellular SERS methodology is established through selection of AuNP size, investigation of their optical properties in relevant cell-culture suspensions, excitation wavelength and enhancement provided for detection of both standard biomolecules and intracellular environments.

3.4.1 Nanosensor Characterisation

Essential determinants of LSPR excitation frequency are AuNP size and aggregation state. Theoretical description has been presented to explain the red-shift in LSPR frequency of spherical NPs with increased diameter (within range 10-100 nm) and plasmon hybridisation by tunnelling of conductance band electrons to neighbouring NPs. The latter parameter is dependent upon the aggregation state of AuNPs- which varies with the ability of suspension media to provide stabilising surface coatings that prevent attractive forces between NPs. Absorbance measurements were performed upon citrate-capped AuNPs of 40, 60 and 80 nm diameter in order to observe the impact on NP aggregation state and optical properties induced by varying NP diameter and cell culture-relevant suspension solution. NPs were removed from citrate buffer solutions and resuspended within each solution at a concentration of 5 x 10^9 NPs mL^{-1} for a period of 2 h before UV-Vis analysis.

Monodispersity was observed in AuNP-water suspensions (Figure 3.5 A), with NPs of diameters 40 (red) and 60 (blue) nm exhibiting single absorbance peaks at 534 and 540 nm respectively. Meanwhile, 80 nm diameter AuNPs in water (green) demonstrated a predominant absorbance peak at 550 nm with a shoulder peak at 605 nm. The strong overlap of absorbance peaks observed in water suspensions within the range 534-550 nm implied monodispersity of AuNPs with small increases in peak location attributable to their increasing diameter. The shoulder peak (605 nm) observed in 80 nm AuNP-water suspension suggested the commencement of AuNP aggregation (causing red-shift of NPs LSPR), possibly from degradation of the stock solution that was used. Suspension of AuNPs of all sizes in PBS solution (Figure 3.5 B) revealed a much more pronounced shift effect. While absorbance peaks were located at 562, 562 and 541 nm for AuNPs of 40, 60 and 80 nm diameter respectively, two further peaks were manifested in each spectrum

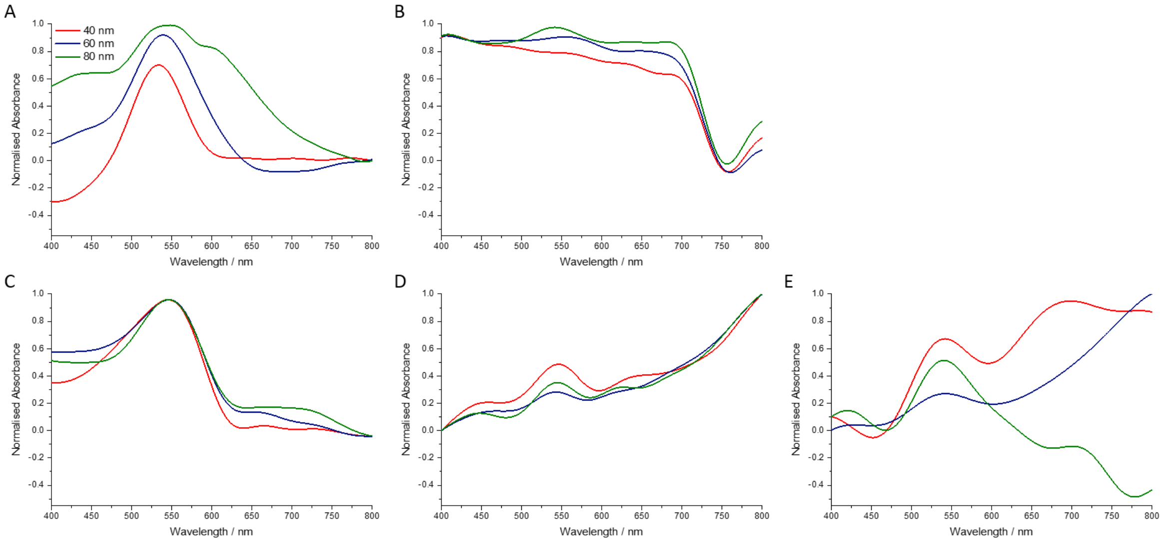

Figure 3.5 Absorbance measurements of citrate-capped AuNPs (ϕ = 40, 60, 80 nm) suspended in (A) water, (B) PBS solution, DMEM containing (C) 0 %, (D) 1 % and (E) 10 % FBS (v/v) within the region 400-800 nm.

at higher wavenumbers. Peaks attributable to NP aggregation caused by high salt concentrations within PBS solutions were observed at 629, 648 and 638 nm for each diameter interval respectively, in addition to a large reduction in intensity at 687 nm for all samples.

Since AuNPs were to be administered to cells by prolonged incubation within cell culture medium DMEM, absorbance measurements were performed with AuNPs suspended within DMEM containing 0, 1 and 10 % FBS (Figure 3.5 C-E) in order to identify any shifts on AuNP LSPR before internalised by cells. Results demonstrated an increased shift of absorbance peak wavelengths with increased media-FBS content, with monodispersity inferred by single peaks located at 546 nm in the absence of FBS (Figure 3.5 C) that became reduced in intensity following appearance of secondary, red-shifted peaks at 618-638 nm in 1 % FBS-DMEM for all NP sizes (Figure 3.5 D). Within 10 % FBS-DMEM (Figure 3.5 E), the relative peak intensities between the monodisperse peaks at 546 nm and shifted peaks at 620-640 nm were shifted further in the spectra from 40 and 80 nm NPs. The absorbance of 60 nm AuNPs exhibited the largest decrease compared to the initial monodispersity absorbance peak, however the secondary, shifted peak appeared to be at wavelength greater than 800 nm, beyond the observed range.

In all AuNP sizes, the shifting of scattering spectral peaks from theoretically-correlated monodisperse shapes to higher wavelengths was increased with increasing media-FBS content. This was attributable to either adherence of serum proteins to AuNP surfaces or the NP aggregation effect that was observed in PBS suspensions. The peak shapes adopted by spectra showed from those expected of scattering measurements, particularly for suspension of AuNPs in

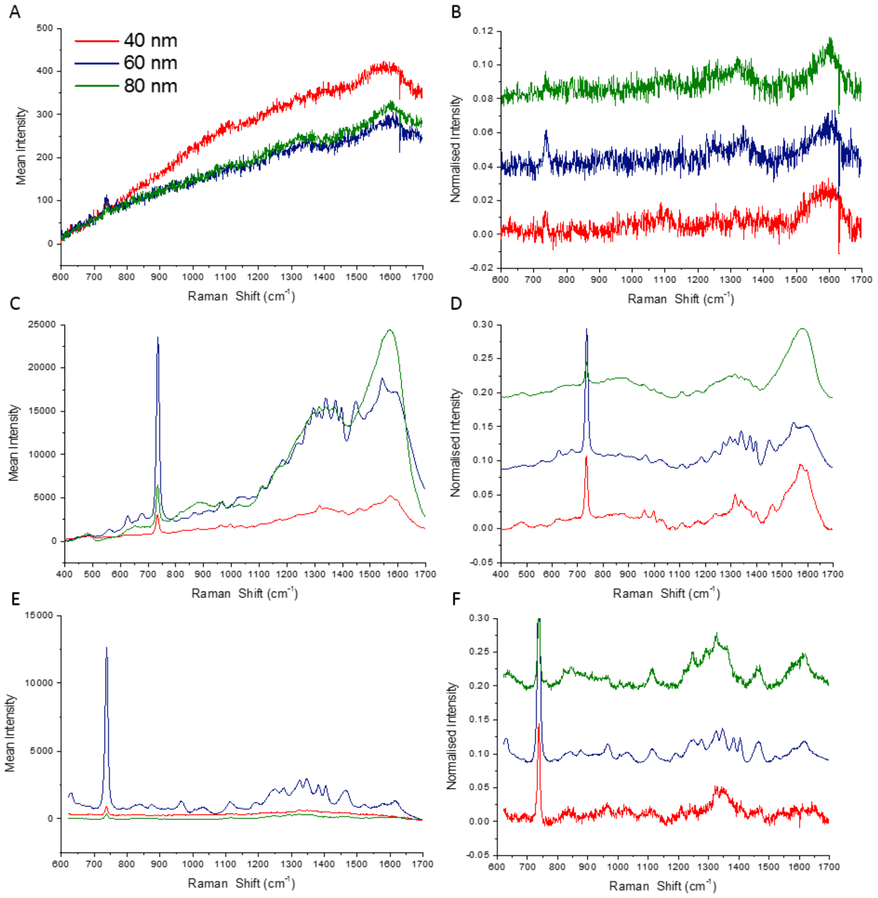

Figure 3.6 Mean unprocessed (A, C, E) and processed (B, D, F) SERS spectra of adenine (10 µM) solution generated by spectroscopy of analyte-soaked AuNPs of 40, 60 and 80 nm diameter using excitation wavelengths of (A-B) 532 nm, (C-D) 633 nm and (E-F) 785 nm. Processed spectra are stacked for clear visual comparison.

PBS and cell culture medium of increasing FBS content. While this may be attributable to high concentrations of salts and complex chemical compositions of DMEM and FBS, repeated measurements would be required to confirm absence of experimental errors associated with acquisitions and confirm the trends described. Nevertheless, TEM performed upon cells treated with AuNPs in 10 % FBS media (Appendix Section A.2) similarly inferred extracellular aggregation. The demonstrated altering of AuNP optical properties in incubation media, before cellular internalisation (causing uncontrolled aggregation by exchange of protein corona and lowering of pH in maturing endosomes) occurs, suggested that excitation wavelengths greater than 532 nm would be required to excite NP LSPR to produce strongly enhanced Raman signal for intracellular studies.

3.4.2 SERS Enhancement

Appropriate combinations of AuNP size and laser excitation wavelengths to produce intense SERS signals were investigated by measurement of 40, 60 and 80 nm AuNPs were soaked in example biomolecule adenine (10 µM) solution (PBS) for 2 h. Resulting AuNP aggregates were mounted onto glass coverslips for Raman investigation using excitation wavelengths 532, 633 and 785 nm. A consistent power of 0.35 mW was used to acquire ten spectra from each sample using single second acquisition times in the range 400-1700 cm^{-1}.

The mean spectrum of each NP size and excitation wavelength combination is presented before and after spectral processing in Figure 3.6. The low intensities observed following irradiation by 532 nm excitation showed no significant enhancement of adenine Raman spectra in all cases. Raw spectra (Figure 3.6 A) showed no intensity above 400 counts while identification of spectral details could not be aided by (Figure 3.6 B) background subtraction and vector normalisation of spectra. Only the characteristic vibrational peak of adenine at 735 cm $^{-1}$ was weakly discernible, corresponding to its in-plane symmetric ring breathing vibrational mode[260–262]. Excitation by 633 nm radiation provided the highest mean SERS signal for every NP diameter investigated (Figure 3.6 C-D). Overall raw intensities were observed to be greatest in 60 and 80 nm AuNPs suspensions (≈ 28000 counts) compared to weaker intensity from 40 nm AuNPs (≈4500 counts). However, discrimination of spectral details was shown to be more sensitive in spectra generated from 40 and 60 nm NPs compared to 80 nm following spectral processing. The spectral processing presented removal of intense and broad signal (1200-1700 cm^{-1}) attributable to graphitic carbon, indicating an extent of sample burn by local heating of AuNPs. In Figure 3.6 D, sensitivity of the detected 735 cm^{-1} vibrational peak was greatest in 60 nm NPs, followed by 40 and then 80 nm. Similarly, observation of the spectral region 1250-1400 cm^{-1} (relating to in-plane C-N and C-C stretching modes, C-H and N-H bending modes and NH_2 scissoring modes) demonstrated a greater number of peaks detected in spectra of 60 nm AuNPs than for 40 and 80 nm NPs. Adenine peak positions identified were in agreement with previous similar studies[261,262]. Excitation by 785 nm irradiation yielded significant enhancement of Raman intensity only from 60 nm AuNPs (Figure 3.6 E-F), for which spectral processing revealed similar spectral sensitivity to that observed under 633 nm despite lower raw intensity (max ≈ 12500 counts). Spectra measured from 40 and 80 nm AuNPs demonstrated greater sensitivity than corresponding samples irradiated with 532 nm but not 633 nm excitation. The significantly increased intensity observed in spectroscopy of 60 nm AuNPs was consistent with the large shift in aggregated-state absorbance peak in Figure 3.5 E, while other AuNP sizes demonstrated secondary peaks at wavelengths below 750 nm.

Thus, initial AuNP absorbance and biomolecular SERS investigations inferred that 60 nm diameter AuNPs irradiated with either 633 or 785 nm excitation may provide the largest SERS enhancements for an optimised intracellular SERS platform.

3.4.3 Intracellular SERS Enhancement

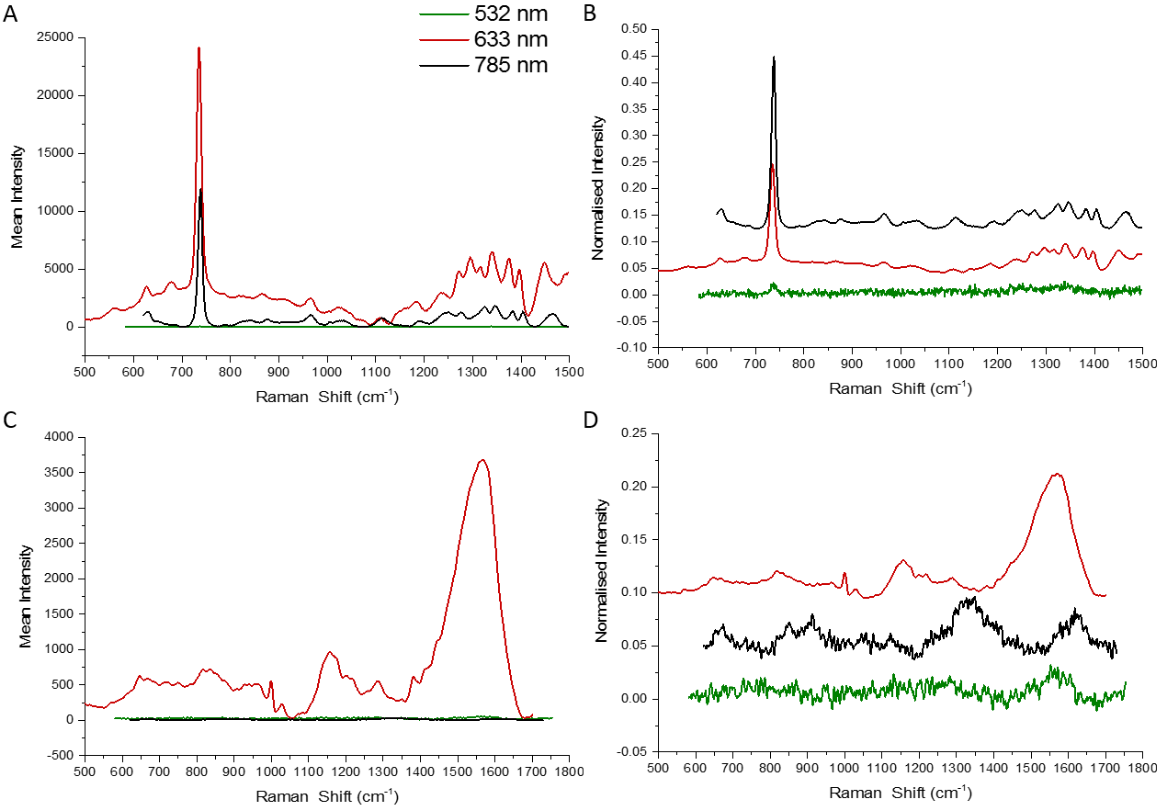

Figure 3.7 Mean unprocessed (A, C) and processed (B, D) SERS spectra of (A-B) adenine (10 µM) solution and (C-D) fixed SH-SY5Y intracellular matrix following incubation (24 h) with AuNPs (ϕ = 60 nm, 150 µM, 1.35 x 10^{10} NPs mL^{-1}) following 532, 633 and 785 nm excitation. Processed spectra were stacked for clear visual comparison.

To further inform the intracellular SERS methodology developed in this thesis, 60 nm diameter AuNPs were again soaked in adenine (10 µM) solution for investigation of optimal excitation wavelength. Additionally, samples of fixed SH-SY5Y human neuroblastoma cell samples, incubated (24 h, DMEM + 5 % FBS) with 60 nm AuNPs (150 µM, 1.35 x 10^{10} NPs mL^{-1}), were prepared to evaluate the enhancement achieved following intracellular uptake and aggregation. As previous, excitation wavelengths of 532, 633 and 785 nm were applied to cells at a power of 0.35 mW. Acquisition times were 1 s and 5 s for measurements of adenine and SH-SY5Y cell samples respectively.

Repeated adenine solution SERS spectra (Figure 3.7 A, B) showed identical trends in intensity and peak positions to those observed in Figure 3.6. The relative intensity of the 735 cm^{-1} ring breathing peak compared to other peaks was lower following 633 nm excitation than 785 nm, suggesting more homogenous sensitivity. Once again, no enhancement of Raman signal was yielded by 532 nm excitation. In contrast, SERS intensity from SH-SY5Y cells was greatly increased

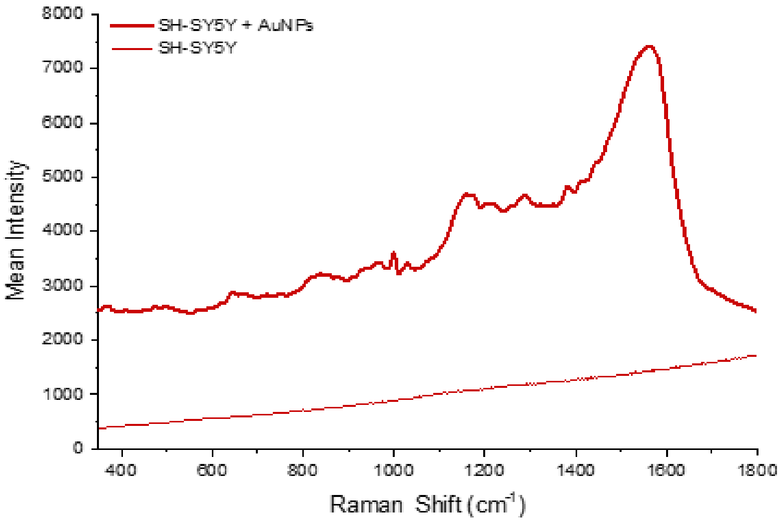

Figure 3.8 Comparison of spectra collected following 633 nm (5 s, 0.35 mW) irradiation of SH-SY5Y cells in the absence (spontaneous Raman, fine red) and presence of internal 60 nm AuNPs (SERS, thick red) demonstrated the significant enhancement of Raman signals detected using the optimised intracellular SERS platform.

following 633 nm excitation compared to negligible enhancement from both 532 and 785 nm excitation wavelengths (Figure 3.7 C, D). Unprocessed intensity was lower in the mean intracellular (max ≈ 3700 counts) than adenine solution (max ≈ 24500 counts) sample spectra, possibly reflecting the lower number of available NPs for forming aggregates within individual endolysosomes or a minimum size of extracellularly-formed aggregates that could be internalised. Background subtraction and normalisation of intracellular SERS spectra did not afford significantly improved visualisation of spectra generated from 532 and 785 nm excitation, which exhibited low signal-to-noise intensity ratios.

The processed mean SERS spectrum of SH-SY5Y cells exhibited a number of vibrational peaks that were characteristic of intracellular content, such as C-C ring breathing (1003 cm^{-1}) and C-H bending (1030 cm^{-1}) vibrations of phenylalanine. Additional regions of the spectrum relating to protein (1150 cm^{-1} C-C/C-N stretch, 1205-1250 cm^{-1} Amide III, 1550 cm^{-1} C-N stretch/N-H bend), lipid (1298 cm^{-1}, CH_2 deformation fatty acids) and nucleic acid (1420 cm^{-1} ring breathing deoxyribose) content were identified, inferring measurement of intracellular content beyond components available within culture medium and FBS. Large SERS enhancements were achieved compared to mean spontaneous Raman spectra of control cells (no AuNPs) under identical acquisition parameters (Figure 3.8). The spontaneous Raman spectrum produced no detection of intracellular Raman peaks, resembling a lowly-intense fluorescence baseline that verified the strongly-enhanced intracellular SERS intensity produced by 60 nm AuNPs with 633 nm excitation employed in this thesis.

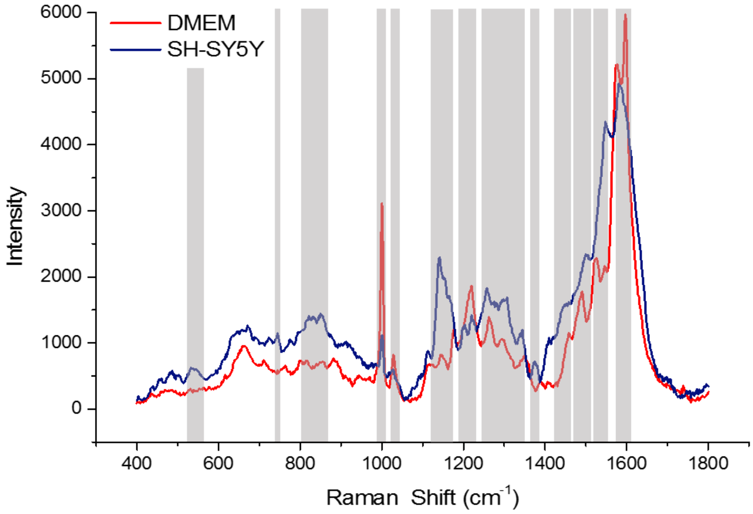

Figure 3.9 Mean SERS spectra acquired from SH-SY5Y cells (blue) and control cell culture media (red, 5 % FBS) using 633 nm excitation and 60 nm diameter AuNPs. Selected spectral differences (grey highlight) were assigned in Table 3.1.

Table 3.1 Peak differences and assignments between mean SERS spectra acquired from 60 nm AuNPs incubated within cell culture medium or internalised into SY-SY5Y cells for a period of 24 h. 0 = Absent, + to +++ = weak to strong intensity.

Raman Shift / cm^{-1}	DMEM (5% FBS)	SH-SY5Y	Assigment
532	0	+	S-S Disulfide *str*
744	0	+	C-C *ring breathing*, DNA Bases
821	+	+	C-C *str*, Proteins
826	0	+	O-P-O *str*, DNA backbone
850	+	+	C-C *ring breathing*, Pro/Pro-OH/Tyr
1003	+++	+	C-C *ring breathing*, Phe
1030	+	+	C-H *bend*, Phe
1142	+	++	C-C *str*, Ala/Val/Glu/His
1153	0	++	C-C *str*, Carbohydrate
1166	0	++	C=C/C-OH *str*, Lipids
1220	++	+	C-N *str*, Amide III
1258	+	++	C-N *str* /N-H *bend*, Amide III/ C-N *ring breathing*, DNA Bases
1308	+	++	CH_3/CH_2 *deform*, Lipids
1345	+	++	CH_3/CH_2 *wag*, Protein/Carbohydate/D/RNA
1375	0	+	CH_3 *bend*, Lipids / *ring breathing*, DNA bases
1458	+	+	CH_3/CH_2 *deform*, Lipids / Deoxyribose *str*, Nucleic Acids
1491	++	0	C-N to C-H couple, Amino Acids
1526	++	0	conj -C=C- *str*, Proteins
1548	+	+++	C=C *str*, Trp/NADH
1578	+++	+++	C=C *bend*, Phe / Nucleic Acids
1598	+++	++	C=C *bend*, Phe

Finally, confirmation was required that SERS spectra were indeed originated from intracellular matrix of SH-SY5Y cells and not simply the protein content of incubation media. SERS spectra were acquired from control AuNPs suspended in DMEM (5 % FBS) for 24 h in the absence of cells for comparison with the AuNP-treated SH-SY5Y sample. Key differences between the average spectra (Figure 3.9) of each group detailed biomolecular variation within the sample AuNP microenvironments.

A characteristic of SERS spectra acquired from DMEM (5 % FBS) was the strongly intense vibrational peaks relating to phenylalanine (Phe) content, manifested at 1003, 1030, 1578 and 1598 cm^{-1}, relative to the intracellular SERS spectra. The dominance of spectra by protein content vibrations was a direct result of FBS addition to culture media, supplying living cells with a supply of amino acids and nutrients for proliferation. In contrast, spectra acquired from within SH-SY5Y cells were elevated in intensity of numerous Raman peaks, such as 744 cm^{-1} (C-C, DNA bases), 826 cm^{-1} (O-P-O, DNA backbones), 1153 cm^{-1} (C-C, carbohydrate), 1166 cm^{-1} (C=C/C-OH, lipids), 1308 ($CH_{2/3}$, lipids), 1375 cm^{-1} (CH_3, lipids/ ring breathing, DNA). The appearance of these vibrational modes in cellular samples was reflective of the greater diversity of biomolecules required in intracellular matrices for metabolic process and cell function.

Preliminary SERS experiments presented within this section have identified 633 nm excitation of 60 nm AuNPs to provide the strongest enhancement of Raman scattering intensity in both an example biomolecule solution and intracellular matrix. Confirmation that SERS measurements were taken intracellularly is further evidenced by TEM inspection of AuNP-treated SH-SY5Y cells (Appendix Section A.2). Thus, an intracellular SERS experimental platform is presented that offers sensitive analysis of nanosensor biochemical environments at the molecular level. Research presented in Chapter 4 serves to continue this optimisation process by investigating the effect of AuNP incubation parameters upon extents of cellular uptake and biochemical compositions within cells as measured by SERS.

Chapter 4 Investigating SERS Nanosensor-Induced Variation

4.1 Abstract

The introductory sections of this thesis have explained that plasmonic gold nanoparticles (AuNPs), are easily internalised into cells and therefore employed as nanosensors for reporter-based and reporter-free intracellular SERS applications[11]. While AuNPs are generally considered non-toxic to cells, many biological and toxicity studies report that exposure to NPs induces cell stress through generation of reactive oxygen species (ROS) and upregulated transcription of pro-inflammatory genes, which can result in severe genotoxicity and apoptosis[130]. Despite this, the extent to which normal cellular metabolism is affected by AuNP internalisation remains a relative unknown, along with the contribution of the uptake itself to the SERS spectra obtained from within so called 'healthy' cells as indicated by traditional viability tests. The following chapter interrogates the perturbation of cells' natural state by treatment with AuNPs themselves under different conditions and corresponding effects on the SERS spectra obtained. Changes induced by varying AuNP concentrations and media-serum compositions are characterised using cellular assays and correlated to the corresponding intracellular reporter-free SERS spectra. Altering incubation media serum conditions led to different extents of nanoparticle internalisation. It was observed that changes in SERS spectra were correlated to increased extents of internalisation, confirmed qualitatively and quantitatively by confocal microscopy and ICP-MS analysis, respectively. The spectra were analysed to characterise deviations that can be attributed to NP-induced changes, identifying optimised conditions for non-perturbative administration of the SERS nanosensors. Thus, the study highlights a need for understanding condition-dependent NP-cell interactions and standardising NP treatments for assessing validity of intracellular SERS experiments and use in drug discovery applications.

4.2 Contributions

The research presented in this chapter has been published in the following journal:

J. Taylor, A. Milton, M. Willett, J. Wingfield and S. Mahajan, 'What do we actually see in intracellular SERS? Investigating nanosensor-induced variation'; Faraday Discuss, 2017, **205**, 409-428.

Research was carried out by the candidate exclusively, with the exception of ICP-MS measurements (marked '*') which were performed in collaboration with James A. Milton at the National Oceanography Centre, University of Southampton.

4.3 Background

The biocompatibility offered by plasmonic gold nanoparticles (AuNPs) is one of the major advantages of their use in intracellular SERS experiments. Employed as SERS probes, their applications include monitoring of cellular functions[137,138], dynamics[140,141,259], enzyme kinetics[142,143], stress response[145,263,264], apoptosis and cell death[146,147,263] along with probing specific compartments such as the mitochondria[149] and tracking of drugs released into the cytoplasm by NP carriers[150–152,265]. Cellular uptake is achieved through voluntary incorporation into living cells by endocytotic mechanisms, following a simple incubation period with NP-doped cell culture media. Although the explicit mechanism depends on several parameters such as NP size, surface charge/coating and cell type, it is accepted that NPs are internalised by cells into endosomal transport vesicles following the adherence of extracellular serum proteins to their surface to form a biocompatible 'protein corona' around the inorganic NP. The make-up of the protein corona gives an NP its biochemical identity as experienced by cells and thus affects both uptake and intracellular localisation[122,266,267]. It is subject to dynamic changes in composition and thickness (usually measured between 3-15 nm) depending on the media in which it is suspended[85,268]. Initial formation of the corona occurs rapidly upon contact and in the case of culture medium, a stable and biocompatible structure is formed which lowers the free energy of NP-membrane interaction[85,266,269,270]. Functionalisation of NP surface may also be performed with cell penetrating agents to achieve direct localisation towards the cytosol or desired organelles, evading removal by exocytosis for probing a diverse range of intracellular targets[61]. For details on approaches to intracellular SERS and the role of NPs as SERS probes, the reader is directed to Section **Error! Reference source not found.** of this thesis and published exhaustive reviews[10,11,21,189].

Despite reports that NPs (particularly AuNPs) of SERS relevant diameter (20-100 nm) are non-toxic to cells, typically evidenced by traditional cell viability tests such as trypan blue or MTT (3-(4,5-dimethylthiazol-2-yl)-2,5-diphenyltetrazolium bromide) assays, their nanotoxicity is often questioned[122,130,271,272]. Much debate arises from not only inconsistencies in the manner in which intracellular SERS experiments are performed and reported, but also from the sheer complexity of NP-cell interactions. For instance, toxicity depends on features such as cell phenotype, NP material, size, morphology, concentration, surface charge and modifications. Despite this, the accepted consensus is that NPs, particularly Au nanospheres, have negligible effect on cell viability as shown by the traditional, biological assays.

The property of being non-toxic does not however rule out that uptake of bulky, inorganic cargo such as AuNPs can impact molecular-level homeostatic mechanisms of living cells. Particularly implicated with exposure to NPs is oxidative stress, defined as an imbalance between cellular production of reactive oxygen species (ROS) and antioxidant defences[130,273–275]. ROS, such as $\cdot O_2^-$, $\cdot OH$ and H_2O_2, production is a normal cellular process which performs roles in cell signalling and immunodefence. However, such species also inflict damage upon macromolecules like proteins, lipids and DNA when production surpasses the level which are counterbalanced by the action of antioxidants such as glutathione and superoxide dismutase[276]. Oxidative stress related effects observed following inorganic NP internalisation include increased ROS generation, decreased mitochondrial membrane potential, lipid peroxidation and decreased activity of enzymatic antioxidants[130]. DNA damage is also commonplace, exhibiting chromosomal fragmentation, DNA strand breakages and induced gene mutations[130,277,278]. The response to DNA damage involves either initiation of DNA repair mechanisms or invoking cell cycle arrest and apoptosis in extreme cases, involving biological pathways implicated in oxidative and cell stress[273,279,280].

SERS has recently been applied to achieve ratiometric sensing of oxidative stress in live cells using a SERS-reporter based platform by gold nanoflowers functionalised with 4-mercaptophenol (4-MP) reporter molecules[158]. The probe was tailored specifically to the ROS/antioxidant pair hypochlorite (ClO^-) and glutathione (GSH), indirectly detecting heightened ClO^- levels by its binding to 4-MP and subsequent alterations in SERS signature, with recovery of the initial spectrum achieved following treatment with GSH[158]. Similarly, organic Raman reporter molecules have been chemisorbed onto Au nanoshells to provide ratiometric, quantitative and reversible measurement of chemically-induced cellular hypoxia[281]. Evaluation of the cytotoxicity of nanomaterials (ZnO, TiO_2 NPs and single-walled carbon nanotubes, SWCNTS) towards cells has also been performed using a reporter-free SERS methodology[264]. Comparison of data from WST-1 (cell proliferation) and Annexin V-FITC/PI (apoptosis and necrosis) assays with AuNP-generated SERS spectra provided molecular-level insights into the toxic events induced by nanomaterial internalisation. Inconsistencies were identified between the two biological assays, induced by NP-dye interactions despite careful washing of samples. More significantly, potential SERS-markers of cell stress induced by the nanomaterials were identified, citing alteration of peaks relating to protein

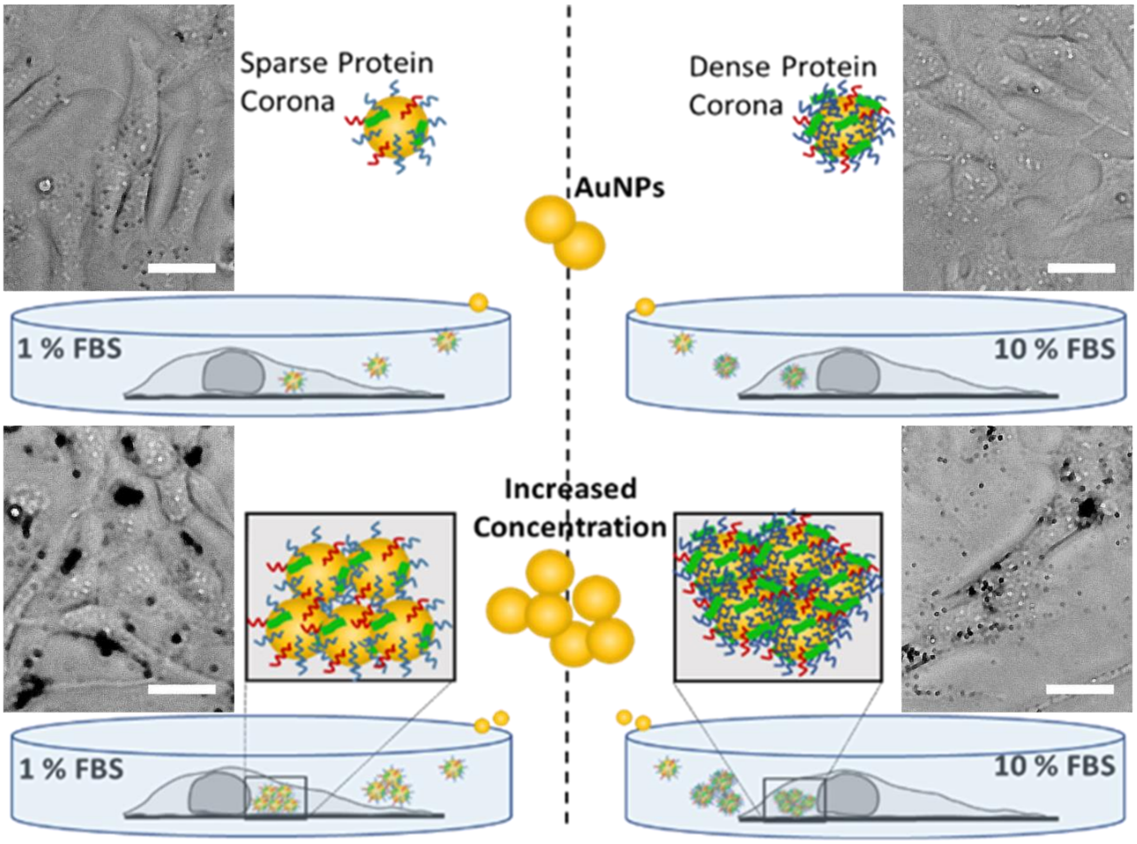

Figure 4.1 Schematic demonstrating incubation of SH-SY5Y cells with varying AuNP treatments and the effect of media-serum content on the protein corona formed around NPs. Uptake was visualised after 24 h by brightfield microscopy. Scale bar = 30 µm.

structure, ratios of phenylalanine (Phe) peak intensities and redistribution of cellular endoplasmic reticulum and mitochondria[264].

The presented research, however, aims to understand intracellular SERS in a fundamental manner, by observing the hugely complex cellular events induced by exposure to the nanoparticle SERS-probes themselves. While previous studies employ SERS NPs to monitor cellular oxidative stress upon induction by exposure to chemical stress agents such as TBHP or other nanomaterials, a gap exists in our knowledge of the biochemical changes induced arising from simple AuNP internalisation itself. Therefore, the most ubiquitously employed SERS probes, spherical AuNPs, were administered to human neuroblastoma cells at a range of incubation concentrations to observe spectral differences arising from wider biochemical changes induced due to exposure to nanoparticles (Figure 4.1). The effect of altering the foetal bovine serum (FBS; nutrient protein) content of the medium in which AuNPs are administered to cells was also considered, with previous reports demonstrating that reducing or removing the serum content of incubation medium results in increased cellular uptake[267]. Confocal fluorescence microscopy and inductively coupled plasma mass spectrometry (ICP-MS) were performed on cell treatments in order to visualise intracellular NP localisation and quantify their uptake, respectively. Reactive oxygen species (ROS) activity assay, dichlorofluorescein-diacetate (DCF-DA) a fluorescent dye which is converted to dichlorofluorescein (DCF) in the presence of ROS to imply oxidative stress, was used to determine its manifestation following NP administration. Correlation of ROS activity with internalisation of NPs allowed identification of one of the effects in the complex cellular events which unfold during NP-cell interaction and affect SERS spectra. Principal component analysis (PCA) and linear discriminant analysis (PCA-LDA) have previously been applied to SERS datasets to achieve characterisation of the endolysosomal pathway[259] and distinguishing cell phenotypes[120]. In this application, PCA was carefully applied to observe alterations of cellular SERS spectra induced following various AuNP treatments to provide molecular-level detail of the changing cellular environment. These conclusions are contrasted with viability data obtained by classical trypan blue exclusion assay, challenging the validity of intracellular SERS experiments based upon ‘healthy’ cells provided by simple viability assays. Finally, analysis of spectral changes due to increased NP internalisation identified SERS markers of AuNP-induced cellular changes. This knowledge is fundamental to establish understanding of cellular pathways and their response to NP uptake and holds implications for circumventing issues in the development of intracellular SERS-based applications.

4.4 Methods

4.4.1 Cell Culture

SH-SY5Y (human neuroblastoma cell line) cells were cultured in DMEM supplemented with 10 % foetal bovine serum (FBS), 1 % penicillin-streptomycin (pen-strep) mixture. Cells were incubated at 37 °C, 5% CO_2, split every 4 days and underwent regular checks to ensure freedom from mycoplasma[251]. Cells were seeded at 25000 cells onto lumox® 96 well plates (Sarstedt Ltd) and poly-L-lysine coated glass cover slips for ROS assay and SERS measurements respectively, within either culture DMEM or reduced-serum DMEM (1 % FBS) including retinoic acid (RA, 10 µM) to induce neuronal differentiation over 48 h.

4.4.2 AuNP Administration

Following washing by phosphate buffered saline (PBS) solution, AuNP incubations were performed using 60 nm colloidal AuNPs (BBI international) by suspension in fresh DMEM to be applied to cells. AuNP incubation was performed at concentrations ($[\text{AuNPs}]_{\text{Incub}}$) of 250, 100, 10, 1 and 0.1 µM ($22.5 \times 10^9 - 9 \times 10^6$ NPs mL^{-1}) in DMEM (10 % FBS, 1 % pen-strep) or reduced-serum DMEM (1 % FBS, 1 % pen-strep), both without phenol red. Control cells were maintained in the same media composition without AuNPs for the same time period, while NP-only controls were prepared by suspension of AuNPs in relevant media compositions for the same duration to provide a measure of extracellular NP SERS signal. The AuNP incubation was performed over 24 h, representing the duration for which maximal intracellular residency of AuNPs ($[\text{AuNPs}]_{\text{Incub}}$ = 150 µM, 1 and 10 % FBS) was previously estimated (compared to 6, 12, 48 h) by image analysis of brightfield microscopy (Figure 8.2). Full experimental details are provided in Appendix Section A.1.

Following exposure, cells were washed with PBS and fixed in para-formaldehyde (4 %) for 15 mins before washing and storage in PBS (5 ^{o}C) for analysis.

4.4.3 Cell Viability Assay

Cells were seeded at 25000 cells in 12-well plates and underwent previously outlined differentiation and AuNP administration treatments. This was followed by detachment of cells from plates using trypsin, centrifugation and resuspension of cells in a 1:1 (v/v) solution of culture medium and 0.4% trypan blue solution (Sigma-Aldrich). After 5 mins cells were transferred to a haemocytometer for counting of viable and non-viable cells. 2 Repeats were performed at each combination of AuNP and FBS conditions.

Viability data, in addition to that acquired from ROS assay and ICP-MS in this study and other single-variable, numerical response data throughout this thesis, was analysed using scientific graphing and data analysis software Origin (OriginLab Corporation). One-way analysis of variance (ANOVA) testing was performed, a statistical technique based upon the quadratic rational F statistic, that tests for significant deviation of a class's mean value from others in the dataset. As all instances in this thesis produce three or more treatment classes, ANOVA testing reduces the likelihood of errors for analysis compared to performing individual Student's t-tests. Post-hoc analysis was required as ANOVA is an omnibus technique. Therefore, Tukey's multiple comparison, or honestly-significant difference (HSD), test subsequently performed pairwise comparisons of class means between whole the datasets to identify significant differences. Reported as a P-value, the significance of differences between means are indicated by asterisks

(*, **, *** and **** denoting significance to $P \leq 0.05$, 0.01, 0.001 and 0.0001 respectively) throughout this thesis.

4.4.4 ROS Detection Assay

ROS detection assay kit (Abcam plc) was performed on differentiated and AuNP-treated cells within 96 well plates. Fluorogenic dye, 2', 7'-dichlorofluorescein diacetate (DCF-DA, exc/emm 495/529 nm, 25 µM) was administered after thorough washing by PBS (to minimise NP-dye quenching through removal extracellular AuNPs). Fluorescence readings were recorded using a Promega GLOMAX® fluorescence plate reader and a 490/510-570 nm filter set. Assay validation was provided by differentiated cells treated only with chemical stress agent tert-butyl hydroperoxide (TBHP, 250 µM, 4 h) before staining and measurement.

4.4.5 Confocal Fluorescence Microscopy

For visualisation of AuNPs' localisation within cells under each treatment condition, confocal microscopy was performed to sequentially observe NP scattering within fluorescently stained cells. Following AuNP incubation, cells were washed and incubated with CellTracker Red CMTPX (ThermoFisher Scientific, Exc/Em 577/602 nm, 10 uM, 30 mins) in DMEM free of FBS and phenol red. Cells were fixed and stored in PBS before mounting in glycerol onto glass slides for imaging.

Confocal laser scanning microscopy was performed with a Leica SP-8 confocal microscope. High-magnification images were obtained with a Nikon plan apochromat 63x oil-immersion objective (NA = 1.2). AuNPs were imaged in reflection mode using a 514 nm argon laser line and PMT detection 518 – 550 nm (green) and averaged 4 times. CellTracker red fluorescence was imaged using a 561 nm solid-state laser line and PMT detection 558 – 603 nm (red), averaging twice. Z-stacking was performed with step-size of 0.33 µm. 3D and cross section images were processed using Fiji ImageJ.

4.4.6 Inductively Coupled Plasma – Mass Spectrometry (ICP-MS)*

Cells seeded at 25000 cells underwent the previously outlined differentiation protocol and AuNP incubation at concentrations of 0, 10, 100 and 250 µM in 1 and 10 % FBS media. Cells were washed 3 times with PBS to aid removal of extracellular NPs before being collected by trypsinisation. Suspensions of control and NP-containing cells, along with AuNP standards (10, 100, 250 µM in 1 and 10 % FBS media), were dissolved in aqua regia (3:1 $HCl:HNO_3$) within Teflon vessels on a hotplate for 30 h. Following dissolution, the samples were diluted with 5 % HCl for analysis.

ICP-MS measurements were performed by Andrew James Milton, University of Southampton (Ocean and Earth Science) *.

Briefly, cell lysis samples, calibration standards and blanks were spiked with rhenium internal standard (1 ppb) before acquisition of Au [197] and Re [185] isotopes on a Thermo Scientific ELEMENT XR HR-ICP-MS. The instrument was purged with 5 % HCl solution between samples until background levels of all elements were achieved. Reproducibility within runs was typically better than 2 % RSD for the 4 repeats. Data handling was performed by internal correction, blank correction, calibration against 5 standards and dilution correction.

4.4.7 Raman Microspectroscopy

Cover slips were mounted and sealed onto glass microscope slides for analysis by Raman microspectroscopy. Raman spectra were recorded using a Renishaw Raman InVia micro-spectrometer equipped with streamline accessory (Renishaw plc, Wotton-under-Edge, UK). System parameters consisted of a 633 nm point laser, Renishaw-automated 100 nm encoded XYZ stage, Rayleigh edge filter, 1200 lines/mm (1.7 cm^{-1} spectral resolution) diffraction grating dispersing Raman signals onto a master Renishaw Peltier cooled charge coupled detector (1024 pixel x 256 pixel). Calibration of Raman shifts was carried out using an internal silicon wafer. A colour camera mounted on the microscope was used to obtain brightfield images in transmission to visualize areas for spectral acquisition. A 63x water-immersion objective (Leica, NA = 1.20) was used. Streamline mapping utility was employed to reveal AuNP localisation across whole cells by rapid scanning for the phonon-plasmon scattering mode from AuNPs, providing a Raman peak at 150 cm^{-1}[282]. Cellular regions exhibiting strong scattering intensities in this mode, thus highest internal concentrations of AuNP aggregates, were interrogated by point maps of 300 nm step size and either 3x 1 s or 3x 10 s exposures of 0.3 mW laser exposure. Both data sets displayed similar spectral intensities and resolution, so 3x 10 s exposure data was used. 72 spectra in the range 350-2150 cm^{-1} were collected from intense scattering regions across 6 cells for 2 repeats within each condition. The broadness of some spectral features observed in class mean spectra are a natural consequence of spectrally averaging the large biomolecular variation within cells.

4.4.8 Raman Spectral Processing and Multivariate Analysis

Cosmic rays were removed from the SERS spectral maps using Renishaw Wire 3.4 software. Spectra were truncated to the spectral range 350–1650 cm^{-1} before polynomial (order 5) baseline correction and wavelet de-noising were performed. This data was used for plotting class mean spectra following vector normalisation.

Raman spectra provide large and complex data matrices which require sensitive decomposition algorithms to extract key features and discriminate subtle but crucial characteristics between categorised data. These are unidentifiable by univariate analysis alone, therefore IRootLab graphical user interface toolkit for MATLAB R2018a (TheMathsWorks, Natick, MA, USA) was utilised for multivariate analysis. PCA was performed on the background-subtracted and de-noised spectra obtained above after mean-centring and vector normalisation[256]. PCA is an unsupervised statistical technique which reduces the dimensionality of original data to produce scores and loadings plots from derived principal components (PCs) of the mean-centred, processed spectra. PC loadings were correlated to the original data to discern which variables (wavenumbers) were most responsible for the separation achieved by calculation of weighting coefficients of the variance. Each PC was examined individually to determine which represented the best segregation of classes and derived PC loadings identified the corresponding vibrational modes.

4.5 Results and Discussion

4.5.1 Cell Viability

The effect of administering SERS nanosensors at varying concentrations and within high and reduced serum media on SH-SY5Y cell viability was assessed using trypan blue assay (Figure 4.2). Cells incubated with AuNPs in DMEM containing 1 % FBS exhibited a generally lower viability (range of means 96.3-85.3 %) compared to those within serum-rich DMEM (96.2-92.1 %). Comparison of these values with control spectra (viability 95.3 and 88.0 % for 10 % and 1 % FBS media content respectively) confirmed this to be an effect of serum content rather than AuNP exposure. This result is consistent with literature citing the use of 10 % FBS media as optimal for culturing healthy SH-SY5Y cells[251]. The decrease in viability resulting from the differing media-serum concentration was only found to be statistically significant in the untreated control ($P \leq 0.05$) and 0.1 µM ($P \leq 0.001$) $[\text{AuNP}]_{\text{Incub}}$ treatment groups (Figure 4.2) by Tukey means comparison analysis.

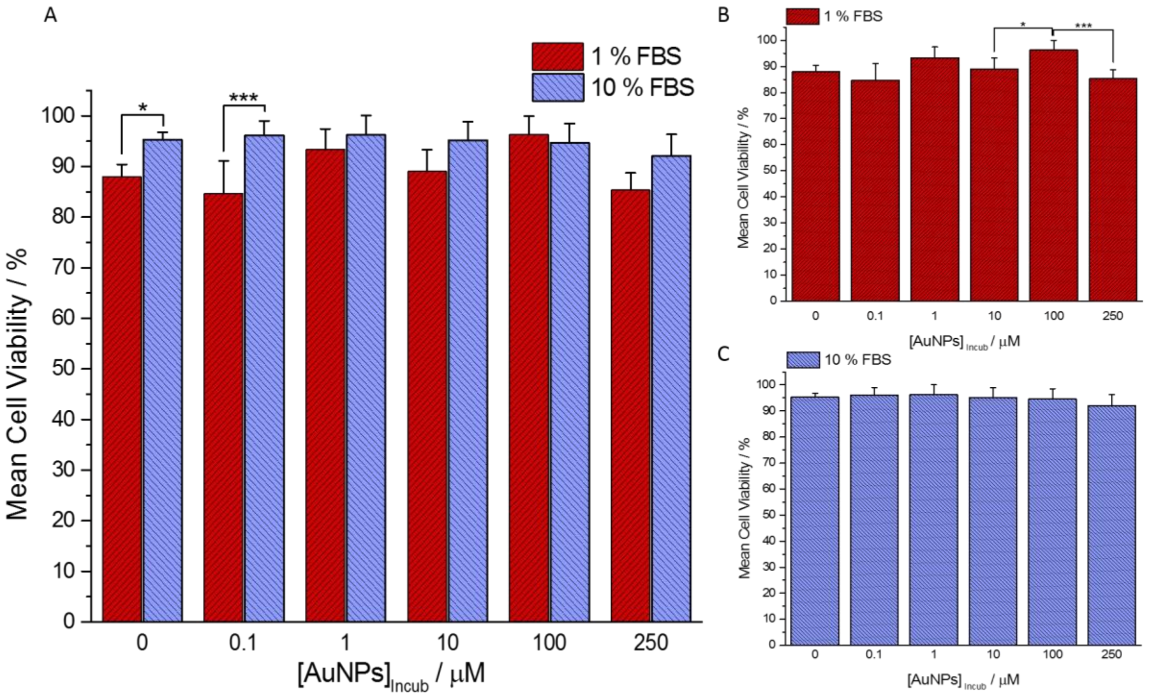

Figure 4.2 Comparison of mean cell viability by trypan blue exclusion assay of (A) AuNP-treated SH-SY5Y cells at concentrations of 0.1, 1, 10, 100 and 250 μM within media containing 1 (red) and 10 % (blue) FBS for 24 h. Mean viabilities demonstrated no statistically significant correlation to $[\text{AuNPs}]_{\text{Incub}}$ within (B) 1 % or (C) 10 % media-FBS compositions.

Within 1 % FBS AuNP treatments, no correlation was discerned between cell viability and $[\text{AuNP}]_{\text{Incub}}$, with values fluctuating about the level of the control cells (Figure 4.2). Statistically significant ($P \leq 0.001$) decrease in cell viability was demonstrated in 250 μM treatment compared to the 100 μM incubation, however the 100 μM incubation also exhibited greater cell viability ($P \leq 0.05$) than the next lowest $[\text{AuNPs}]_{\text{Incub}}$ of 10 μM. AuNP concentrations of 250 μM exhibited the lowest viabilities in both 10% and 1% FBS media (92.1 ± 4.2 % and 85.3 ± 3.4 % respectively), however neither decreased significantly (0.05 % level) from the means of the control cells in both cases. Thus, no significant loss in viability following application and uptake of AuNPs was determined by the trypan blue exclusion assay.

4.5.2 ROS Detection Assay

Cellular ROS levels following AuNP treatment were determined by DCF-DA cellular assay and subsequent fluorescence measurements, quantified by comparison to control cells (Figure 4.3). In all AuNP-treated cases, ROS generation was shown to be elevated in cells that were incubated with NPs in media containing 1 % FBS relative to those in media containing 10 % FBS (Figure 4.3 A). This increase became highly significant ($P \leq 0.0001$) in the highest [AuNP]Incub conditions of 100 and 250 μM, suggesting that the increased availability of serum in media may either help to

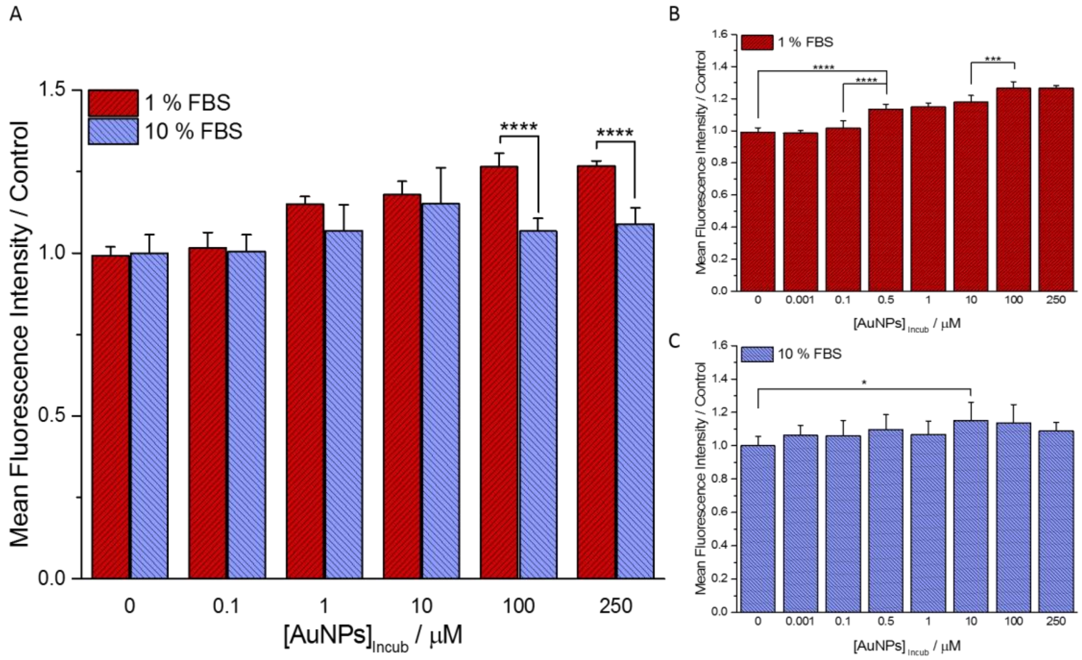

Figure 4.3 ROS detection observed in SH-SY5Y cells treated with increasing concentrations of AuNPs in media containing 1 or 10 % FBS media for 24 h, relative to untreated control cells. ROS detection was elevated in cells treated with AuNPs in 1 % FBS media (A) compared to 10 % and also with (B) increasing $[AuNPs]_{Incub}$. No trend in ROS detection was observed with $[AuNPs]_{Incub}$ within the (C) 10 % media-FBS treated cells.

alleviate ROS generation induced in the presence of high concentrations of AuNPs or result in reduced extents of internalisation.

ROS generation was observed to be increased with AuNP treatments relative to control cells. However, cells incubated with AuNPs in 10% FBS media exhibited no discernible pattern in ROS levels with increased incubation concentrations of AuNPs (Figure 4.3 C). A single instance of significantly increased ($P \leq 0.05$) mean ROS concentration was identified between cells treated with 10 µM AuNPs and the untreated control cells. The mean intensity of all other AuNP treatments in media containing 10 % FBS remained within an 8.9 % increase compared to the control group. In contrast, cells incubated with AuNPs in 1 % FBS-medium showed an incremental increase in ROS generation with increased AuNP concentration (Figure 4.3 B). The mean relative fluorescence intensity observed in cells treated with 0.5 µM AuNPs (1.14 ± 0.03) demonstrated significant ($P \leq 0.0001$) elevation in ROS from cells in all lower $[AuNPs]_{Incub}$ treatment groups (control, 0.001, 0.1 µM). As $[AuNPs]_{Incub}$ was increased, the next significant increase in mean detected ROS occurred at the highest applied nanoparticle concentrations, with the 100 and 250 µM treatment classes being elevated ($P \leq 0.001$) in ROS compared to the 10 µM treatment (1.26 ± 0.04 and 1.27 ± 0.02 respectively compared to 1.18 ± 0.04). Thus, ROS generation increased significantly with administration of increasing concentrations of AuNPs in 1 % FBS media, implying enhanced degrees of oxidative stress experienced by cells following uptake of AuNP cargos in these conditions. It was notable that cells treated with AuNPs in 10 % serum media displayed lower ROS detection than those in 1 % media. It is likely that AuNPs suspended in the 10 % serum-protein rich medium have 'thicker' or more protein-like nutrient corona around them and therefore cause lower stress. Importantly, the trend in ROS generation caused by AuNPs in 1 % FBS media was not reflected in cell viabilities. This suggests that AuNP treatment can cause changes in cell metabolism which are not captured by traditional viability tests.

4.5.3 Identification of NP-induced SERS Spectral Variations

A total of 432 SERS spectra were acquired from cells incubated with 10, 100 and 250 µM AuNPs in 1% and 10% FBS media to interrogate variation in corresponding SERS spectra. Residence of AuNPs in cells was observed to be maximal after 24 h of incubation period, so this duration was selected for use (Figure 8.2). Cells treated with $[\text{AuNPs}]_{\text{Incub}}$ of 100 and 250 µM displayed significant enhancement of cell Raman signal in both serum-media compositions. Within 10 µM AuNP-treated cells, only those incubated in media containing 1 % FBS media provided sufficiently enhanced SERS spectra while 10 % FBS conditions did not yield reliable SERS spectra under the acquisition parameters used. Similarly, $[\text{AuNPs}]_{\text{Incub}}$ treatments of concentration lower than 10 µM in both media compositions did not demonstrate sufficient enhancement of signal to reliably produce SERS spectra of reasonable quality for analysis. This may have resulted from limited NP availability for uptake or reflect pre-aggregation of AuNPs within 10 % FBS media (evidenced by absorbance measurements and TEM in thesis sections 3.4.1 and A.2 respectively) into composites of large, uptake-limiting size.

Outlined in Chapter 1.1, presented research aims to investigate Raman methods for development of industry-viable assays. Therefore, low $[\text{AuNPs}]_{\text{Incub}}$ treatment conditions that did not yield reliable signal enhancement were identified as unsuitable to produce a robust assay that could ultimately be automated. The observation that a 10 µM concentration of AuNPs was able to provide enhancement in 1 % serum-media but not 10 % serum-media provided an initial demonstration of the importance of protein availability within incubation medium. $[\text{AuNPs}]_{\text{Incub}}$ treatments of 250, 100 and 10 µM (22.5×10^9, 9×10^9 and 9×10^8 NPs mL^{-1}) in 1 % FBS incubation media and of 250 and 100 µM in 10 % FBS conditions reliably allowed observation of high SERS signals and were therefore used for the remainder of the study.

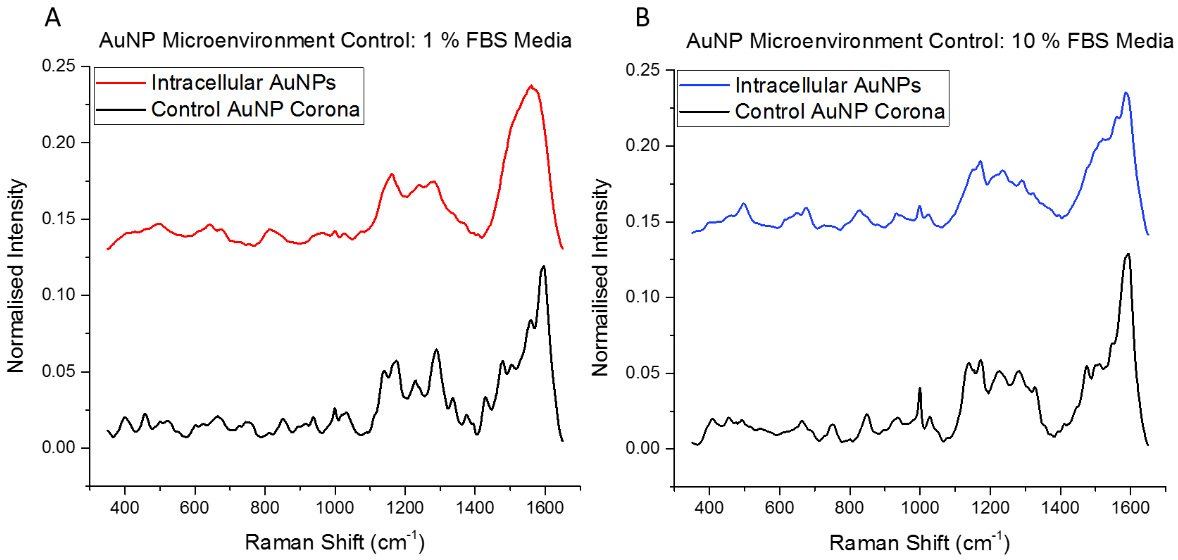

Figure 4.4 In order to confirm SERS measurement from intracellular AuNPs, control AuNPs were incubated in 1 and 10 % FBS-media compositions for 24 h before washing, storage and taking SERS measurements in PBS. 5 spectra were recorded from different regions of AuNPs in each treatment. Acquired spectra from (A) 1 % and (B) 10 % FBS conditions are compared to respective spectra taken from cells incubated with 100 µM AuNPs. In both cases, distinct vibrational peaks, attributed to serum proteins forming a protein corona about the AuNPs, are observed. Cellular internalisation was confirmed by the spectral differences between control and cell spectra, primarily involving increased complexity of spectra in cellular cases which gives rise to broadened, overlapped peaks as a direct result of sampling complex cellular environments.

The collection of SERS signal from inside cells was confirmed by comparison of intracellular SERS spectra with those obtained from control AuNPs suspended in each serum condition in the absence of cells (Figure 4.4). The SERS spectra from control AuNPs show many peaks arising from proteins which likely constitute their protein corona formed upon addition to the media. The intracellular SERS spectra have understandably some similarities with that obtained from control AuNPs as mostly proteins would be adsorbed. Crucially, intracellular spectra have less distinct individual peaks, as other molecules in the immediate environment of NPs would contribute and superpose on the protein corona peaks to yield a much more complex and convoluted pattern. Furthermore, the protein corona around a NP is subject to dynamic compositional changes through molecular exchange with its environment. Therefore, even though NP protein corona composition may be reported, SERS measurements can interrogate changing intracellular conditions by substitution of the diverse range of biomolecules into, at minimum, its outer layers.

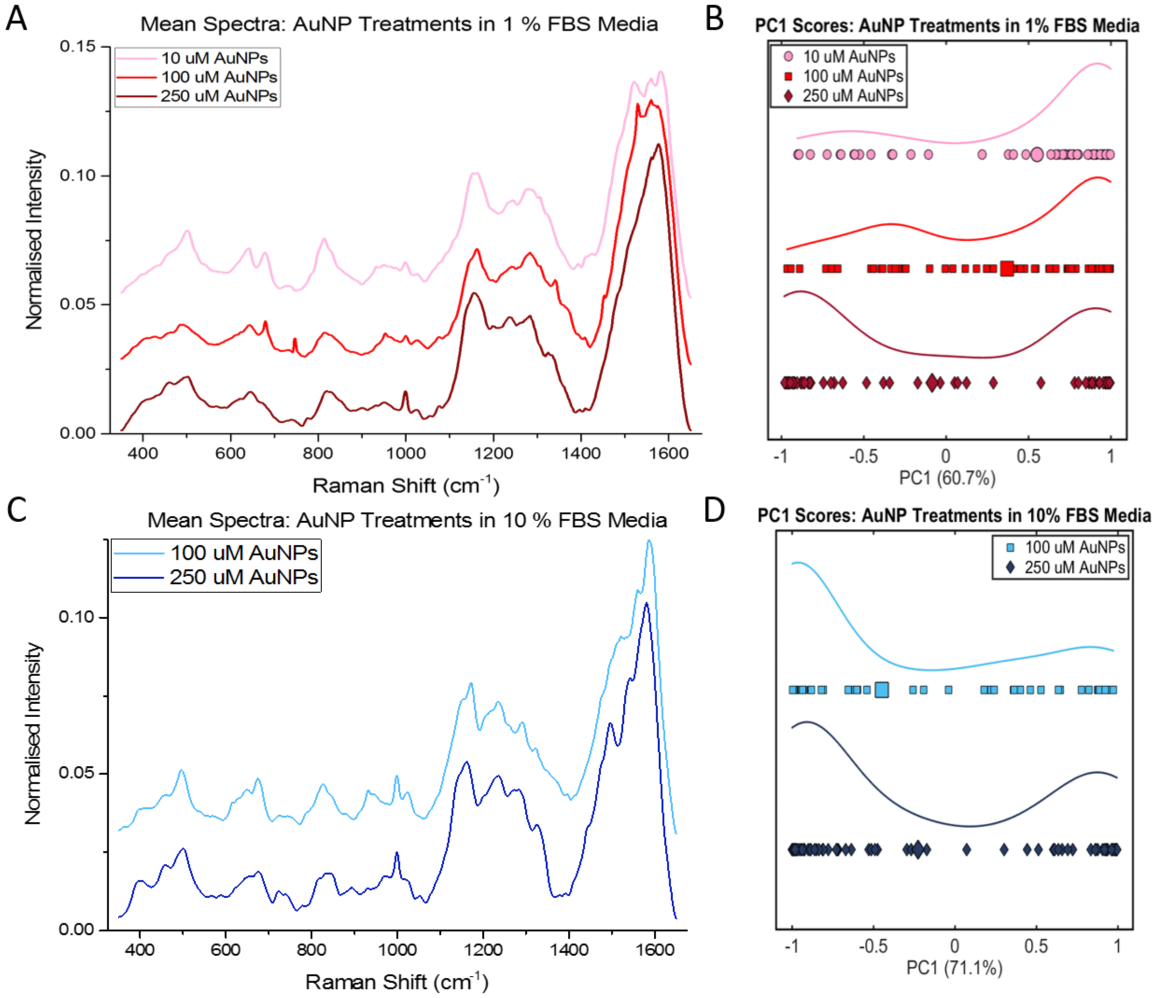

Figure 4.5 Mean SERS spectra of SY-SY5Y cells following 24 h incubation with AuNPs at 10, 100 and 250 µM in 1 % serum media (A) and 100 and 250 µM in 10 % serum media (C). Classification of SERS spectra was observed by PC1 scores in an AuNP-dependent manner within 1 % media (B) and to a lesser extent in 10 % media (D). The baselines of spectra in (A) and (C) are offset for clarity.

Detailed SERS spectral comparison of intracellular environments and protein-rich culture media has been presented in Section 3.4.3.

Mean spectra representing cells exposed to different $[AuNPs]_{Incub}$ and media-serum compositions (Figure 4.5 A, C) show spectral variation between them while displaying typical cellular Raman peaks. These include peaks at 500 cm^{-1} (disulphide protein cross-links), 642 cm^{-1} (Tyr/Phe), 677 cm^{-1} (DNA bases), 813 cm^{-1} (RNA/nuc acids), 1000 cm^{-1} and 1030 cm^{-1} (Phe), 1160-70 cm^{-1} (collagen/lipids), 1240-80 cm^{-1} (amide III) and 1550-60 cm^{-1} (amide II). A full list of tentative spectral assignments is provided in Table 4.1.

Table 4.1 Tentative assignment of peaks arising in mean SERS spectra acquired from cells across studied concentrations in (Left) 1 % FBS and (Right) 10 % AuNP treatments.

Raman Shift / cm^{-1}	Assignment
500	S-S disulfide *str*, Collagen
543	S-S disulfide *str*, Cys
648	C-C *twist*, Tyr/Phe
679	C-C *ring breathing*, DNA Bases
815	Pro, Pro-OH, Tyr/ O-P-O *str* Nuc Acids
826	Out of plane *ring breathing* Tyr, O-P-O *str* DNA
951	CH_3 *str*, Proteins
1000	C-C aromatic ring *str*, Phe
1026	C-C aromatic ring *str*, Phe-H^+
1076	PO_2^-/PO_4^{3-} *sym str*/C-C *sym str*, DNA/Lipids
1150-70	C-C/C-N *str*, Lipids/Proteins
1198	C-N aromatic *str*, C-O Nuc Acids & Phosphates
1200-1300	Amide III Band:
1234	PO_2^- *str*, Nuc Acids
1241	PO_2^- *str*, Amide III/RNA
1275-80	C-N *str* /N-H *bend* Amide III, Collagen/α-helix
1305	CH_2 *deformation*, Lipids
1334	CH_3CH_2 *wagging*, Proteins/Nuc Acids
1395	CH *rocking* , Lipids/Proteins
1409	COO^- *str*, Proteins/Glu/Asp
1480-1575	C-N *str*, N-H *bend* coupling, Amide II
1524	C=C *in plane bend*
1543	CH *deform* /Amide II, NADH/Trp
1561	C=C *ring breathing*, Trp
1569	C=C *ring breathing*, D/RNA Bases
1580	C=C *bend*, D/RNA Bases/Phe

Raman Shift / cm^{-1}	Assignment
500	S-S disulfide *str*, Collagen
543	S-S disulfide *str*, Cys
648	C-C *twist*, Tyr/Phe
678	C-C *ring breathing*, DNA Bases
816	Pro, Pro-OH, Tyr/ O-P-O *str* Nuc Acids
828	Out of plane *ring breathing* Tyr, O-P-O *str* DNA
934	C-C *str*, Pro
1000	C-C aromatic ring *str*, Phe
1028	C-C aromatic ring *str*, Phe-H^+
1070	PO_2^-/PO_4^{3-} *sym str*/C-C *sym str*, DNA/Lipids
1150-70	C-C/C-N *str*, Lipids/Proteins
1198	C-N aromatic *str*, C-O Nuc Acids & Phosphates
1200-1300	Amide III Band:
1234	PO_2^- *str*, Nuc Acids
1241	PO_2^- *str*, Amide III/RNA
1277-80	C-N *str* /N-H *bend* Amide III, Collagen/α-helix
1289	CH_2 *wagging* /Amide III, Lipids/Proteins
1325	CH_3 *deform* /Amide III, Lipids/Proteins
1409	COO^- *str*, Proteins/Glu/Asp
1480-1575	C-N *str*, N-H *bend* coupling, Amide II
1522	C=C *in plane bend*
1543	CH *deform* /Amide II, NADH/Trp
1561	C=C *ring breathing*, Trp
1569	C=C *ring breathing*, D/RNA Bases
1580	C=C *bend*, D/RNA Bases/Phe

While spectral variation is clear between cells treated with different AuNP concentrations both in 1 % and 10 % FBS-media, the observation by itself does not implicate AuNP internalisation as a cause for the differences. Varying media-serum content has been reported to alter intracellular localisation of AuNPs as a result of varying protein corona make-up, with decreased enrichment of protein corona found to increase the likelihood of NPs evading endolysosomal vesicles to achieve free cytosolic residence[267]. Due to the sensitivity of intracellular SERS measurements, sampling from different cellular locations can give drastically different spectral signatures and has been used as such for cellular characterisation and mapping[56,203,259,283].

In order to distinguish between spectral variations that might arise due to location of AuNPs from those possibly arising from NP internalisation and concomitant stress induced, understanding of how similar or different spectra are within and between different treatments was required. Spectral differences arising from increased AuNP treatment concentrations are subtle. PCA was therefore performed on the data from cells within each media serum composition. The results presented in Figure 4.5 B, D show the extent of segregation observed in PC1 scores. PC1 represents the component which accounts for the largest variance within the dataset, taking values of 60.7 and 71.1% for 1 and 10 % FBS treatments respectively. The variance accounted for by higher order PCs incrementally decreased with their generation. Spectra collected from cells with AuNPs administered in 10% FBS media (Figure 4.5 D) form two clusters, the largest of which is located at PC1 value -0.92 and to lesser extent at PC1 = 0.85. The cluster at PC1 score of -0.92 exhibits a tighter clustering of points than that at 0.85. The PC1 distributions of scores corresponding to spectra from 100 and 250 µM AuNP incubation concentrations under high serum (10 %) conditions are fairly consistent. A subtle, yet notable observation is an increased clustering of scores at PC1 = 0.85 in cells incubated with 250 µM compared to 100 µM AuNPs. The observation of two clear regions of clustering within the same media-composition class may indicate that spectral differences between the clusters could be attributed to cellular location or some other effect, but its occurrence resulting as a function of $[AuNPs]_{Incub}$ shows that the spectral variation was caused by biochemical changes arising from either increased NP residency within media or uptake. This effect, albeit only subtle and detected through statistical analysis of SERS spectra, does not correlate with the results of the cellular ROS (Figure 4.3 C) or viability assay which demonstrated no statistically significant difference between the mean ROS levels or viabilities of 100 and 250 µM AuNP treatments in 10% serum conditions. The comparison demonstrates firstly that the SERS-PCA methodology may possess increased sensitivity than both traditional cellular assays in assessing deviations from the ‘healthy’ cellular state, but also that the deviations induced by increased exposure of NPs is more complex than being solely attributable to increased ROS generation and resultant oxidative stress.

Spectra obtained from cells incubated with AuNPs in media containing 1% FBS exhibited a more pronounced effect of AuNP concentration-dependent shifts in PC1 score distribution (Figure 4.5 B). The clustering of a portion of scores observed at PC1 = 0.92 was consistent across 10, 100 and 250 µM AuNP treatments and decreases with $[AuNPs]_{Incub}$. Spectra acquired from cells incubated with 250 µM AuNPs exhibited a shifted distribution, towards a larger peak in scores at PC1 = -0.88. This shift in distribution was similarly seen for 100 µM treatments, displaying a secondary peak in score distribution at PC1 = -0.35. Therefore, accentuation of some SERS spectral effect was suggested, which tended towards the clustering at PC1 = -0.88 in a NP concentration-dependent manner.

The trend in PC scores correlated well with the results of the DCF-DA assay which showed incremental increase in ROS upon increasing $[AuNPs]_{Incub}$ in 1 % FBS. The result suggests that ROS generation is at least a consequence of exposure to a greater concentration of AuNPs. The trend in the distribution of PC1 scores observed in SERS spectra of increasing AuNP concentrations was similar in both 1 % and 10 % FBS media, but crucially the corresponding ROS assay results were only pronounced for the 1 % FBS condition. The result is owed to the complexity of the

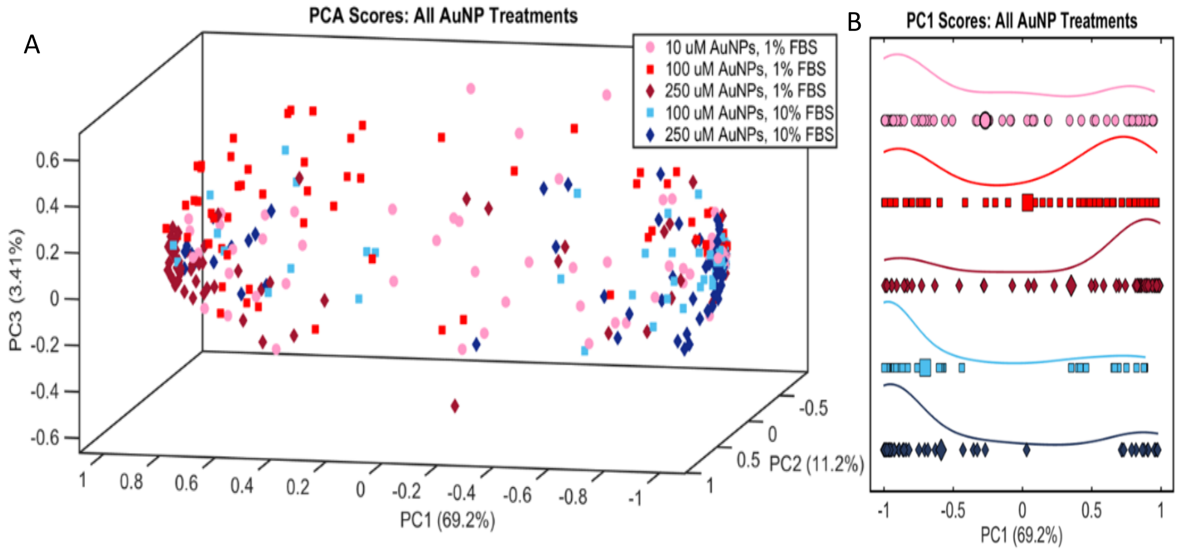

Figure 4.6 PCA analysis performed on the AuNP-treated SERS spectra as a single dataset. PCA scores demonstrate SERS spectra collected from cells treated with 10 µM AuNPs in 1 % FBS (pink circles) to share more features with those treated with 100 and 250 µM in 10 % FBS (light and dark blue squares and diamonds respectively) in (A) three- and (B) one-dimensional scatterplots. PC1 scores suggest an AuNP-dependent variation in the SERS spectral characteristics within the 1 % FBS treatments.

relationship between exposure of cells to (and possibly uptake of) inorganic material and molecular-level changes induced, as well as the increased sensitivity of SERS-PCA experimentation compared to fluorescence assays.

The trend observed by PCA of SERS spectra for both 1 % and 10 % considered separately (Figure 4.5) was explored further by carrying out PCA on the dataset in its entirety, combining both media-serum conditions and all AuNP treatment concentrations (Figure 4.6). New insights were provided as the PCA calculation was run taking the entire dataset into consideration, generating different axes in PC space (PCs). Observation of scores in 3 dimensions (PCs 1-3, Figure 4.6) is complex but nevertheless displays that the data clustered around two major PC1 score values of 0.78 and -0.92, dominated by data points from 10 % in 250 µM and 1 % in 250 µM treatments respectively. Moreover, it can be seen that majority of the data points from 100 µM in 10 % treatment were also coincident with those of 250 µM in 10 %. Similarly, a majority of the 100 µM in 1 % spectral data points tended to align with the 250 µM in 1 % cluster. The spectral data points from 10 µM in 1 % treatment were dispersed within and in-between the two dominant clusters.

Simplification of the analysis to a single dimension, accounting for the greatest variance in the dataset (PC1, Figure 4.6), allowed observation of the trends more clearly. A significant separation was observed between spectra acquired from cells treated with AuNPs at 250 µM in 10 % and 250 µM in 1 % serum media, forming the two previously described clusters respectively. Again, the

100 µM in 10 % FBS treatment yielded almost an identical scores distribution to the corresponding 250 µM treatment. The shifts of PC score distributions with increasing NP internalisation were aligned with those generated from PCA calculations run on each media composition separately. Furthermore, the effect was accentuated in the case of 100 µM AuNP in 1 % FBS media treatment, which shared its predominant peak in score distribution with the 250 µM in 1 % FBS treatment at PC1 = 0.78 (having shifted away from the clustering at PC1 = -0.92, shared with the low concentration treatment). This supports the idea of AuNP dose-dependency in the changing of molecular environment detected by SERS measurements and that the changes identified were consistent between media-serum compositions. Strikingly, PC1 scores revealed a clustering (and thus strongest spectral resemblance) of 10 µM AuNPs in 1 % FBS cell spectra with those of the 100 µM and 250 µM in 10 % FBS treated cells, at PC1 = -0.92. While incubation concentrations of AuNPs were much larger in the 10 % FBS treatments, the expected increase in density of protein corona around NPs may have limited cellular internalisation to levels similar of those in the 10 µM in 1 % FBS treatment. Therefore, spectral similarity would be accounted for.

While a demonstrable change in SERS spectral characteristics arising from increased exposure to AuNPs was presented, its cause remained undetermined. Further experimentation was required to determine whether this effect arose as a result of hypothesised NP-induced changes to intracellular biochemical compositions, or simply due to variable presence of NPs between the intra- and extracellular environment. The internalisation of AuNPs under the varying conditions was therefore investigated both qualitatively and quantitatively by confocal fluorescence microscopy and ICP-MS respectively.

4.5.4 Investigation of AuNP Doses and Uptake

To understand the dose dependence of the SERS spectra and PC analysis, it was important to determine extents of AuNP internalisation into cells. Therefore, confocal microscopy and ICP-MS were performed NP-treated cell preparations in order to image AuNP distribution and quantify internalisation respectively.

Cellular internalisation was visualised by three dimensional imaging (Figure 4.7) of scattering by AuNPs (green) within fluorescently stained (CellTracker, red) cells. Figure 4.7 confirmed the residency of AuNPs inside cells by localisation of NP scattering signal within the cell contour. Cells treated with 10 µM AuNPs in 1 % serum media (Figure 4.7 A) showed only a small amount of AuNPs uptake, represented by a low number of NP aggregates (green), and healthy cell appearance (near complete staining and clearly discernible membrane/nuclear features). A trend of increasing NP internalisation with increasing $[\text{AuNPs}]_{\text{Incub}}$ was observed through visualisation of

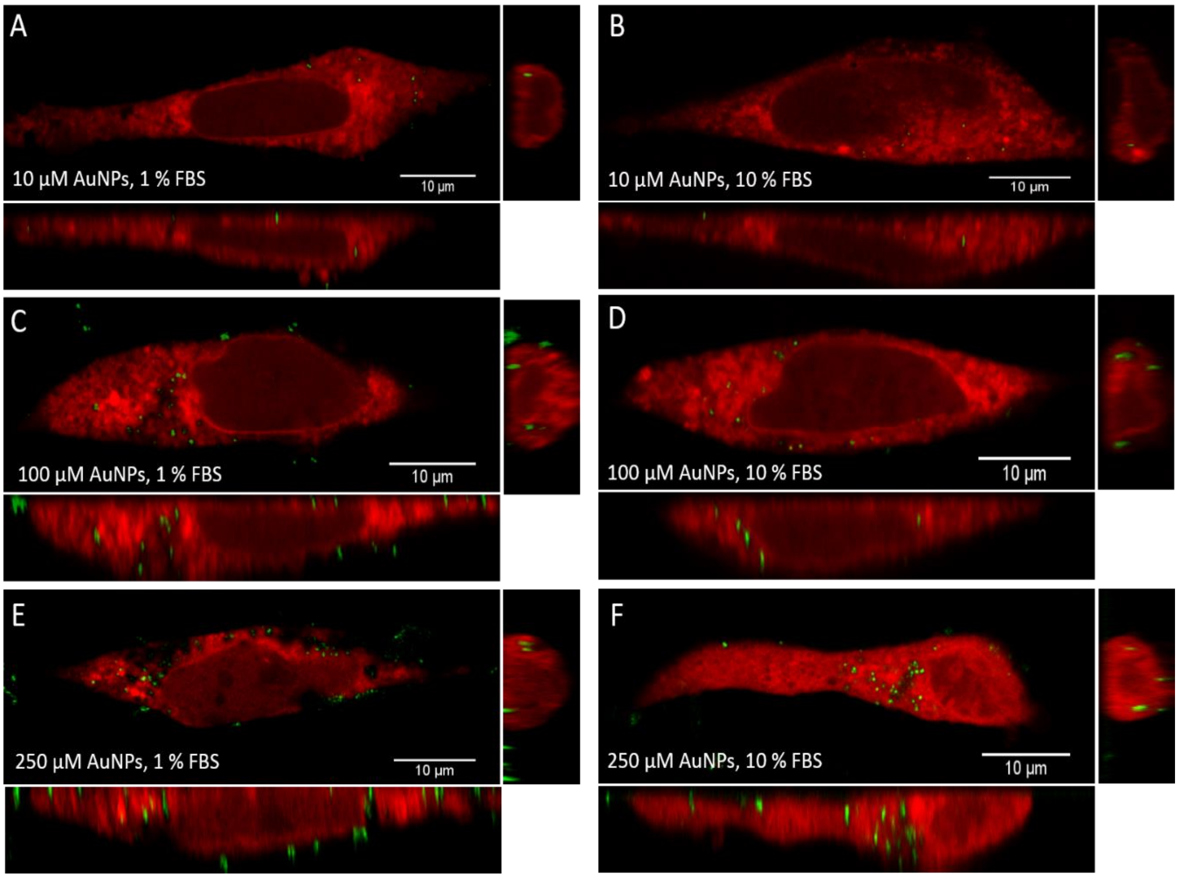

Figure 4.7 Verified internalisation of AuNPs (green) into cells (red) by 3D confocal microscopy. A central slice of a representative cell with corresponding orthogonal sections are shown with increasing concentrations (A) 10 µM (C) 100 µM and (E) 250 µM under reduced serum (1 %) treatment and at (B) 10 µM (D) 100 µM and (F) 250 µM under high serum (10 %) conditions are shown. The number of nanoparticles inside cells increased with increasing AuNP dose concentration. The cells treated under 10 % serum condition are visibly healthier even at a high dose of 250 µM. The cells were stained with the fluorescent dye CellTracker red to visualise the cytoplasm and the cell contour. The AuNPs were imaged using their scattering with a 514 nm laser excitation and CellTracker fluorescence was excited by a 561 nm laser. Scare bar = 10 µm.

increased scattering regions in both media-FBS compositions. In 1 % FBS treatments (Figure 4.7 C & E), this was accompanied by visible signs of cell stress such as incomplete staining, disruption of membranes and cytosolic vacuolisation (represented by unstained voids within the displayed cell areas) and enlargement of nuclei (large area of lowly-intense fluorescence at centre of cells). The signs of damage were observed to correlate with the increased ROS generation detected by DCF-DA assay. Treatment in 10 % serum media (Figure 4.7 B, D, F) revealed cells significantly less damaged in appearance than the corresponding NP doses in 1 % media. Cells treated with 10 µM

NPs in 10 % FBS showed very minimal scattering intensity from AuNPs, both in intensity and numerical frequency of aggregates, suggesting that lack of internalisation may have been responsible for the previously reported poor enhancement of Raman signals. The frequency of internalised aggregates increased with $[\text{AuNPs}]_{\text{Incub}}$ treatments of 100 and 250 µM. Small accumulations of AuNPs were observed at cellular membranes, adhered to the outside of the cell or undergoing internalisation at time of fixing. However, this effect only became observable at high concentrations $[\text{AuNPs}]_{\text{Incub}}$ (100 µM and 250 µM for 1 and 10 % FBS media) and the vast majority of AuNPs were internal. Therefore, qualitative confirmation of AuNP intracellular residency is presented under the NP incubation parameters investigated by SERS experiments.

Qualitative trends in extents of NP internalisation with incubation parameters identified in this study are further supported by TEM data presented in Appendix Section A.2 of this thesis. AuNPs were administered to SH-SY5Y at concentrations of $[\text{AuNPs}]_{\text{Incub}}$ = 10 and 150 µM at DMEM-FBS compositions of 1, 5 and 10 % for a duration of 48 h. Despite the variation in incubation time (24 h used in this study), AuNP uptake was similarly shown to increase upon application of higher dose concentrations within decreased media-serum content (Supplementary Figure 8.3 and Figure 8.4). Very high uptake and accompanying damage of cells treated with high AuNP doses ($[\text{AuNPs}]_{\text{Incub}} \geq$ 100 µM) in 1 % FBS media was observed in both confocal fluorescence and TEM experiments. Similarly, the highly limited uptake of AuNPs into cells dosed at $[\text{AuNPs}]_{\text{Incub}}$= 10 µM in 10 % FBS-media, that prevented sufficient and reliable enhancement of SERS intensities identified in this study, was corroborated even after 48 h incubation time by TEM. Thus, although not directly comparable, support of AuNP uptake trends observed with changing NP doses and media compositions presented in this study by TEM is inferred.

ICP-MS measurements performed on lysate solutions of AuNP-treated cells (25000 cells per sample) provided a quantitative measure of relative AuNP uptake between varying incubation conditions. Lysate Au concentrations presented increases (greater ten-fold between 10 and 250 µM treatments) with increased $[\text{AuNPs}]_{\text{Incub}}$ in both 1 and 10 % serum media compositions (Figure 4.8). Comparison between different media compositions revealed vastly increased concentrations of Au in cell lysates under 1 % FBS conditions for all $[\text{AuNPs}]_{\text{Incub}}$ (Figure 4.8 A). Incubation of AuNPs at 250 µM in 1 % serum media produced a mean Au concentration of 101.2 (± 1.3) µM compared to 10.4 (± 0.4) µM in 10 % FBS media (Table 4.2). A high standard deviation was observed in the measurement of cells treated with 100 µM AuNPs in 1 % FBS.

Interestingly, similar Au concentrations were measured in lysates of cells incubated with AuNPs at 10 µM in 1 % FBS and 100 µM in 10 % FBS ([Au] = 1.35 ± 0.57 and 2.55 ± 0.98 µM respectively). These treatments also represented the minimum $[\text{AuNPs}]_{\text{Incub}}$ for which SERS spectra could be

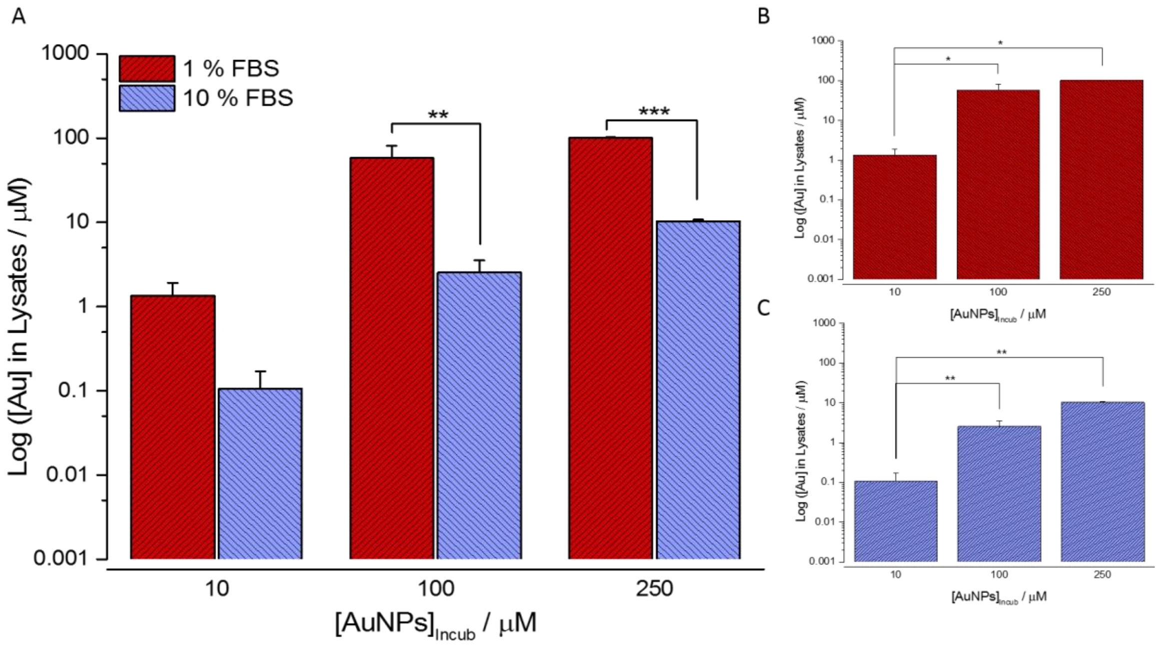

Figure 4.8 Comparison of total Au concentration in lysates of SH-SY5Y cells following incubation at [AuNPs]$_{Incub}$ of (A) 10, 100 and 250 µM within culture media containing (B) 1 and (C) 10 % foetal bovine serum, as quantified by ICP-MS. The uptake amount in low serum conditions was an order of magnitude higher than the corresponding treatment under high serum conditions. Note the y-axis is a log-scale.

Table 4.2 Mean Au concentrations and calculated number of AuNPs per lysate measured within SH-SY5Y cells by ICP-MS, following 24 h incubation with AuNPs at concentrations of 10, 100 or 250 µM in serum containing 1 or 10 % FBS.

[AuNPs]$_{Incub}$ / µM	Media FBS / %	Mean Au (± SD) / µM	Corresponding AuNPs per Lysate / #
10	1	1.35 (± 0.57)	2.44 (±1.03) x10^{8}
100	1	57.96 (± 23.28)	1.05 (±0.42) x10^{10}
250	1	101.16 (± 1.26)	1.83 (±0.02) x10^{10}
10	10	0.11 (± 0.06)	1.99 (±1.08) x10^{7}
100	10	2.55 (± 0.98)	4.61 (±1.77) x10^{8}
250	10	10.35 (± 0.44)	1.87 (±0.08) x10^{9}

reliably acquired within their respective media-FBS concentrations, possibly establishing a required Au concentration of lysates that corresponded to robust SERS enhancements. Importantly, the result supports the previous postulation (SERS-PCA results) that the similarities observed in SERS spectra between 10 µM AuNP treatment in 1 % serum and higher NP doses in 10 % serum media treatment were a result of similar extents of NP internalisation.

Overall, the visualised and measured increases in NP uptake accompanying incubation in reduced-serum media correlate to variation identified in corresponding SERS spectra and PC analysis

(Figure 4.5 & Figure 4.6), confirming that the changes are indeed a result of greater extents of AuNP internalisation.

4.5.5 Characterising AuNP-induced SERS Spectral Changes

Comparison of SERS spectra between cells treated with AuNPs in conditions identified as achieving lower extents of AuNP uptake and no significant elevation in ROS (10 µM AuNPs in 1 % FBS media and all 10% FBS treatments) with those of cells treated in conditions yielding increased uptake and elevated ROS levels (100 and 250 µM AuNPs in 1% media) was used to identify SERS-markers of AuNP-induced changes to the intracellular environment (Figure 4.9).

PC1 scores (Figure 4.9 B) demonstrated that there was spectral dissimilarity between cells exhibiting very high AuNP uptake ($[AuNPs]_{Incub}$ = 250 µM in 1 % FBS) and those exhibiting a less excessive extent of uptake ($[AuNPs]_{Incub}$ = 10 µM in 1 % FBS and 250 µM AuNPs in 10 % FBS). Presented ICP-MS results suggested that this variation may be attributed to the identified increase in AuNP internalisation and independent of increased FBS content. Therefore, subtraction of the mean spectra of cells treated with 10 µM from that of those treated with 250 µM AuNPs (both 1 % FBS) produced a difference spectrum (Figure 4.9 C) that highlights the strongest spectral variations arising from the different extents of NP uptake achieved (since no other variable differs between the classes). Assignment of the variations (Figure 4.9 D) therefore offers a route to delineate potential cellular events accompanying increased AuNP exposure. Predominant peak intensity increases and decreases are highlighted in dark and light grey shades respectively and are discussed below.

Flattening of S-S stretching vibration regions (540-500 cm^{-1}) was observed in the 250 µM AuNP treatment, implying destabilisation of protein folding by the breaking of cysteine-cysteine bonds that was in agreement with previous cell stress studies[263,264]. Conversely, the intensity of the C-C ring breathing vibration in Phe (1000 cm^{-1}) and that of its acidified form (1030 cm^{-1})[264] yielded little change between the treatments. Elevated intensities of peaks were seen within the amide III (1200-1260 cm^{-1}) and amide II (1560-1580 cm^{-1}), arising from coupling of C-N stretching and N-H bending vibrations[284]. Increased intensity of amide I C=C/C=O stretching (1601 cm^{-1}) in Phe/proteins was also observed with increased AuNP uptake. Thus, supported by the observation of decreased disulphide bridging, the unfolding of proteins arising from AuNP-induced denaturation could be inferred[263,284].

The increased peak intensity located at 1241 cm^{-1} may also correspond to protein denaturation through exposure of glycine (Gly) backbones and Pro sidechains, or asymmetrical stretching of PO_2^- from phosphodiester groups of nucleic acids. Other RNA peaks however manifested at 802

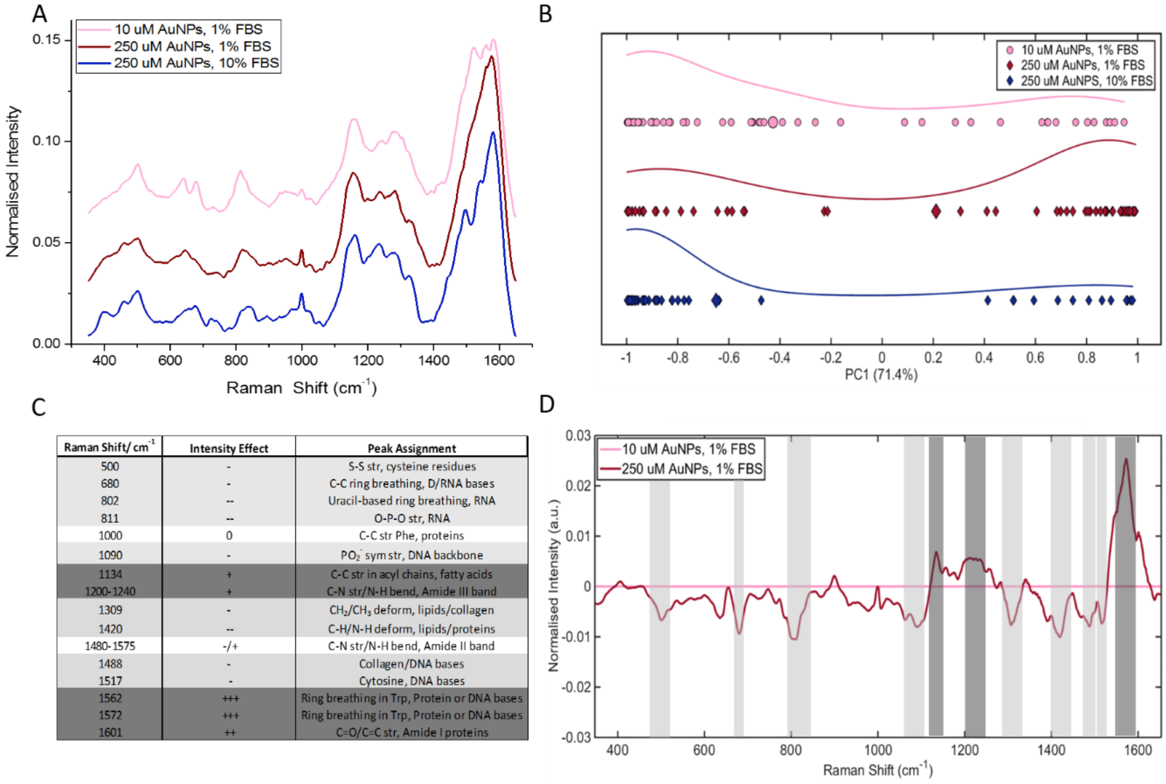

Raman Shift/ cm^{-1}	Intensity Effect	Peak Assignment
500	-	S-S str, cysteine residues
680	-	C-C ring breathing, D/RNA bases
802	--	Uracil-based ring breathing, RNA
811	--	O-P-O str, RNA
1000	0	C-C str Phe, proteins
1090	-	PO_2^- sym str, DNA backbone
1134	+	C-C str in acyl chains, fatty acids
1200-1240	+	C-N str/N-H bend, Amide III band
1309	-	CH_2/CH_3 deform, lipids/collagen
1420	--	C-H/N-H deform, lipids/proteins
1480-1575	-/+	C-N str/N-H bend, Amide II band
1488	-	Collagen/DNA bases
1517	-	Cytosine, DNA bases
1562	+++	Ring breathing in Trp, Protein or DNA bases
1572	+++	Ring breathing in Trp, Protein or DNA bases
1601	++	C=O/C=C str, Amide I proteins

Figure 4.9 Identification of SERS spectral changes induced by high AuNP uptake. (A) Mean SERS spectra of cells treated with conditions displaying intermediate (10 µM in 1 % FBS, 250 µM in 10 % FBS) with high (250 µM, 1 % FBS) AuNP internalisation. The spectra were offset for clarity. (B) PC1 scores of the selected treatments revealed spectral similarity between the lower uptake treatments and variation from the high uptake class. (C) Assignment of peaks presenting predominant variations in the (D) difference spectrum between mean spectra of cells demonstrating high AuNP uptake ($[AuNPs]_{Incub}$ = 250 µM, dark red) and intermediate uptake ($[AuNPs]_{Incub}$ = 10 µM, pink) in 1 % FBS incubation media.

and 811 cm^{-1} (uracil-based ring breathing and O-P-O stretch respectively)[284] and present decreased intensities following high degrees of AuNP internalisation. Therefore, AuNP internalisation is proposed to play a role in the disruption of normal RNA-based cellular events such as transcription and translation. The higher intensities of these peaks may represent degradation through exposure or exchange of constituent chemical groups into NP electronic fields or protein corona respectively.

The fine vibrational peaks resolved within the amide II region (1480-1575 cm^{-1}) exhibited no consistent trend in SERS intensity changes following increased AuNP uptake. Increases may suggest exposure of coupled C-N and N-H vibrations to AuNPs and thus protein denaturation as previously described. However, the increased intensity of 1572 cm^{-1} has also been reported to arise from ring breathing vibrations in NADH[284,285], with its phosphorylated form NADPH known to provide a reductive environment for the cells to nullify increased ROS during oxidative stress[286]. The increased intensity of vibration 1562 cm^{-1} may support this, with the peak corresponding to vibrations in tryptophan (Trp), converted to quinolinate, a *de novo* precursor to the pyridine ring of NAD derivatives in eukaryotic cells[287,288]. This may be due to upregulation of cellular antioxidant defences in response to AuNP internalisation. However, further investigation by complementary techniques is required to establish this definitively.

Within the lower wavenumber amide II range however, peaks at 1488 and 1517 cm^{-1} decreased in intensity. While C-N/N-H coupling contributes to these peaks, they may also represent C=C breathing modes in DNA bases guanine and cytosine respectively[284]. Decreased SERS intensity of DNA-attributed vibrational modes was also observed at 680 and 1090 cm^{-1}. The possibility of AuNP-induced stress causing DNA fragmentation is therefore implied, which is a well-known to occur under cell stress[130,277,278]. A similarly complex picture is presented in lipid-assigned SERS peaks. The vibrational mode at 1305 cm^{-1} relates to CH_2 deformation in lipids, with its decreased intensity inferring possible degradation of phospholipids. This cell stress event has previously been detected by SERS within HSF and A549 cell lines upon stress induced by exposure to ZnO NPs[264]. In contrast, the C-C stretching mode of acyl chains at 1134 cm^{-1} exhibited increased SERS intensities.

Intracellular SERS measurements have revealed changes to SERS spectra accompanying varying degrees of AuNP internalisation, as identified by the application of multivariate analysis techniques and supported by internalisation data. Such changes are tentatively assigned to NP-induced cell stress events such as protein misfolding and denaturation, oxidation of proteins and lipids and changes to DNA/RNA regulation/structure. However, the investigation of their underlying biomechanistic causes that are either induced by or triggered by increased nanoparticle uptake are beyond the scope of this thesis. More precise conclusions detailing NP-induced effects on specific cellular pathways can only be drawn after further comprehensive examination of increased sample sizes and diversity of AuNP treatments (including NP morphology, diameter, incubation period, surface modifications and cell lines), representing a highly significant body of research.

4.6 Conclusions

The presented study has combined biological assays for cell viability and ROS detection with intracellular SERS measurements to evaluate potential perturbation of healthy cellular activity induced in human neuroblastoma cells by AuNP nanosensors. The NP dose-dependent increase in ROS generation observed by DCF-DA assay was especially not reflected in the viability results. This suggests that simple viability measurements do not suffice to qualify the ‘internal health’ of the cell for SERS studies. Moreover, SERS measurements and PCA analysis revealed that altered spectral characteristics in cells treated with increased doses of AuNPs in low serum media, can be concluded to be a result of increased AuNP internalisation that was confirmed by ICP-MS. Serum-rich AuNP incubation led to lower internalisation in general that was comparable to low dosage at reduced serum conditions. This resulted in spectra under high serum conditions holding similarity to those at low dosage under reduced-serum conditions, again confirming that spectral changes we observe are indeed due to increased internalisation of AuNPs. Confocal imaging of AuNPs within cells verified NP internalisation to confirming the intracellular nature of analysed SERS spectra. Correlative information provided by ROS assay identified that oxidative stress plays some role in the complex spectral changes observed following excessive NP uptake by cells. Assignment of spectral variations arising from AuNP-induced stress identified SERS peaks which have been previously attributed to oxidative stress following administration of other inorganic NPs, such as protein denaturation and misfolding events, lipid decomposition and DNA fragmentation[263,264].

Overall, the study shows that nanosensors themselves can perturb the environment which they measure and therefore care must be taken in the application of NPs, including AuNPs, for intracellular SERS investigations. Their high uptake causes changes in their biochemical environment, which is a deviation from the ‘natural’ cellular state and thus affects spectra acquired. Although the changes are unarguably complex and need to be better understood, oxidative stress is implied as one of the effects. Understanding and employing AuNP incubation conditions that achieve non-perturbative intracellular SERS experiments is essential for confirming study validity, as well as insights the technique offers into NP-cell interactions, characterisation of cellular processes and further applications in drug discovery.

In the broader context of this thesis, optimisation data is presented in this study concerning two of the key incubation parameters involved in achieving intracellular AuNP residency for SERS sensing applications. AuNP residency within cells was demonstrated by analysis of brightfield microscopic images to reach a maximum after 24 h of AuNP incubation compared to 6, 12 and 48 h time points. The residency remained high after 48 h, but a large increase was observed between the 12 and 24 h treatments, implying that a minimum duration of 24 h should be employed for the studied model. High AuNP uptake is required of the SERS platform in order to reliably produce sufficient enhancement of Raman signals for sensitive yet robust measurements, especially for the case of automated development. For this, any given cell or (group of cells) must invariably contain a sufficient amount of AuNP aggregates to provide sensitive readouts. While more comprehensive population studies would be required to statistically confirm the finding, minimum values of $[AuNPs]_{Incub}$ were identified as 10 and 100 µM to allow sufficient uptake for reliable provision of SERS enhancement in 1 and 10 % media compositions respectively corresponding to cell lysate Au concentrations of 1.35 and 2.55 µM respectively.

Altering the FBS content of incubation media was shown to make a profound impact upon the extent to which AuNPs were internalised by cells. Incubations performed in 1 % FBS composition exhibited, typically, a ten-fold increase in uptake compared to those of the same $[\text{AuNPs}]_{\text{Incub}}$ in 10 % FBS. However, the increased uptake must be considered to be balanced against cellular health, as incubation in low-serum media was shown to negatively impact cell health by ROS generation, visual examination of fluorescently stained cells and the developed SERS-PCA platform. The effect was also observed in the less sensitive cell viability assay, highlighting reduced (but still high) viability in control cells treated without AuNPs in 1 % FBS relative to those in 10 % FBS. Thus, a careful balance must be struck by incubation parameters for achieving AuNP internalisation into cells such that the amount of Au residing within is not excessive and producing toxic effects.

Achieving intracellular residency of AuNPs in a non-perturbative manner is essential for drug discovery applications in order to provide a model as close to the cell natural ‘healthy’ state as possible, particularly during compound screening in order to avoid NP toxicity effects being falsely recorded as drug actions or side effects. Therefore, based upon the presented results, incubation parameters would be recommended to include media of serum content greater than 1 %, while a decrease from the 10 % traditionally used in complete culture medium could prove advantageous for increasing extents of internalisation. The $[\text{AuNPs}]_{\text{Incub}}$ applied should take the media-serum composition into account, as its effect on internalisation has been clearly presented. Cell lysate concentrations of Au were on the order of 1-5 µM, factoring in the standard deviations of the ICP-MS results and the identified minority of outer membrane-adhered AuNP aggregates.

The careful application of suitable AuNP incubation parameters can therefore allow sensitive yet robust SERS measurement of intracellular environments with minimal disruption of healthy cellular metabolism for use in drug localisation studies. The sensitive nature of the SERS-PCA platform may also find utility in monitoring the response of cells to chemical intervention as a broader-scale assay, offering higher sensitivity and specificity of information than viability assays. An increased richness of data available is available from single experiments compared to sensitive yet very specific biological assays, a factor that would be particularly beneficial with modern research tendencies towards large datasets and –omics methodologies.

Chapter 5 SERS Mapping of Intracellular Compound Localisation

5.1 Abstract

Determining the localisation and concentrations of drug molecules inside intact cells is essential for understanding molecular pharmacodynamics *in vivo* to augment the therapeutic development for improved clinical outcomes. Surface-enhanced Raman spectroscopy (SERS) is an extremely sensitive molecular fingerprinting technique that has been increasingly applied to intracellular applications. In this study, the ability of reporter-free SERS to detect the uptake of exogenous small molecules (such as drugs) into organelles of interest, inside human neuroblastoma cells is demonstrated. As an exemplar molecule of interest, the commercially available fluorescent dye LysoTracker Red was selected, owing to its known localisation into cell lysosomes. SERS maps were acquired of treated cells, showing clear detection of LysoTracker molecules trapped inside cellular endolysosomes, following pre-incubation of AuNPs informed by results in Chapter 4. Compared to univariate analysis of simple peak intensities, multivariate analysis using principal component analysis (PCA) was shown to improve the visualisation of SERS maps. This allowed better colocalisation of the LysoTracker SERS signals to the molecule's intrinsic fluorescence emission, thus validating the methodology. The study establishes the ability of intracellular SERS in combination with multivariate analysis approaches to allow measurement of molecular uptake within cellular endolysosomes. Proof-of-concept is presented for the proposed reporter-free SERS-based analytical methodology for monitoring drug molecule localisation and therapeutic nanocarriers in cell based-assays in the drug discovery pipeline and specifically to study organelle-related disorders such as lysosomal storage diseases (LSDs).

5.2 Contributions

Research was carried out by the candidate exclusively. Based upon the study presented, a journal article manuscript has been produced in collaboration with Dr Imran Patel (University of Cambridge), and is currently under revision. The candidate is a joint first author and has individually reproduced relevant experimental results.

5.3 Background

Measuring the localisation and metabolism of drug molecules at their intracellular target is crucial for understanding their pharmacodynamics to improved clinical outcomes[8]. Combined with their ability to act as label-free SERS probes for interrogation of their immediate chemical environment, voluntary uptake of plasmonic AuNPs into cells offers SERS as a highly-sensitive technique for monitoring the intracellular environment at the molecular level. For this SERS methodology to be effective, NP administration to cells must be carefully considered and is underpinned largely by striking a balance between achieving sufficient enhancement of Raman signal while maintaining biocompatibility. Induction of cell stress impacts experimental validity through deviation from a cell's natural state that can be reflected in the spectra acquired.

Overall, it is now well accepted that appropriately-performed SERS is a highly sensitive technique with molecular characterisation ability that can be utilised for intracellular measurements[10,11,21]. Despite this, application in drug discovery contexts remain limited. Established Raman-active therapeutics, such as chemotherapy agent doxorubicin have been the subject of intracellular SERS detection experiments involving either combination with fluorescence tracking or indirect detection using spectral variation in functionalised SERS-reporter molecules[136,197,265,289,290]. Decreases in SERS intensities of SERS-reporter molecules have also been used to imply intracellular delivery of therapeutics enclosed within AuNP-based vehicles[265].

The reporter-free SERS approach, where the entirety of a NP's immediate biochemical environment is directly interrogated in a non-selective manner, generates greatly enriched spectral datasets detailing the full molecular fingerprint of a sample. This is particularly useful in examining the effects of drug treatments on cell environments at the molecular scale. The response of MCF-7 cells, pre-incubated with nuclear-targeted Au nanostars, to chemotherapy agents cisplatin, camptothecin and fluorouracil has been monitored using SERS[291]. Similarly, the SERS-detectable response of cells to both thermally and chemically-induced apoptosis has been demonstrated using mitochondria-targeted AuNPs, while spheroids treated with doxorubicin or paclitaxel also undergo discernible spectral changes compared to healthy cells, both providing indicative SERS markers for drug action and cell death[118,292]. These applications are useful in pharmaceutical development, however do not provide direct location or pharmacodynamic information of a drug molecule itself. Co-administered drugs 6-mercaptopurine and methimazole have been detected inside cells utilising chemical structures previously demonstrated to favourably adsorb onto the surface of silver nanoparticles in an example of reporter-free intracellular SERS drug detection[293]. However, the use of specific drug-NP interactions such as binding or favourable adsorption detracts from both the ability to sample the NP's entire intracellular environment and the development of SERS as a ubiquitous pharmacodynamic assay. The reporter-free SERS methodology is therefore yet to be applied for monitoring exogenous molecule uptake in a wider (assay-based) platform for a given target organelle, achieving detection by simple colocalisation alone.

The following chapter builds upon previously established data concerning AuNP incubation parameters to demonstrate for the first time a reporter-free SERS platform capable of directly detecting uptake and localisation of an administered exogenous molecule at its intracellular target organelle. This example is specific only to the endolysosomal targets, with detection achieved purely by spatial colocalisation of drug to NPs, in order to maintain an assay platform independent from drug chemical structural requirements. Additionally, the platform holds potential for use at other intracellular drug targets by manipulation of NP properties (size, surface modification) to achieve localisation at various organelles. Studies interrogating endolysosomes for detecting lysosome-targeting compounds have not been carried out. Lysosomes are pivotal organelles in cellular homeostasis and their dysfunction is reported in a collection of genetic disorders known as lysosomal storage diseases (LSDs), exhibiting impaired turnover and disposal of specific variant-dependent substrates[294,295,296]. Enzyme replacement therapy (ERT, delivery of functional recombinant enzymes into lysosomes) and/or molecular chaperones provide therapeutic routes for a number of LSDs, which remains an active area of research as most standard treatments remain limited to symptom alleviation[296]. The ability to probe delivery and behaviour of prospective therapeutic agents within lysosomes therefore presents a crucial opportunity to improve pharmacodynamic understanding and efficacy.

Herein, a commercially available molecule, LysoTracker Red, is adopted as a model compound or ‘drug mimic’. Its known localisation to lysosomes represents a drug candidate required to act within or upon the organelle. In this study, it was found that the uptake of AuNPs did not compromise the viability of SH-SY5Y cells and the reporter-free SERS approach proved effective in detecting the localisation of the exogenous molecule inside cells. The citrate-stabilised AuNP SERS probes are resident inside the cell, at the selected target organelle, at the time of drug administration, offering utility as a pharmacodynamic assay platform. Using this approach, the intracellular distribution of LysoTracker was determined and correlated to its localisation through SERS mapping, verified by but not dependent upon observation of its fluorescent emission. The ability to improve detection accuracy using multivariate analysis was demonstrated by comparison against individual SERS peaks of the molecule. Thus, the study clearly establishes the AuNP-based SERS methodology and that it is generic. This approach can be of immense utility in deciphering pharmacodynamics and intracellular distribution of drugs inside cells and at the organelle level to provide a useful tool for cell-based assays in the drug discovery pipeline.

5.4 Methods

5.4.1 Cell Culture

Human neuroblastoma cell line SH-SY5Y was cultured in DMEM supplemented with 10% foetal bovine serum (FBS), 100 µg/ml penicillin and 100 µg/ml streptomycin (pen-strep). Cells were incubated at 37 °C, 5% CO_2 and split every 4 days. For experimentation, seeding was performed at 25,000 cells onto 18 mm poly-L-lysine-coated glass cover slips. Morphological cell differentiation was induced by incubation in reduced-serum DMEM (1% FBS, 1% pen-strep mixture) containing retinoic acid (20 µM) for 72 h.

5.4.2 AuNP Administration

AuNPs (60 nm diameter, BBI international) were administered to differentiated cells following removal of citrate buffer, washing with PBS and suspension of NPs (150 µM, 1.35×10^{10} NPs mL^{-1}) in culture medium DMEM (5 % FBS, 1 mL) to allow cellular uptake by endocytosis. The applied $[AuNPs]_{Incub}$ was selected following optimisation experiments performed in Chapter 4 of this thesis, employing a high total dose in an intermediate media-serum composition to strike a balance between AuNP uptake and minimising cell stress. The extent of AuNP uptake (percentage of cell area occupied) was investigated under these conditions by analysis of brightfield images following AuNP incubation for 6, 12, 24 and 48 h (Appendix Chapter A.1). Cell viability was also assessed (n = 2) under these conditions by trypan blue exclusion assay to identify cell membrane compromise. Incubation of cells in AuNP-doped media was performed for 48 h to increase probability of recording SERS measurements from mature endolysosomes while maintaining a high degree of intracellular AuNP residency and cell viability. Differentiated cells were incubated without AuNPs for 48 h to verify culture conditions.

5.4.3 LysoTracker Red Incubation

LysoTracker treatment was performed following cell incubation with AuNPs, which lay resident within cellular endolysosomes for detection the molecule’s arrival at its intended target. AuNP-treated SH-SY5Y cells were incubated with LysoTracker Red DND-99 (50 nM, Life Technologies) in DMEM (free of phenol red) for 2 h before washing, subsequent fixation by paraformaldehyde (4 %) and short-term storage in PBS solution (4 °C) before analysis. Control cells were prepared by incubation of differentiated and AuNP-treated cells in fresh culture medium without LysoTracker molecule for the same 2 h period before processing, as well as LysoTracker staining of differentiated cells which had not been treated with AuNPs. Reference samples, without cells, comprised of AuNPs suspended in LysoTracker solution (50 nM) were generated to obtain the molecule's SERS spectrum.

5.4.4 Confocal Fluorescence Microscopy

Confocal laser scanning microscopy was performed on an inverted Leica SP8 confocal microscope. Cover slips were mounted in glycerol onto glass microscope slides and sealed. High-magnification brightfield images (184x184 µm) were obtained with a 63x objective (Nikon HC PL APO, NA = 1.3) and averaged twice. The scattering arising from AuNPs internalised within cells was imaged in reflection mode using a 514 nm laser line and PMT detection in the 520 – 550 nm range. LysoTracker Red fluorescence was sequentially imaged using a 561 nm laser line with PMT detection between 565 – 660 nm. Z-stacks were acquired with a 0.33 µm step size and typically consisted of around 35 slices. A total of 26 cell image stacks were acquired across two repeats, including control treatments of AuNPs or LysoTracker singly to validate the detection.

Images were processed and analysed using FIJI image analysis software. Processing steps involved manual selection of an image slice 1 µm above the base, from which a binary mask of the cell contour was produced by applying a Gaussian blur, background removal by thresholding (consistent between treatments) and removal of remaining bright and dark outlier signal. LysoTracker fluorescence and NP scattering channel stacks were processed by 3D Gaussian blurring and clearing of signal outside the applied cell contour mask. Co-localization analysis was performed using FIJI plugin JACoP[297] to perform Pearson's correlation analysis and Manders test following thresholding of the individual channels. A total of 22 fields of view treated with both AuNPs and LysoTracker were analysed.

5.4.5 Raman Microspectroscopy

Raman spectroscopy was performed using the Renishaw Raman InVia microspectrometer equipped with streamline accessory (Renishaw plc, Wotton-under-Edge, UK) described in Section 3.2.1. System parameters consisted of a 633 nm point laser, Renishaw-automated 100 nm encoded XYZ stage, Rayleigh holographic edge filter and a diffraction grating (1200 lines/mm) dispersing Raman signals onto a master Renishaw Peltier cooled charge coupled detector (1024 pixel x 256 pixel). System calibration was carried out using an internal Renishaw silicon calibration source for wavenumber shifts. A white light camera mounted on the microscope was used to obtain brightfield images and visualize areas for spectral acquisition.

SERS cell mapping conditions employed a 633 nm streamline focus laser, 63x water immersion objective lens (NA = 1.20), 10 s exposure and 500 nm x 1250 nm step size was used to scan across the whole cell area. The potential for photothermal damage to cells was minimised by the use of low laser power (3.5 mW), spatially dispersed by linefocussing, at acquisition times significantly lower than those employed in plasmonic photothermal therapy applications[298]. A 532 nm excitation laser (0.2 mW, 30 s) was employed on the same cells to collect fluorescence intensity from applied LysoTracker to verify colocalisation of the signals. Spectra were acquired from a total of 25 cells over three repeats.

5.4.6 Spectral Processing and Multivariate Analysis

Cosmic rays were removed from spectral maps using Renishaw Wire 3.4 nearest-neighbour software. Spectra were truncated to the spectral range of 200–1800 cm^{-1} before wavelet de-noising, polynomial baseline correction and normalization were carried out. Univariate analysis was performed by examining individual Raman peak intensities corresponding to vibrational modes of interest and plotting their distribution across cell maps. IRootLab graphical user interface toolkit for MATLAB (TheMathsWorks, Natick, MA, USA) was utilised to process spectra and apply multivariate analysis PCA compiled by Trevisan e*t al*'[256]. Scores are plotted into a calculated PC space to reveal clustering of similar data (spectra) and therefore discriminate between classes of data whereas PC loadings are correlated to the original data to discern which variables (wavenumbers) contribute most to the generated PCs. Each PC was examined individually to determine which represented the best segregation of classes and derived PC loadings identified the vibrational modes from which this arose[256].

Back-projected PC score images were generated using a custom MATLAB script to individually subtract spectral backgrounds using asymmetric least squares[299]; smooth using a Savitzky-Golay filter, mean-centre and normalise data. Calculated PC score intensities within each component were back-projected onto their original pixel locations, along with plotting of associated loadings. Analysis of PCA outputs localisation to LysoTracker fluorescence was performed using FIJI.

5.4.7 Colocalisation Analysis

Pearson's Correlation Coefficient (PCC) is a well-established technique within fluorescence microscopy for examining the relationship between intensities of two channels in homologous pixels. PCC can adopt a range of values from -1 to 1, representing perfect negative and perfect positive correlation of intensities, while a value of 0 reports no correlation between the channels[300,301]. It is mathematically similar to the Manders Overlap Coefficient, differing by observation of intensity deviations from the mean or absolute intensities respectively. Manders coefficients M_1 and M_2 individually describe the contribution of each channel to pixels of interest[302]. M_1 reports the fraction of intensity in channel 1 that was found to co-occur with intensity in channel 2 above a defined threshold, and *vice versa* for M_2. Coefficients assume values between 0 and 1, representing zero and full co-occurrence of one channel to the other.

In this study, colocalisation was reported using PCC to describe the correlation of intensities between fluorescence emission from LysoTracker molecule with scattering from AuNPs, intensities of selected individual SERS peaks and PC scores generated by PCA of SERS mapping acquisitions. The relationship between respective channels was reported by calculation of M_1 and M_2 coefficients to describe relative colocalisation of each to the other. Acquired values of PCC and M split coefficients were checked for colocalisation significance using Costes' significance test (a random scrambling method evaluating probabilities that calculated values are greater than would be achieved in random overlap)[303].

5.5 Results and Discussion

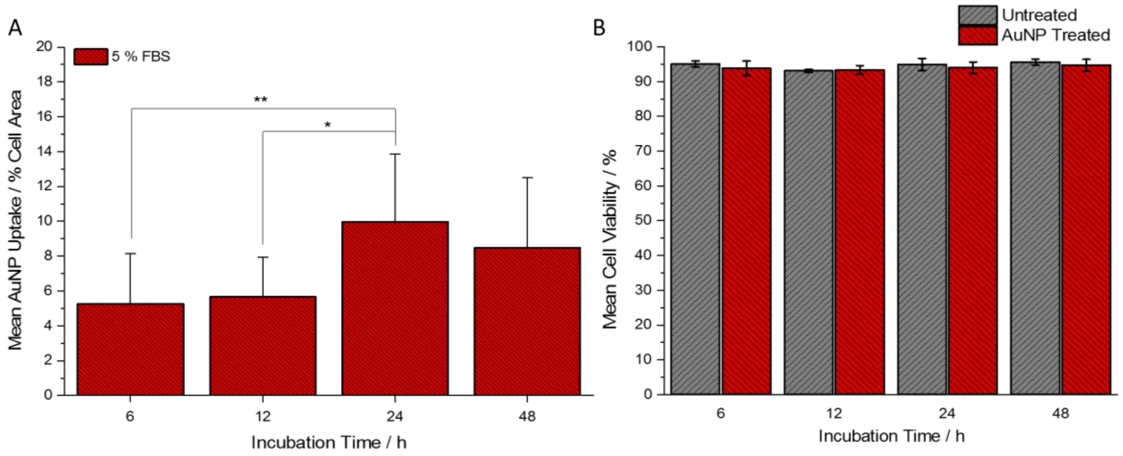

Figure 5.1 Investigation of AuNP incubation suitability following incubation of SH-SY5Y cells with AuNPs (ϕ = 60 nm, 150 µM, 1.35 x10^{10} NPs mL^{-1}) for 6, 12, 24 and 48 h by observation of (A) AuNP residency within cells (measured as % Cell Area) by brightfield microscopy and (B) cell viability by trypan blue exclusion assay, compared with untreated control cells.

5.5.1 Cell AuNP Uptake & Viability

The cellular uptake of AuNPs into SH-SY5Y cells was investigated in detail to understand the best conditions for lysosomal tracking. To quantify uptake, brightfield images acquired of AuNP-treated cells at each time point were analysed to produce a measure of AuNP uptake by residency within cells, measured as a percentage of the total cell area (Figure 5.1 A). Details of this method, in addition to more detailed explanation of the results acquired, are provided in Appendix Chapter A.1. After 6 and 12 h of treatment clear accumulation of AuNPs aggregates inside cells was observed, occupying around 5 % of the total cell area in both cases. Incubation times of 24 and 48 h yielded significantly increased extents of intracellular AuNP residency compared to the 12 h incubation, taking values of 9.97 (± 3.88) and 8.47 (± 4.02) % respectively. The decrease in intracellular AuNP abundance between the 24 and 48 h incubation times may indicate saturation of uptake at 24 h, leading to reduced rates of internalisation relative to NP exocytosis by cells after this time. However, no statistical significance was observed in this decrease by Tukey means testing.

The effect of AuNPs on SH-SY5Y cell viability (Figure 5.1 B) was assessed using trypan blue assay. Both untreated control and AuNP incubated cells were investigated at each specific time point. The viability of both control and AuNP treated cells was consistently within a narrow and high range of 93.1-95.6 % over the incubation period. Even after 24 and 48 h, representing the highest

AuNP and longest time of exposure respectively, differences of only 0.9 and 1.1 % in mean viability were observed between AuNP-treated and control cells. No statistically significant impediment of cell viability was observed between AuNP-treated and control cells was observed at any incubation duration, or indeed between AuNP incubation durations. Therefore, in terms of basic viability at least, the 5 % level of media-FBS appeared to supply sufficient nutrients to cells while providing biocompatible protein corona to the dose $[AuNPs]_{Incub}$ of 150 µM (1.35 x 10^{10} NPs mL^{-1}) for high cell survival.

While no significant decrease in cell viability was observed, it must be considered that NP internalisation can disrupt natural cellular pathways without causing cell death when considering NP-treated cells' likeness to a 'natural' state[28]. Chapter 4 of this thesis reports a lack of sensitivity in traditional cell viability assays compared to cell stress responses which can deviate SERS cell spectra from the 'healthy' state and affect experimental validity. Spectral deviations relating to cell stress were shown to arise in the event of excessive AuNP internalisation, governed in the study by $[AuNPs]_{Incub}$ and media-serum composition. The acquired mean viabilities in this study were maintained around 95 % (with small standard deviations), demonstrably similar to those previously acquired from cells incubated with AuNPs ($[AuNPs]_{Incub} \leq 250$ µM) for 24 h in 10 % FBS media, rather than the lower general values for cells treated with AuNPs in 1% FBS-media. Cells treated even with 250 µM AuNPs in 10 % FBS-media demonstrated no significant signs of elevated ROS or AuNP-uptake related cell stress following detailed investigation by SERS.

Furthermore, comparison of intracellular AuNP residency between the conditions used in this study (150 µM, 5 % FBS, 48 h) and those previously shown (Chapter 4) to not exhibit AuNP-induced SERS stress response (100-250 µM, 10 % FBS, 24 h) showed remarkably similar extents of internalisation. Measured as % occupancy of total cell area, cellular AuNP uptake was calculated as 8.04 (± 4.48) % under conditions (150 µM, 10 % FBS, 24 h) and 8.47 (± 4.02) % using conditions utilised in this study (150 µM, 5 % FBS, 48 h). The same experiment indicated that a 5 % media-serum composition yielded the smallest decrease (as a percentage of the 24 h maximum) in the level of internalised NPs at the 48 h incubation time compared to other serum levels (Appendix Figure 8.2). This was beneficial since a prolonged incubation time of 48 h was used in order to increase probability of achieving LysoTracker detection within its mature endolysosome organelle target. Therefore, AuNP incubations were conducted in media containing 5% serum, establishing a compromise between favourable AuNP internalisation and ensuring a sufficient supply of nutrients to cells for the 48 h period. Cells were fixed straight after washing with NP-free medium to prevent AuNP exocytosis, which has been related to their extracellular concentration[124,304]. Similar viability responses have been reported in these cells previously, along with commonly used HeLa and A549 cell lines[305,306].

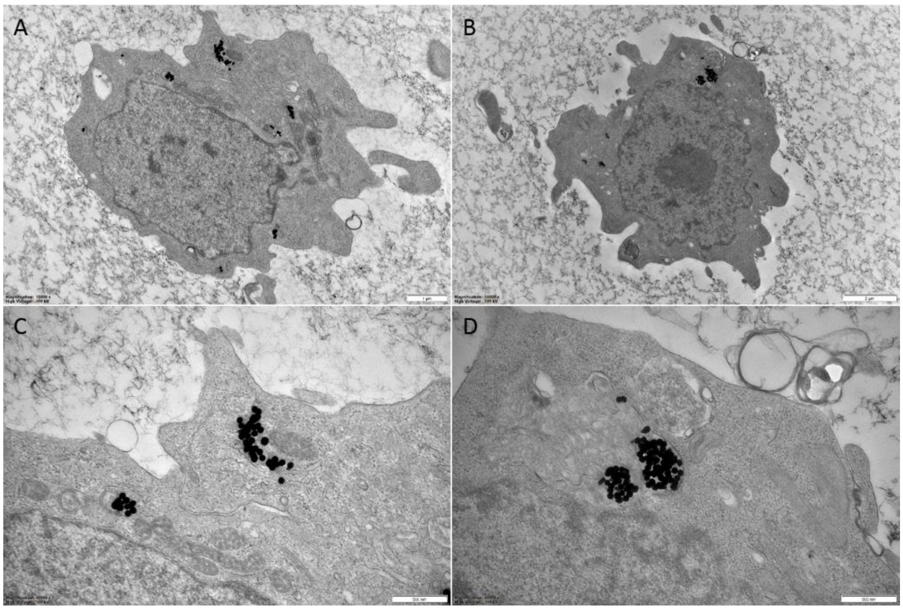

Figure 5.2 TEM micrographs of two exemplar SH-SY5Y cells (A, B) incubated with $[\text{AuNPs}]_{\text{Incub}}$ = 150 µM (1.35 x 10^{10} NPs mL^{-1}) in 5 % FBS-media for 48 h. Localisation of AuNPs was (C, D) confirmed within cell endolysosomes in a tightly-packed manner, exhibiting the spherical morphology of monodisperse NPs with no obvious signs of cell damage. Scale bars (A) = 1 µm; (B) = 2 µm; (C,D) = 500 nm.

Validation of the established AuNP-dosing parameters was further provided by TEM imaging of AuNP distributions within the cells. Figure 5.2 depicts two example cells (A, B), which demonstrated healthy morphologies with intact outer and nuclear membranes. It is noted that cell morphology deviated from the usual morphology of adherent SH-SY5Y cells, adopting a rounded shape. This was an artefact of sample preparation steps that were specifically required for TEM experimentation, full details of which are presented in Appendix Section A.2 of this thesis.

AuNPs were clearly visualised (black spots) inside the cell contours and more specifically (C, D) enclosed within multiple endolysosomal vesicles throughout the cytoplasm. The internalised NPs were discernibly spherical in morphology, implying monodispersity, while close-proximity to a large number of adjacent NPs would allow formation of plasmonic hotspots for SERS enhancement of molecules able to migrate into inter-nanoparticle gaps. Therefore, the employed AuNP incubation parameters were confirmed to achieve residence of the nanosensors to cellular endolysosomes, in sufficient abundance to potentiate sensitive detection of LysoTracker molecules' arrival at the organelle by SERS.

5.5.2 Confocal Fluorescence Microscopy

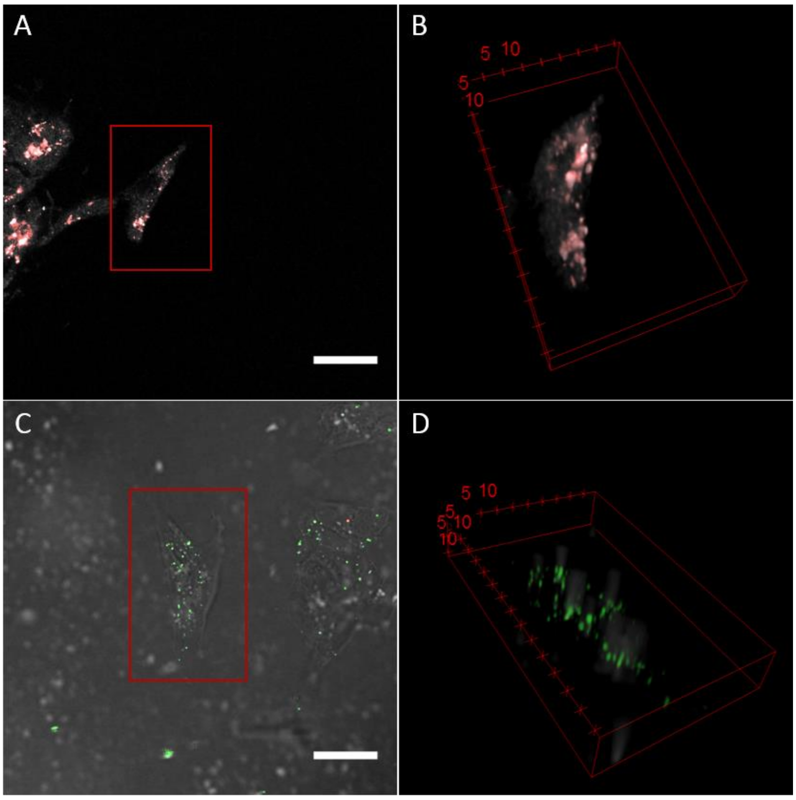

Figure 5.3 Multichannel confocal microscopy of differentiated control cells, treated with either (A, B) LysoTracker (50 nM, 2 h) or (C, D) AuNPs (150 µM / 1.35 x10^{10} NPs mL^{-1}, 48 h) singly. Both LysoTracker fluorescent emission (red) and AuNP scattering (green) channels were imaged simultaneously. Control samples exhibit intensity exclusively in the channel corresponding to their treatment as revealed in (A, C) exemplar slices and (B, D) three-dimensional renders of single cells. Impressions of cell contours (greyscale) are provided by un-thresholded LysoTracker fluorescence signal or inverted brightfield signal for (A, B) LysoTracker and (C, D) AuNP control groups respectively. (A, C) Scale bar = 30 µm

To confirm AuNP localisation inside lysosomes for detecting the arrival of administered LysoTracker, brightfield, reflection and fluorescence confocal microscopy were used. Three-dimensional cell image stacks were acquired to analyse colocalisation of the molecule's fluorescent emission with scattering from pre-administered AuNPs. Stacks were acquired covering a field of view of 184 x 184 µm with a lateral step size of 0.33 µm. 22 fields of view were acquired from cells sequentially treated with AuNPs and LysoTracker over two repeats. The collection parameters in each of the LysoTracker fluorescence and AuNP scattering channels were validated by imaging control cell samples containing each of the reagents in isolation (Figure 5.3). Multiplexed image slices (Figure 5.3 A, C) and three-dimensional renders (B, D) revealed detection

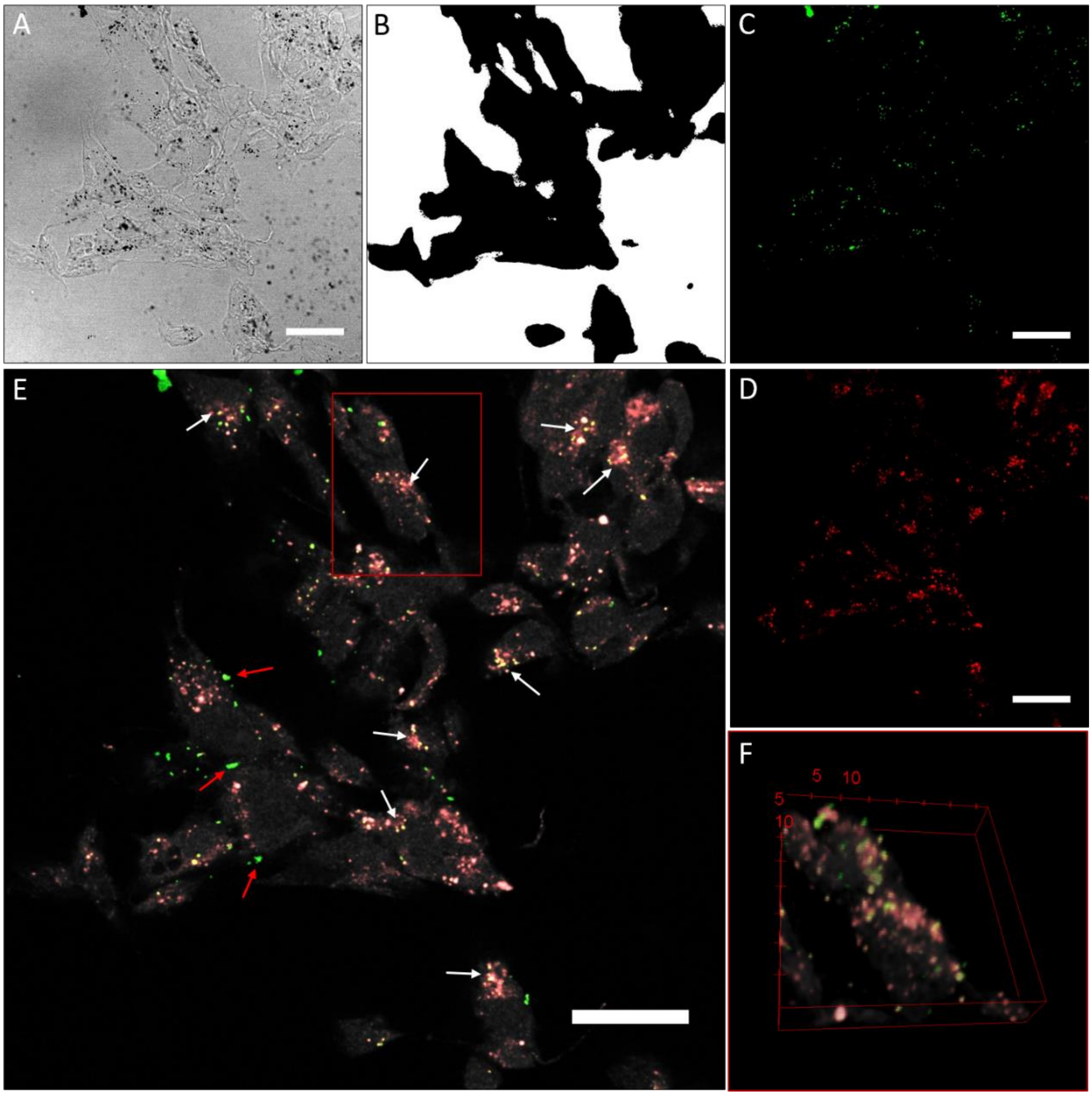

Figure 5.4 Multichannel confocal image stacks were analysed to generate a quantitative measure of colocalisation LysoTracker fluorescence signal and scattering from intracellular AuNPs. (A) Brightfield slices were processed to generate (B) binary masks of cell contours for application to stacks in order to include only cellular (C, green) AuNP scattering and (D, red) LysoTracker fluorescence. Colocalisation (yellow) was observed by overlay of the channels in (E) whole-FOV slices and (F) zoomed single cell 3D renders. Scale bar = 30 µm.

of only the administered reagent in the LysoTracker (A, B) and AuNP (C, D) control group respectively. This demonstrated that no cross-talk was detected between the channels. Therefore, the collection parameters employed validated, with signal exclusive to each control treatment following acquisition of 3 image stacks per control group.

A brightfield transmission image (Figure 5.4 A) shows a representative collection of cells, treated with both AuNPs and LysoTracker molecule, for which the image stacks were acquired. The brightfield image shows internalisation of AuNP aggregates into cells as black spots existing within the cell contours, residing in the cytoplasm and perinuclear regions of the cells. The slice displayed was acquired 1 µm above the cell base in order to highlight that intracellular AuNPs (in focus) existed at a height above the cover slip compared to those existing extracellularly, adhered to the cover slip (out of focus). To ensure that the scattering from extracellular AuNPs (either never internalised or exocytosed during the 48 h time point) was not included in the colocalisation analysis, the brightfield slice was processed (Gaussian blurring, edge location, thresholding) in order to produce a binary mask (Figure 5.4 B) representing only the areas of cell content (black) within the image and excluding extracellular (white) regions. This mask was applied to image stacks generated in the AuNP scattering and LysoTracker fluorescence detection channels. Single slices acquired from the same focal plane as the brightfield image demonstrated that signal generated from AuNP scattering (Figure 5.4 C) and fluorescence (Figure 5.4 D) occupied largely the same spatial locations on the example slice.

An initial, qualitative measure of signal colocalisation in light microscopy is produced by simple overlaying of channels, presented for the example slice (Figure 5.4 E). Overlaying of channels displayed in green (AuNPs) and red (LysoTracker) LUTs gives rise to regions of exact signal colocalisation appearing as yellow in the image. The example confirms localisation of the two channels by visual inspection, primarily within the perinuclear regions of cell cytoplasm (examples indicated with white arrows). Differences between the channels arose in the more abundant nature of LysoTracker fluorescence signal relative to NP scattering, while only a very small amount of scattering signal was observed in isolation (examples indicated with red arrows) from fluorescence. The regions of isolated scattering signal primarily existed at the edge of cell contours (visualised by overlay of low intensity signal detected in the LysoTracker fluorescence channel, greyscale). Three-dimensional visualisation of exemplar cells (Figure 5.4 F), within the stack (Figure 5.4 E, red inset), confirmed the colocalisation of AuNPs to cellular endolysosomes to be pervasive throughout the cellular volume. Within the image, AuNP scattering and fluorescence achieved good colocalisation and retained the patterns observed in the single image slice overlay

Table 5.1 Colocalisation analysis of 22 confocal image stacks images of cells treated with both AuNPs (green) and LysoTracker red DND-99 (Red). Mean values were calculated for the Pearson’s correlation coefficient (PCC), in addition to Manders colocalisation of LysoTracker fluorescence to AuNP scattering staining (M_1) and scattering to fluorescence (M_2).

Coefficient	Value (± Std Dev)
PCC	0.51 (± 0.05)
M_1	0.10 (± 0.06)
M_2	0.75 (± 0.07)

(E). The location of the nuclei in the two cells was clear due to the absence of signal in either channel at the centre of each cell, surrounded by endolysosomes.

Colocalisation analysis was performed in order to provide a quantitative measure of the colocalisation between stained endolysosomes and internalised AuNPs. The analysis was performed at minimum threshold values of 30 and 100 grey levels for LysoTracker fluorescence and AuNP scattering respectively. Across the 22 analysed image stacks, a mean Pearson's colocalisation co-efficient (PCC) of 0.51 (±0.05) was calculated (Table 5.1). The positive value obtained shows that colocalisation between the signals was present while its small standard deviation suggests that the values were fairly consistent between the observed cells. Observation of the mean Manders coefficients exhibited a striking difference between the way that each signal was colocalised to the other. The M1 value of 0.10 (± 0.06) is low and represents the localisation of LysoTracker fluorescence to AuNPs. This corresponds to larger cytoplasmic regions of LysoTracker fluorescence intensity without resident AuNPs, as is presented in Figure 5.4 C-F. Reasons for this effect could include non-specific absorption of the dye but more significantly cellular lysosome production far exceeding the presence of internalised AuNPs during the incubation period. This is to be expected as the cells were incubated with nanoparticles before treatment with LysoTracker. These effects therefore contribute to lowering of the Pearson coefficient.

Conversely, the Manders coefficient relating AuNP scattering to LysoTracker fluorescence was high, taking a mean value of 0.75 (± 0.07). Once more, this reflects the trends depicted in qualitative visualisation of the two signal intensities in Figure 5.4. The result means that a very large proportion of the NP aggregates were localised within endolysosomes. AuNPs which were not localised to LysoTracker intensity may be related to cell-membrane adherence, either unable to enter, or during early phases of endocytosis or recycling of endosomes back to the plasma membrane by the Golgi apparatus. In exocytosis via the lysosomal pathway, AuNPs would still be enclosed in LysoTracker stained lysosomes and therefore co-localisation can still be determined for this late exocytotic process[124]. The overall result of the colocalisation analysis between fluorescence arising from administered LysoTracker molecule and scattering from pre-residing intracellular AuNPs shows that AuNPs uptaken into cells were predominantly situated within endolysosomes. This was supported by the positive mean Pearson's correlation coefficient and high M_2 value. Thus, spatial colocalisation of AuNPs and intended analyte was confirmed to potentiate SERS detection of the molecule within the intended cell organelle.

5.5.3 Intracellular SERS Mapping

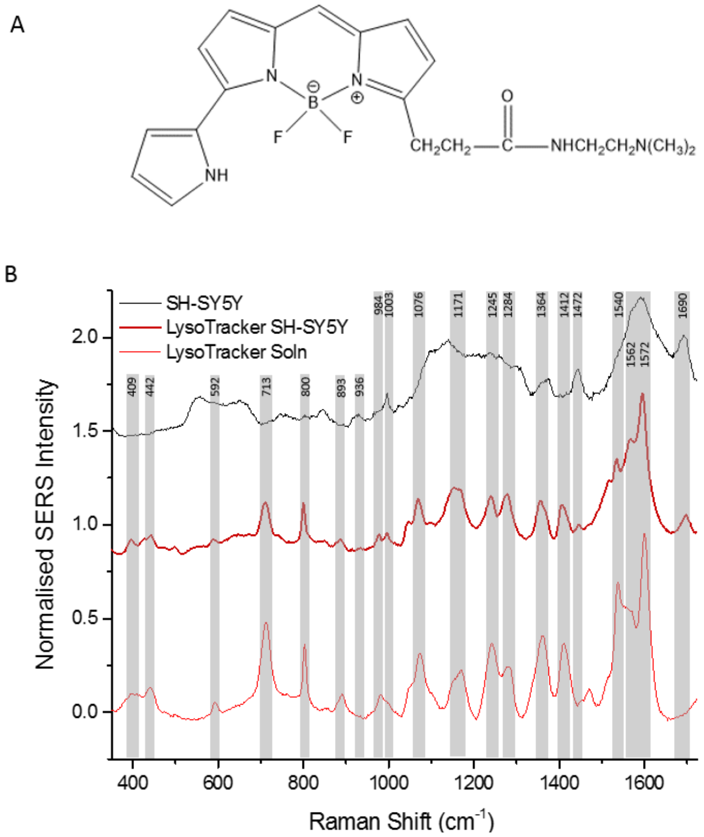

Figure 5.5 Establishment of intracellular SERS detection of (A) LysoTracker molecule through (B) spectral comparison of SERS peaks arising in a reference LysoTracker solution (50 nM), untreated SH-SY5Y cells and LysoTracker-treated (50 nM, 2 h) SH-SY5Y cells.

Having identified the chemical colocalisation of LysoTracker to AuNPs within endolysosomes of SH-SY5Y cells by confocal microscopy, the ability of SERS to detect the analyte inside cells by its Raman fingerprint (and hence chemical structure, Figure 5.5 A) alone was investigated. A LysoTracker reference sample was prepared by suspension of AuNPs within LysoTracker solution (50 nM). Acquired SERS spectra revealed characteristic vibrational peaks associated with the pure compound for comparison with spectra acquired from AuNP-treated SH-SY5Y cells in the presence and absence of LysoTracker (Figure 5.5 B).

The strongest peaks arising in the LysoTracker reference's SERS spectrum were at 1572 (Aromatic C=C ring stretch), 1540 (N-H deformation/C-H stretch), 713 (C-N stretch), 1245 (C-N/B-F stretch/ C-H wagging, Amide III region) and 1364 (CH_2 bending) cm^{-1}, in order of descending peak:baseline signal intensity. While the possible assignments of these peaks all correspond to the chemical structure of the analyte, the shared nature of the bonds with native cellular content or similarity

Table 5.2 Assignment of vibrational modes and their relative occurrences observed between the SERS spectra of a reference LysoTracker solution (50 nM) with untreated control and LysoTracker-treated SH-SY5Y cells.

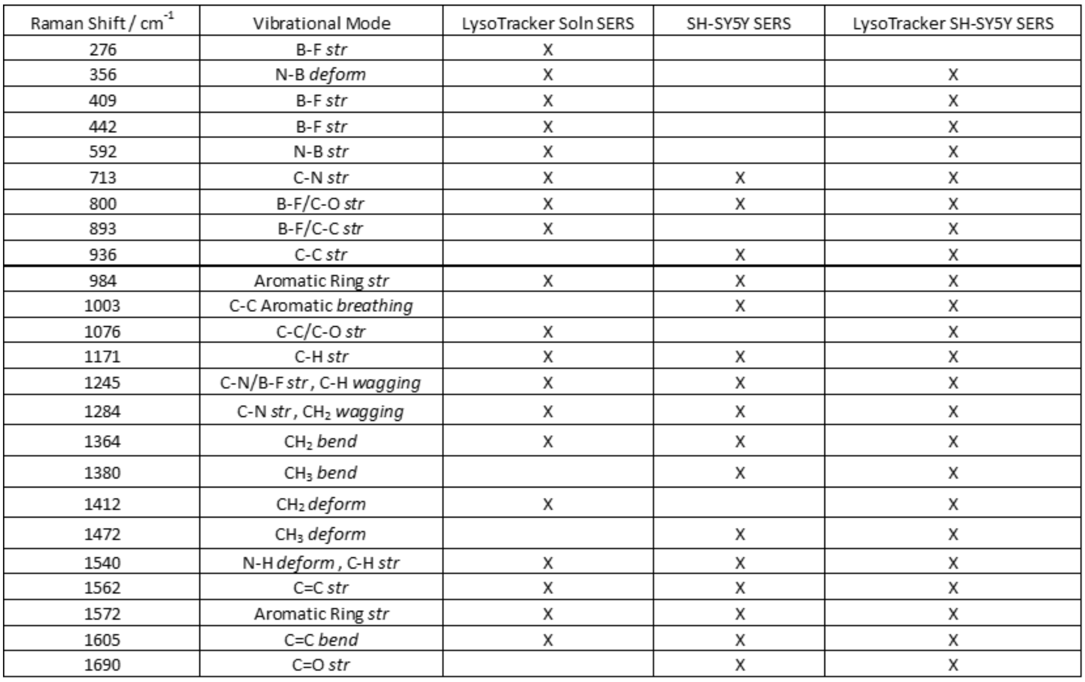

Raman Shift / cm^{-1}	Vibrational Mode	LysoTracker Soln SERS	SH-SY5Y SERS	LysoTracker SH-SY5Y SERS
276	B-F *str*	X		
356	N-B *deform*	X		X
409	B-F *str*	X		X
442	B-F *str*	X		X
592	N-B *str*	X		X
713	C-N *str*	X	X	X
800	B-F/C-O *str*	X	X	X
893	B-F/C-C *str*	X		X
936	C-C *str*		X	X
984	Aromatic Ring *str*	X	X	X
1003	C-C Aromatic *breathing*		X	X
1076	C-C/C-O *str*	X		X
1171	C-H *str*	X	X	X
1245	C-N/B-F *str*, C-H *wagging*	X	X	X
1284	C-N *str*, CH_2 *wagging*	X	X	X
1364	CH_2 *bend*	X	X	X
1380	CH_3 *bend*		X	X
1412	CH_2 *deform*	X		X
1472	CH_3 *deform*		X	X
1540	N-H *deform*, C-H *str*	X	X	X
1562	C=C *str*	X	X	X
1572	Aromatic Ring *str*	X	X	X
1605	C=C *bend*	X	X	X
1690	C=O *str*		X	X

to vibrational energies of other endogenous vibrational modes (C-N/B-F stretch at 1245 cm^{-1}) may inhibit use of these bands for unambiguously confirming intracellular detection. Indeed, assessment of SERS spectra acquired from untreated control SH-SY5Y cells revealed that all five of the described peaks were ubiquitously detected in both samples. Therefore, the peaks were also identified within the mean spectra acquired from LysoTracker-treated SH-SY5Y cells.

However, vibrational peaks in the region 385-450 cm^{-1}, for example 409 and 442 cm^{-1}, arise from inorganic elements (B-F stretches) within LysoTracker's molecular structure. Not only were these clearly observed in the reference compound solution, but their inorganic nature offered direct contrast to native chemical bonds expected within untreated cells. These peaks were similarly identified in the endolysosomal compartments of LysoTracker-treated cells while being absent in control cells. Therefore, SERS detection of LysoTracker vibrational modes within cells was supported. Furthermore, cellular SERS bands such as 1003 (C-C aromatic stretch), 1510 (C=C ring breathing), 1690 cm^{-1} (C=O stretch) were common to the spectra collected from control and LysoTracker-treated cells only. While these bonds exist in the structure of LysoTracker, all three are cited in literature as indicative of protein and/or DNA base presence[284].

Assignment of the vibrational modes giving rise to the identified SERS peaks are presented in Table 5.2. The presented comparison of relative SERS peak occurrences between LysoTracker treated and untreated control cells, with reference to a pure LysoTracker solution sample serves

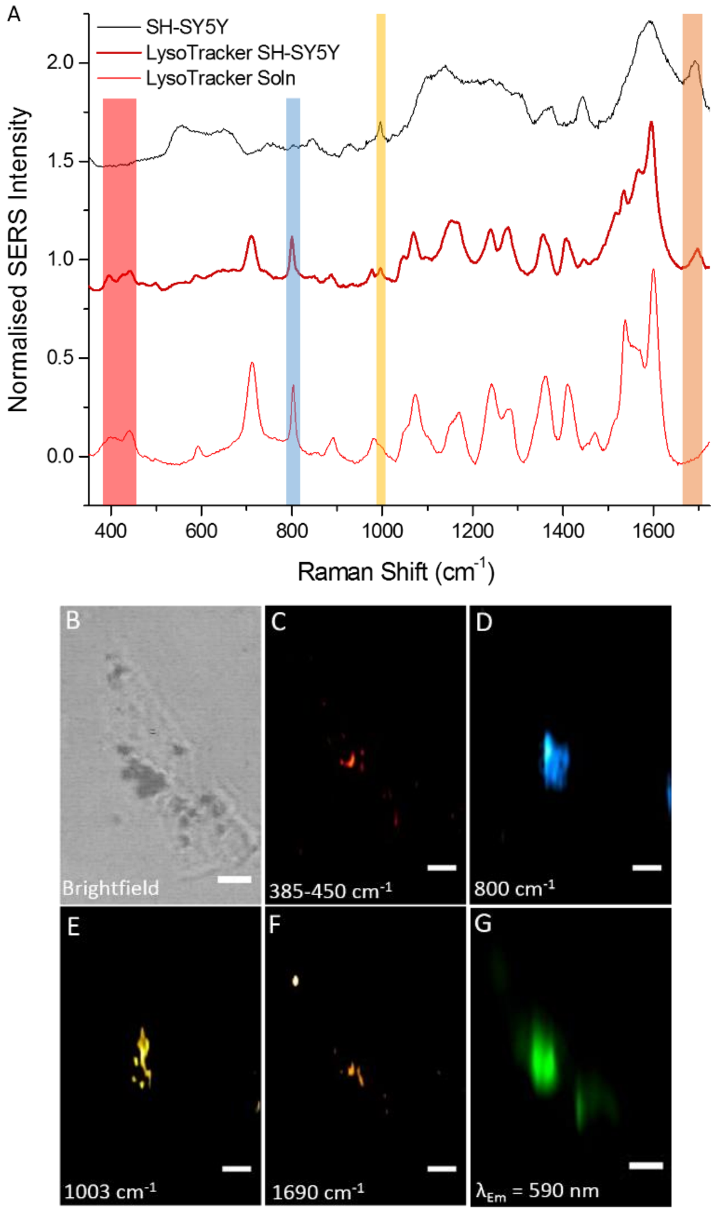

Figure 5.6 Univariate SERS intensity mapping of LysoTracker distribution across SH-SY5Y cells. (A) Mean SERS spectra of pure LysoTracker (fine red), untreated (black) and LysoTracker-treated (bold red) cells confirm detection of the molecule inside cell lysosomes. (B) Intensity maps of Raman peaks relating to LysoTracker (385-450 cm^{-1}, B-F stretches, 800 cm^{-1}, C-H conj ring breathing) and native cellular (1003cm^{-1} C=C ring breathing, Trp, and 1690 cm^{-1}, Amide I) content are displayed across an exemplar cell (B, scale bar 5 µm).

to confirm detection of the selected analyte inside cells, achieved through its proximity to pre-residing SERS nanosensors.

Following confirmation of SERS detection, SERS cell maps were investigated to visualise the intracellular distribution of the administered LysoTracker. A representative brightfield image of a SH-SY5Y cell shows illustrative AuNPs aggregated within the cell (black spots, Figure 5.6). Mapping

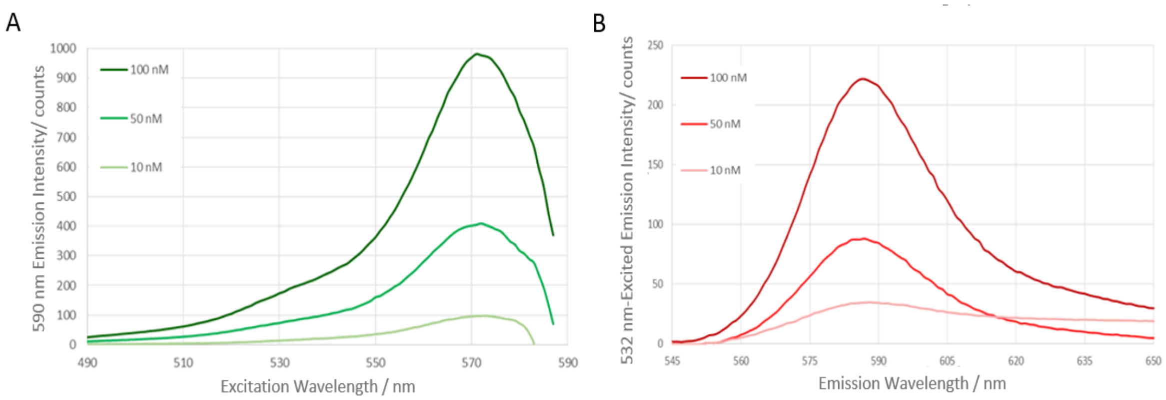

Figure 5.7 (A) Absorbance and (B) emission spectra acquired from LysoTracker solutions (100, 50, 10 µM) using a 590 nm detection and 532 nm excitation wavelength respectively. The result verified that LysoTracker fluorescence was stimulated by the 532 nm excitation wavelength used to verify cell maps.

intensities of single vibrational modes that are characteristic to cellular biomolecules or administered LysoTracker molecule provides a simple univariate approach to imaging their distribution within cells. As such, intensities from modes characteristic of LysoTracker (385-450 cm^{-1}, B-F stretches and 800 cm^{-1}, B-F/C-O stretch) and cellular content (1003 cm^{-1}, C-C aromatic breathing, Phe and 1690 cm^{-1}, C=O stretch, amide I) were projected across LysoTracker-treated cells (Figure 5.6 C-F). Corresponding LysoTracker fluorescence images (Figure 5.6 G) were acquired to compare against the SERS projections in order to assess the accuracy of the mapping achieved. Absorption and emission spectra (Figure 5.7) were collected for LysoTracker solutions at a range of concentrations verified fluorophore excitation by the 532 nm input wavelength used for analyte fluorescence mapping on the Raman microscope.

SERS intensities of the B-F stretching region (385-450 cm^{-1}) and 800 cm^{-1} mapped the locations occupied by AuNPs within regions of cells. However, SERS intensity arising from B-F vibrations at 385-450 cm^{-1} was less prevalent than the 800 cm^{-1} mode, possibly owing to C-O stretching contributions to the 800 cm^{-1} peak that are common in cellular material compared to inorganic B-F vibrations. A similar explanation can be assigned to the mapping of vibrational modes relating predominantly to cellular structure, with 1690 cm^{-1} (Amide I C=O) demonstrating strong localisation to a small region of the 1003 cm^{-1} (C=C, Phe) mode intensity. This was consistent with the mean spectra (Figure 5.6 A) indicating the 1690 cm^{-1} peak to be exclusive to control and LysoTracker-treated cell samples, while the 1003 cm^{-1} mode is also weakly present as a peak shoulder in the pure LysoTracker control spectra.

Pearson correlation and Manders' coefficients were calculated to investigate the colocalisation of each of the SERS modes to LysoTracker's fluorescence signal (Table 5.3). Pearson and Manders

Table 5.3 Results of colocalisation analysis performed on the intensity of selected single SERS vibrational modes with LysoTracker's fluorescent emission. Pearson's correlation coefficient (PCC) was calculated, along with Manders colocalisation coefficients of LysoTracker fluorescence emission to individual SERS modes (M_1) and of the SERS modes to the fluorescence emission (M_2).

SERS Peak (cm^{-1})	PCC	M_1	M_2
385-450	0.45	0.198	0.591
800	0.63	0.552	0.556
1003	0.29	0.13	0.136
1690	0.29	0.079	0.365

coefficients indicated stronger colocalisation of LysoTracker modes at 385-450 cm^{-1} (PCC = 0.45, M_2 = 0.591) and 800 cm^{-1} (PCC = 0.63, M_2 = 0.556) to the molecule's fluorescent signal than those of native cellular content (PCC = 0.29 for each and M_2 = 0.136 and 0.365 for 1003 cm^{-1} and 1690 cm^{-1} respectively). Low values of Pearson and Manders coefficients (M_1) for colocalisation of fluorescence:SERS intensities were consistent with confocal fluorescence/scattering microscopy results. Both are explained by the number of lysosomes produced by cells far exceeding the number that contained resident AuNPs. Nevertheless, the univariate analysis approach showed that mapping exogenous molecule distributions inside cells can be achieved by using pre-resident AuNPs as SERS sensors.

While such direct SERS detection has utility in confirming the presence or absence of administered molecules in the cellular matrix, an improved ability to translate these intensities into useful quantitative data is highly desirable. Accurate quantification is difficult due to highly intense SERS signal from within lysosomes that arise from intracellular aggregation of AuNPs within. The lack of controllability of this phenomenon generates heterogeneous enhancement of signal. SERS hotspots may dominate SERS intensity maps, where bonds located within a few nm of the enhanced electronic field arising between two plasmonic nanoparticles exhibit heightened intensities[307]. Intense signals from the analyte (LysoTracker) may therefore arise from a high local concentration of the molecule, but can also be due to enhancement by SERS hotspots. The effect can both improve sensitivity and distort datasets from allowing reliable quantification of analyte concentrations by investigation of selected peak intensities. While this cannot be avoided using spherical AuNPs that use intracellular aggregation as a means of producing high signals, improvements can be provided by generation of semi-quantitative data using numerical tools.

Multivariate analysis that uses the full vibrational signatures acquired to perform analyte distribution mapping provides statistically-weighted data than consideration of single peak

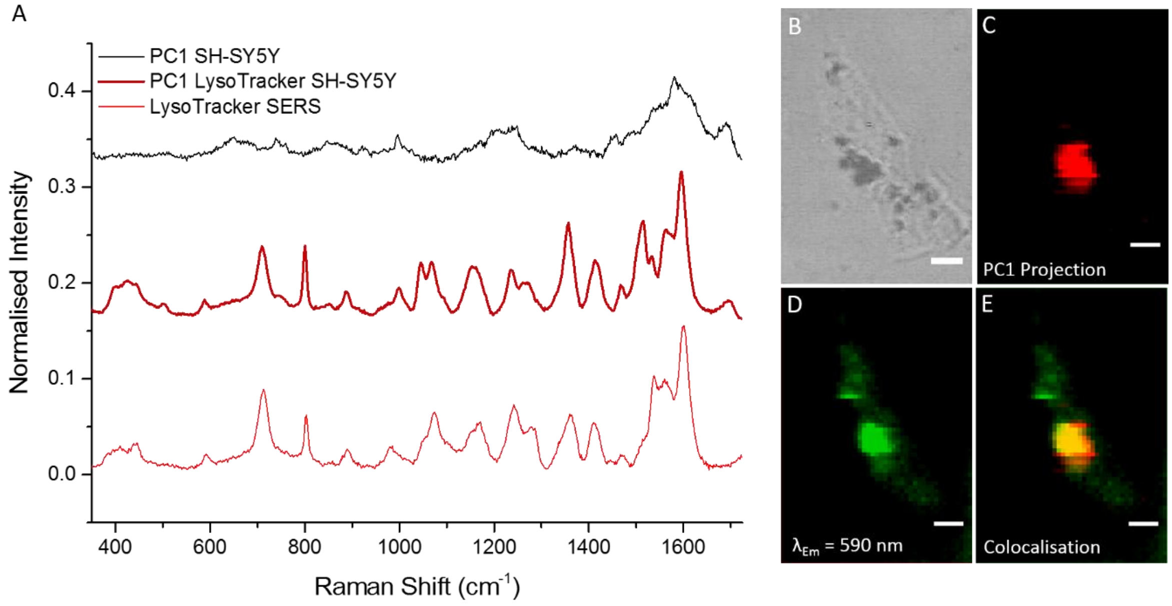

Figure 5.8 Multivariate analysis of SERS cellular maps. PC1 loadings (A, thick red) acquired from LysoTracker-treated cells clearly demonstrated largest contributions from vibrational modes arising in SERS spectra of pure LysoTracker (fine red), in addition to modes contributing to PC1 of control cell maps (black). Back-projection of LysoTracker-treated PC1 scores (C) across the same LysoTracker-treated cell (B) showed strong colocalisation to the molecule's fluorescent emission (D-E).

intensities. Utilising of the hyperspectral nature of SERS (and Raman) maps is also afforded. Application of PCA to SERS datasets is common practice when distinguishing spectral features between sample classes requiring classification. The technique has previously been used to distinguish between neuronal cell types and recently demonstrated spectral variation between cell spheroids following treatment with chemotherapy agents doxorubicin and paclitaxel when combined with linear discriminant analysis (LDA)[292,305].

In this study, PCA was applied to the acquired SERS cell maps, providing a comparison of results obtained by univariate (previously described peak intensities) and multivariate analysis approaches. The approach would allow reporter-free, intracellular SERS mapping datasets to provide increasingly robust and reliable, statistically-weighted, indications of compound distribution inside cells.

For LysoTracker-treated and untreated control cell SERS maps, principal components were generated for observation of how both PC loadings and PC scores differed between the treatment classes. The PC1 loadings extracted from LysoTracker and untreated cell maps were firstly compared (Figure 5.8 A), along with the SERS spectrum of pure LysoTracker. Striking similarity was observed between the PC1 loadings generated from cells treated with LysoTracker (bold red) and the SERS spectrum of LysoTracker (fine red). Every peak observed in the LysoTracker SERS spectrum was also identified in the treated-cell PC1 loadings, including the vibration at 1597 cm^{-1} (C=C bending, amide I), which provided the most intense peak in each. The inorganic stretching region 395-450 cm^{-1} did not contribute strongly to the PC1 loading but provided a clear discriminant from the untreated cell loadings. Peaks offering strongest contribution to the LysoTracker-treated PC1 loadings were identified at 1513 cm^{-1} (aromatic C=C breathing), 1356 cm^{-1} (CH_2 bend), 1564 cm^{-1} (C=C stretch), 800 cm^{-1} (C-H ring breathing) and 710 cm^{-1} (C-N stretch). These peaks were all common to the SERS spectrum of the pure LysoTracker solution but also to cellular content, in particular the aromatic ring modes arising from proteins.

The increased complexity of the native cellular matrix convolutes individual Raman peaks relative to reference solutions, producing broadening and accounting for the reduced overall intensity of the untreated cell loadings. It is probable that endogenous cellular peaks identified in the control loadings are masked by intense LysoTracker signal, possibly from within SERS hotspots, in the treated-cell loadings. The close resemblance of LysoTracker-treated cell PC1 loadings to the molecule's SERS spectrum demonstrated that detection of LysoTracker molecule was a primary source of spectral variation within the cell maps, with PC1 accounting for 77.0 % of variance compared to PCs 2 (2.6 %) and 3 (2.2 %). Given that the SERS NPs were not ubiquitous throughout the cell, PC1 loadings could be anticipated to have simply identified enhancement of Raman signal (arising at locations of NP aggregation) compared to extracellular background and regions of the cell that were free of AuNPs. The result suggests that the majority of SERS spectra collected at locations containing AuNPs contained vibrational signatures corresponding to the presence of LysoTracker molecule. The high value of the M_2 Manders' coefficient previously observed by confocal microscopy (Table 5.1) corroborates this finding.

Projection of each pixel's PC score within PC1 produced an intensity map that details the locations within an example cell from which SERS spectra with the highest degree of spectral similarity to the PC1 loadings were acquired. The resulting PC1 image maps (Figure 5.8 C) were compared to fluorescence intensity maps (Figure 5.8 D), demonstrated using the same exemplar LysoTracker-treated SY-SY5Y cells (Figure 5.8B) used for univariate SERS peak intensity analysis. Overlay of the PC1 projection with fluorescence maps displayed a high degree of qualitative colocalisation between the images (Figure 5.8E), with almost the entirety of the PC1-projected intensity localising in the perinuclear region of the cytoplasm and crucially within the largest region of LysoTracker fluorescence intensity.

Table 5.4 Colocalisation analysis of back-projected SERS principal component maps generated from SH-SY5Y cells treated with AuNPs and LysoTracker Red to the molecule's fluorescence intensity maps. Comparison of resulting Pearson's correlation coefficients (PCC), Manders colocalisation coefficients of fluorescence to PC maps (M_1) and of PC maps to fluorescence (M_2) clearly demonstrated that PC1 held the highest degree of colocalisation to the fluorescence channel, supported by the highest observed PCC and M_2 values.

PC	PCC	M_1	M_2
1	0.636	0.456	0.957
2	0.193	0.547	0.878
3	0.076	0.333	0.724
4	0.052	0.455	0.676

As previous, colocalisation analysis was performed on the dataset in order to provide a quantitative measure of the spatial overlap between the fluorescence and SERS-PCA (generated PCs 1-4) signals (Table 5.4). The analysis revealed a decrease in Pearson's correlation coefficient with each generated principal component. A positive value of 0.636 was observed between PC1 scores and LysoTracker's fluorescence, bearing a degree of positive correlation, which decreased to values of 0.193 in PC2 and no correlation observed between PCs 3 and 4 with the fluorescence channel revealed by PCC values of 0.076 and 0.052 respectively. Manders' coefficients provided strong correspondence with those obtained by previous fluorescence/scattering and univariate SERS analysis experiments, observing a higher degree of colocalisation of AuNP-derived intensity (SERS-PCA scores in this case) to the fluorescent signal (M_2) than of the fluorescent signal to the PC projections (M_1).

Of greatest importance, due to the peak occurrences identified in its PC loadings spectrum, were the values acquired in PC1 scores. The M_2 value of 0.957 displayed almost complete colocalisation of the scores to LysoTracker's fluorescence, in keeping with qualitative examination of the overlay maps. The value was higher than those obtained for univariate peak intensity maps associated with the LysoTracker SERS signal, possibly resulting from peak occurrences in SERS spectra that didn't LysoTracker's full vibrational signature and thus reduced the coefficient value. This was the case for the vibrational mode at 800 cm^{-1}, assigned as either B-F or C-O stretches. The peak was prominent in the mean SERS spectra collected from pure LysoTracker solutions as well as LysoTracker-treated cells, exhibiting a matching PCC value to the projected LysoTracker-treated cell PC1 value (0.63 and 0.636 respectively). However, the Manders coefficient comparing the 800 cm^{-1} peak's colocalisation to LysoTracker fluorescence (M_2) was significantly lower than that of

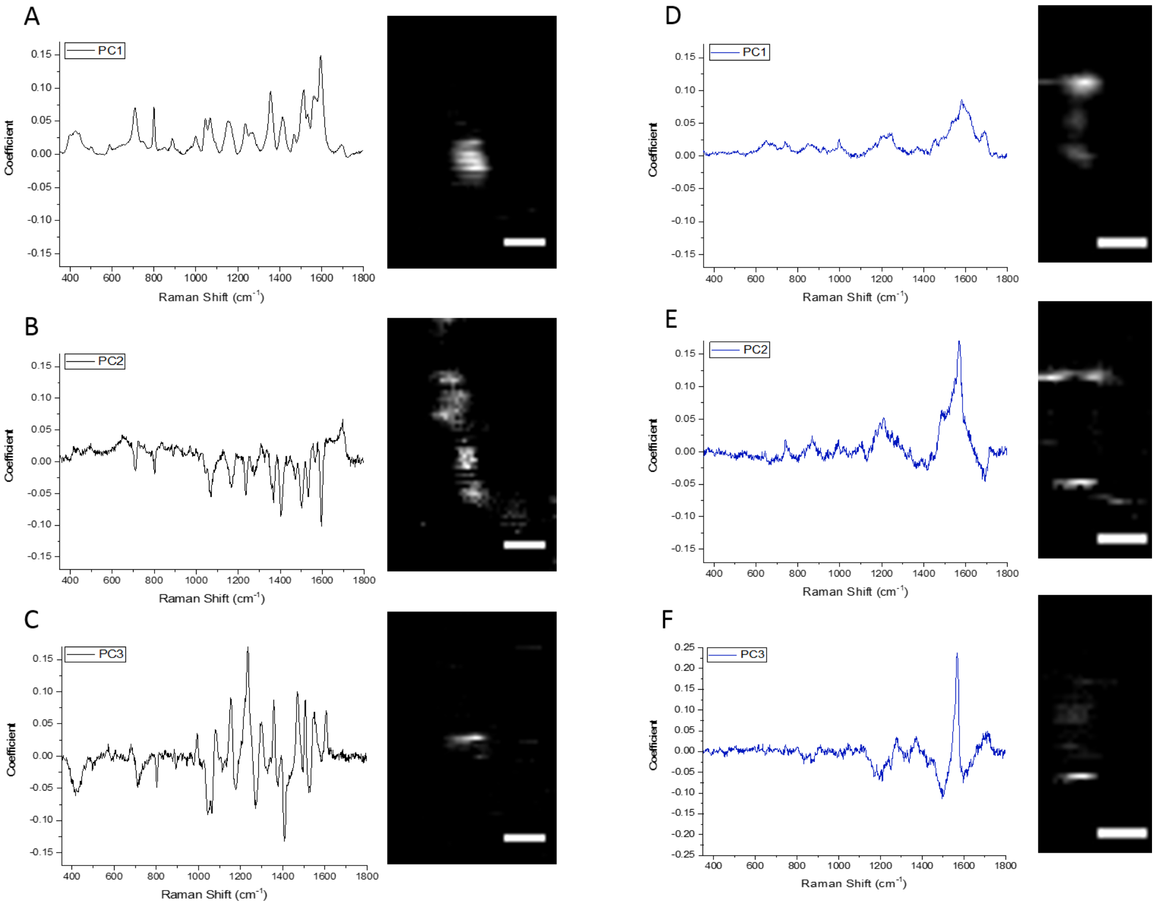

Figure 5.9 Comparison of principal component (PC) loadings derived from SERS spectral maps acquired from AuNP-incubated SH-SY5Y cells treated with (A-C, black) and (D-F, blue) without LysoTracker Red molecule. Projections of exemplar cells' PC scores within each loading are presented for the treated and untreated group, revealing the locations of the cell from which SERS spectra most representative of the PC loadings were acquired.

the PC1 loadings (0.591 compared to 0.957 respectively). This may be attributed to the lack of exclusivity of the SERS peak to the LysoTracker's molecular structure, with C-O bond stretching vibrations being observable ubiquitous throughout the molecular composition of endogenous cellular content. The SERS PCA approach's requirement for high similarity of a pixel's entire SERS spectrum (identification of all LysoTracker-associated SERS peaks) to treated-cell PC loadings therefore produced a more rigorous measure of intracellular detection and localisation.

In order to validate the analysis, observation of PC loadings were also generated from untreated-control cells. This was required to ensure that peaks arising in the PC1 loadings of LysoTracker-treated cells, were not observed in the molecule's absence. Loadings plots of PCs 1-3, along with mapping of their associated scores across example cells, generated from LysoTracker-treated and untreated cells are presented in Figure 5.9.

PC 1-3 loadings of LysoTracker-treated cell spectra contained a larger number of more intense, defined peaks compared to those from control cell spectra. Despite this, a common peak between the PC1 loadings of the treated and untreated cell maps was presented in the amide I region (1690-1695 cm^{-1}), thus confirming that the generated PC1 was indeed intracellular. The peak was also the most heavily-contributing positive mode to PC2 of the treated cell group, projected scores of which were maintained within the cell contour. The increased weighting coefficient of the 1690 cm^{-1} peak in PC1 of control cells, relative to LysoTracker-treated cells, also supports the notion that peaks arising in the LysoTracker molecule were more intense than those of endogenous cellular material. This would contribute to their dominance of treated-cell group SERS spectra and PC1 loadings.

Within all control cell PC loadings, the largest contribution to spectral classification was observed in the region 1570-1610 cm^{-1}, corresponding to C=C vibrational modes related to protein content. This would be present in both endogenous cellular material and within the protein corona formed around AuNPs in culture medium. However, projection of PC1 scores onto untreated cell maps revealed PC scores to be highest within the cell contour, particularly in the cases of PCs 1 and 3. Importantly, SERS peaks arising from the molecular structure of LysoTracker, including those at 800 cm^{-1} and the inorganic stretching region 385-450 cm^{-1} are absent in the PC loadings derived from the control cell SERS spectra. The detection and mapping of the molecule's intracellular localisation by PCA-SERS was thus validated by comparison with the negative control group.

The multivariate nature of PCA, utilising the entirety of SERS spectra to define shared spectral characteristics for mapping of chemical compositions across single cells, thus provides a more powerful and accurate approach to imaging analyte distribution than mapping of single peak intensities. The primary principal component (PC1), accounting for the greatest amount of variance, within LysoTracker-treated cell spectra clearly identified the SERS signature of the LysoTracker molecule as making the largest contribution to classification of pixel maps. These contributions were absent in components generated from control cell spectra.

Moreover, increased detection specificity was strongly illustrated by comparison of M_2 Mander's coefficients of colocalisation to LysoTracker's fluorescent emission, in which LysoTracker-attributed individual SERS peak intensities (0.591, 0.556) and confocal observation of AuNP scattering (0.75) yielded lower values than those obtained using PC1 projection (0.957). Causes of decreased M_2 values in non-SERS-PCA approaches are hypothesised to be spectral overlap of individual SERS peaks with endogenous cellular content and inclusion of membrane-adhered AuNP aggregates respectively. Multivariate analysis allowed exclusion of such aggregates by inspection of corresponding pixel spectra, for comparison to LysoTracker-detection PC loadings and subsequent exclusion if a minimum similarity was not achieved. The higher value of Pearson correlation coefficient observed in multivariate analysis (PC1 = 0.63) than from AuNP scattering (0.51) and univariate analysis of LysoTracker-specific Raman peaks (B-F stretches, 385-450 cm^{-1}, PCC = 0.45) suggests that the technique may also demonstrate increased sensitivity. However, this would have to be investigated further through lower detection limit experiments performed on all three of the analysis approaches.

Through both chemical and microscopic analysis, it has been demonstrated that 75% of 60 nm AuNPs localise to endolysosomes of SH-SY5Y cells 48 h after administration, reside in the perinuclear region of the cytoplasm and do not compromise cell viability. Within the lysosome, detection of an exogenous small molecule administered at nM concentration was detected using SERS, while application of PCA was demonstrated to increase specificity of analyte mapping inside cells. Unlike similar techniques that pre-adsorb and enclose the compound with SERS sensors for monitoring, the approach allows the molecule to move at will for probing by spatial colocalisation to AuNPs[293,308]. The molecular-fingerprinting capability of SERS offers potential tracking of dynamic biochemical changes to cells induced by drug arrival in addition to mapping intracellular distributions. Changes in molecule-associated SERS peaks may also indicate drug metabolism and removal from probed target organelles.

The enhanced specificity of the SERS-PCA approach would be directly advantageous in a drug-discovery assay by utilisation of whole SERS spectra to generate statistically-weighted maps of compound localisation, reducing likelihood of false-positive results. For AuNP probes of greater than 15 nm, internalisation through normal cellular process of endocytosis would direct the AuNP to lysosomes, the site of origin for LSDs. Therefore, the developed SERS model offers direct application towards label-free pharmacodynamic assessment candidate drugs for LSD therapies. AuNPs have also been commonly studied for their potential as nano-carriers, delivering cancer and cardiovascular disease therapeutics[309–311]. Patra *et al* used 5 nm conjugated AuNPs with gemcitabine and EFGR for treatment of pancreatic cancer; their small size allowing evasion of phagocytosis and penetration through plasma membranes[310,312]. Similar engineering of AuNPs conjugated with drugs for lysosomal replacement strategies, along with crucial factors for phagocytic evasion and blood vessel permeation[310], could provide a higher bio-distribution of enzymes to lysosomes and across the blood brain barrier for improved efficacy *in vivo*.

Since performance of this study, SERS research interrogating the accumulation of lipids within 3T3 fibroblast cells following treatment by tricyclic antidepressant drugs has been published[144]. While the work focusses on statistical characterisation of drug effect using machine learning techniques, several key factors serve to support methodologies developed in this thesis for performing intracellular SERS measurements within lysosomes. The study utilised pre-incubation of colloidal AuNPs to cells for achieving lysosomal residency before administration of drug compounds. More significantly, investigation of AuNP dosing regimens confirmed that the pre-incubation technique, compared with incubation subsequent to or simultaneous with drug administration, gave the best possibility of observing vibrational modes corresponding to direct drug molecule detection. Furthermore, the study presented intensity maps of weakly-detected and individual peaks arising from a drug molecule inside lysosomes. Therefore, while the study held aims differing to research presented within this chapter, strong support is offered for the use of AuNP pre-incubation to detect exogenous molecule arrival in cell lysosomes. Research presented in this thesis furthers the methodology by the demonstrated improvement of molecular detection afforded by PCA-generated scores that encompass the whole contribution of analyte to intracellular SERS spectra.

5.6 Conclusions

In conclusion, label-free imaging of exogenous small molecules within cancer cell organelles can be attained through combination of SERS with multivariate analysis. In this work, the ability to detect and image the localisation of LysoTracker Red molecule, incubated to SH-SY5Y cells at nM concentration, within cellular endolysosomes has been demonstrated. The uptake, cytotoxicity and localisation of AuNPs in the cell line was assessed, confirming predominant localisation of AuNPs into lysosomal vesicles. Understanding AuNP distribution is pivotal for harnessing their potential to serve as pre-residing intracellular probes, awaiting arrival of a desired analyte at its intended site of action. These *in-vitro* tests can offer new insights into the dynamics of drug molecules within cells, allowing one to probe arrival at target and its subsequent biochemical actions. Therefore, the potential for utilising the reporter-free SERS approach to study intracellular pharmacodynamics of drug candidates at other intended intracellular targets in an assay-based platform is shown to be possible. Expansion of the study would comprise of testing the assay on fluorescent compounds localising to organelles beyond endolysosomes, followed by progression to non-fluorescent drug molecules of hypothesised intracellular localisation and finally candidate compound screening experiments at desired drug-target organelles. The data presented in this chapter provides proof-of-concept for developing reporter-free SERS mapping of intracellular molecule localisation, with direct implications towards monitoring delivery of lysosome-targeted drug candidate such as those required for LSD therapy.

Chapter 6 Live Imaging of Intracellular Drug Action by CARS microscopy

6.1 Abstract

While the capability of SERS to perform highly sensitive intracellular measurements of both cell response to nanosensor exposure and localisation of an exogenous analyte has been demonstrated in this thesis, a limiting factor in its use for drug discovery research exists in the required use of an intracellular probe. The following study presents an alternative route to enhancing Raman signal using the coherent Raman imaging technique of CARS microscopy. Optimisation of the technique towards label-free observation of intracellular responses to drug treatments in live cells is demonstrated. CARS was performed using the 2850 cm^{-1} vibrational stretch of lipids to analyse dynamic changes in abundance of cytosolic lipid droplets (LDs) in live samples of human breast cancer cell line MCF-7 during incubation with Pt-based chemotherapy agent carboplatin. LDs are a significant organelle in monitoring both proliferation and stress/damage mechanisms within cancer cell lines and therefore represent an interesting intracellular target for monitoring in small molecule drug discovery. A challenge in live-cell imaging of LDs by CARS is avoiding their generation as a stress response to laser exposure. Presented research sought to optimise CARS microscopy for minimal perturbation of live cell samples. The developed platform potentiates quantitative analysis of intracellular biomolecules' response to both tolerance of laser exposure and chemical intervention, highlighting its potential utility as a non-invasive and versatile platform for assessing drug efficacy *in vitro* with the capacity for development as an automated preclinical assay.

6.2 Contributions

Research performed within this chapter was performed by the candidate only. Design, construction and maintenance of the home-built multiphoton microscope carried out by Kostas Bourdakos, Peter Johnson, Tual Monfort and Sumeet Mahajan is kindly acknowledged.

6.3 Background

To this point, research presented in this thesis has focussed solely on SERS as an enhanced Raman scattering technique for intracellular study. However, an alternative method of enhancing weak Raman scattering intensity is offered by coherent wave mixing processes (Section 2.2.3). Coherent Raman imaging techniques predominantly concern observation of either coherent anti-Stokes Raman scattering (CARS) or stimulated Raman scattering (SRS) from samples. While enhancement of signals is lower than that offered by SERS, a major experimental advantage of these approaches is held in sample preparation, with no internalisation of inorganic matter into cells required. Therefore, not only is a greater degree of sample validity maintained but also experimental systems can achieve higher throughput as no incubation time for the internalisation process is required. The remaining chapters of this thesis explore the ability of CRI platforms to contribute new insights to pharmaceutical research in the context of visualising intracellular responses to drug molecules in a completely label-free manner. Presented in Chapter 7 is investigation of the relative chemical selectivity in intracellular C-H vibrational imaging achieved by both CARS and SRS microscopies. Herein, the ability of CARS microscopy to visualise intracellular lipids is optimised towards a live-cell imaging platform that is non-invasive, free of fluorescent tags and versatile in its utility. Stages of development, optimisation and application of the CARS platform are demonstrated for monitoring the response of live MCF-7 cells to applied Pt-based chemotherapy agent carboplatin.

The ability of CARS microscopy to visualise intracellular lipid content is well established, with cytosolic lipid abundances measured as a quantitative parameter in monitoring viral infection of live fibroblast cells, adipogenic differentiation of mesenchymal cells, development of oocytes across multiple species and developmental stages and structure of Caco-2 intestinal epithelial membranes used in drug permeability testing[224,240,313,314]. Interest in cytosolic lipid droplets (LDs) arises from their role as dynamic organelles at the centre of lipid and energy homeostasis. Originating from the endoplasmic reticulum (ER), their structure consists of a core, containing neutral lipids triacylglycerols and sterol esters, surrounded by monolayer of ER-derived phospholipids that is sparsely decorated with surface proteins[315–317]. Functions of LDs include acting as both a reserve and repository for sequestered fatty acids that can be mobilised to fuel cell metabolic processes, protection against ER stress following unbalancing of protein folding capacity and protection of mitochondria to damage during autophagy. They have been shown to undergo dynamic interactions with a broad spectrum of organelles, giving rise to cycling of LD expansion and shrinkage cycles[315]. It also remains unclear as to whether LD formation aids cellular stress-adaptive responses or contributes to the effects of homeostatic disruption[317].

Dysregulation of the LD life cycle and function is associated with human pathologies including obesity, non-alcoholic fatty liver disease, neutral lipid storage disease and cardiovascular diseases such as atherosclerosis[315]. However, in the context of this thesis investigating methods for analysing intracellular behaviour of small molecule compounds, focus on LD dynamics is centred on their role in the proliferation of cancer cell lines.

Cancer cells are known to exploit LDs for critical growth and development processes, although understanding remains limited and no direct inhibitors of LD biogenesis have been developed as anti-proliferative therapies. The parameter of relative cytosolic lipid abundance has been established as a biomarker of both breast cancer cell malignancy and homeostasis. Raman spectroscopy has demonstrated increased LD abundance within increasingly malignant breast cancer cell lines, with highly malignant MDA-MB-211 cells exhibiting two- and four-fold increases relative to intermediately malignant MCF-7 and non-malignant MCF-10A cells respectively[252,318]. However, lipids also play roles in both apoptotic and non-apoptotic cancer cell death[315,319]. Mobile lipids have been reported to rapidly accumulate in tumour cells during apoptotic cell death, with increased *de novo* lipid synthesis arising from reduced activity of lipogenesis enzymes that inhibit oxidation of fatty acids. The effect results in fatty acids being driven towards lipid synthesis pathways and is caused by elevated ROS and mitochondrial membrane potential[320]. The measurement of relative cytosolic lipid abundances has previously been performed by CARS microscopy following application of therapeutics etoposide, camptothecin and staurosporine to HCT 116 colon tumour cells over a 48 h period[241]. All three drug treatments yielded a statistically significant increase in the abundance of cytosolic lipids (measured as a total percentage of cell area) relative to control cells. Therefore, relative abundance of cytosolic LDs has been established as an indicator of drug-induced apoptosis in tumour cells that can be measured in a label-free manner by CARS microscopy.

The research presented in this chapter builds upon aforementioned studies by CARS imaging of drug action upon LD abundance within live breast cancer cells. The drug applied to the cells was carboplatin, a derivative of potent PT-based chemotherapy agent cisplatin that shares a similar mechanism of action but differs in structure and demonstrates lower toxicity. Carboplatin is not routinely used in the treatment of breast cancer but has been shown to possess mild activity against the MCF-7 cell line, inducing both apoptosis and necrosis accompanying interesting morphological alterations[321,322]. The effect of carboplatin, and briefly cisplatin, upon live MCF-7 cells was observed by CARS microscopy in terms of relative LD abundances, with the aim of tracking early apoptotic events. Experiments were performed in both repeated and single-exposure acquisition formats for comparison of potential cell damage induced by laser exposure. The research demonstrates the ability to extract quantitative data relating to drug activities imposed onto live intracellular environments from images acquired using a label-free CRI platform.

6.4 Methods

6.4.1 Optimisation of Lipid Imaging in Live Cells by CARS Microscopy

6.4.1.1 Cell Culture

Human breast cancer cell line MCF-7 (donated by Dr Mark Coldwell, University of Southampton) were cultured in DMEM (Gibco, high glucose) containing FBS (10 % v/v) and penicillin-streptomycin additive (1 % v/v) and maintained at 37 °C in an atmosphere containing 5 % CO_2. Cells were passaged every four days and routinely screened for mycoplasma infection. Cultures were discarded following 20 passages and new stocks resurrected. For imaging, cells were seeded onto either poly-L-lysine coated coverslips ($\phi = 16$ mm) at a density of 30,000 cells within a 12-well plate or into glass-bottomed multi-well slides (µ-Slide 8 well, Ibidi) at 5000 cells. Cells were incubated for 24 h to allow attachment and entry into the cell cycle before any imaging or drug administration was performed. Any fixed cell sample was prepared using paraformaldehyde (4 % in PBS) and mounting onto glass slides as described in previous chapters.

6.4.1.2 Raman Spectroscopy

In order to validate assignments of C-H stretching vibrations observed by CRI platforms, spontaneous Raman spectra were recorded from fixed MCF-7 cells, in addition to reference samples of oleic acid, bovine serum albumin and DNA solution to represent pure lipid, protein and nucleic acid Raman fingerprints respectively. Spectra were recorded from each biomolecule reference sample using a 532 nm laser excitation coupled into the same Renishaw InVia Raman microscope used throughout this thesis. Each spectrum was recorded as a sum of three five-second acquisitions following application of 3 mW laser power through a 63x water immersion objective (NA = 1.2, Leica). Cell Raman spectra were acquired by averaging of a total of 36 spectra, collected by point-mapping of three separate cells at 2 µm spatial steps. The spectrum collected at each point consisted of three three-second acquisitions. All spectra were recorded in the 2700-3100 cm^{-1} region of the Raman spectrum.

6.4.1.3 CARS Platform Optimisation

CARS microscopy was performed using a fibre-based, picosecond-pulsed laser split into Stokes (1032 nm) and Pump (tuned within region 784-807 nm to target desired vibrational modes) lines that were spatially and temporally overlapped upon arrival at the sample. Full system details are

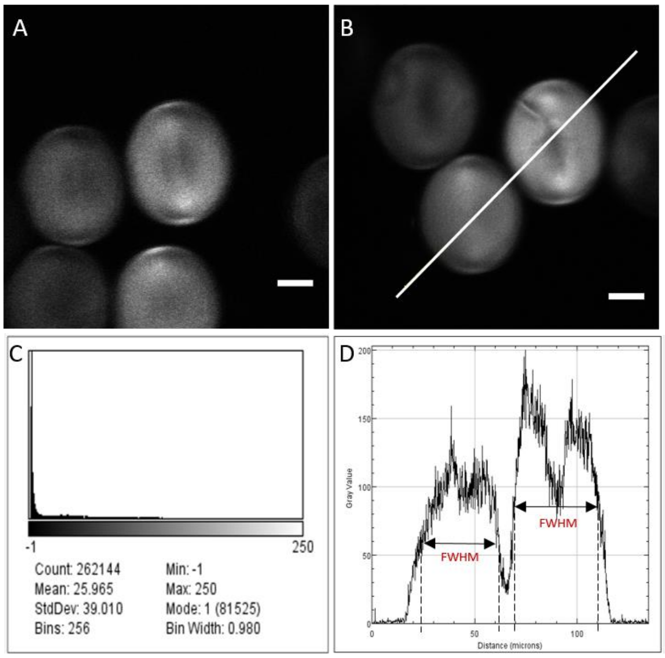

Figure 6.1 Example CARS calibration images (A-B) of acquired from the 2850 cm^{-1} vibration of polystyrene beads using laser powers of (10:5 mW) acquired on separate days. System performance was monitored by observation of (C) resulting pixel intensity value distributions while plotting of intensity profiles along a straight line through the beads (D) verified the size of the beads for object size calibration.

provided in (Section 3.2.2). For excitation of the 2850 cm^{-1} C-H stretching vibration within both polystyrene and alkyl chains of lipids, an OPO was used to tune the pump excitation to a wavelength of 787.5 nm. This generated a CARS scattered field at 649.8 nm. Scattered radiation was subsequently passed through a 700 nm short-pass and 643 nm band-pass filter for detection of isolated CARS intensity by a PMT detector. System calibration and performance was monitored between experiments by imaging the 2850 cm^{-1} C-H stretching vibration of polystyrene beads (ϕ = 40 µm, Figure 6.1). A ratio of pump/Stokes laser powers (10/5 mW) was used, as measured at the sample, and focussed through a 40x water immersion objective (Nikon, NA = 1.15). Acquired images were of size 512 x 512 or 1024 x 1024 pixels and utilised a digital zoom factor that varied between experiments. Polystyrene beads of known diameter were imaged at each digital zoom factor employed, providing a calibration scale of object size.

Determination of minimal laser powers that provided good optical contrast at 2850 cm^{-1} was performed on fixed MCF-7 cell samples. Cell FOVs were selected using brightfield microscopy before imaging of the same cells using a range of incrementally increasing Pump and Stokes laser powers and scan speeds.

Investigation of the maximum laser power that could be applied to live cell samples without inducing visually-discernible damage was performed by time-lapse imaging over a 48 h period and sequentially reduced laser powers with every experimental iteration. Live samples were mounted onto the CARS microscope within an imaging dish containing fresh culture media and within a stage-top live cell incubator. The temperature within the incubator was maintained at 37 °C in an atmosphere containing 5 % CO_2 with continuous monitoring and correction. To avoid evaporation during the experiment, a 63x glycerol objective was used. At each time point, focal drift and cellular motion were accounted for by acquisitiion of a z-stack for each FOV, using a 1 µm step size. Images selected for analysis represented the mid-height cross-section of the cells imaged. Experiments were performed individually using decreasing laser powers (Pu/St) of 100/75 mW, 60/40 mW and 50/30 mW measured at the sample. A pixel dwell time of 8 µs and image size of 512 x 512 pixels were used. In order to assess damage induced in cells by laser exposure, images were acquired from nearby control cell FOVs that had not previously been exposed to laser irradiation at each time point.

6.4.2 CARS Imaging of Lipid Response to Chemotherapy Agents in Live Cells

6.4.2.1 Live Cell CARS Microscopy Assay

The effect of chemotherapy agent carboplatin on lipid distributions within MCF-7 cells was investigated by live time-lapse CARS microscopy over a 48 h period. A stock solution of carboplatin was prepared by dissolution of the solid in sterile water[323], which was subsequently diluted in complete DMEM (10 % FBS, 1 % Pen-Strep) to produce incubation solutions of 5, 50 and 100 µM concentration. Dosing was performed immediately before mounting of cells into the live cell chamber by media replacement with the carboplatin working solutions. Imaging parameters of 50/30 mW laser power with an 8 µs pixel dwell time were employed, collecting 512 x 512 pixel image stacks (2 µm step size) of 20 cell FOVs to be repeatedly imaged at fewer intervals of 0, 6, 24 and 48 h in order to further reduce the possibility of laser-induced cell damage. Previously unexposed control cell FOVs were imaged at each time point to identify potential cell degradation by the applied laser powers. The sample set was acquired across two repeats.

As a further control for identifying laser-induced apoptosis in cells, the experiment was repeated in its entirety with imaging of separate samples, at each time interval. Multi-well slides were maintained in an incubator and mounted onto the live cell instrument only at the time of acquisition. Exactly the same dosing and imaging parameters were employed, acquiring 20 FOVs at each time point across two repeats. Therefore, it was ensured that cells had experienced no previous laser irradiation before imaging, in order to assess the validity of previous datasets acquired from cells repeatedly exposed to irradiation.

6.4.2.2 CARS Image Analysis

Image stacks generated from the time course experiments were processed using FIJI software. The selected mid-height slice from each time-point FOV z-stack was selected to show a large total cell area with clear visualisation of subcellular details. Slices for analysis were processed using a purpose-written FIJI macro which calculated the both the total area of the FOV occupied by cells and by LDs, in order to output the abundance of intracellular LDs measured as % Total Cell Area. Briefly, image processing steps involved generation of a binary mask of cell contours following Gaussian blurring and smoothing of raw image intensities, followed by background exclusion using minimum thresholding. The resulting mask was further de-noised by removal of outlier signal and stored as a ROI. Image intensity arising from cellular lipids was isolated from a duplicate of the original image slice, which underwent the same smoothing by Gaussian blurring and thresholding steps to isolate just the highly intense signal arising from the high concentration of lipids contained in cytoplasmic LDs. Image thresholds were selected to only include cell contours and LD objects respectively using a mixed training set that was representative of the whole experiment’s variation. The decided thresholds were then consistently applied for all treatment groups.

Finally, generated cell contour masks were measured within the binary image of isolated LD intensity, outputting the occupancy of the total cell contour occupied by lipid CARS signals as a percentage value. Mean lipid densities arising for treatment group (and time point) were calculated to evaluate the response of lipids to applied chemotherapy agents as a function of drug concentration and time. Statistical analysis was performed on the outputs using Origin 2016 data analysis software (OriginLab) by way of 1-way ANOVA testing with Tukey mean comparison.

6.4.2.3 Cell Growth Inhibition and Apoptosis Assays

Results obtained from the live cell CARS assay prompted investigation of carboplatin’s action against MCF-7 cells by growth inhibition and apoptosis assays. Cells were seeded into clear-bottomed and cell culture-treated 384 well plates (Greiner Bio-One) at a density of 1000 cells and incubated for 24 h to allow attachment and entry into the cell cycle. After this time, carboplatin was applied to cells within complete DMEM at pharmaceutically-relevant concentrations 0.01-30 μM. Both assays were performed using an Incucyte Zoom® live cell analysis system (Essen Bioscience), maintained at 37 °C in a 5 % CO_2 atmosphere. Growth inhibition assay was performed by phase contrast imaging of wells using a 10x objective at 2 h intervals for a total duration of 100 h. Apoptosis assay was performed using Incucyte caspase-3/7 green apoptosis assay reagent (3 µM, Essen Bioscience) dosed into cell culture medium (for detection using the instrument's GFP fluorescence module). GFP fluorescence and phase contrast images of confluence were acquired. The area of GFP fluorescence within images was divided by the total area of cell confluence in order to provide a measure of the proportion of the cell population undergoing apoptosis at a given time. Images were acquired at 3 h intervals for a total duration of 100 h using a 10x objective in both channels. Both assays were performed independently, with each condition measured in triplicate for three repeats. Negative and positive control wells were included in both assays using solvent (H_2O, 0.5 %) only and staurosporine (0.001-10 µM) treatments respectively.

6.5 Results and Discussion

6.5.1 Intracellular Lipid Imaging

To positively identify the signals observed by CARS microscopy, Raman peaks within the C-H stretching region (2700-3100 cm^{-1}) of MCF-7 cells were investigated by comparison of their spontaneous Raman spectra with those collected from biomolecule reference compounds (Figure 6.2). Assignment of the dominant vibrational peak in the spectra of oleic acid, BSA and DNA

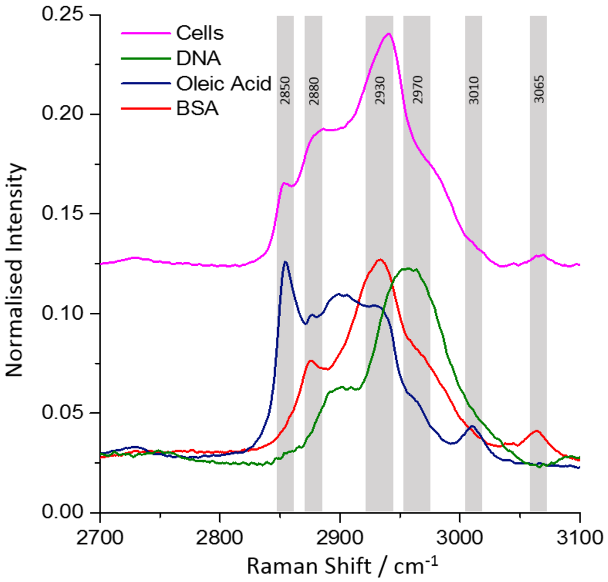

Figure 6.2 Spontaneous Raman spectroscopy of biomolecule reference samples bovine serum albumin (BSA), oleic acid and DNA solution provided information of Raman shifts associated with protein, lipid and nucleic acid content respectively. A mean Raman spectra collected from fixed MCF-7 cells within the region 2700-3100 cm^{-1} was acquired for comparison. Intensities were normalised and stacked in order to highlight the similarity of mean cell spectra to a superposition of the combined reference biomolecule spectra.

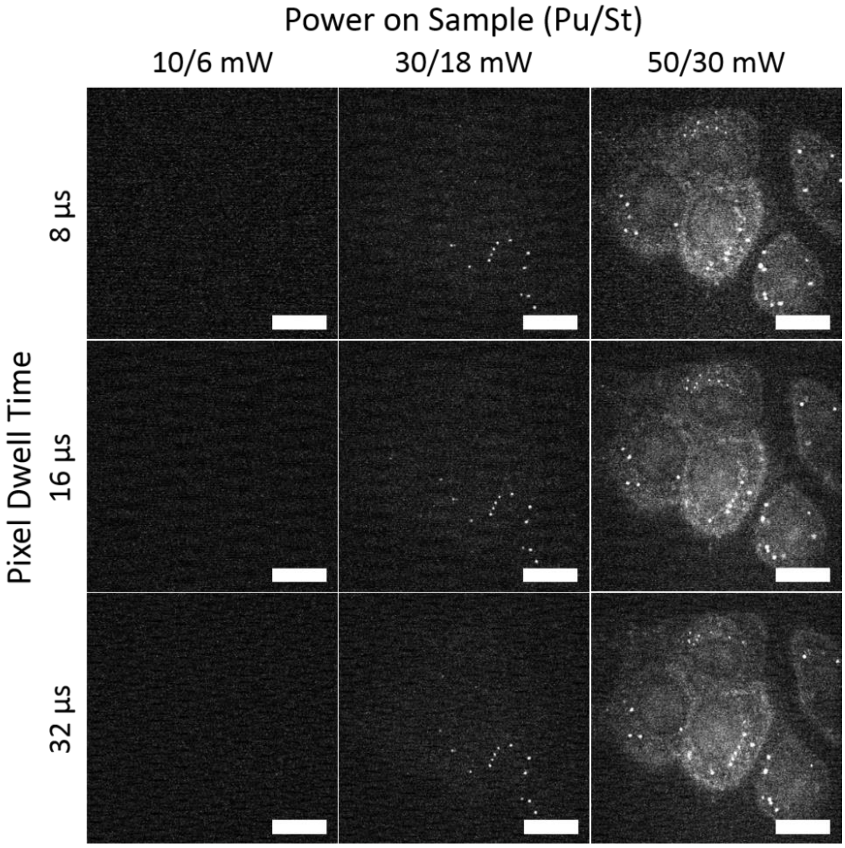

Figure 6.3 CARS microscopy of the 2850 cm^{-1} CH_2 symmetric stretch of lipids within fixed MCF-7 cells under incrementally increased laser powers and decreased pixel dwell times. Scale bar = 20 µm.

corresponded to Raman shifts of 2850, 2930 and 2970 cm^{-1} respectively. The Raman peak located at 2850 cm^{-1} in spectra collected from oleic acid relates to symmetric CH_2 stretches observed in lipid alkyl chains, while higher wavenumber peaks 2880 and 2930 cm^{-1} arose due to asymmetric CH_2 vibrations more common to both protein and lipid content[284,324]. The dominant vibrational peak arising from the DNA sample spectra occurred at 2970 cm^{-1}, showing agreement (as with all reference peaks) with similar work performed by Lu *et al*[225]. The normalised mean spectra collected from MCF-7 cells was demonstrated to only possess peaks accounted for between the three reference molecule spectra, confirming the biomolecular composition of the cellular Raman spectrum within the investigated region.

While CARS peaks possess dispersive shapes that typically deviate (5-10 cm^{-1}) in Raman shift from spontaneous Raman spectra (owing to convolution with non-resonant background contributions), the CH_2 symmetrical stretching vibration of lipids was shown also shown to offer strongest intensity at 2850 cm^{-1} by hyperspectral CARS imaging of MCF-7 cells in Chapter 7 (Figure 7.1). Along with its increased specificity relative to other peaks within the cellular CH region, the mode was selected for use in optimisation of the CARS microscopy platform. The first step in this process was determination of minimum power and image collection parameters that would yield

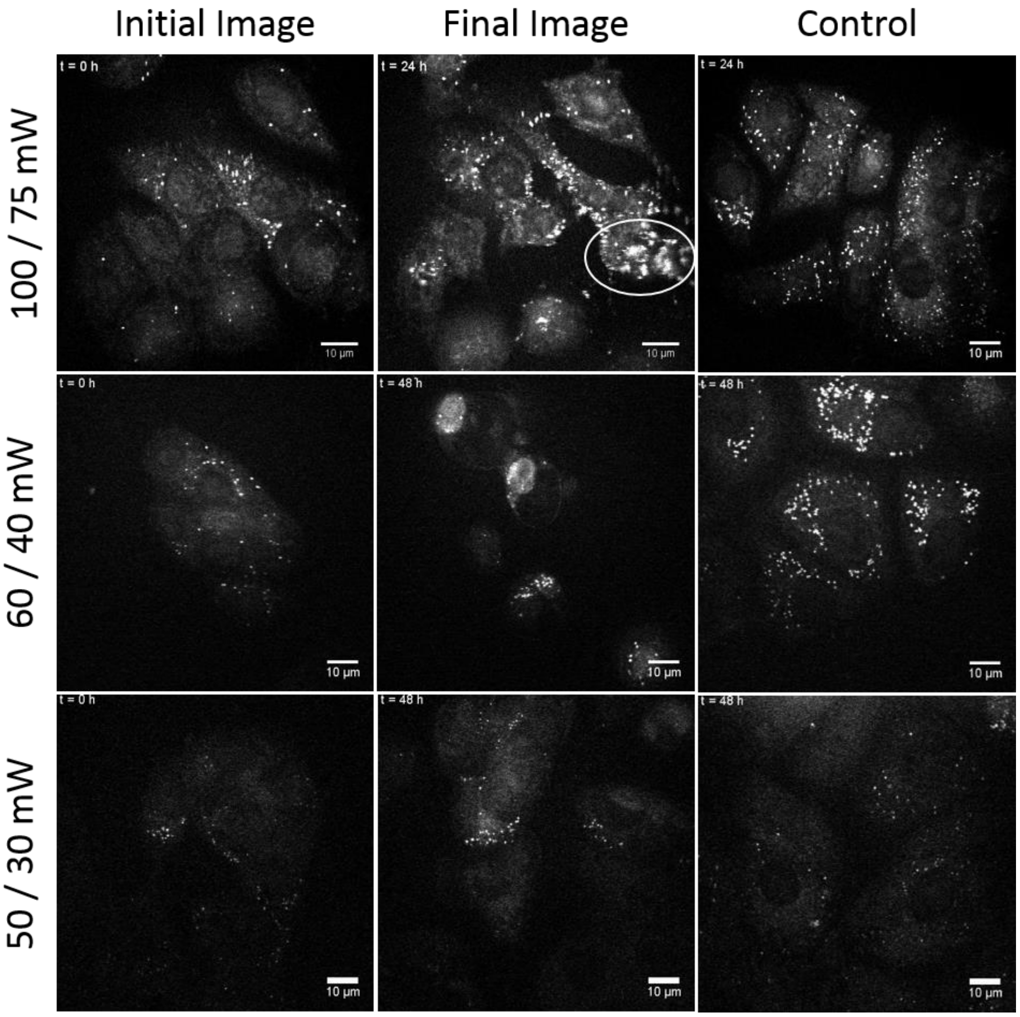

Figure 6.4 Live cell CARS microscopy of cellular lipids (2850 cm^{-1}) under incrementally decreased total laser powers. Exemplar FOVs are presented for each experiment, showing repeatedly-imaged cells at t = 0 h (left) and at either (centre) the first sign of cell damage (100/75 mW) or final time point (60/40 and 50/30 mW). Control cells (right), not previously exposed to irradiation, were imaged at the corresponding time interval to identify possible laser-induced cell damage. Scare bar = 10 µm.

strong and reliable optical contrast while minimising the potential for laser-induced apoptosis and damage to live cell samples. CARS images of the 2850 cm^{-1} vibrational mode were acquired from the same cell FOV under laser powers (Pu/St) of 10/6, 30/18 and 50/30 mW and laser scan speeds varied between 8, 16 and 32 µs pixel dwell times.

Resulting images (Figure 6.3) demonstrated that total laser power applied to the sample was significantly more effective in increasing optical contrast than increasing acquisition times. As such, with incremental increases in laser power, the details observable in the cellular lipid images increased. CARS signal was indistinguishable from background intensity following imaging with 10/6 mW, while visualisation of only a number of bright intracellular LDS was achieved at 30/18 mW. Complete cellular lipid details were observed following irradiation with 50/30 mW Pump/Stokes excitation. The total cell contour was visualised in weak CARS intensity from phospholipids of the cellular membrane, whereas intensely bright regions of small diameter represented LDs within the cytoplasm, owing to their high local concentration of lipids. The location of cell nuclei were also inferred by central elliptical regions of decreased signal intensity relative to the cell cytoplasm. The nuclei were observed to be of 15-20 µm diameter and were void of lipid vesicles. Within each laser power increment, increasing pixel dwell time produced no significant increase in signal intensity. Therefore, parameters of 50/30 mW laser power and 8 µs pixel dwell time were selected as the minimum laser exposure quantities that provided reliable and robust optical contrast for CARS imaging of intracellular lipids.

The next stage for optimisation was to determine maximum laser powers that would allow sensitive molecular imaging of lipids without causing burning or damage to live cells. Three individual time-lapse experiments were performed, acquiring CARS images at the 2850 cm^{-1} vibrational mode of lipids within live MCF-7 samples. With each experiment, laser powers (Pump/Stokes) used for imaging were incrementally decreased from 100/75 mW to 60/40 mW and finally 50/30 mW, representing the previously established minimum condition. Samples were incubated on the microscope within a stage-top live cell apparatus for repeated imaging of ten separate FOVs (typically containing 3-8 whole cells) at intervals of 0, 2, 6, 12, 24, 36 and 48 h.

Figure 6.4 presents exemplar FOVs of cells that reflected the overall trends observed with each power-reduced increment of the time-lapse experiment. Within all three repeats, the initial images recorded at t = 0 h depicted cells of healthy appearance, demonstrated by a large cell area, visibly intact nucleus and a low number of intensely bright LDs. Cellular details visible in the lipid images decreased with reduction of total laser power, confirming the requirement to find a maximum possible power ratio to provide maximum sensitivity and contrast without damaging the live sample. The first experiment, employing laser powers of 100/75 mW, induced such damage to the cells by burning after imaging at 24 h, indicated with the ellipse in Figure 6.4. In contrast, control cells (right hand column) did not exhibit the highly intense and blurred signal that is characteristic of sample burn, with cells and nuclei within remaining intact and qualitatively similar in appearance to the cells imaged at t = 0 h. Thus, the laser power was deemed too high as repeated exposure of cells to irradiation had directly burned the sample.

Reduction of laser power to (60/40 mW) allowed the full time-lapse experiment to be completed without any evidence of direct sample burn. However, changes in the cells were clearly evident following repeated imaging, demonstrated by the cells' appearance at the 48 h interval (Figure 6.4, centre). Two of the original five cells appear to be in late-stage apoptosis, while the remaining

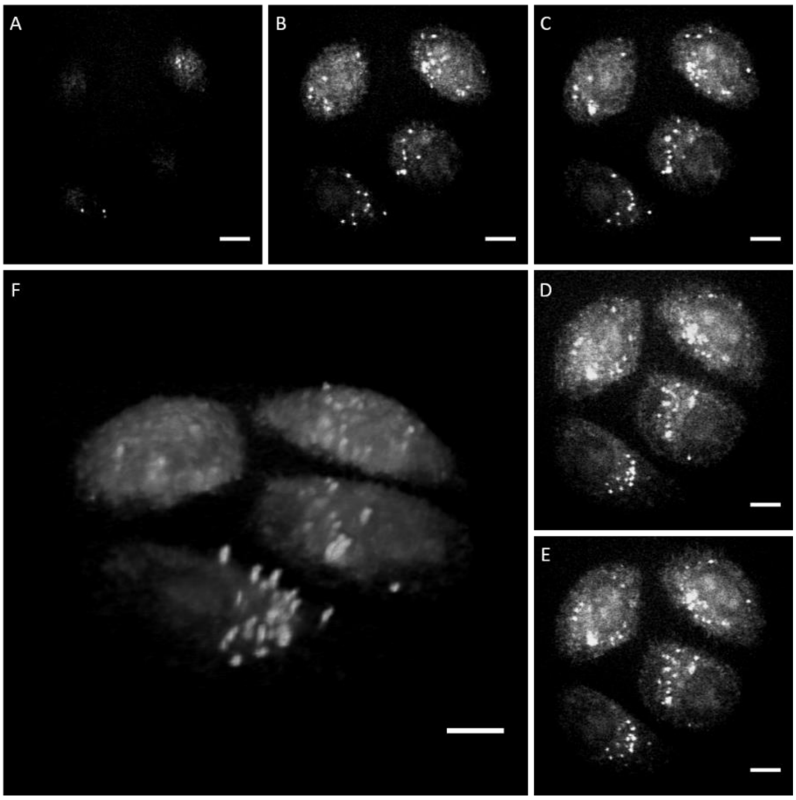

Figure 6.5 Z-stacking of CARS images (2850 cm^{-1}) acquired from a live sample of MCF-7 cells following 48 h incubation within a live-cell imaging chamber. Images were acquired using a laser powers of 50/30 mW (Pump/Stokes) at a step size of 0.5 µm, commencing from (A) the cell top, (B-D, examples only) through the cells' depth to (E) their coverslip-adhered base in order to produce (F) a detailed, three dimensional image of intracellular lipid distributions within a group of cells. Scale bar = 20 µm.

three appeared to only exist as apoptotic bodies with small (roughly 10 µm) total diameter and no discernible nucleus or cytoplasm. In contrast, control cells at the 48 h time point demonstrated large, expansive cell area with clearly intact cell and nuclear membranes. Increased abundance of cytoplasmic LDs was however observed relative to the original cell images at t = 0 h. Therefore, while sample burn had been avoided, it was evident that repeated laser exposure had induced apoptotic death in repeatedly imaged cells compared to controls within the same sample.

In the final iteration of the optimisation experiment, laser power was further reduced to a ratio of 50/30 mW, corresponding to the minimum threshold at which CARS images of sufficient contrast for analysis could be acquired. Additionally, the regularity with which cells were imaged was reduced to intervals of 0, 6, 24 and 48 h. The experiment was run for the full 48 h duration without any significant indication of cell death within repeatedly imaged cells (Figure 6.4, lower row). Additionally, CARS lipid images acquired from original FOVs at the 48 h time interval bore significantly greater resemblance to the initial images at t = 0 h in terms of general cell appearance (with allowances for cell movement). Despite slightly increased general intensity of

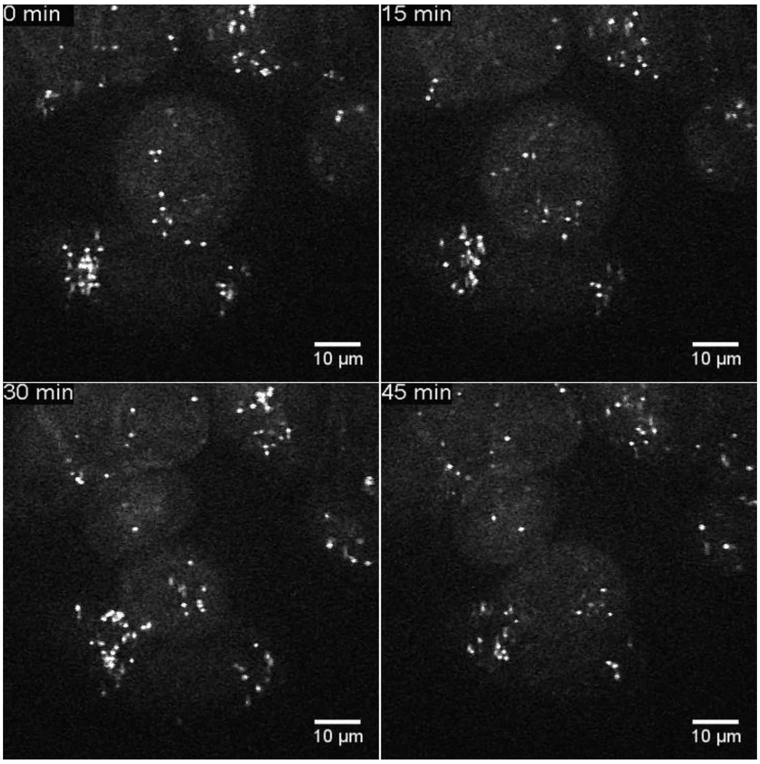

Figure 6.6 Observation of intracellular lipid distributions during late-stage mitosis in MCF-7 cells incubated within a live-cell imaging chamber for 48 h by three-dimensional CARS microscopy (2850 cm^{-1}). Representative mid-height image slices are presented, with stacks acquired at 15 minute intervals using a step size of 2 µm and laser powers of (Pu/St) 50/30 mW. Scale bar = 10 µm.

cell cytoplasmic regions, outer and nuclear membranes were evidenced to be intact and discernible, while newly-imaged control cell FOVs again exhibited completely healthy morphological appearances. Further experimentation was performed on the live-cell sample after completion of the time-lapse investigation. The three-dimensional sectioning capability of the platform was demonstrated (Figure 6.5), while image stack acquisitions of a cell in late-stage mitosis appeared not to inhibit its progression through telophase despite imaging at 15 minute intervals (Figure 6.6). The full image sequences for cell FOVs presented in the power optimisation experiments (Figure 6.4) are provided in Appendix Chapter A.2 of this thesis.

Further experimentation is required to determine whether further-reduced laser powers were the most significant factor in the achieved limiting of damage to live cells, or whether the larger intervals between laser exposures played a significant role in allowing cells to recover from induced stress. The finding would be significant in considering the platform for future use, as using higher laser powers to improve optical contrast at larger time intervals could be possible, while longer intervals between imaging sessions also limits the amount of information available. This would be particularly important for monitoring uptake of exogenous compounds, occurring within timeframes on the order of hours rather than days. Nonetheless, while uptake of a compound occurs on short timescales, manifestation of its actions can take several days, thus maintaining the relevance of the live-cell CARS microscopic assay.

The determined laser powers of 50 and 30 mW for pump and Stokes beams respectively were high compared to existing CARS studies monitoring intracellular lipids in live cells. Reported tolerance thresholds are, however, conflicting. Saarinen *et al* reported a minimum power requirement of 18-32 and 8-14 mW in pump and Stokes fields for achieving optical contrast of the 2860 cm^{-1} vibrational mode in Caco-2 cell cultures. Continuous exposure of live cells to powers of 40/20 mW for two minutes also showed no changes in cell morphology within two hours of observation[240]. However, observation of lipids during viral infection of live fibroblast cells has been reported to induce cell rounding and retraction, as well as detachment, within a two hour period of 35 mW laser exposure[313]. Elsewhere, a laser power ratio of 62/6.5 mW has been utilised to acquire z-stacks at thirty minute intervals during adipogenic differentiation of the same mesenchymal stem cells for a total 120 hour duration[314].

While variation is evident, the total laser power applied to cells in studies is in the region of 80 mW when combining the two beams. Presented results were acquired using conditions at the higher limit of this, however the variation is not so large that it cannot be attributed to subtle differences within experimental systems. It must be considered that all optimisation performed within this study is specific to the custom-built microscope and instrumentation used; the model and condition of its components; and alignment of the excitation beams at a given time. The biological sample can also produce variations in tolerance of laser exposure. For instance, different cell lines have demonstrated varying susceptibility to damage by NIR laser irradiation, as well the same types of cells being investigated across different species[217,224,240,314,325]. Taking this variation into account, presented data demonstrates optimisation of the employed experimental setup for monitoring intracellular lipid dynamics of live MCF-7 cells by CARS microscopy over a 48 h period.

6.5.2 Live Imaging of Intracellular Lipid Response to Drug Treatment

Having established parameters for live CARS imaging of intracellular lipid distributions, responses of MCF-7 cells to chemotherapy agent carboplatin were examined. The experiment was performed within poly-L-lysine coated and multi-well slides, with cells being allowed 24 h attachment before treatment with carboplatin at either 0 (control cells), 5, 50 or 100 µM concentrations. Every treatment was performed in duplicate, across which ten FOVs containing typically 3-6 whole cells were repeatedly imaged throughout the experiment.

Exemplar CARS images of intracellular lipid response to the drug treatment within each treatment are presented in Figure 6.7 A. Images acquired at t = 0 h remained consistent with previous experiments, exhibiting healthy cell morphological appearances. However, progression of the experiment presented contraction of cell areas towards smaller sizes that were more circular in shape. This effect was minimal at images acquired after 6 h, but became highly pronounced at later time points and with higher drug doses. Imaging of control cells also demonstrated cell contraction, however to a lesser extent than the drug-treated cells. Larger cell areas were observed again in control cells between t = 24 and 48 h. This may imply cellular recovery between imaging events that was not observed in the drug-treated classes. Carboplatin's effect on cells produced the aforementioned cell contraction, disappearance of discernible nuclear envelopes within and a generally increased scattering intensity within the cell cytoplasm. The number and size of LDs remained constant throughout the experiment but were confined within a smaller total cell area within images acquired at longer incubation times.

Cytosolic lipid abundances, quantified as the percentage of total cell areas, occupied by highly intense lipid signal (Figure 6.7 B, C) reflected this by relative increase with both incubation time and, to a lesser extent, drug incubation concentration. Mean values of lipid abundances were similar between 0 and 6 h images, followed by increases at both t = 24 and 48 h incubation in all treatment classes (including control cells). While observed increases between control and 5 µM carboplatin treated cells remained similar, the effect was greater in high dose (50, 100 µM) treatments after long incubation times. Increased relative LD abundance was statistically insignificant ($P > 0.05$) in all cases except between the 48 h images with 0 and 6 h images of 50 ($P \leq 0.01$) and 100 ($P \leq 0.05$) µM groups. The lack of statistically-significant ($P > 0.05$) differences between control and drug concentrations within every time interval (Figure 6.7 B) strongly implied that drug activity did not impact lipid distributions in a manner that was detectable by the CARS assay.

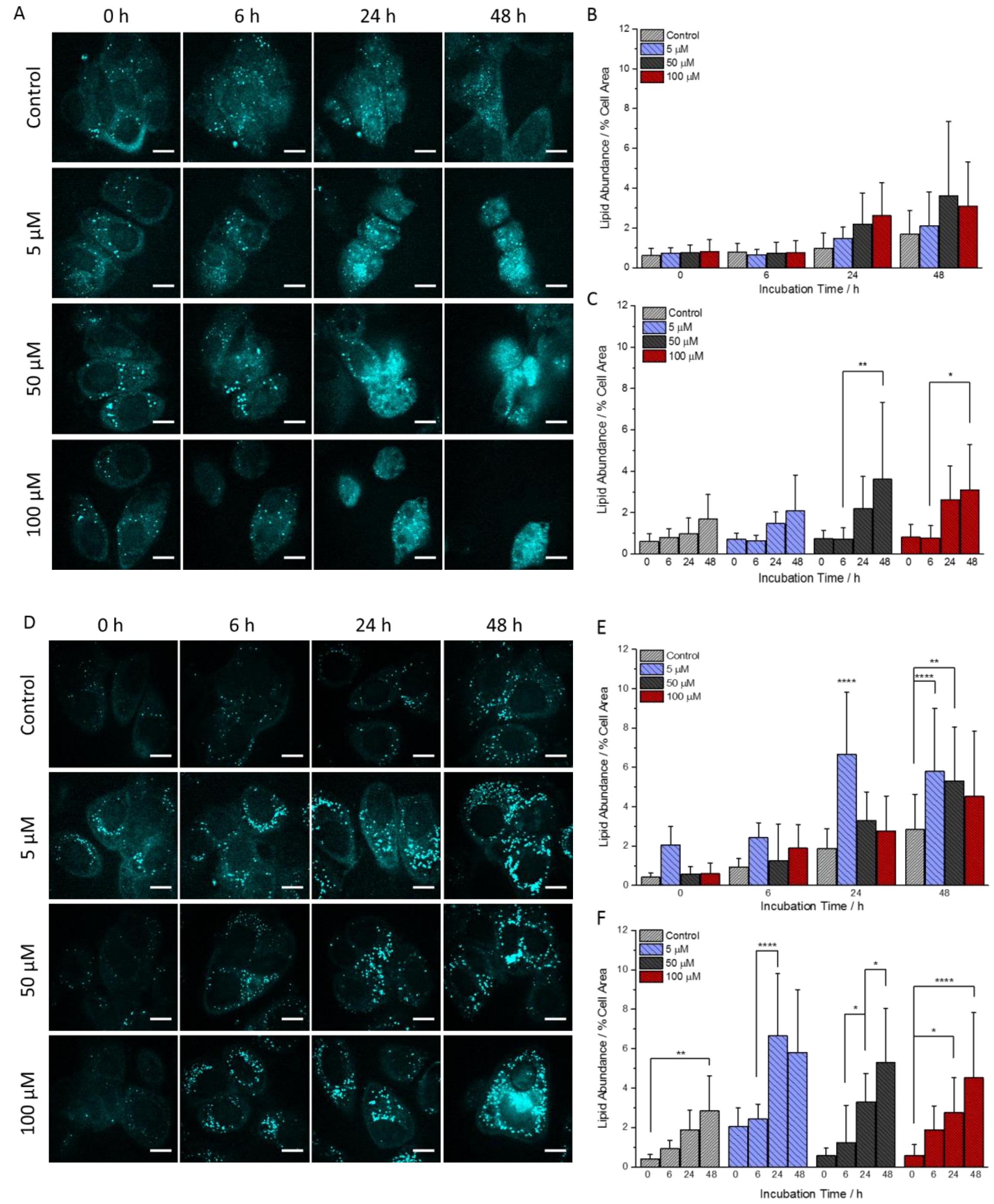

Figure 6.7 Monitoring of intracellular lipid response to treatment by carboplatin (0-100 µM) in live MCF-7 cells by CARS microscopy of 2850 cm^{-1} CH$_2$ stretching molecular vibrations performed by (A-C) repeated imaging of the same cell FOVs and (D-F) imaging of new cell samples at each time interval. Images (A, D) were analysed in order to quantify the abundance of lipid droplet vesicles within investigated cells, measured as % occupancy of the two-dimensional total cell area and compared as a function of (B, E) drug concentration and (C, F) incubation time. Scale bar = 15 µm.

The nature of the changes qualitatively observed in intracellular lipid abundance of control and carboplatin-treated cells resembled those observed in the previous experiments on live, untreated cells. Therefore, investigation of whether the observed changes in drug-treated cells were actually caused laser exposure was required. Rather than repeatedly imaging the same cells throughout the experimental duration, a repeat experiment was performed using separate multi-well slide samples for exclusive imaging of cells at just a single time interval. This way, it was ensured that analysed cells had experienced no previous exposure to the laser irradiation.

A total of 20 FOVs (typically containing 3-6 cells) were imaged across two repeats within every treatment group. Acquired images (Figure 6.7 D) demonstrated qualitatively different changes in intracellular lipid dynamics during experimental progression and under different drug concentrations compared to the previous, repeated laser-exposed cells. Within all drug concentrations, total cell area appeared to remain consistent, with cells exhibiting large total areas, discernible cell nuclei and intensely bright cytoplasmic LDs at both early and late-stage imaging intervals. A concentration-dependent difference was manifested within images acquired from the 5 µM carboplatin treatment group. Cells demonstrated an increased intensity across the whole cell areas relative to control and higher dose treatments, with regions of lower intensity such as cell outer membranes exhibiting greater image contrast than the other treatments. This effect was ubiquitous across all images acquired for the treatment, irrespective of replicate or incubation time.

The most qualitatively significant alteration of lipid distribution was visualised in cells treated with 100 µM for 48 h. LD numbers were greatly increased, while large cytoplasmic regions of intense scattering intensity (diameter around 15 µm) were observed with appearance of a vacuole-like structure that was void of signal and independent of the visible cell nucleus. The appearance of this structure was qualitatively reminiscent of cell damage induced in untreated cells following repeated exposure to laser powers of 60/40 mW after 48 h (Figure 6.4, centre). The morphological change may have related to cellular repackaging events during death, with cytoplasmic vacuolisation being commonly observed in mammalian cells following exposure to bacterial or viral pathogens, as well as low molecular weight drugs[326–328]. TEM has also confirmed this effect in MCF-7 cells treated with Pt-based chemotherapy agents[322]. The phenomenon may be transient or irreversible, potentially indicating induction of non-apoptotic cell death mechanism methuosis, characterised by displacement of cell cytoplasm by fluid-filled vacuoles derived from macropinosomes[329]. Further investigation would be required to confirm this and whether the vacuolisation was induced as a result of drug or laser exposure.

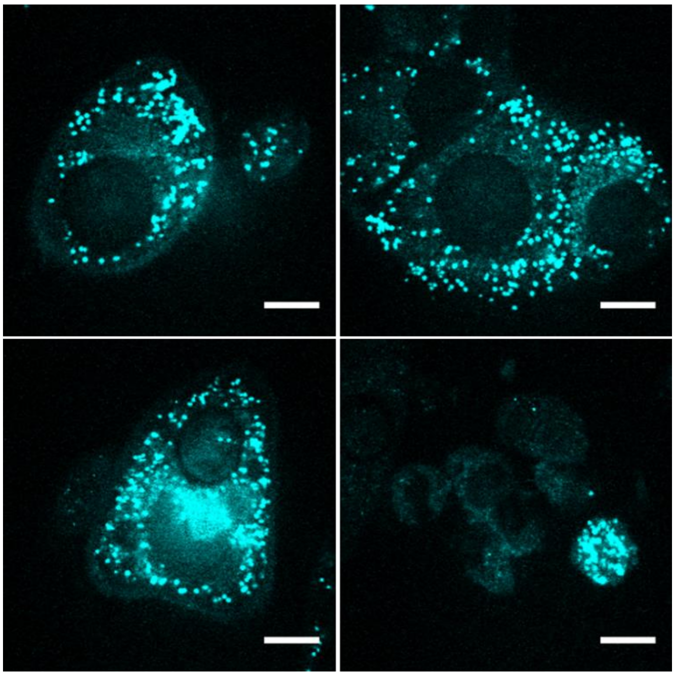

Figure 6.8 Demonstrated variability of lipid abundances and morphologies within live MCF-7 cells undergoing the same 48 h incubation with 100 µM carboplatin. Scale bar = 15 µm.

A predominant contrast between the singly and repeatedly imaged cell experiments arose in the mechanism by which LD abundances increased during the time course. Singly-imaged cells clearly exhibited increased numbers of LDs while total cell areas remained constant. On the other hand, repeatedly imaged cells (in the previous experiment), appeared to decrease in total cell area while the abundance of cytosolic LDs remained constant. Thus, a flaw in the parameter’s quantification was observed since vastly different cellular response processes produced the same numerical trend.

Within all singly-imaged cell treatment (including 0 µM) groups, the observed increase in lipid abundances was quantified (Figure 6.7 E-F). This was particularly relevant after 48 h, when cells of all groups demonstrated statistically significant increases (to at least $P \leq 0.01$) relative to cells at t = 0 h. At each time interval, no statistically significant trend in relative lipid abundance was observed between varying carboplatin doses. As qualitatively suggested, the mean lipid intensity of 5 µM carboplatin treated cells was increased relative to all other groups, particularly at t = 24 h (significant to $P \leq 0.0001$). As the result was observed between different samples and replicates, further repetition is required to determine whether an increased activity against the cells was accurately detected for the lower dose. If the result was reproducible from new samples and drug stocks, it would represent a significant display of CARS microscopy’s sensitivity in detecting subcellular drug actions.

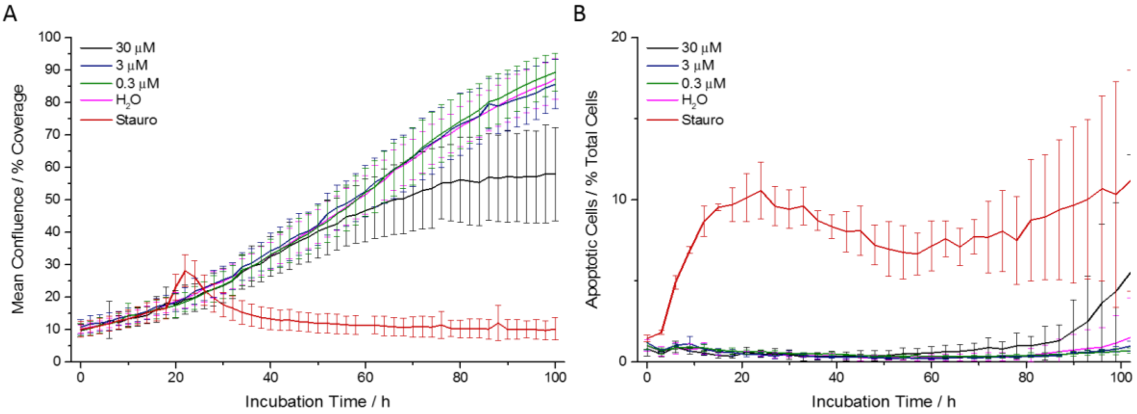

Figure 6.9 Activity of carboplatin (30, 3, 0.3 µM) against live human breast cancer cell line MCF-7 as investigated by (A) growth inhibition and (B) activation of caspase-7 mediated apoptosis compared to negative and positive controls of H_2O and staurosporine (Stauro, 1.25 µM) respectively.

A limitation of the platform was identified in variability between cells within the same treatment conditions, presented in the case 100 µM carboplatin treatment for 48 h (Figure 6.8). Large differences in both LD abundance and total cell areas, along with morphology, provide explanation for the high standard deviation values presented in error bars of Figure 6.7. Despite imaging of 20 FOVs per treatment (containing a minimum of 50 individual cells), requirement to analyse large numbers of cells is implied to overcome the high variability by applying population statistics. While no concentration-dependent effects of carboplatin upon cytosolic lipid abundances could be confirmed without further experimentation, single-exposure CARS imaging of cells did identify likely cell damage induced by repeated laser irradiation in the original experiment. A comparison of the different mechanisms by which cell damage was observed in repeatedly- and singly-laser exposed cells is discussed in Appendix Chapter A.4. Thus, single-exposure imaging was identified as the most viable system for long-duration, CARS-based analysis of lipid dynamics within live cells. This conclusion is in agreement with a previous study performing CARS microscopy on live fibroblast cell lipids during viral infection[313].

Having not detected any significant action of carboplatin upon intracellular lipid abundances, confirmation was required to determine whether the cause was poor sensitivity of CARS microscopy or simply lack of drug activity against the MCF-7 cell line. Therefore, traditional cellular assays were performed to assess growth inhibition and induction of caspase-7 mediated apoptosis by carboplatin treatment.

Cell confluence (derived from phase contrast imaging) over a 100 h period was analysed to monitor growth inhibition. The total duration was selected such that control cells (0.5 % H_2O

solvent, negative control) reached near 100 % confluency (Figure 6.9 A). Only treatment with 30 µM carboplatin was shown to significantly impact cells, limiting growth to 55 % confluence at the end of the incubation. Lower carboplatin concentrations exhibited no impediment of increasing cell proliferation which progressed at the same rate as the negative control. In contrast, positive control cells (treated with 1.25 µM staurosporine) demonstrated strong inhibition of cell growth that reached a maximum at 26 % surface coverage, validated the assay due to the compound's known cytotoxicity. Similar trends were observed by the apoptosis assay, reporting fractions of the total cell populations undergoing caspase-7 mediated apoptosis at a given time (Figure 6.9 B). Despite reported deficiency in the MCF-7 cell line of caspase-3[330], activation of just caspase-7 proved sufficient for GFP expression by staurosporine treatment. An average level of apoptosis was maintained between 5-10 % for the duration of the assay following 6 h of incubation in the positive control group. Again, only 30 µM carboplatin treatment demonstrated deviation from the negative control result which was manifested following at least 60 h incubation.

The cellular assays demonstrated no potency of carboplatin against the MCF-7 cell line within the incubation times examined by the CARS lipid-imaging experiments. Under both assays, data collected up to the 50 h incubation interval was indistinguishable from negative control treatments. However, prolonged exposure for 100 h did present mild drug action activity, with deviation from control treatments observed (to low extents) in both growth inhibition and apoptosis assays following 50 and 60 h incubation respectively. Although the drug concentration of 30 µM was lower than two of those employed in the CARS microscopic experiment, it represents a high value when considering drug efficacy against a target within drug discovery research. Therefore, the lack of significantly increased lipid abundances detected by the single-exposure live-cell CARS experiment was in fact reflective of the molecule's low potency and not due to a deficiency in the system developed. The potency of carboplatin's action on MCF-7 cells has been shown in literature to be similarly mild. Very high incubation concentrations of 200 and 400 µM were required to induce 28.8 and 37.8 % cell death during a 48 h period[321]. The low potency, along with the ability of MCF-7 cells to become resistant to the drug following prolonged culture within low concentrations, demonstrate why carboplatin is usually used as a combinative therapy with other chemical agents in the treatment of cancers[321,331,332].

The possibility therefore remains that the increased lipid abundances observed by CARS in singly-laser-exposed cells actually represented early detection of drug effect upon the cells. This case is supported by the larger incremental increases than were observed in control cells at 48 h incubation times.

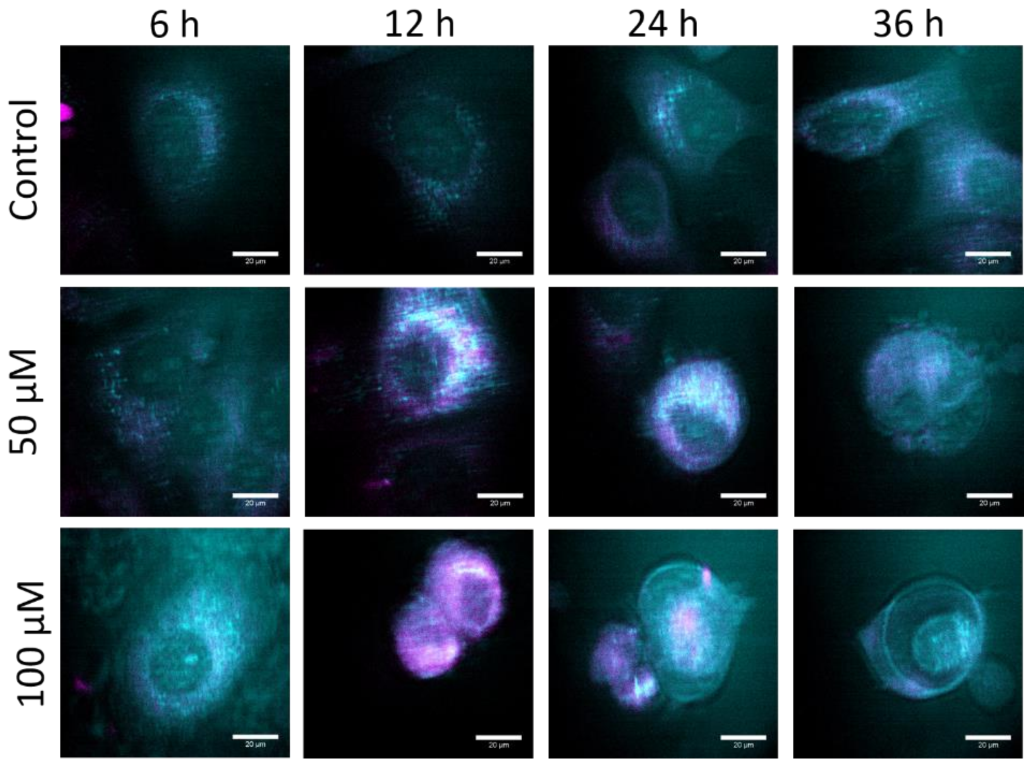

Figure 6.10 Multimodal and label-free imaging of intracellular lipid (cyan) and unbound FAD (magenta) distributions in response to incubation with cisplatin by CARS (2850 cm^{-1}) and two-photon autofluorescence (520 nm) at intervals of 6, 12, 24 and 36 h. Scale bar = 20 µm.

Further experimentation is required to confirm the ability of CARS microscopy to positively observe responses of intracellular lipids to treatment with therapeutics of well-understood activity against target. Such an experiment was performed using a potent chemotherapy agent, cisplatin (LD_{50} = 50-70 µM[333,334]), acquiring CARS images of singly-imaged live cells over a 36 h period.

Images acquired (Figure 6.10) demonstrated progression of MCF-7 cell death in a drug concentration-dependent manner, compared to no alteration in the morphological state of control cells throughout. Cell damage was evidenced by cell morphological changes, including initial increased lipid (2850 cm^{-1}, cyan) abundance within the cell cytoplasm. This was followed by contraction and rounding of the cells' total area before breakdown of a visually-discernible nuclear envelope and cell blebbing. The images were acquired simultaneously with two-photon autofluorescence arising from unbound flavin adenine dinucleotide (FAD), a redox-active coenzyme that is often used as a marker of metabolic activity in conjunction with fellow redox cofactor nicotinamide adenine dinucleotide (NAD). Areas of cells exhibiting bright autofluorescence intensity appeared to increase during the early stages of discernible apoptosis, occurring after 12-24 h and 12 h incubation with cisplatin concentrations of 50 and 100 µM respectively. Unfortunately, due to poor system performance at the time of experiment, acquired images were astigmatic and of poor resolution. The required use of increased laser powers and low number of cell FOVs successfully imaged (roughly 3 per treatment) removed capability to provide reliable quantification of the trends qualitatively observed in Figure 6.10. However, based upon results presented in this chapter, the ability of CARS microscopy to monitor changes in intracellular lipid dynamics and morphologies of live cancer cells in response to applied chemotherapeutic drugs is clearly established.

Review of existing literature corroborates the morphological changes observed by CARS microscopy. Electron microscopy has been utilised in reviewing the effect of carboplatin and cisplatin treatment upon MCF-7 cell ultrastructure[322]. Scanning electron microscopy revealed formation of small membrane pores that indicated drug influx, while early apoptotic shape modifications, including lamellipodia retraction, caused cells to adopt the smaller and rounded morphologies similarly observed by CARS. Transmission electron microscopy has also observed cytosolic vacuolisation induced by carboplatin and appearance of autophago- and autolysosomes that contain destructed organelles and act as a sink for deposited drug molecules. Interestingly, such deposits of the Pt-based compounds were identified within and around LDs of treated cells[322]. This suggests an active role of LDs in potentiation of drug actions and apoptosis that provide opportunity for further CARS platform development by simultaneous imaging of both LD dynamics (as demonstrated) and direct imaging of localisation, adherence and entry into LDs by a deuterium-labelled carboplatin. This approach features shifting of the C-H vibrational modes (2700-3000 cm^{-1}) into the region 2000-2300 cm^{-1} for C-D vibrations, an otherwise silent region of the cellular Raman spectrum. The approach has been previously utilised for CARS imaging of a docosanol isotope's arrival inside keratinocytes[247] and offers great potential for monitoring intracellular dynamics of molecules that can be isotopically labelled. While D/H substitution represents a form of labelling, it does not affect drug potency against target and has been verified by investigation (performed within this studentship, not presented) using carboplatin and four molecules belonging AstraZeneca's compound library.

While relative cytosolic lipid abundance was the parameter measured in the presented study, the acquired images could also be used to examine shifts in cell morphology, changes in nuclear size or cycling of LD expansion and contraction during interaction with other organelles in response to drug treatment. Additionally, a C-H stretching vibration of lipids was probed. Targeting vibrational modes of other key biomolecules such as proteins and DNA can potentiate extraction of a diverse and important range of quantifiable parameters relating to intracellular compositions during vital cell processes or response to drug treatments.

Research presented within this study therefore only presents just an example of CARS microscopy's ability to visualise dynamic intracellular processes following drug administration in a chemically-selective and label-free nature that can be further developed to provide a powerful tool in early-stage drug discovery.

6.6 Conclusions

This chapter has demonstrated development, optimisation and application of the CRI technique CARS microscopy for visualising the behaviour of a key organelle's response to applied drug molecules within live cells. The scope of this research differs from previously-presented SERS experimentation, focussing on native cellular content that could be reveal drug effects rather than directly mapping its localisation. The most significant contribution of this platform arises in its completely label-free nature, offering increased validity of experimental models compared to fluorescent tagging of endogenous analytes or internalisation of inorganic NPs required for SERS measurements.

While laser power remains a limiting factor in maintaining the health of repeatedly-imaged cells, observation of larger number of singly-laser-exposed cells presented a potential solution assuming datasets are acquired of sufficient size to generate population statistics. Towards this, CARS microscopy offers low acquisition times in a manner that would be easily automated. However, It must also be considered that defined parameters are only relevant to the home-built microscope used in this study and that improved performance can allow long-term imaging of the same live cells through requirement for lower laser powers[314]. High concentrations of chemotherapy agent carboplatin were quantitatively shown to produce no significant increase in cytosolic lipid droplet abundance within the experimental timeframes. Despite this, observed increases may represent earlier detection of carboplatin actions than could be identified by traditional assays, shown to occur after prolonged (50-60 h) incubation. Limited application of the CARS platform to cells treated with cisplatin suggested that extraction of quantitative parameters associated with cell apoptosis is achievable following repetition with normal instrument performance. The multimodal capability of the platform was also demonstrated by multiplexed image acquisition with two-photon autofluorescence arising from a marker of intracellular redox metabolism. The demonstrated ability of CARS microscopy to monitor responses of intracellular biomolecules (in this case lipids) to drug treatments without the use of fluorescent tags holds great potential for providing new pharmacological insights during early-stage drug discovery research.

Chapter 7 Comparing Chemical Selectivity of CRI Hyperspectral Image Stacks

7.1 Abstract

CRI techniques present a unique opportunity to observe the progression of intracellular structures in a label-free and non-invasive manner. In Chapter 6, single-frequency CARS microscopy was used to monitor intracellular lipid droplet dynamics during treatment by chemotherapy agents. However, investigation of single chemical species is of limited utility when visualisation of multiple or unknown intracellular biomolecules or drug targets is required. Therefore, a hyperspectral imaging approach is necessary to improve the wealth of information provided by CRI platforms. The following research investigates the relative capability of CARS, along with other predominant CRI technique SRS microscopy, to visualise different biomolecular components of the intracellular matrix by hyperspectral imaging. C-H vibrational modes within the region 2700-3000 cm^{-1} of the same MCF-7 cell sample were examined using both modalities to assess the relative chemical selectivity offered by each technique. Critical to extraction of quantitative information from hyperspectral datasets is statistical analysis, applied here in the form of PCA to investigate improvement of chemical selectivity in both CARS and SRS microscopy. Results indicated that the approach particularly improved selectivity of SRS image hyperstacks for classification of different endogenous biomolecules. The ability of the demonstrated CRI-PCA platform to perform statistically-weighted mapping of intracellular features based upon their chemical composition holds great potential for studying and screening drug actions against targets.

7.2 Contributions

Research performed within this chapter was performed by the candidate only, although the design, construction and maintenance of the home-built multiphoton microscope carried out by Kostas Bourdakos, Peter Johnson, Tual Monfort and Sumeet Mahajan is kindly acknowledged. The customised Matlab script used to perform PCA was developed in collaboration with Niall Hanrahan.

7.3 Background

In the previous chapter, CARS imaging of lipid distributions was performed using their CH_2 symmetrical vibration, owing to its simple distinction from peaks resulting from other biomolecular contents within the cellular Raman spectrum. While this has high utility in monitoring the response to drugs of a dynamic and clinically-relevant organelle in LDs, the ability of CRI techniques to visualise various desired molecular vibrations (afforded by tuning of excitation pulse frequencies) remains unexploited. The final study of this thesis serves to explore the wider functionality of CRI by comparing the relative chemical selectivity achieved by CARS microscopy with the second predominant CRI platform, SRS microscopy. Crucial advantages of SRS microscopy are held in signal intensity being linearly proportional to analyte concentrations and energy transfer only following specific stimulation of the desired vibrational mode. The first factor aids extraction of quantitative data while the latter improves chemical selectivity by preventing contribution from off-resonance vibrational modes other than that probed for, known as the non-resonant background (observed in CARS microscopy). Disadvantages of SRS microscopy relative to CARS include weak signal which requires amplification and isolation from laser noise by frequency modulation, along with a lower theoretical spatial resolution than CARS due to the lower order of its non-linear dependence on excitation frequency.

Since the first application of SRS microscopy in biological context[335], the number of single-frequency and hyperspectral SRS applications utilising its ability to perform non-invasive and label-free imaging has increased exponentially. Lipid dynamics have been monitored in cells, tissues and whole organisms[212,213,229,336,337], including quantification of lipid compositions *in vivo* for RNA interference screening of fat regulatory genes in *Caenorhabditis elegans*[213]. Hyperspectral SRS has also been utilised to observe changes in cells and mineralisation within fresh articular cartilage, associated with monitoring the progression of osteoarthritis[338]. For monitoring intracellular processes, changes in DNA condensation have been used to make inferences about chromosome dynamics during cell division by SRS imaging of DNA, which has also permitted visualisation of cell nuclei within live animals and fresh human tissues[225]. Deuterium-labelling of exogenous glucose and amino acids have allowed observation of *de novo* lipogenesis and protein synthesis respectively within mammalian cells, utilising the shift of C-D vibrational frequencies into the biological silent region of the Raman spectrum[339,340]. Spectroscopically bio-orthogonal alkyne tags similarly produce characteristic vibrational markers which have afforded SRS visualisation of DNA synthesis by tagging of a thymidine analogue[232,341].

Research presented in the following chapter serves to assess relative chemical selectivity of CRI platforms CARS and SRS by analysis of hyperspectral image stacks collected of the same FOV in each modality. Hyperspectral imaging allows generation of vibrational spectra for every pixel of an image by tuning of excitation pulse frequencies during acquisition. This affords large, rich datasets from which quantitative information can be extracted by careful image processing and data treatment. Multivariate analysis is commonly applied to CRI hyperspectral image stacks, with lipid characterisation achieved in live cells by single valued decomposition analysis of CARS image stacks, utilising broadband excitation and CCD detection[342]. The following research applies multivariate method PCA to manually-acquired CRI hyperspectral images of human breast cancer cell line MCF-7, in order to investigate whether the selectivity of each CRI microscopy can be improved. The outputs of the analysis are compared between the modalities, with results obtained by the hyperspectral SRS-PCA platform compared to raw images for assessing the viability of producing statistically-weighted maps of chemical composition at the intracellular level. This ability would prove invaluable in identifying the actions of prospective drug treatments across a range of targets, discerning drug efficacy without use of fluorescent tags or sample destruction.

7.4 Methods

7.4.1 Sample Preparation

Human epithelial breast cancer cell line MCF-7 was cultured on glass coverslips and fixed as described in Section 6.4. Due to SRL detected in the forward-direction, coverslips were mounted onto large glass coverslips instead of microscope slides.

7.4.2 Hyperspectral Image Stack Acquisitions

In order to compare the relative performances of CARS and SRS imaging on the home-built microscope, fixed cell images were acquired of the same cells in both modalities. A total laser power of 60 mW was applied to samples, in Pu/St ratios of 40/20 and 30/30 mW for CARS and SRS microscopy respectively, complementing the techniques' respective scattering mechanisms. Multiple cell FOVs were imaged following excitation of vibrational modes at 2850, 2930 and 2967 cm^{-1} in order to observe relative intensities of previously determined vibrational modes associated with lipid, protein and nucleic acid content respectively. Subsequent to this, hyperspectral image stacks were acquired in both modalities from the same FOV within the spectral region 2700-3050 cm^{-1}. Excitation wavelengths were selected such that the size of wavenumber intervals was reduced around the location of vibrational peaks corresponding to lipid (2850 cm^{-1}) and nucleic acid (2970 cm^{-1}) content. Images of size 512 x 512 pixels were acquired using an 8 µs pixel dwell time.

7.4.3 Image Processing and Analysis

In order to compare the spectral similarity observed in cells by CARS and SRS modalities to those acquired using spontaneous Raman scattering, mean spectra of cellular content were calculated from the hyperspectral stack acquired in each modality. Images were background-subtracted by application of a minimum threshold to isolate only pixels containing cellular content before measurement of their mean intensity at selected vibrational frequencies for both CARS and SRS image stacks. The mean intensity of all cellular pixels was then plotted against Raman shift in order to compare peak locations within the C-H stretching region of the Raman spectrum 2700-3050 cm^{-1}. The spontaneous Raman, CARS and SRS spectra were normalised in order to account for the different methods of acquisition.

To directly compare the chemical selectivity of CARS and SRS images, intensity profiles of images produced at vibrational frequencies of 2850, 2930 and 2967 cm^{-1} (previously demonstrated by Raman spectroscopy in Chapter 6 as corresponding to lipid, protein and nucleic acid content respectively) were plotted along a cross-section of 10 individual cells. Cells were selected for analysis such that each displayed clearly discernible regions of extracellular background, cytoplasm, perinuclear lipid droplets, nucleus and nucleoli within, to be traversed by the intensity profiles. Generated profiles in CARS and SRS channels were compared for each cell to provide insights into relative specificity of imaging in vibrational mode.

In further analysis, multivariate technique PCA was applied to the CARS and SRS hyperspectral stacks to investigate whether chemical selectivity for each biomolecule could be improved. Analysis was performed on the CARS and SRS stacks individually using a custom-built MATLAB script. Image pixels were first grouped into larger blocks (3x3 pixels), the mean intensities of which were plotted as a function of Raman shifts in order to generate a dataset of spectra to be background subtracted (polynomial order 7) and mean centred for application of PCA. A total of six principal components (PCs 1-6) were calculated from each dataset, for which PC loadings revealed the Raman shifts accounting for the largest degrees of variance calculated within each component. The scores of each pixel block within each PC were projected back onto its original image coordinates. The loadings associated with each PC revealed Raman shifts that provided largest contributions to spectral classifications, inferring the biomolecular compositions of intracellular features.

7.5 Results and Discussion

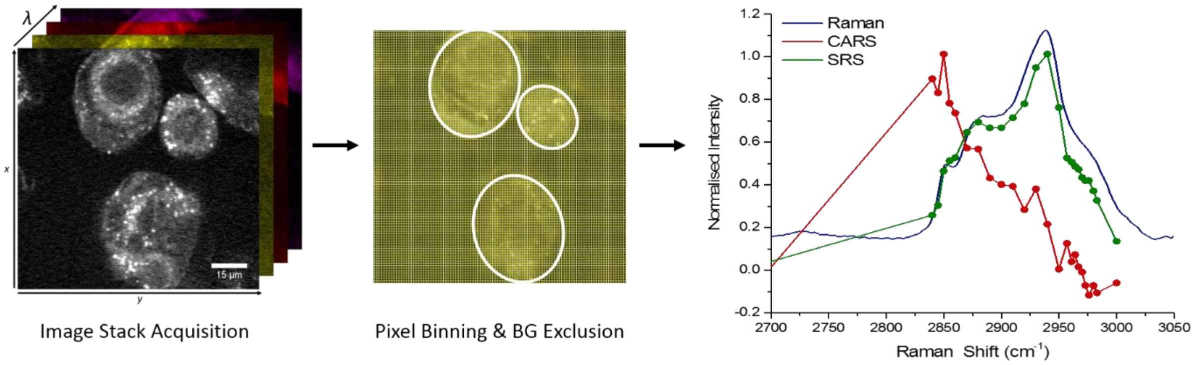

Figure 7.1 Workflow diagram for plotting of the mean CARS (red) and SRS (green) spectrum of fixed MCF-7 cells from hyperspectral images stacks acquired in each modality. Image pixels were averaged (3x3 blocks), before removal of extracellular background contributions and plotting of pixel block mean intensities at each wavenumber interval. The mean spectrum of all cellular blocks in both modalities was plotted and compared to a mean spontaneous Raman spectrum of the same cell line.

7.5.1 CRI Spectral Comparison

To begin, the mean intracellular spectrum detected within each CRI modality was calculated following hyperspectral imaging of the same MCF-7 cells in the range 2700-3000 cm^{-1}. Pixel intensities were averaged into larger blocks for plotting their average intensity against the probed vibrational frequency, generating a set of spectral data for both CARS and SRS image stacks. Mean spectra acquired from only pixel blocks corresponding to cellular content were plotted for comparison of each to MCF-7 cell spectra acquired by spontaneous Raman spectroscopy.

The plot (Figure 7.1) revealed a striking resemblance between the cell spectra acquired from spontaneous Raman and SRS acquisitions, in agreement with the linear relationship between intensity and analyte concentration and freedom from non-resonant background contributions shared by the techniques[337,343]. Each of the four major C-H vibrational peaks were identified by the SRS spectral scan, with the predominant peak arising at 2930-40 cm^{-1} and exhibiting shoulder peaks at 2850, 2880 and 2970 cm^{-1}, all corresponding to vibrational modes assigned in spontaneous Raman spectroscopy of biomolecule standards (Figure 6.2). Spectral assignments were in agreement with similar CRI study of the cellular C-H stretching region[225]. The only highly intense peak revealed in the CARS cell spectrum was that at 2850 cm^{-1}, representing the characteristic vibration of lipid content that was selected for analysis in Chapter 6. Small elevations in mean intensity were demonstrated at the other identified Raman shifts, although these were lower in intensity and obscured by a more variable background. This high level of non-resonant background contribution was consistent with a similar spectral comparison made between the techniques from imaging of articular-cartilage-derived extracellular matrix[338].

7.5.2 Intracellular Imaging of Biomolecule Distributions

The predominant peaks arising in generated CRI cell spectra, corresponding to vibrations of biological macromolecules lipids (2850 cm^{-1}), proteins (2930 cm^{-1}) and nucleic acids (2970 cm^{-1}), were visualised by CARS and SRS microscopy of fixed MCF-7 cells. Figure 7.2 presents raw images acquired in each modality at each Raman shift for an exemplar cell. Within both CRI channels, the cell structure is clearly discernible, exhibiting an intact cell membrane with abundant lipid droplets that surround a central nucleus and nucleoli within. Comparison of the 2850 cm^{-1} vibrational mode between the channels reveals similar, highly-intense signal arising from cytosolic lipid content. CARS images presented higher intensity in the extracellular background but also the perimeter of the cell cytoplasm, allowing clearer observation of the cell's outer morphology and membrane structure. The high signal intensity observed in the 2850 cm^{-1} mode was reflective of its mean cellular CARS spectrum (Figure 7.1). In contrast, SRS imaging produced lower intensity of the extracellular background and cell outer membrane. Intensity of nuclear content was also significantly reduced relative to CARS images, a result that may imply higher chemical selectivity since the nucleus should contain predominantly nucleic acid and protein content. This demonstrated higher non-resonant contributions to the CARS than SRS intensity, as would be expected.

Imaging of scattering at 2930 cm^{-1} demonstrated a much lower signal-to-background ratio in CARS images compared to SRS, with only the cell nucleus being noticeably elevated in intensity relative to the extracellular background. The SRS image at 2930 cm^{-1} displays the whole cell area against dark background, with the outer cytoplasm more visible than in the 2850 cm^{-1} mode. This low but definite signal may be explained by the ubiquitous presence of diffuse cytoplasmic proteins such as actin microtubules throughout the cell cytoskeleton. The 2930 cm^{-1} SRS image also revealed intense signal arising from the nucleoli, protein structures within the cell nucleus. CRI images of 2970 cm^{-1} vibrations demonstrated the least exclusive regions of intensity within both modalities. However, a stark contrast was observed in relative signal-to-background intensity between the channels. CARS imaging experienced almost inversion of signal, as nucleoli and lipid transport vesicles appeared darker than the homogenous extracellular and cytoplasmic signal. SRS imaging of the vibrational frequency showed a clear dark background with the majority of elevated cell signal arising from the nucleus and nucleoli. Overlay of the images acquired in each channel

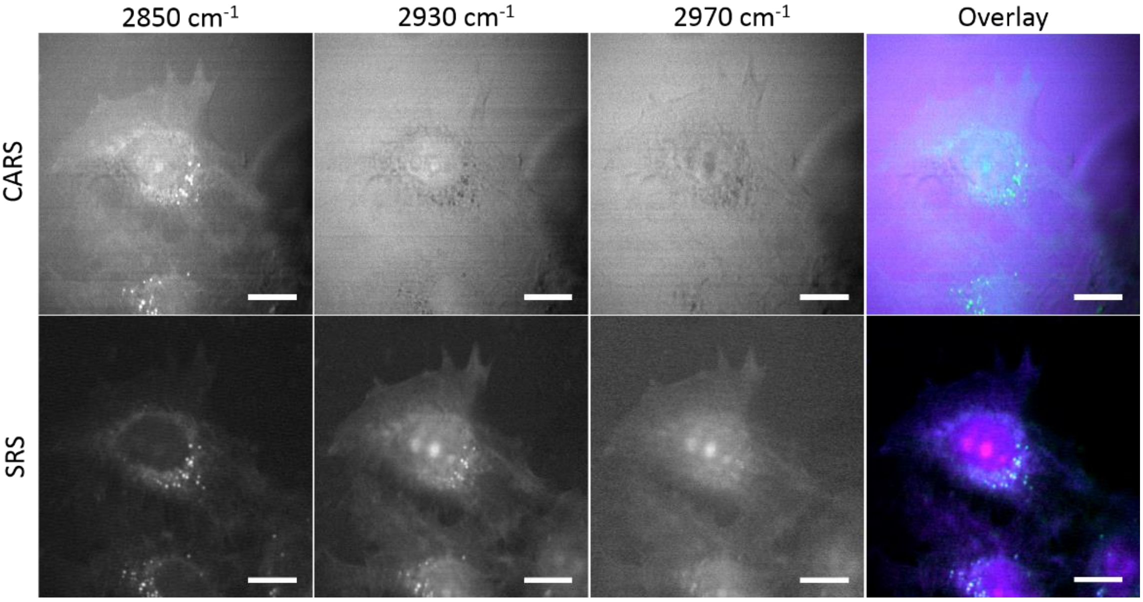

Figure 7.2 Example images of vibrational modes corresponding to lipid (2850 cm^{-1}), protein (2930 cm^{-1}) and nucleic acid (2970 cm^{-1}) content within a fixed MCF-7 cell acquired by CARS (upper) and SRS (lower) modalities. Overlay images demonstrate the spatial is overlap of signal intensities arising from scattering at Raman shifts of 2850 cm^{-1} (green), 2930 cm^{-1} (blue) and 2970 cm^{-1} (magenta) within each modality. Scale bar = 20 µm.

(Figure 7.2) demonstrates the lack of biomolecular selectivity observed between images acquired at 2930 and 2970 cm^{-1} in CARS microscopy, with low signal-to-background ratios.

Chemical specificity was compared by plotting line profiles of intensity at particular vibrational frequencies (Figure 7.3, white cross-sections). Regions were selected such that cross-sections traversed clear regions of extracellular background, cell cytoplasm, perinuclear lipid vesicles, nucleus and nucleolus, for examining the signal arising from each of the defined compartments. Intracellular CARS intensities were dominated by signal at 2850 cm^{-1} (green), while 2930 cm^{-1} (blue) and 2967 cm^{-1} (magenta) intensities contributed most strongly to cellular SRS intensities, in agreement with Figure 7.2. The intensity profiles confirmed the lower relative extracellular background detected by SRS than CARS, although in all examples the cell area was identifiable by elevated 2850 and 2930 cm^{-1} intensity. Similarly, the location of both cells' nuclei were revealed by a maintained void in lipid (2850 cm^{-1}) intensity in the regions 15-25 µm and 28-55 µm of cell A and B respectively, in both cases surrounded by sharp peaks arising from perinuclear lipid droplets.

A difference between the modalities was observed within cell nuclei. In both cells (Figure 7.3, Cells A and B), CARS imaging of the 2850 cm^{-1} vibration showed elevated intensity at the nucleoli,

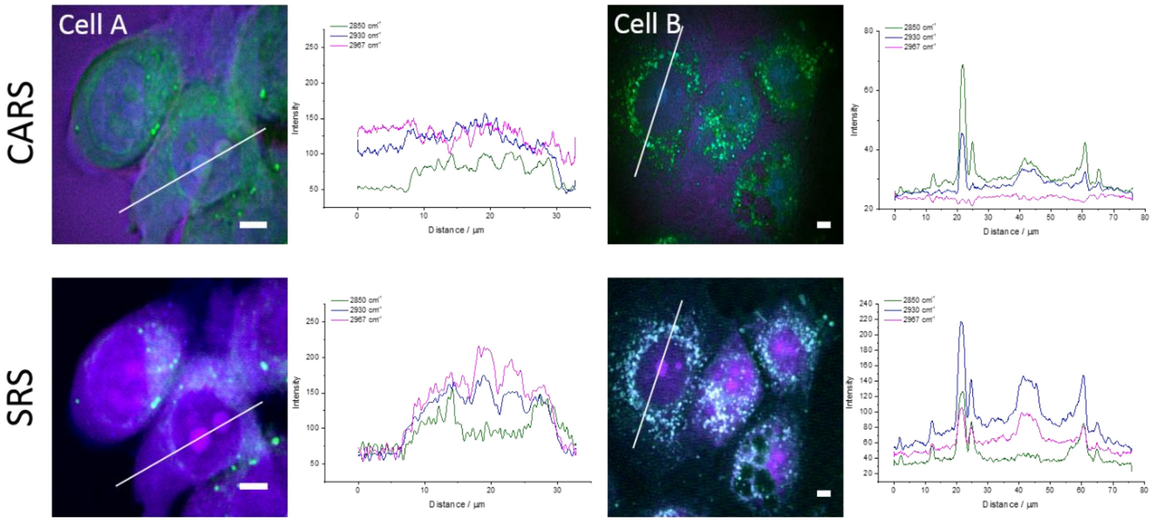

Figure 7.3 Intensity profiles of signal intensities arising from vibrational frequencies of 2850 cm $^{-1}$ (green), 2930 cm $^{-1}$ (blue) and 2967 cm $^{-1}$ (magenta) across whole cells within CRI platforms CARS (upper) and SRS (lower). Scale bar = 5 µm.

accompanying the corresponding increase in 2930 cm^{-1} scattering intensities explained by protein content. In contrast, no such elevation of lipid scattering intensity at nucleoli were observed by SRS imaging. Therefore, explanation by non-resonant excitation of protein C-H vibrations contributing to the 2850 cm^{-1} intensity of the CARS signals was supported. The mode assigned as nucleic acid content (2967 cm^{-1}), displayed significantly enhanced signal-to-background ratios in SRS images compared to CARS, with intensity peaks of location and size that corresponded to cell nucleoli (17-21 and 22-25 µm in cell A, 16-22 µm in cell B). In contrast, the CARS intensity of the nucleic acid mode was barely distinguishable from cytoplasmic or extracellular regions.

The intensity profiles of both cells demonstrated that CARS signal from the 2850 cm^{-1} vibration of lipids was easily discernible with high intensity. However, non-resonant contributions also overwhelmed signal in images arising from vibrational modes at 2930 and 2967 cm^{-1}, giving rise to poor biochemical resolution of protein and nucleic acid content respectively. Meanwhile, SRS image intensities exhibited lower overall sensitivity to the 2850 cm^{-1} vibration but distinctly higher signal-to-background ratios for all investigated peaks. Molecular selectivity was also shown to be enhanced relative to CARS microscopy through identification of frequency-specific intensity within defined intracellular compartments. This was particularly evidenced in discrimination between lipid and protein content.

7.5.3 Multivariate Analysis of Hyperspectral Image Stacks

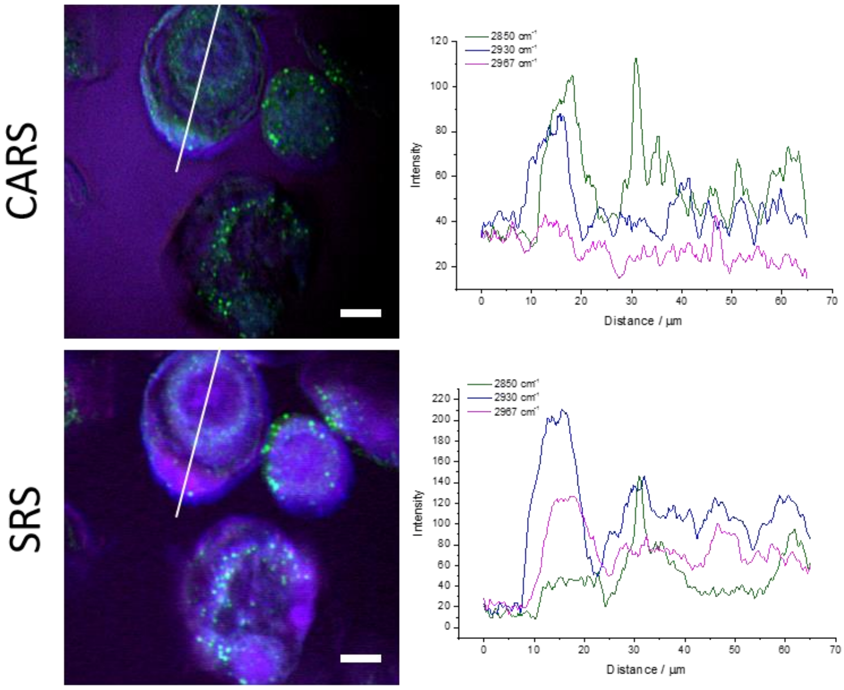

Figure 7.4 Intensity profiles of signal intensities arising from vibrational frequencies of 2850 cm^{-1} (green), 2930 cm^{-1} (blue) and 2967 cm^{-1} (magenta) across a whole cell from which CRI hyperspectral image stacks were acquired. Scale bar = 10 µm.

To investigate the effect of applying PCA to intracellular CRI data, hyperspectral image stacks were acquired by both CARS and SRS to visualise the same fixed-cell FOV within the range 2700-3000 cm^{-1}. Raw images resulting from the wavelength scans across the range in both microscopic platforms are presented in Appendix section A.5. Confirmation that the acquired stack was representative of the wider MCF-7 cell sample was provided by observation of relative intensity profiles between vibrations corresponding to 2850, 2930 and 2967 cm^{-1} through distinct intracellular compartments (Figure 7.4). Both techniques exhibited sharp intensity peaks in the 2850 cm^{-1} vibration detected immediately outside the nucleus (40-55 µm), corresponding to perinuclear LDs. Within the cell nucleus, SRS acquisitions again demonstrated greater chemical selectivity between the 2850 cm^{-1} and the 2930 and 2967 cm^{-1} vibrations, the latter both showing expected intensity peaks corresponding to nucleoli that were absent in the former. CARS acquisitions exhibited stronger signal from the 2850 cm^{-1} vibration of lipids, although a greater contribution from non-lipid content and non-resonant background was again displayed. These trends in relative intensity between vibrational modes in both CARS and SRS channels were reflective of those presented in the wider cell sample (Figure 7.3), therefore allowing valid conclusions to be drawn about relative chemical selectivity of the techniques when combined with PCA.

PCA was performed on spectra generated from 3x3 pixel bins within each of the CARS and SRS scans individually. The output PC (PCs 1-4) loadings and back-projected scores, calculated for both CRI modalities, are presented in Figure 7.5. Higher order PC outputs (PCs 5-6, Supplementary Figure 8.13) generated in both technique hyperstacks accounted for 1 % or less of the total variance (Table 8.2) and are presented in Appendix section A.7.

PC1 loadings in each of the modalities generated loadings plots (Figure 7.5, top row) identified largest weighting coefficients at 2850 and 2930 cm^{-1} for CARS and SRS scans respectively. The loadings plots also closely resembled the background-subtracted mean cell spectra generated in (Figure 7.1) in both techniques. Since the mean spectra were acquired from all cell image pixels, the likeness implied that PC1 produced discrimination of pixels corresponding to cellular content from the extracellular background. Observation of the projected PC1 scores within each technique demonstrated stronger differentiation of intracellular content from background by SRS. All intracellular regions in the FOV took clearly higher score values relative than those of dark extracellular background, whereas CARS PC1 scores also yielded dark regions inside cell contours and a weighting of intensities towards the lower edge in one of the cells. This result corresponded to the relative peak-to-baseline ratios previously identified in direct peak intensities.

PC2 loadings generated in each CRI modality (Figure 7.5, second row) demonstrated largest contributions from the same peaks as PC1 (2850 and 2930 cm^{-1} for CARS and SRS respectively). However, the weighting was stronger relative to other wavenumber contributions in both cases. The effect of this on corresponding PC2 scores projections varied between the CRI modalities. The PC2 projection of cellular content from CARS images showed increased intensity within all cellular areas, as opposed to the dark intracellular regions observed in PC1. This allowed for better classification of cell signals from the extracellular background. The ubiquity of the intensity within all regions of the cells may have arisen due to off-resonant contribution of protein vibrations. In contrast, PC2 scores calculated from SRS microscopy showed strong intensity arising from structures around the cytoplasm’s inner perimeter which may allude to imaging of pseudopodia, protein-rich structures performing roles in cell motility. The loading exhibited strong distinction of the peak, with the weighting of nearby vibrational modes assigned negative coefficients.

PC3 loadings (Figure 7.5, third row) calculated from the CARS image stack was most significantly contributed to by a broad wavenumber region 2870-2910 cm^{-1}. The wavenumber was assigned to

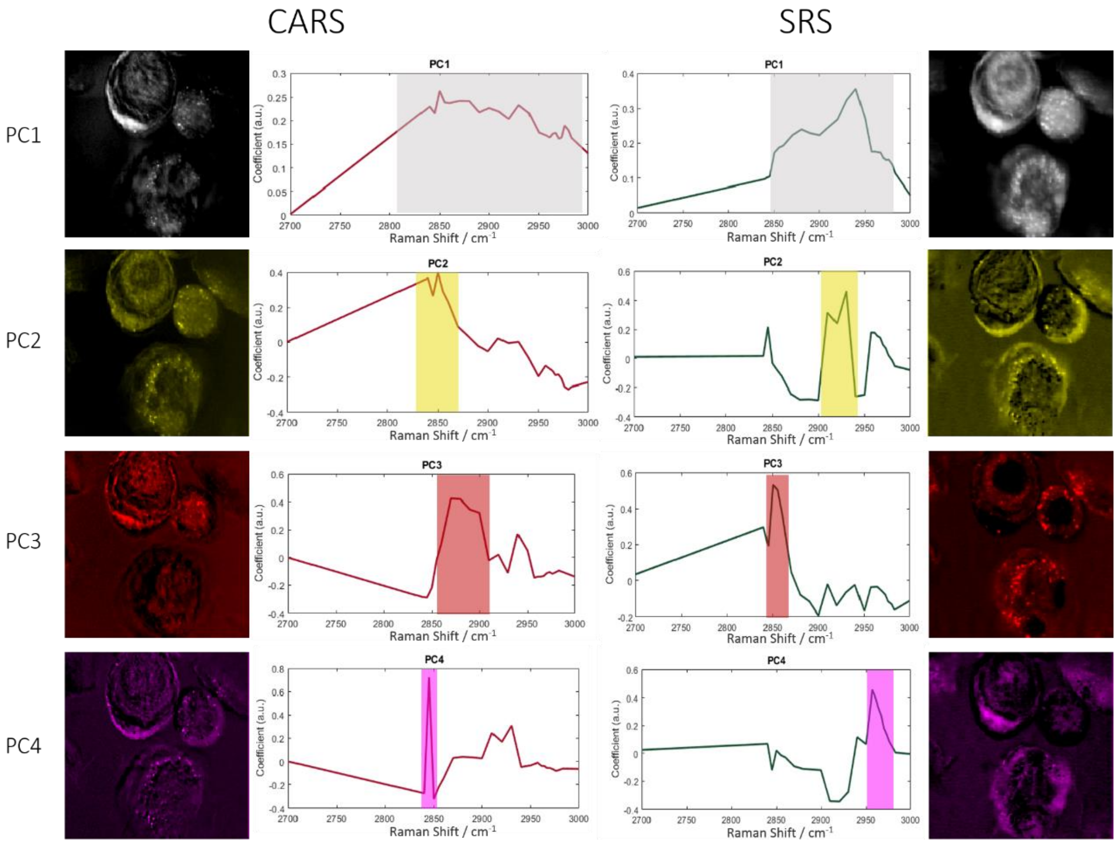

Figure 7.5 Output from PCA (PCs 1-4) performed on hyperspectral image stacks acquired by both CARS (left, red) and SRS (right, green) microscopy of the same cluster of MCF-7 cells. Plotted PC loadings (spectra) reveal vibrational modes providing strongest contribution to the achieved classification of pixel blocks. Back-projection of pixel block scores within each generated PC onto their original coordinates (pseudo-colour images) produces quantitative mapping of biomolecular compositions within whole cells.

asymmetrical stretching of CH_2 bonds in both lipids and proteins. In contrast to PCs 1 and 2, PC3 loadings of the SRS image stack revealed distinctly high contributions from the vibrational frequency 2850 cm^{-1}. Weakly negative coefficients were calculated for all Raman shifts of higher wavenumber. This was reflected in the projected image of PC3 scores by highly specific intensity of bright perinuclear structures resembling lipid vesicles, while zero low scores values were observed within cell nuclei and previously-intense regions of peripheral protein signal.

The greatest degree of biomolecular selectivity observed by CARS-PCA analysis was in PC4 (Figure 7.5, lower left), with loadings bearing resemblance to those of SRS PC2 by way of a strongly defined peak in weighting coefficient within the lipid-associated vibrational frequencies at 2850 cm^{-1}. Interestingly, the exact location of the peak was shifted by 5 cm^{-1} to 2845 cm^{-1}. CARS PC4 scores however appeared to show lower specificity of score values than expected to pixels containing intracellular lipid droplets, with cytoplasmic peripheries also exhibiting contrast. On the other hand, PC4 loadings calculated from the SRS hyperstack (Figure 7.5, lower right) was the only component (across both modalities) that demonstrated a peak in weighting coefficient at Raman shifts corresponding to nucleic acid content, 2960-70 cm^{-1}. The peak was isolated in bearing a positive weighting contribution, compared to weaker negative weightings at 2850 and 2930 cm^{-1}. Projection of PC4 scores revealed greatest score values at both the peripheral cytoplasm (also exhibiting high protein content) and within a specific region of the uppermost cell's nucleus that was specific only to this calculated component. The structure visually resembled that of nucleoli.

Overall, PCA applied to the acquired SRS spectral scan revealed significantly increased classification of vibrational modes associated with key cellular biomolecules than that by CARS microscopy. The greater specificity towards lipid-rich structures associated with the 2850 cm^{-1} vibrational frequency identified in CARS images was consistent with findings of PCA analysis of human head and neck tissue sections[343]. Similarly, both studies detail a greater degree of spectral difference between generated PCs and more significant contribution from modes at 2930 and 2967 cm^{-1} from SRS hyperstacks.

The selectivity of the SRS-PCA approach was compared against direct SRS image intensities by measuring intensity profiles of the SRS-generated PC score projections through the intracellular cross section (Figure 7.6). Interpretation of intensity profiles generated from PCs 1-4 scores (Figure 7.6 D) confirmed the assignment of PC1's discrimination of cellular content from extracellular background. Its intensity profile (black, offset to simplify visualisation) represented a cumulative addition of PCs 2, 3 and 4 profiles; identifying combined protein, lipid and nucleic acid content respectively. Compared to intensity profiles of the directly observed vibrations (Figure 7.6 B), PC2-4 profiles show greatly increased exclusivity of intensity peak locations. While the total cell diameter could be estimated as 58 µm from all of the PC intensity profiles, only PC2 (blue) showed consistent elevation of intensity throughout the entire cell. This corresponds to its

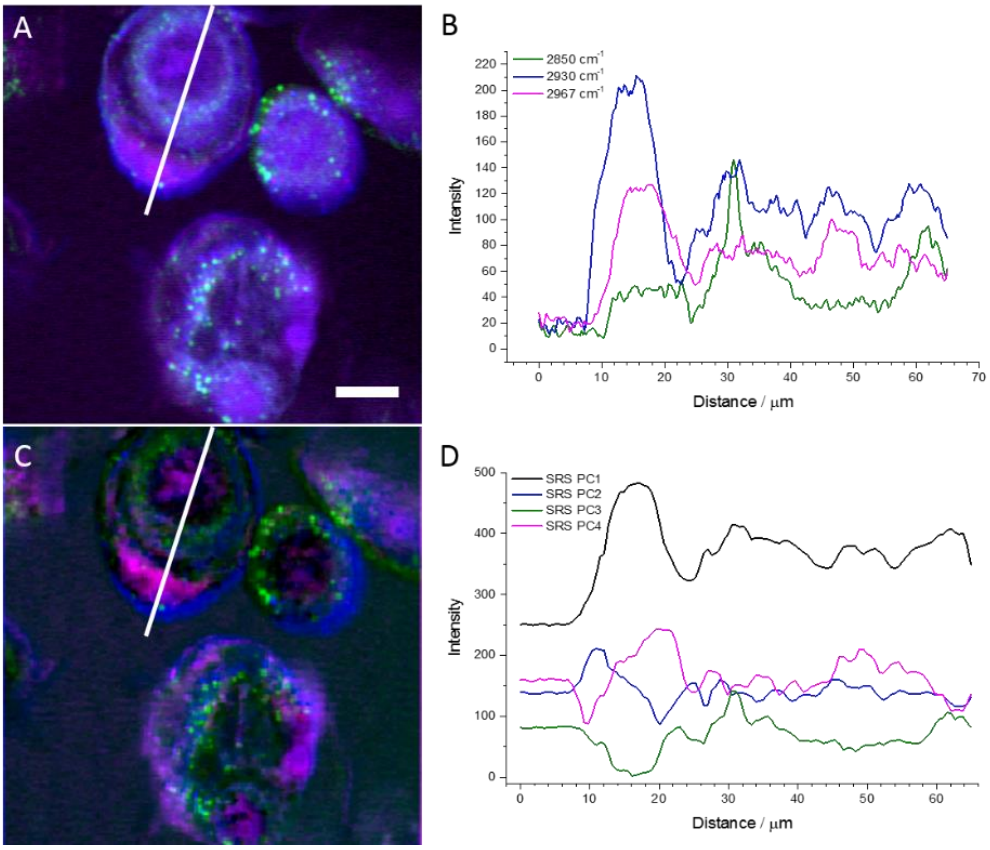

Figure 7.6 Comparison of relative biomolecular imaging selectivity observed by SRS hyperspectral microscopy (A-B) before and (C-D) following application of PCA. The intensity of (B) vibrational modes relating to lipid (2850 cm^{-1}, green), protein (2930 cm^{-1}, blue) and nucleic acid (2967 cm^{-1}, magenta) content was plotted through (A) a cellular cross-section. Principal components to which each characteristic biomolecular vibration most significantly contributed (PC2-4) had the intensity of their (C) projected scores (D) plotted along the same profile to reveal enhanced specificity of peaks relative to corresponding raw image intensities. The PC intensity profiles were stacked for visualisation of the PC1 profile's (black) accounting for of all intensity associated with PCs 2-4 projections and therefore combined cellular content. Scale bar = 10 μm.

predominant contribution from the 2930 cm^{-1} vibration of protein CH_2, with the consistent contrast across the cell supported by ubiquity of protein structures.

The large similarity of intensity profiles exhibited by direct detection of 2930 and 2967 cm^{-1} vibrational frequencies (Figure 7.6 B) was directly contradicted score intensity profiles of corresponding PCs 2 and 4 respectively (Figure 7.6 D, blue, magenta). Within plotted cytoplasmic regions (8-42 and 60-66 μm), the relationship between the PC2 and PC4 profiles was almost inverse, while similarity was evident (PC2 to a lesser extent than PC 4) within the cell nucleus (42-58 μm). The increased intensity of PC4 scores within the nucleus supports hypothesised chemical selectivity for nucleic acid content while protein content inferred by PC2 would also be present as nucleoli.

Inspection of overlaid PC 2-4 score projections (Figure 7.6 C) demonstrated a significantly decreased amount of spatial overlap between the PC scores than was observed for direct SRS peak intensities (Figure 7.6 A). This was particularly evident in PCs 2 and 4. Their loadings presented high exclusivity of intracellular features, while the SRS peaks of proteins 2930 cm^{-1} and nucleic acids 2967 cm^{-1} (holding greatest contribution to PC 2 and 4 respectively) showed strong spatial overlap. The isolation of nuclear features by PC4 scores is of particular interest, with DNA visualisation proving particularly difficult to achieve by vibrational microscopy (owing to weak intensity of its C-H vibrational mode and overlap with the 2930 cm^{-1} mode in proteins) and the vast library of DNA-targeting compounds used in drug discovery research. However, a region of strong PC4 intensity was also present within the cell cytoplasm.

Further experimentation is required to determine whether this result accurately reflected the chemical composition of the cell or the contrast was an artefact of spectral overlap between protein and nucleic acid vibrational modes (or corresponding PC loadings). In the latter case, experimental or statistical improvement of the developed platform would be required to increase the specificity of nucleic acid detection. In either case, presented results demonstrated a significant improvement of chemical selectivity for visualising lipids, protein and nucleic acids by hyperspectral SRS imaging following application of PCA. Back-projection of scores onto their spatial coordinates was demonstrated to achieve intracellular mapping of statistically-weighted chemical compositions with highly exclusivity of features.

The results presented within this study are consistent with findings of a recent study comparing CRI chemical selectivity in human tissue samples, wherein multivariate analysis was used to differentiate between glandular, muscular and adipose tissue rather than intracellular components[343]. The significantly increased selectivity of CARS microscopy towards imaging of lipid-rich structures is widely reported throughout the field[212,338,343] and remains the case following application of multivariate analysis to acquired hyperspectral images. Impediment in its selectivity for imaging biomolecules modes other than lipids is concluded, by both studies, to arise due to the non-specific, non-resonant background contributions that are inherent to the technique's scattering mechanism[338,343]. Meanwhile, SRS microscopy demonstrates enhanced chemical selectivity in direct peak intensities that was further improved by application of multivariate techniques in this study and in human tissue samples[343]. The predominant contribution arises from protein C-H vibrations but was clearly discernible from lipid structures by PCA, while some selectivity was also implied towards DNA imaging by the SRS-PCA platform. A major challenge associated with SRS microscopy was identified in its complexity to implement, requiring isolation of weak signals from laser noise. While this was achieved to perform hyperspectral imaging by measurement of SRL in the pump field, background noise was also detected that was not present in CARS microscopic images. This noise was primarily attributed to electrical noise from the laser and surrounding components, with example images provided in Appendix Section A.6. However, removal of such systematic background signal could be achieved by simple image processing steps.

Supported by the vast increase in numbers of recent publications, the ability of CRI microscopy to visualise both organelles and minimally-tagged exogenous molecules is of immense interest in drug discovery. CARS microscopy offers label-free investigation of lipid content with excellent sensitivity. An advantage of CARS, in the context of instrumentation used in this thesis, is its detection in epi-orientation, lending itself to higher throughput with the use of glass-bottomed microplates. Samples prepared for SRS investigation in this thesis required mounting between glass coverslips for forward detection, although epi-detected SRS can be performed. Beyond lipid imaging, SRS is presented as the CRI technique holding greatest chemical selectivity that can be improved by PCA. The selectivity affords a more diverse range of drug targets that can be visualised. Quantification is also more simply performed, owing to linear relationship of signal intensity to analyte concentrations. Development of statistical methods for quantitative extraction of chemical compositions remain of high interest. A recent publication has developed single valued decomposition analysis to account for factors such as sample movement during hyperspectral image acquisitions that could potentiate quantitative Raman imaging of live cell samples[344].

7.6 Conclusions

Research presented in this study has presented the relative ability of CRI techniques CARS and SRS to perform chemically-selective imaging of intracellular biomolecules on a home-built multiphoton microscope. Manually-collected hyperspectral image stacks of human breast cancer cells were collected in each modality, revealing increased sensitivity towards lipid structures in CARS microscopy that was otherwise inhibitory to selective detection of protein and nucleic acid content. SRS microscopy exhibited greater selectivity of direct peak intensities than CARS, which was furthered by PCA to produce strong separation of intracellular components that could potentiate selective DNA imaging. The significance of this study is in assessment of CRI modalities that could be developed into a versatile tool for label-free and high resolution visualisation of intracellular drug activity. With technological developments to improve hyperspectral CRI acquisition times and statistical improvements of methods for data extraction, great potential is held for weighted-statistical mapping of biomolecular compositions inside cells. Minimal sample preparation and simple translation into microplate-based systems can afford a high throughput and label-free imaging platform that is required in drug discovery.

Chapter 8 Conclusions and Future Perspectives

Throughout this thesis, the ability of enhanced-Raman scattering techniques to provide new insights into the intracellular dynamics of administered exogenous compounds have been investigated, towards developing Raman-based assays for use in pharmaceutical research. The techniques available offer two predominant avenues of experimentation: intracellular SERS using Raman signal enhancement by plasmonic nanosensors and non-invasive microscopy by CRI techniques CARS and SRS. Both approaches have been utilised in the presented research, identifying their relative strengths and weaknesses to inform development of an industry-relevant, label-free assay.

Investigation of reporter-free SERS capabilities was performed by developing an experimental platform that utilised 60 nm diameter gold nanospheres as intracellular probes for sensitive measurement of their biochemical environment. Incubation parameters were optimised with evaluation of AuNP exposure-induced stress to cells that resulted from applying unsuitable administration conditions. The increased sensitivity of SERS was demonstrated over traditional cell viability and ROS assays, with changes in acquired SERS spectra revealing molecular-level changes in intracellular environments related to cell stress events. The work contributes to the field of intracellular SERS by aiding fundamental (and still limited) understanding of how NP incubation can effect both uptake and the validity of SERS spectra acquired. The optimised platform was used to interrogate cellular endolysosomes for arrival of an administered exogenous molecule, in this case a commercial dye, achieving sensitive detection of its vibrational characteristics by pre-resident AuNPs upon its arrival into the target organelle. Multivariate technique PCA demonstrated increased platform selectivity for analyte detection and produced statistically-weighted maps of compound localisation at the subcellular level. Such mapping by purely spatial colocalisation of analyte to pre-resident nanosensors has not previously been performed using label-free SERS methodologies.

Research presented in the second half of this thesis used a purpose-built multiphoton microscope to visualise intracellular environments by label-free and chemically-selective coherent Raman imaging techniques CARS and SRS. Within the C-H stretching region (2700 – 3000 cm^{-1}) of the Raman spectrum, cell compositions were visualised by vibrational modes relating to lipid, protein and nucleic acid structures. CARS microscopy exhibited great selectivity for intracellular lipid content imaging, allowing observation of chemotherapy agent actions upon cytosolic lipid droplets following optimisation of minimally-perturbative live cell imaging conditions. The ability to monitor the response of dynamic organelles as potential drug targets without use of fluorescent tags presents a unique opportunity to drug discovery research. The capacity of CARS, in turn with other prevalent CRI technique SRS, microscopy to perform chemically-selective imaging of intracellular biomolecules beyond lipids was assessed through hyperspectral imaging of human breast cancer cells. The high selectivity and sensitivity of CARS towards imaging of lipid-rich intracellular structures was confirmed, while SRS demonstrated an enhanced ability for discrimination of protein and nucleic acid content that offers access to a greater range of drug targets for imaging. As with SERS, application of PCA to acquired hyperspectral images increased the specificity of detection by CRI and particularly SRS microscopy. Such analysis remains a powerful tool in extraction of useful information from the rich datasets produced in enhanced-Raman scattering experiments.

The significance of the research presented lies in informing the suitability of enhanced-Raman techniques for the specific purpose of monitoring intracellular drug dynamics. The performed studies showed the highly sensitive nature of SERS and that it can be exploited to produce vast datasets from which clinically-useful information can be extracted. This is a particularly important quality in modern pharmaceutical research with trends tending towards –omics studies, attempting to generate as much data as possible from minimal experimentation. In this capacity, the SERS-PCA methodology developed allows not only detection of exogenous molecules but changes in vibrational peaks associated with a range of drug targets can be observed to imply drug actions from the same experimental dataset. The ability to acquire subcellular maps allows discernment of analyte distributions in the case of administered compounds, or endogenous biomolecules, while spectral and spatial resolution is high owing to the narrow band width of Raman peaks and short-range of plasmonic enhancement. Strong enhancement of Raman signals increases biocompatibility for live cell analyses since low laser powers can be applied. The system is tailorable by tuning of NP parameters and surface functionalisation in order to achieve intracellular residency at desired organelle targets. Probing of suspected off-target intracellular sites of drug distribution would also be beneficial. Preparation of samples is relatively simple following system optimisation as AuNPs are voluntarily internalised into cells, while data acquisition is performed on commercially-available Raman microscopes that are already commonplace in pharmaceutical research labs. Therefore, accessibility remains an advantage of intracellular SERS experimentation. The development of novel AuNP-based drug delivery systems also presents an exciting opportunity for simultaneously increasing bioavailability of therapeutics.

However, predominant limitations of intracellular SERS exist in quantification of data and experimental timescales for use as an industrially-relevant assay. Once internalised into cells, control of AuNPs is lost which directly impacts enhancement of Raman signals. The ability to quantify drug distribution within cells by measuring concentrations would represent a huge breakthrough for pharmaceutical research in order to measure compound bioavailability at target organelle in assessment of efficacy. Development of novel nanostructures such as plasmonic nanostars and superstructures increases reproducibility of measurements by limiting aggregation of NPs designed with self-contained SERS hotspots. These structures represent an interesting avenue for developing the presented SERS-PCA methodology, in terms of providing reliable quantification as well as observing potential changes in intracellular localisation.

Targeting of SERS nanosensors to intracellular organelles beyond the endolysosomal pathway, for detecting a range of exogenous molecules should represent the primary aim for developing the presented SERS methodology. Experimental work should progress from establishing AuNP residency at targets, to detection of fluorescent and non-fluorescent molecules known to localise at the intended target before final proof of screening capability using unknown drug compound libraries. Due to the wide range of complex approaches undertaken in this thesis, this workflow could only be partially fulfilled in order to provide proof-of-concept and inform future, more rigorous development.

Experimental timescales are a limitation in the use of intracellular SERS, particularly relevant to the screening stages of this workflow. While long-term incubation periods have been shown to be required for high extents of AuNP internalisation, data acquisition times would be far more limiting to industrial research. Intracellular maps required acquisition times of approximately ten minutes to image single cells, representing a significant time requirement for generating clinically-relevant sizes of sample set. Sample size requirements are also increased by highly variable extents of AuNP uptake, demonstrated within this thesis, between cells within the same population. In terms of capacity for automation, the developed SERS methodology could be adapted for increased throughput by sample preparation within a glass-bottomed microplate format and use of an inverted microscope geometry. The requirement for high magnification mapping of intracellular details could be compensated for using automated stages and cell recognition algorithms to identify single cells for imaging rather than scanning across entire well areas.

In contrast, the short acquisition times possessed by CRI platforms are distinctly advantageous. Although applied laser power is high due to weaker enhancement, single-frequency frame images are acquired on the order of milliseconds and represent a 1000x increase in speed relative to the line-scanning Raman acquisitions used in SERS[336]. Additionally, removal of requirement to internalise inorganic matter into cells was a primary motivation for using CRI. This offered increased simplicity and speed of sample preparation while avoiding the NP-induced deviation from healthy cell models demonstrated in this thesis. In order to generate informationally-rich datasets, hyperspectral CRI can be performed to identify Raman modes of interest within samples and generate pixel-specific spectra for multivariate analysis of intracellular compositions.

In this thesis, hyperspectral imaging was performed by manually tuning excitation frequencies using an OPO that required several minutes between acquisitions, however systems that employ broadband excitation and CCD detection have been developed that overcome this limitation. CRI technologies therefore offer versatility to in characterise varying intracellular features as well as high-speed imaging at established single frequencies of interest. While the requirement for imaging with high laser powers produced a small degree of perturbation to repeatedly-imaged live cells, this is specific to the exact instrument used and not representative of all CRI microscopes that have demonstrated ability to perform long-duration experiments[345]. The varying strengths of CRI techniques CARS and SRS have been experimentally demonstrated within this thesis. CARS achieves high sensitivity and selectivity for lipid imaging that can be utilised to extract quantitative information about the dynamics of lipid-rich organelles following drug treatment such as increases in LD abundance. Such ability holds direct potential for efficacy assays whereby apoptosis is induced in cancer cells. Meanwhile, SRS microscopy benefits from increased chemical specificity (that can be enhanced using multivariate analysis) due to the absence of non-resonant background contributions that convolute CARS image intensities. The second major advantage held by SRS over CARS is the linear relationship between signal intensity and analyte concentration that offers a direct route toward quantitative mapping of intracellular distributions. As such, SRS presents an immensely powerful tool with clinical potential that is reflected by the large number of recent publications, including quantitative monitoring of tyrosine kinase inhibitor trapping within intracellular lysosomes[250]. Although not performed in repeatedly-imaged live cells, the study was in agreement with research performed in this thesis regarding utility of singly-imaged live cells at required time intervals. More significantly, the study demonstrates the most advanced application of enhanced Raman scattering technologies for visualising intracellular drug localisation measurements.

Development of CRI techniques for use in industrial research contexts suffer from an initial barrier of accessibility. Multiphoton microscopes are barely commercially available and required laser systems and optical components are hugely expensive. Aside from this factor, the low acquisition times of CRI microscopies present a reasonably direct route to industrial implementation. Within this thesis, CARS signal was detected in an epi-configuration that lends itself to automation of sample handling and use of glass-bottomed microplates. SRS was performed with forward detection, requiring close access of a condenser objective to samples mounted between glass coverslips and inhibiting adaptation to a plate formatted assay. However, epi-detection has been demonstrated for SRS, with SRL providing stronger epi-detected signal than SRG and recent application in performing highly sensitive differentiation between mesenchymal and pro-neural subtypes of glioblastoma[346,347]. A major advantage of CARS over SRS lies in its simplicity to implement, isolating anti-Stokes shifted signal with optical filters rather than employing photodiode detection which must be amplified above laser noise. The complexity of SRS implementation proved inhibitory to CRI study within this thesis and therefore demonstrates a significant barrier to overcome for production of a robust assay. An extension to the presented CRI studies exists in performing intracellular mapping of deuterated-drug isotopes by shifting of C-D vibrational modes into the 'Raman silent' region of the Raman spectrum. The development would enable simultaneous visualisation of drug localisation and effect upon targeted biomolecules without structural impediment of drug activity.

In conclusion, this thesis has demonstrated the capability of enhanced-Raman scattering technologies to perform highly-sensitive interrogation of the intracellular environment. SERS nanosensors can be administered to cancer cells for monitoring molecular-level changes at target organelles related to essential cell processes, or to confirm arrival of an administered exogenous compound and map its localisation. CRI techniques present high-speed visualisation of intracellular chemical compositions in a format that is more simply adapted to high throughput experimentation. CARS microscopy possesses high sensitivity and selectivity for imaging of intracellular lipid structure that can be used to extract quantitative measures of cellular responses to drug treatment, while the enhanced chemical specificity of SRS offers a more versatile tool for quantitatively imaging a broad range of intracellular structures and molecules within. In all cases, the application of multivariate analysis to Raman datasets proves to significantly improve chemical selectivity of experimental systems. Thus, with the aforementioned developments, enhanced-Raman scattering techniques presented within this thesis hold significant potential for sensitively measuring a diverse range of intracellular drug compound dynamics and actions as label-free and non-destructive alternatives to existing method

Appendix A Supplementary Information

A.1 Investigation of AuNP Internalisation by Brightfield Microscopy

A.1.1 Method

In order to establish the AuNP incubation times (a further parameter which must be carefully controlled for intracellular SERS experiments) used for research presented in this thesis, an AuNP concentration ($[\text{AuNP}]_{\text{Incub}}$ = 150 µM, 1.35 x10^{10} NPs mL^{-1}) was selected for administration to SH-SY5Y cells for incubation times of 6, 12, 24 and 48 h and within media containing 1, 5 or 10 % FBS. The concentration was selected as it is relatively high, in order to emphasise any changes in uptake observed as a result of the investigated variables. Control cells were incubated for the same durations in fresh DMEM containing the corresponding amount of FBS without AuNPs, with all cells at each time point fixed in tandem using paraformaldehyde (4 %, 12 mins) and stored in PBS at 5 ^{o}C. Brightfield images were acquired of each sample using a Nikon Eclipse Ti-E inverted microscope stand and a 40x (NA = 1.2) objective. NIS-Elements (Nikon) software was used to acquire images using a X-Y-Z automated stage and CCD camera.

Image analysis software FIJI was used to measure uptake by observing the percentage of the total cell area occupied by AuNP aggregates. Briefly, fields of view (FOVs) containing single or few cells (Figure 8.1 A, D) were selected from raw images to create cell area masks that were produced by manual outlining of the total cell contour (Figure 8.1 B, E). A mask of the cell contour was applied to inverted copy of the original image and a minimum threshold was applied to filter out all intensity except that arising from cellular AuNP aggregates, appearing as dark regions in the original images (and therefore possessing highest intensity following inversion). The thresholded AuNP signal was turned into a binary image (Figure 8.1 C, F), with the total area of intensity constrained within the cell contour being measured to give the % cell area occupied. A total of 306 cell FOVs were analysed across all treatments and over two repeats. Significance testing was performed using one-way ANOVA and Tukey means comparison testing in Origin 2016 software on the generated dataset in order compare the treatments.

A.1.2 Results

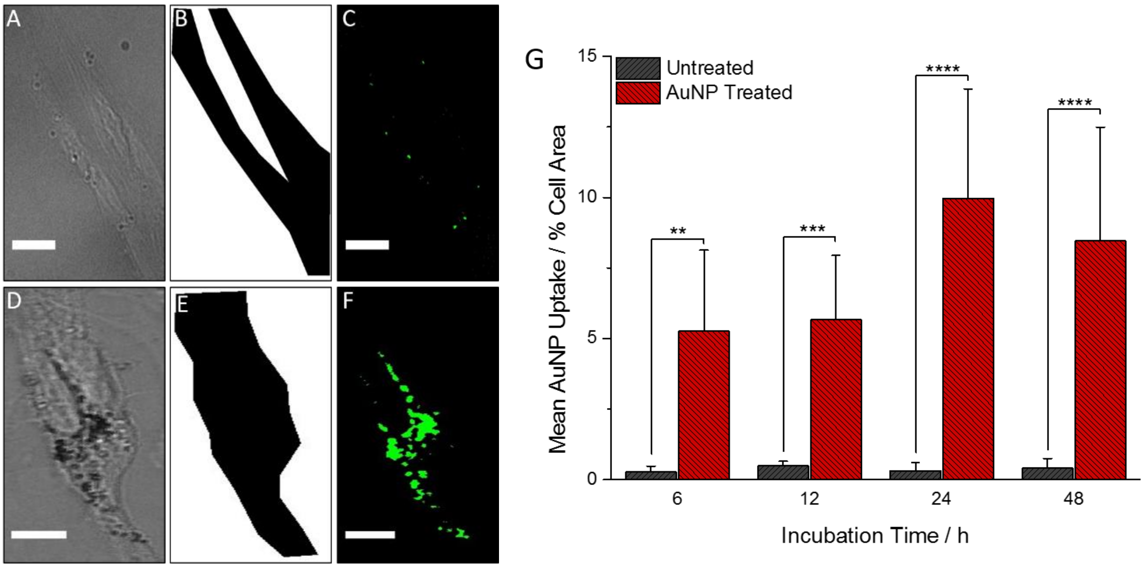

Figure 8.1 Image analysis of brightfield images taken from either (A) control or (B) AuNP-treated SH-SY5Y cells measured the percentage of (B, E) cell areas occupied by (C, F) AuNP aggregates within the defined cell area in order to (G) estimate the extent of AuNP internalisation following incubation durations of 6, 12, 24 and 48 h. Example presented $[AuNPs]_{Incub}$ = 150 µM (1.5 x 10 ^{10} NPs mL^{-1}) in 5 % FBS-DMEM. Scale bar = 10 µm

Full tabulation of the AuNP residency measured within each treatment class is presented in Table 8.1. The total area of signal arising from AuNPs was significantly higher in AuNP-treated cells than the untreated control cells, as demonstrated in cells treated with AuNPs in 5 % FBS-media, in NP mask images (Figure 8.1). Tukey means comparison testing of the detected 'AuNP' signal areas between untreated and AuNP-treated cells was significant to at least $P \leq 0.01$ for all incubation times and was significant to $P \leq 0.0001$ after 24 and 48 h incubation times. A small amount of intensity remained in the control treatment images, resulting from the darkest portion of image shadows that couldn't be removed by thresholding without losing areas of AuNP intensity. As a consequence, the uptake figures were produced by subtracting the overall mean of these false-positive areas (arising from control cells) from every AuNP-treated cell measurement. This method provided a valid background subtraction as no significant difference in false-positive AuNP uptake was observed between any of the investigated time points.

Analysis of the AuNP-treated cells revealed that the largest extent of AuNP uptake under the investigated conditions was achieved after 24 h under all media-serum compositions, with 20.16 (± 7.65), 9.97 (± 3.88) and 8.08 (± 4.48) % occupancy of cell areas by AuNP aggregates for 1, 5 and 10 % FBS compositions respectively (Figure 8.2). Uptake was decreased after 48 h incubation in all

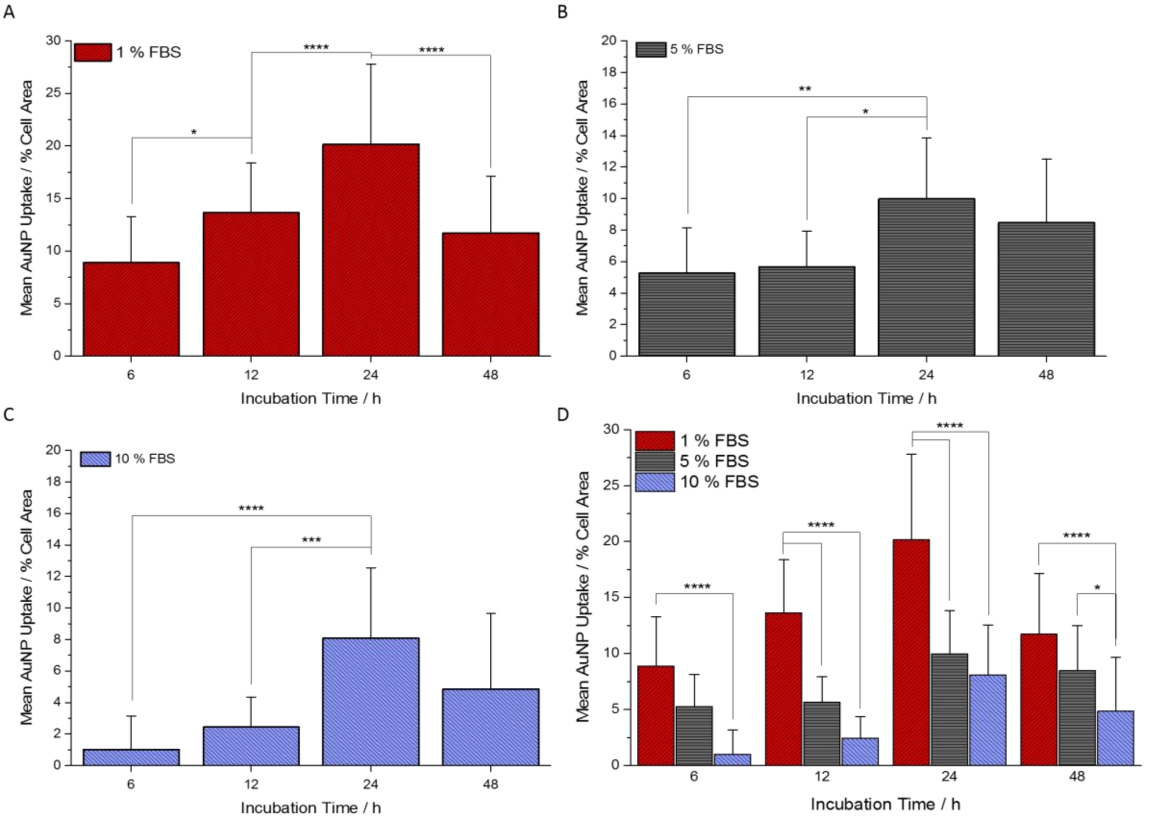

Figure 8.2 Extents of AuNP uptake, observed as % cell area occupied, following incubation of SH-SY5Y cells with AuNPs in media containing (A) 1 %, (B) 5 % and (C) 10 % (v/v) FBS for durations of 6, 12, 24 and 48 h.

cases, suggesting that the rate of NP endocytosis could have become outweighed by the rate of exocytosis of earlier-internalised particles. This decrease was only observed to be statistically significant under 1 % FBS incubation conditions (Figure 8.2 A), which was also the only class in which 12 h incubation time yielded a higher cellular NP content (13.66 ± 4.72 %) than the decreased 48 h time point (11.73 ± 5.41 %). Treatments in 5 and 10 % FBS media (Figure 8.2 B-C) demonstrated small increases in uptake between 6 and 12 h durations, followed by sharper increase at 24 h before the described saturation and decline to an insignificantly ($P \geq 0.05$) decreased value at 48 h. The shift in this trend that was observed within 1 % media-FBS composition may suggest that either the lower availability of proteins for maintaining cell homeostasis or that thinner/deficient protein coronas cause cell damage that increases NP permeability to cells AuNP for faster uptake into and removal from cells. Similarly, the extent of AuNP uptake was observed to be greatest in 1 % FBS treatments at all time points and was significantly greater ($P \leq 0.0001$) than the corresponding measurements from cells incubated with NPs in 10 % FBS-media. The overall trend demonstrated between media-serum compositions showed incremental increase in extent of intracellular AuNP residency with decreasing media-content. Incubation within 5% FBS-media resulted in intermediate uptake between 1 and 10 %

Table 8.1 Mean values and standard deviations of the percentage of cell areas occupied by AuNPs following co-incubation for durations of 6, 12, 24 and 48 h generated from analysis of 308 brightfield images of cells to estimate the dependence of AuNP uptake on incubation time and media-serum composition.

Incubation Time / h	Media FBS Content / %	Mean AuNP Uptake / % Cell Area
5	1	8.89 (±4.38)
5	5	5.27 (±2.87)
5	10	1.02 (±2.14)
12	1	13.66 (±4.72)
12	5	5.66 (±2.28)
12	10	2.44 (±1.92)
24	1	20.16 (±7.65)
24	5	9.97 (±3.88)
24	10	8.08 (±4.48)
48	1	11.73 (±5.41)
48	5	8.47 (±4.02)
48	10	4.85 (±4.81)

treatments for all incubation times that was significantly decreased ($P \leq 0.0001$) from only 1 % levels (bearing resemblance to 10 % levels of uptake) after 12 and 24 h durations, yet significantly ($P \leq 0.05$) increased uptake from the 10 % treatment class (resemblance to 1 % treatments) only after 48 h. This may reflect either greater retention of NPs within cells after 24 h in 5 % media-serum conditions or simply the slower rate of uptake with increased media-serum that was proposed following observation of the high early-duration values observed in 1 % FBS.

Therefore, this image analysis technique has provided an indication that both incubation time and FBS composition of the AuNP incubation media play significant roles in mediating the rate of cellular internalisation. The method however contains limitations. The large standard deviation about the means of each AuNP-treated class compared to control cells imply that the uptake of AuNPs was far from homogeneous throughout cell populations. A source of error also exists in the two-dimensional nature of the brightfield imaging for monitoring AuNP uptake. AuNPs and their aggregates appear in the image when out of focus, meaning that NPs that are possibly adhered to the top or bottom of the cells are counted as being internalised as long as they exist within the lateral dimensions of the cell area. This is explained by the use of a non-confocal microscope, allowing out-of-focus projects onto the two-dimensional image plane. It must also be emphasised that the finding is only relevant for the incubation parameters used (SH-SY5Y cell line, 60 nm diameter, spherical NPs) and is subject to change following alteration of any of the factors discussed within the literature review portions of this thesis.

The generated results however offer utility in guiding AuNP incubation parameters used in this thesis for more rigorous investigation. The stark differences in uptake behaviour observed between 1 and 10 % media compositions were chosen for investigation in Chapter 4, which also adopted the 24 h incubation time that was demonstrated to achieve the highest extent of AuNP internalisation. Within the chapter, further investigation into extents of uptake is offered in greater detail using both confocal fluorescence/scattering microscopy to visualise the 3D distribution of AuNPs around and within cell contours and ICP-MS in order to provide quantitative measures of intracellular AuNP residency. The intermediate nature of intracellular NP levels observed under 5 % FBS conditions were employed in Chapter 5, providing a balance between extent of uptake and increased biocompatibility of higher-serum incubation conditions proposed in the previous chapter. The intermediate media-serum composition also presented the smallest decline in intracellular NP residency (by %) between the 24 and 48 h incubations, proving advantageous in a study utilising the 48 h incubation-duration in order to maximise opportunity for achieving analyte detection within matured endolysosomes. The easily-performed tailoring of such incubation parameters in order to suit differing experimental requirements reflects the flexible nature of the intracellular-SERS platform and thus it’s potential for ubiquitous use in a multitude of cellular assay systems.

A.2 Observation of AuNP Internalisation by TEM

Studies presented in Chapter 4 and Chapter 5 of this thesis rely upon internalisation of AuNPs into SH-SY5Y cells, achieved by establishment of incubation parameters including AuNP dose, $[\text{AuNPs}]_{\text{Incub}}$, and FBS content of incubation media. In support of both the methods and results presented by intracellular SERS studies in this thesis, TEM investigation was performed on SH-SY5Y cells following their incubation with AuNPs at two different $[\text{AuNPs}]_{\text{Incub}}$ (representing high and low doses) and media-FBS compositions (1, 5, 10 %). Relevant contributions to each study are discussed both in this section and the respective chapter's discussion.

A.2.1 Sample Preparation

Human neuroblastoma cell line SH-SY5Y was cultured in DMEM containing foetal bovine serum (FBS, 10 %) and penicillin-streptomycin supplement (Pen-strep, 1 %). Cells were passaged every 4 days and regularly checked for mycoplasma infection. Cells were seeded into 6-well plates at a density of 25000 cells per well and left for 24 h to allow cell attachment and growth. After this period, cells were washed before morphological differentiation was induced in the cells by 72 h incubation in reduced-serum DMEM (1 % FBS, 1 % Pen-strep). After differentiation of cells, spherical gold nanoparticle (AuNPs, 60 nm diameter, BBI International) stocks were washed in phosphate buffered saline (PBS) solution before resuspension in DMEM of varying FBS content (1, 5 or 10 %) at two different incubation concentrations (10, 150 µM or 9 $\times 10^8$, 13.5 $\times 10^9$ NPs mL^{-1}). The incubation was performed for 48 h. Upon completion of NP incubation, wells were washed twice in PBS before individual collection by trypsinisation and pelleting by centrifugation. Fixation was performed in glutaraldehyde.

Samples were transported to the Biomedical Imaging Unit (BIU) at Southampton University Hospital for processing and imaging, performed by BIU staff and not the candidate*.

A.2.2 Results

TEM images acquired of exemplar whole cells (Figure 8.3) provide insights into overall cell health, extent and localisation of intracellular AuNPs following the different incubation conditions. Internalised AuNPs are visualised as black spots within the cell contour of each images. Cells were generally demonstrated to possess healthy morphologies, with intact cell outer and nuclear membranes discernible in all cells except for that treated with 150 µM AuNPs in 1 % FBS media (Figure 8.3 B). This case represented the most forcing of conditions and appeared to induce cell

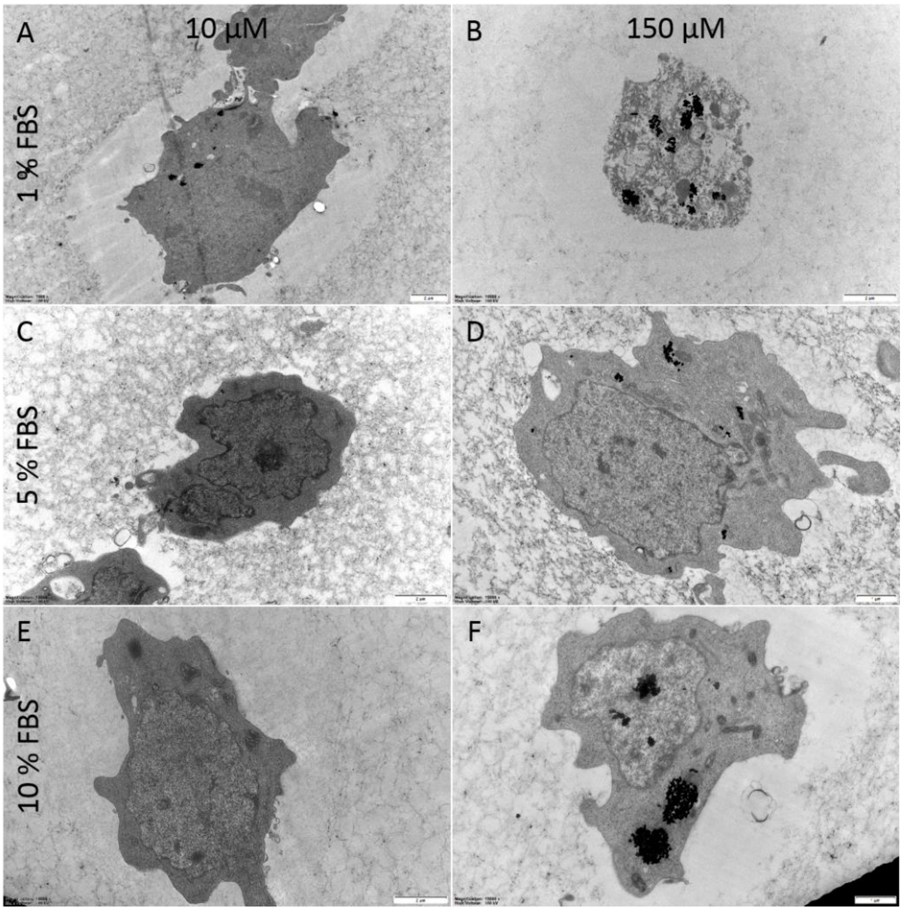

Figure 8.3 Observation of AuNPs internalised into whole, single SH-SY5Y cells following incubation at doses $[\mathrm{AuNPs}]_{\mathrm{Incub}}$ = (A, C, E) 10 and (B, D, F) 150 µM within culture medium containing (A, B) 1 %, (C, D) 5 % and (E, F) 10 % FBS. Scale bar (A-C, E, F) = 2 µm, (D) = 1 µm.

damage as evidenced by cytoplasmic vacuolisation, rupturing of vesicle membranes and lack of a discernible nucleus. The damage was accompanied by high uptake of AuNPs, suggesting that the low serum availability was either insufficient to provide biocompatible protein corona coatings to the high number of AuNPs or supply the cells with nutrients to accommodate the large-scale uptake of inorganic matter. A trend of increased AuNP uptake with increased $[\mathrm{AuNPs}]_{\mathrm{Incub}}$ was observed between 10 µM (Figure 8.3 A, C, E) and 150 µM (B, D, F) for all FBS compositions. Similarly, the extent of uptake appeared to increase with reduction of media-serum compositions from 10 % (Figure 8.3 E, F) to 5 % (C, D) and again to 1 % (A, B) FBS compositions. A striking contrast was observed between cells treated with 10 and 150 µM AuNPs in 10 % FBS (Figure 8.3 E and F respectively), with no significant internalisation observed in the low dosed cell compared to high uptake following dose increase. In all treatment cases, AuNPs were visualised to be entrapped within multiple membrane-bound cytosolic vesicles. Therefore, the employed AuNP incubation parameters were confirmed to allow uptake of the nanosensors into SH-SY5Y cells for performance of SERS measurements. The only exception arose in treatment by $[\mathrm{AuNPs}]_{\mathrm{Incb}}$ = 150

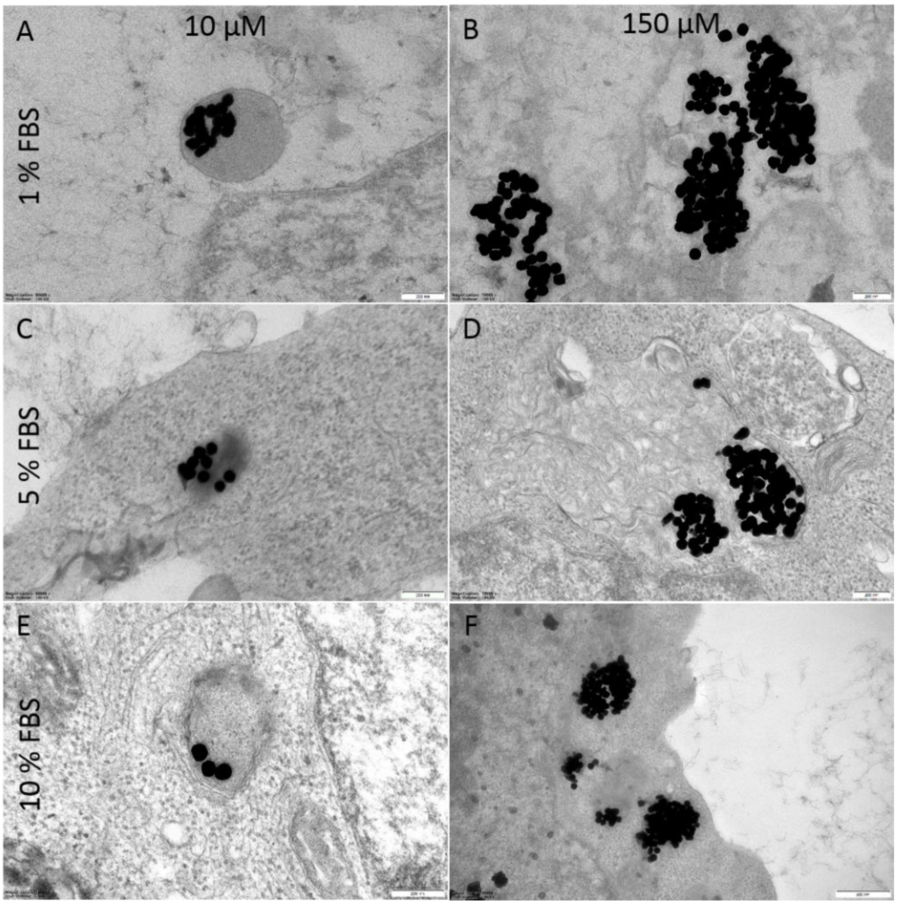

Figure 8.4 High magnification TEM micrographs of AuNPs (black spots) internalised into SH-SY5Y cells transport vesicles following incubation at doses $[\text{AuNPs}]_{\text{Incub}}$ = (A, C, E) 10 and (B, D, F) 150 µM within culture medium containing (A, B) 1 %, (C, D) 5 % and (E, F) 10 % FBS. Scale bar (A-E) = 200 nm, (F) = 600 µm.

µM within 10 % FBS media (Figure 8.3 F), which presented an accumulation of AuNPs either within or above the nuclear region of the image.

Closer inspection of high magnification TEM images (Figure 8.4) provided insights into the relative abundance, encapsulation and aggregation state of administered AuNPs. The images show clear entrapment of internalised AuNPs within membrane-bound vesicles in all cases, with relative degrees of uptake inferred by the number of individual AuNPs contained per vesicle. Once more, the trends of increased AuNP uptake with increased dose and decreased FBS content of media were presented. Under 10 µM incubations, the number of NPs trapped in endolysosomes was low, varying between around 20 to just 3 for 1 and 10 % FBS treatments (Figure 8.4 A and E) respectively. A similar trend was observed within 150 µM doses, with 5 % FBS media compositions presenting an intermediate extent of uptake. In agreement with Figure 8.3 E, AuNP uptake was extremely limited following incubation with 10 µM AuNPs in 10 % FBS media.

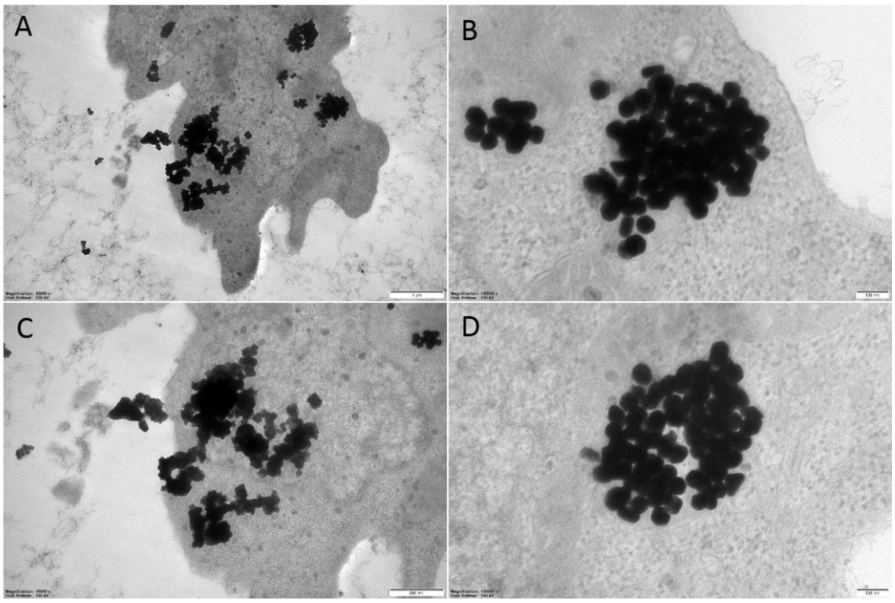

Figure 8.5 TEM images depicting the variable nature of internalisation observed following incubation of SH-SY5Y cells with dose of $[\mathrm{AuNPs}]_{\mathrm{Incub}}$ = 150 µM in 10 % FBS-media. An exemplar (A) whole cell image presented separate regions of AuNPs (B, D) enclosed within endosomal vesicles and (C) above the focal plane of both the cell nucleus and extracellular space. Scale bars (A) = 1 µm; (C) = 300 nm; (B, D) = 100 nm.

Closer investigation of the noted variability in AuNP localisation within cells treated with 150 µM AuNPs in 10 % FBS media was performed. Figure 8.5 demonstrates that while a high number of spherical, monodisperse AuNPs were located within endolysosomes (B, D), showing agreement with the distribution achieved in other treatments groups, other AuNPs appeared in irregular, aggregated formations that were located above the focal plane of the cell. Combined with the fact that the appearance of these NP aggregates were similar irrespective of location above the cell nucleus or extracellular space, it was concluded that these AuNPs were not internalised and may have been simply adhered to the cell outer membranes. This conclusion also supported by aggregation of 60 nm AuNPs following suspension in 10 % FBS-DMEM that was detected by absorbance measurements in Section 3.4.1. While further experimentation would be required to confirm that this aggregation prevented any cellular internalisation, the case is presented that SERS measurements performed using high AuNP doses and FBS-media compositions must be carefully acquired to ensure that spectra were acquired from only internalised AuNPs.

In the case of simple, spherical AuNPs, without use of novel morphologies or substructures to produce self-contained plasmonic hotspots, close localisation with an abundance of neighbouring NPs is required for significant SERS enhancement of signals intracellular signals. Therefore, selection of AuNP administration parameters resulting in high extent of uptake is essential, without causing disruption to the natural balance of cell homeostatic pathways. The significance of the performed TEM experiments is in validation of both the methods and conclusions drawn from intracellular SERS studies presented in Chapter 4 and Chapter 5 of this thesis. Despite the use of 48 h incubation durations instead of the 24 h employed in Chapter 4, the trends of increased AuNP uptake with increased doses and decreased media-FBS levels were corroborated. This was particularly pertinent in highlighting the cell damage induced by incubation of high ($\geq$ 100 µM) $[\text{AuNPs}]_{\text{Incub}}$ doses within media containing 1 % FBS. Similarly, evidence is presented to support the very low uptake of AuNPs observed under 10 µM dose in 10 % FBS media, from which sufficiently-large and reliable SERS enhancements could not be generated for the presented analysis. Meanwhile, AuNP incubation parameters ($[\text{AuNPs}]_{\text{Incub}}$ = 150 µM, 5 % FBS-media, 48 h duration) matched exactly those utilised in Chapter 5, thus confirming that the conditions achieved intracellular AuNP residence within cell endolysosomal vesicles and validating the established methodology. The abundant number of NPs closely-packed into the vesicles were therefore able to generate significant plasmonic hotspots for sensitive detection of LysoTracker Red molecule’s arrival at its intracellular target.

A.3 Optimisation of Laser Powers for Time Course Imaging of Live Cells by CARS

Section 6.5.1 presents CARS microscopy of cytosolic lipids (CH_2 stretch, 2850 cm^{-1}) in live cells following repeated imaging over a 48 h duration and under incrementally decreasing laser powers. Further to Figure 6.4, the full image sequence of presented cell FOVs are presented below following imaging with laser powers of 100/75 (Pump/Stokes) mW (Figure 8.6), 60/40 mW (Figure 8.7) and 50/30 mW (Figure 8.8).

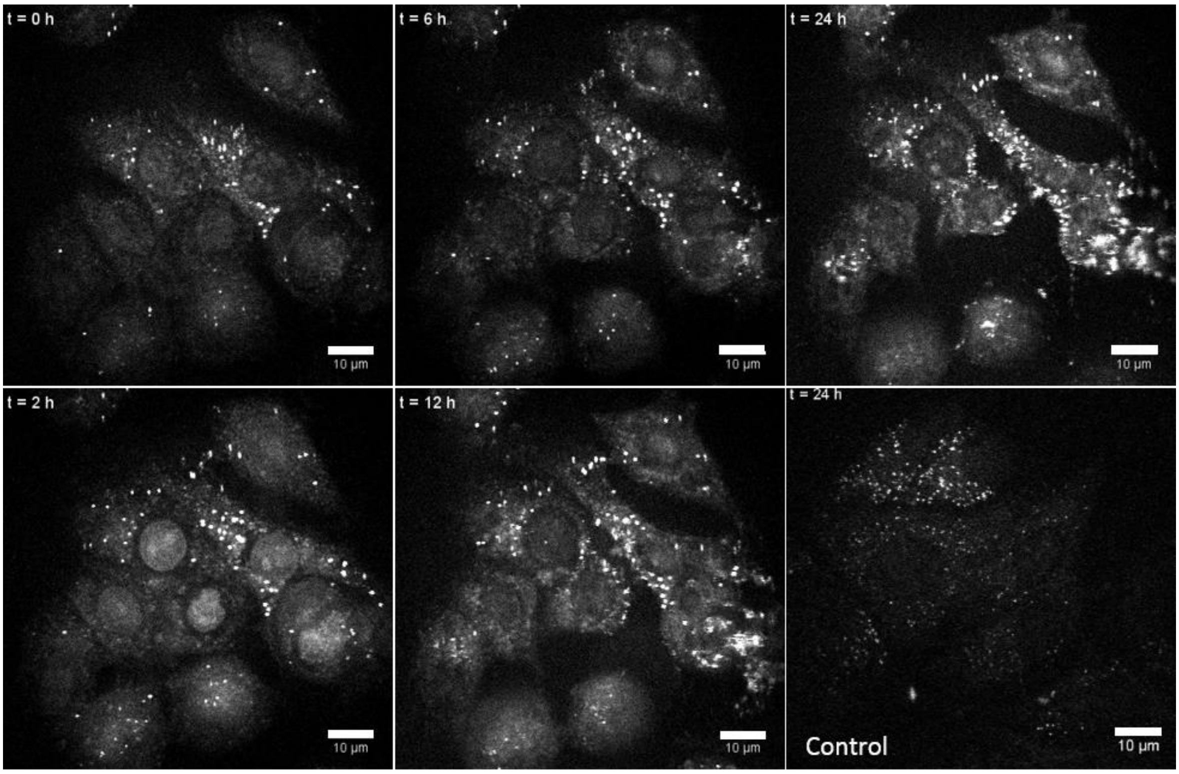

Figure 8.6 CARS microscopy of intracellular lipid content (2850 cm^{-1}) in live MCF-7 cells by repeated exposure to laser power of 100/75 mW at time intervals of 0, 2, 6, 12, 24 h. Burning of the repeatedly imaged cell FOVs was evidenced after 24 h (intensely bright and blurred signal, top right panel) that was shown to be a result of repeated laser exposure by imaging of previously unexposed control cells (lower right panel) within the same sample and at the same incubation time. Scale bar = 10 µm.

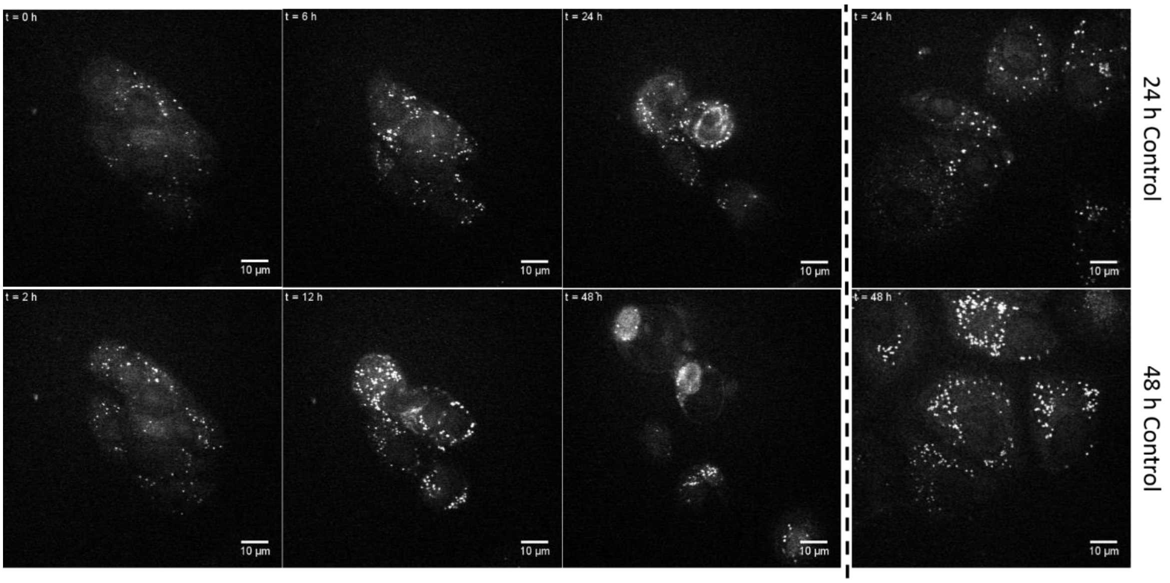

Figure 8.7 CARS microscopy of intracellular lipid content (2850 cm^{-1}) in live MCF-7 cells by repeated exposure to laser power of 60/40 mW at time intervals of 0, 2, 6, 12, 24 and 48 h. While no sample burn was observed, deterioration of repeatedly-imaged cell FOVs was evidenced throughout the experiment’s progression (shrinking and rounding of cell area, increased LD abundance) until cells appeared to be in late-stage apoptosis at t= 48 h. Visualisation of separate control cell FOVs at intervals t = 24 and 48 h displayed absence of these phenotypes, confirming that cell damage had been induced as a result of repeated laser exposure. Scale bar = 10 µm.

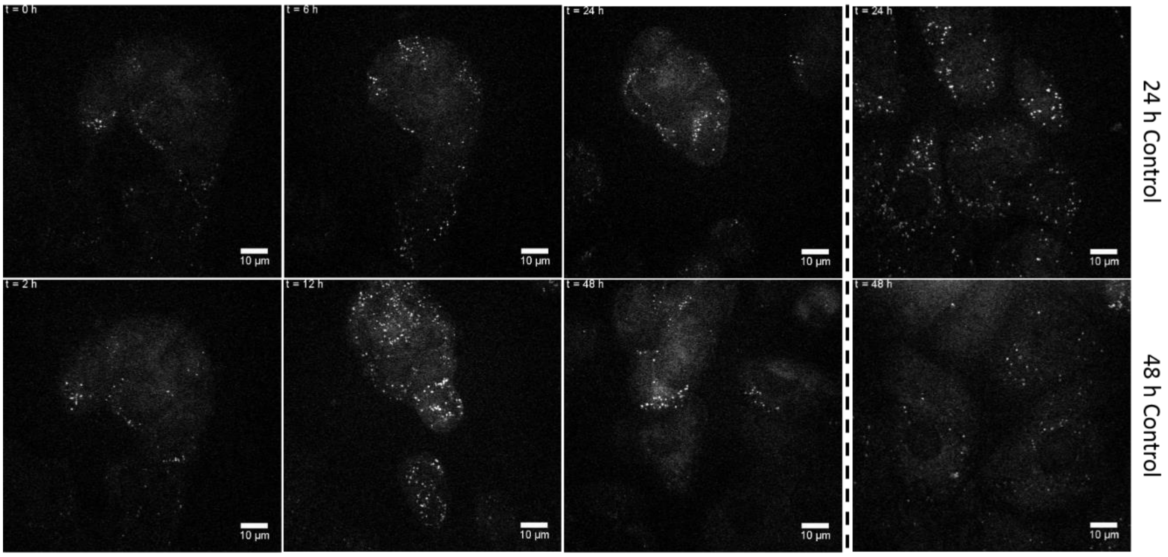

Figure 8.8 CARS microscopy of intracellular lipid content (2850 cm^{-1}) in live MCF-7 cells by repeated exposure to laser power of 50/30 mW at time intervals of 0, 2, 6, 12, 24 and 48 h. At the established-minimum laser powers required for sufficient optical contrast, the progression of cells throughout the time course demonstrated minimal effect of cell damage following repeated imaging. Initial cell shrinking during short time interval imaging (2-12 h) was alleviated by t = 24 h, suggesting cellular recovery and expansion of cell areas at t = 48 h. Comparison to previously unexposed control cells at intervals t = 24 and 48 h showed significantly reduced cell damage resulting from repeated laser exposure compared to experiments performed at higher power. Scale bar = 10 µm.

A.4 Cell Damage Mechanisms Observed by CARS Microscopy

CARS microscopy of intracellular lipids (2850 cm^{-1}) following exposure to live MCF-7 cells to chemotherapy agent carboplatin (Section 6.5.2) revealed contrasting mechanisms of cytosolic lipid droplet distribution and cell damage between cells that were either repeatedly or singly exposed to laser irradiation for imaging. The different mechanisms of cell response observed are presented in Figure 8.9. As described in the main text, progression of damage in repeatedly images cells (A-D) was typified by contraction and rounding of the cell morphology, accompanied by reduction of cell-cell contact, disappearance of a discernible nuclear envelope and generally increased CARS intensity throughout the cytosol. Images of singly-exposed cells (E-I) are taken from different time intervals and FOVs but demonstrate how the process of drug-induced apoptosis may appear as visualised by CARS microscopy. Cells exhibit an increased abundance of cytosolic LDs (an early-stage marker upon which the CARS assay was designed, E), with cytosolic contraction and commencement of vacuolisation (F-H) before cell death and formation of apoptotic bodies (I). All images were acquired in the presence of carboplatin, suggesting that the difference in the damage mechanisms observed was caused by laser-induced damage to repeatedly imaged cells that overpowered detection of drug-induced changes to LD abundances.

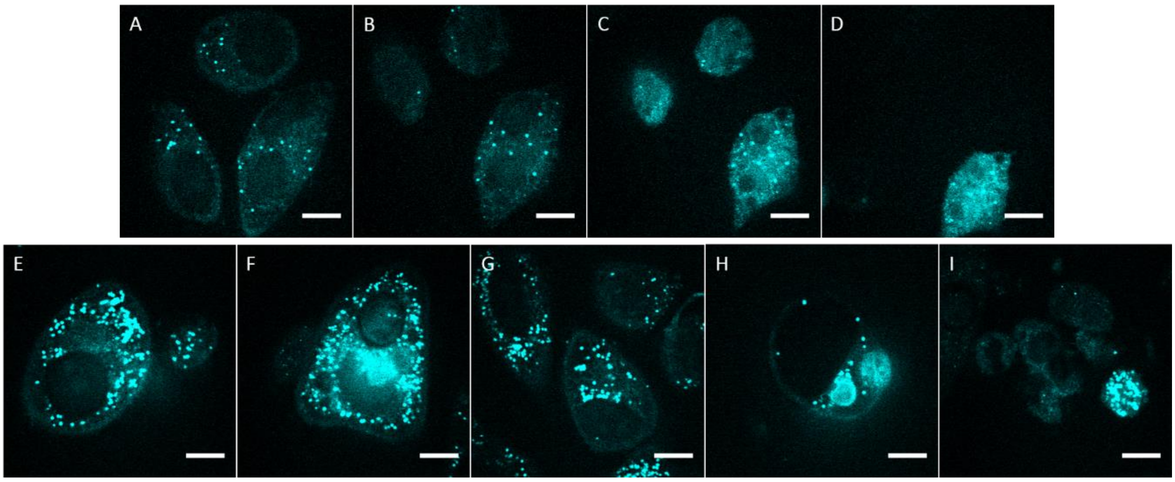

Figure 8.9 Progression of cell damage (left to right) observed in CARS microscopy of live MCF-7 cell lipids (2850 cm^{-1}) in the presence of carboplatin. Cells that were repeatedly exposed to laser irradiation for imaging (A-D) showed significantly different morphological changes than those (E-I) singly-exposed for imaging only at an individual time interval. The progression of damage in singly exposed cells is only implied as images are taken from different intervals and FOVs. Scale bar = 15 µm.

A.5 Intracellular Hyperspectral Image Scans by CRI

In order to optimise CRI platforms used in Chapter 6 and Chapter 7, determination of vibrational frequencies giving rise to strongest signal intensities was required to perform chemically-selective imaging of selected vibrational modes. To achieve this in cell samples, images were acquired at small intervals in excitation frequency (by tuning of Pump beam frequency) across the C-H region of MCF-7 cells' Raman spectrum. Resultant hyperspectral image stacks were generated in both CARS (Supplementary Figure 8.10) and SRS (Supplementary Figure 8.11) modalities in order to highlight differences in intensity between images acquired either off or on resonance with C-H vibrational modes in the sample.

Both microscopic techniques showed no signal in the intensity range 20-255 (8 bit image depth) at the Raman-silent frequency of 2700 cm^{-1}. Within the region 2840-3000 cm^{-1}, CARS images (Supplementary Figure 8.10) exhibited strong intensity at wavenumbers associated with lipid C-H vibrations at 2840, 2850 and 2860 cm^{-1}. At higher wavenumbers, image intensities then drop until the region 2930-50 cm^{-1}, in which slight increase of intensity around intracellular protein structures becomes apparent. At highest wavenumbers 2980-300 cm^{-1}, intracellular CARS intensity is weak and tends towards being lower than the extracellular background. SRS images (Supplementary Figure 8.11) demonstrated lower background intensities throughout the scanned images, with selectivity for lipid and protein structures in regions 2840-60 cm^{-1} and 2930-50 cm^{-1} respectively. Additionally, some increase in intensity was detected at 2967 cm^{-1} from internuclear regions of imaged cells that could be attributable to DNA structure. The image stack also revealed greater differences in spatial distribution of intensity between images acquired at vibrational frequencies relating to lipid and protein CH modes relative to CARS images. The wavelength scans in both CARS and SRS microscopy produced very low signal intensities at the maximum wavenumber of 3000 cm^{-1}, representing the upper limit of the C-H region of the cellular Raman spectrum.

The displayed hyperspectral scans were utilised in Chapter 7 to assess the impact of performing multivariate technique PCA on chemical selectivity between the imaging platforms.

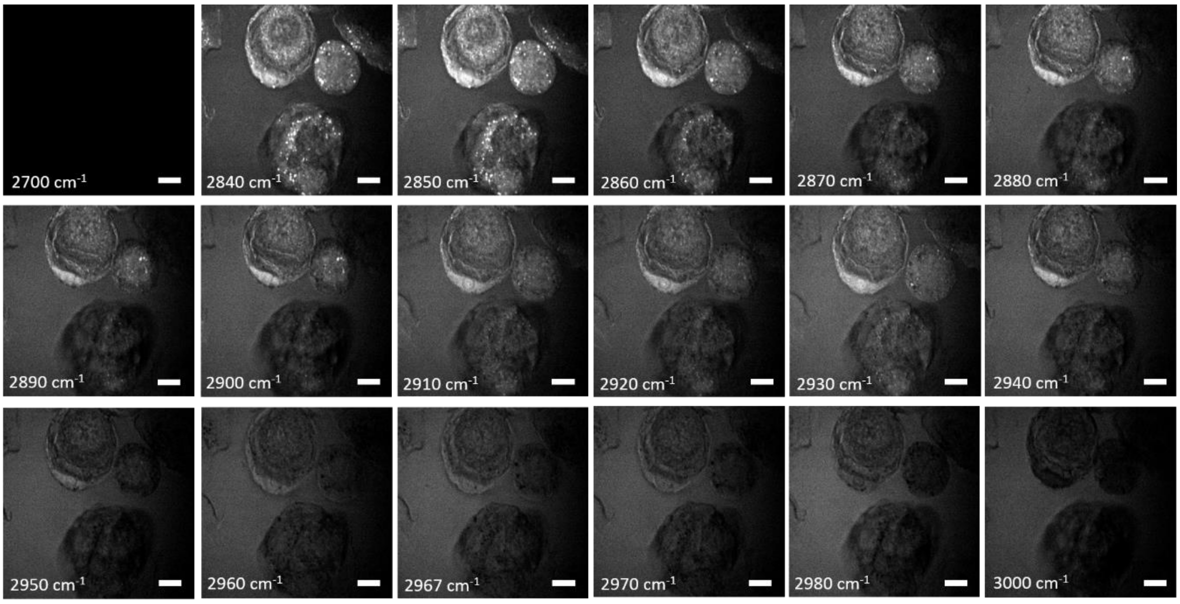

Figure 8.10 Hyperspectral image stack of MCF-7 cells by CARS microscopy, produced by scanning excitation frequencies to target C-H vibrational modes in the region 2700-3000 cm^{-1}. Laser powers of 40 and 20 mW were used for Pump and Stokes beam respectively, as measured at the sample. Scale bar = 10 µm.

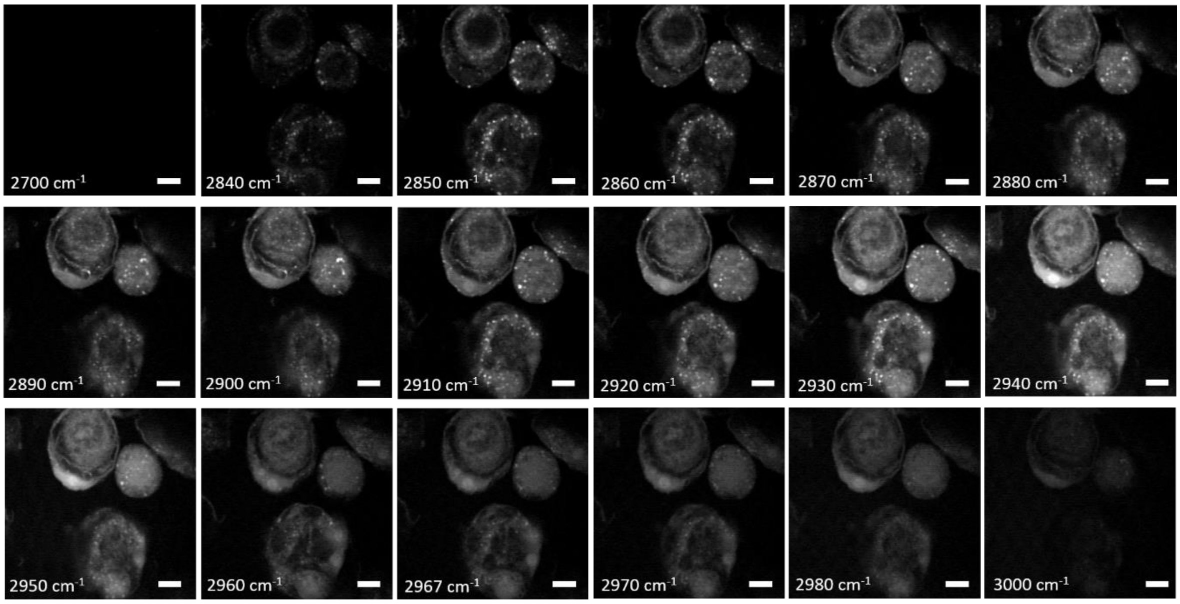

Figure 8.11 Hyperspectral image stack of MCF-7 cells by SRS (SRL) microscopy, produced by scanning excitation frequencies to target C-H vibrational modes in the region 2700-3000 cm^{-1}. Laser powers of 30 and 30 mW were used for Pump and Stokes beam respectively, as measured at the sample. Scale bar = 10 µm.

A.6 Noise Detection in SRS Microscopy

One of the largest challenges to overcome in performing intracellular CRI by SRS microscopy lies in its complexity to implement experimentally. While hyperspectral imaging was successfully performed in Chapter 7, the difficulty of isolating generated signal (SRL in this thesis) from background noise was experienced in the study. Figure 8.12 demonstrates the manifestation of background noise intensities detected in acquired SRS (SRL) images that was not observed by CARS microscopy. During optimal system performance removal of the presented background noise could be achieved by simple application of minimum intensity thresholds and smoothing steps during image processing.

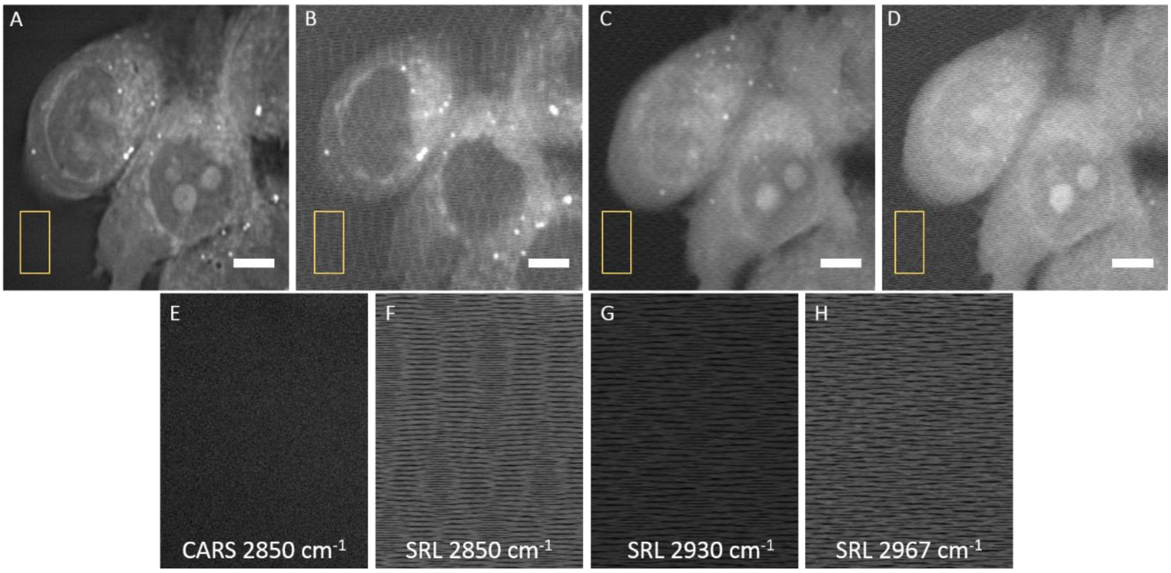

Figure 8.12 Comparison of background signals generated by (A, F) CARS and (B-D, F-H) the implemented SRL microscopy in (A-D) imaging of human breast cancer cells. ROI insets (E-H) demonstrate (F-H) the manifestation of irregularly-patterned background intensities in SRS images compared to (E) absence in the CARS (2850 cm^{-1}) modality. The noise detected by SRS microscopy varied with the vibrational frequency probed. Scale bar = 5 µm.

A.7 Higher Order PCA Outputs from Hyperspectral CRI

In Chapter 7, multivariate technique PCA was performed upon hyperspectral image stacks of human breast cancer cell line MCF-7 acquired by both CARS and SRS microscopic methods. A total of 6 PCs were calculated for each datasets, with outputs of PCs 1-4 presented and analysed in the main chapter text. PCs 5 and 6 accounted for 1 % or less of the total variance within both technique datasets (Table 8.2), with loadings and corresponding scores presented below (Figure 8.13).

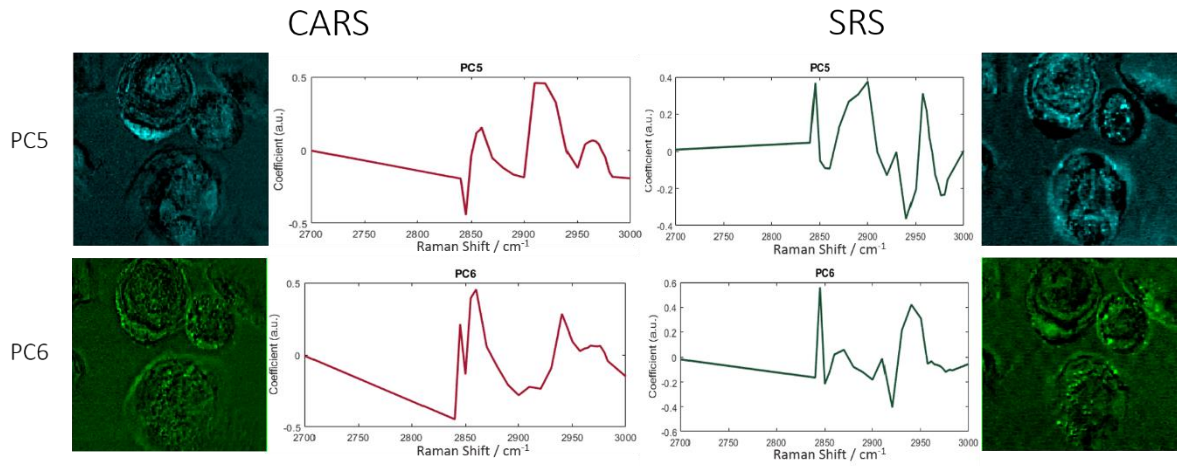

Figure 8.13 PC 5 and 6 outputs generated from analysis of hyperspectral image stacks acquired from MCF-7 cells in the region 2700-3000 cm^{-1} by CARS (left) and SRS (right) microscopy. PC loadings (spectra) demonstrate the weighted contribution of investigated Raman shifts to the separation of pixel blocks visualised in PC score projections (images).

Table 8.2 Total percentage variances accounted for in PCs 1-6 generated from hyperspectral image stacks of MCF-7 cells using both CARS and SRS microscopy.

PC	Var_{CARS}/ %	Var_{SRS} / %
1	74.0	84.7
2	16.5	5.6
3	2.6	3.7
4	2.3	2.3
5	1.0	1.0
6	0.8	0.5

List of References

1 B. Munos, *Nature Reviews Drug Discovery*, 2009, **8**, 959–968.

2 M. E. Bunnage, *Nat Chem Biol*, 2011, **7**, 335–339.

3 S. M. Paul, D. S. Mytelka, C. T. Dunwiddie, C. C. Persinger, B. H. Munos, S. R. Lindborg and A. L. Schacht, *Nature Reviews Drug Discovery*, , DOI:10.1038/nrd3078.

4 F. Pammolli, L. Magazzini and M. Riccaboni, *Nature Reviews Drug Discovery*, 2011, **10**, 428–438.

5 J. Arrowsmith, *Nature Reviews Drug Discovery*, 2011, **10**, 87–87.

6 D. B. Fogel, *Contemporary Clinical Trials Communications*, 2018, **11**, 156–164.

7 T. J. Hwang, D. Carpenter, J. C. Lauffenburger, B. Wang, J. M. Franklin and A. S. Kesselheim, *JAMA Internal Medicine*, 2016, **176**, 1826.

8 C. T. Dollery, *Clinical Pharmacology & Therapeutics*, 2013, **93**, 263–266.

9 R. Martinez-Zaguilan, L. S. Tompkins, R. J. Gillies and R. M. Lynch, in *Calcium Signaling Protocols*, eds. D. G. Lambert and R. D. Rainbow, Humana Press, Totowa, NJ, 2013, vol. 937, pp. 253–271.

10 K. A. Willets, *Analytical and Bioanalytical Chemistry*, 2009, **394**, 85–94.

11 J. Taylor, A. Huefner, L. Li, J. Wingfield and S. Mahajan, *The Analyst*, 2016, **141**, 5037–5055.

12 M. Vater, L. Möckl, V. Gormanns, C. Schultz Fademrecht, A. M. Mallmann, K. Ziegart-Sadowska, M. Zaba, M. L. Frevert, C. Bräuchle, F. Holsboer, T. Rein, U. Schmidt and T. Kirmeier, *Scientific Reports*, , DOI:10.1038/srep44277.

13 J. Baik and G. R. Rosania, *Molecular Pharmaceutics*, 2011, **8**, 1742–1749.

14 H. Giloh and J. Sedat, *Science*, 1982, **217**, 1252–1255.

15 E. J. Lanni, S. S. Rubakhin and J. V. Sweedler, *Journal of Proteomics*, 2012, **75**, 5036–5051.

16 Y. Lin, R. Trouillon, G. Safina and A. G. Ewing, *Anal. Chem.*, 2011, **83**, 4369–4392.

17 P. J. Trim, S. Francese and M. R. Clench, *Bioanalysis*, 2009, **1**, 309–319.

18 M. K. Passarelli, A. Pirkl, R. Moellers, D. Grinfeld, F. Kollmer, R. Havelund, C. F. Newman, P. S. Marshall, H. Arlinghaus, M. R. Alexander, A. West, S. Horning, E. Niehuis, A. Makarov, C. T. Dollery and I. S. Gilmore, *Nature Methods*, 2017, **14**, 1175–1183.

19 Y. Schober, S. Guenther, B. Spengler and A. Römpp, *Analytical Chemistry*, 2012, **84**, 6293–6297.

20 M. Kompauer, S. Heiles and B. Spengler, *Nature Methods*, 2017, **14**, 1156–1158.

21 S. Schlücker, *Angewandte Chemie International Edition*, 2014, **53**, 4756–4795.

22 E. C. Le Ru, *Principles of surface-enhanced Raman spectroscopy: and related plasmonic effects*, Elsevier, Amsterdam ; Boston, 1st ed., 2009.

23 G. Sabatté, R. Keir, M. Lawlor, M. Black, D. Graham and W. E. Smith, *Analytical Chemistry*, 2008, **80**, 2351–2356.

24 A. Pallaoro, G. B. Braun and M. Moskovits, *Nano Letters*, 2015, **15**, 6745–6750.

25 S. Nie, *Science*, 1997, **275**, 1102–1106.

26 K. Kneipp, Y. Wang, H. Kneipp, L. T. Perelman, I. Itzkan, R. R. Dasari and M. S. Feld, *Physical Review Letters*, 1997, **78**, 1667–1670.

27 E. C. Le Ru, M. Meyer and P. G. Etchegoin, *The Journal of Physical Chemistry B*, 2006, **110**, 1944–1948.

28 J. Taylor, A. Milton, M. Willett, J. Wingfield and S. Mahajan, *Faraday Discuss.*, 2017, **205**, 409–428.

29 C. Zhang, D. Zhang and J.-X. Cheng, *Annual Review of Biomedical Engineering*, 2015, **17**, 415–445.

30 C. Krafft, B. Dietzek and J. Popp, *The Analyst*, 2009, **134**, 1046.

31 J.-X. Cheng and X. S. Xie, *The Journal of Physical Chemistry B*, 2004, **108**, 827–840.

32 N. B. Colthup, *Introduction to infrared and Raman spectroscopy*, Academic Press, New York, 2d ed., 1975.

33 M. Moskovits, *Journal of Raman Spectroscopy*, 2005, **36**, 485–496.

34 E. C. Le Ru, E. Blackie, M. Meyer and P. G. Etchegoin, *The Journal of Physical Chemistry C*, 2007, **111**, 13794–13803.

35 K. L. Kelly, E. Coronado, L. L. Zhao and G. C. Schatz, *The Journal of Physical Chemistry B*, 2003, **107**, 668–677.

36 P. K. Jain and M. A. El-Sayed, *Chemical Physics Letters*, 2010, **487**, 153–164.

37 L. Novotny and B. Hecht, *Principles of Nano-Optics*, Cambridge University Press, Cambridge, 2nd edn., 2012.

38 P. Nordlander, C. Oubre, E. Prodan, K. Li and M. I. Stockman, *Nano Letters*, 2004, **4**, 899–903.

39 C. Oubre and P. Nordlander, *The Journal of Physical Chemistry B*, 2005, **109**, 10042–10051.

40 J. Lermé, *The Journal of Physical Chemistry C*, 2015, **119**, 21087–21104.

41 M. B. Ross, C. A. Mirkin and G. C. Schatz, *The Journal of Physical Chemistry C*, 2016, **120**, 816–830.

42 V. A. G. Rivera, F. A. Ferri and E. Marega, in *Plasmonics - Principles and Applications*, ed. K. Y. Kim, InTech, 2012.

43 J. J. Storhoff, A. A. Lazarides, R. C. Mucic, C. A. Mirkin, R. L. Letsinger and G. C. Schatz, *Journal of the American Chemical Society*, 2000, **122**, 4640–4650.

44 P. K. Jain, W. Huang and M. A. El-Sayed, *Nano Letters*, 2007, **7**, 2080–2088.

45 N. Harris, M. D. Arnold, M. G. Blaber and M. J. Ford, *The Journal of Physical Chemistry C*, 2009, **113**, 2784–2791.

46 T. Chen, M. Pourmand, A. Feizpour, B. Cushman and B. M. Reinhard, *The Journal of Physical Chemistry Letters*, 2013, **4**, 2147–2152.

47 G. Aguirregabiria, J. Aizpurua and R. Esteban, *Optics Express*, 2017, **25**, 13760.

48 R. W. Taylor, R. Esteban, S. Mahajan, R. Coulston, O. A. Scherman, J. Aizpurua and J. J. Baumberg, *The Journal of Physical Chemistry C*, 2012, **116**, 25044–25051.

49 A. Campion and P. Kambhampati, *Chemical Society Reviews*, 1998, **27**, 241.

50 K. Faulds, A. Hernandez-Santana and W. E. Smith, in *Spectroscopic Properties of Inorganic and Organometallic Compounds*, eds. J. Yarwood, R. Douthwaite and S. Duckett, Royal Society of Chemistry, Cambridge, 2010, vol. 41, pp. 1–21.

51 S. Liu, X. Zhao, Y. Li, M. Chen and M. Sun, *Spectrochimica Acta Part A: Molecular and Biomolecular Spectroscopy*, 2009, **73**, 382–387.

52 L. L. Zhao, L. Jensen and G. C. Schatz, *Nano Letters*, 2006, **6**, 1229–1234.

53 K. Kneipp, *The Journal of Physical Chemistry C*, 2016, **120**, 21076–21081.

54 E. C. Le Ru and P. G. Etchegoin, *MRS Bulletin*, 2013, **38**, 631–640.

55 C. L. Evans and X. S. Xie, *Annual Review of Analytical Chemistry*, 2008, **1**, 883–909.

56 J. Kneipp, H. Kneipp, M. McLaughlin, D. Brown and K. Kneipp, *Nano Letters*, 2006, **6**, 2225–2231.

57 Z. Ye, C. Li, Y. Xu and S. E. J. Bell, *The Analyst*, 2019, **144**, 448–453.

58 S. Schlücker, S. Bell, G. Charron, E. Cortés, J. Kneipp, M. Lamy de la Chapelle, J. Langer, M. Procházka and V. Tran, *Angewandte Chemie International Edition*, , DOI:10.1002/anie.201908154.

59 E. C. Dreaden, A. M. Alkilany, X. Huang, C. J. Murphy and M. A. El-Sayed, *Chem. Soc. Rev.*, 2012, **41**, 2740–2779.

60 V. Bhardwaj, S. Srinivasan and A. J. McGoron, *The Analyst*, 2015, **140**, 3929–3934.

61 R. Lévy, U. Shaheen, Y. Cesbron and V. Sée, *Nano Reviews*, , DOI:10.3402/nano.v1i0.4889.

62 B. Alberts, *Molecular biology of the cell*, Garland Science, Taylor and Francis Group, New York, NY, Sixth edition., 2015.

63 S. Zhang, H. Gao and G. Bao, *ACS Nano*, 2015, **9**, 8655–8671.

64 J. H. Park and N. Oh, *International Journal of Nanomedicine*, 2014, 51.

65 J. Huotari and A. Helenius, *The EMBO Journal*, 2011, **30**, 3481–3500.

66 B. Alberts, *Molecular Biology of the Cell*, Garland Science, 2008.

67 D. Drescher and J. Kneipp, *Chemical Society Reviews*, 2012, **41**, 5780.

68 P. del Pino, B. Pelaz, Q. Zhang, P. Maffre, G. U. Nienhaus and W. J. Parak, *Mater. Horiz.*, 2014, **1**, 301–313.

69 B. D. Chithrani, A. A. Ghazani and W. C. W. Chan, *Nano Letters*, 2006, **6**, 662–668.

70 S. Zhang, J. Li, G. Lykotrafitis, G. Bao and S. Suresh, *Advanced Materials*, 2009, **21**, 419–424.

71 S. Barbosa, A. Agrawal, L. Rodríguez-Lorenzo, I. Pastoriza-Santos, R. A. Alvarez-Puebla, A. Kornowski, H. Weller and L. M. Liz-Marzán, *Langmuir*, 2010, **26**, 14943–14950.

72 Q. Fu, G. Ran and W. Xu, *RSC Adv.*, 2015, **5**, 37512–37516.

73 J.-F. Li and Z.-Q. Tian, in *Frontiers of Surface-Enhanced Raman Scattering*, eds. Y. Ozaki, K. Kneipp and R. Aroca, John Wiley & Sons, Ltd, Chichester, UK, 2014, pp. 163–192.

74 J. Perezjuste, I. Pastorizasantos, L. Lizmarzan and P. Mulvaney, *Coordination Chemistry Reviews*, 2005, **249**, 1870–1901.

75 M. Yang, R. Alvarez-Puebla, H.-S. Kim, P. Aldeanueva-Potel, L. M. Liz-Marzán and N. A. Kotov, *Nano Letters*, 2010, **10**, 4013–4019.

76 Y. Jin and X. Gao, *Journal of the American Chemical Society*, 2009, **131**, 17774–17776.

77 P. C. Wuytens, A. Z. Subramanian, W. H. De Vos, A. G. Skirtach and R. Baets, *The Analyst*, , DOI:10.1039/C5AN01782C.

78 M. S. Yavuz, Y. Cheng, J. Chen, C. M. Cobley, Q. Zhang, M. Rycenga, J. Xie, C. Kim, K. H. Song, A. G. Schwartz, L. V. Wang and Y. Xia, *Nature Materials*, 2009, **8**, 935–939.

79 W. Xie and S. Schlücker, *Physical Chemistry Chemical Physics*, 2013, **15**, 5329.

80 H. Gao, W. Shi and L. B. Freund, *Proceedings of the National Academy of Sciences*, 2005, **102**, 9469–9474.

81 B. D. Chithrani and W. C. W. Chan, *Nano Letters*, 2007, **7**, 1542–1550.

82 M. Neshatian, S. Chung, D. Yohan, C. Yang and D. B. Chithrani, *Colloids and Interface Science Communications*, 2014, **1**, 57–61.

83 K. Nambara, K. Niikura, H. Mitomo, T. Ninomiya, C. Takeuchi, J. Wei, Y. Matsuo and K. Ijiro, *Langmuir*, 2016, **32**, 12559–12567.

84 D. Bartczak, O. L. Muskens, S. Nitti, T. Sanchez-Elsner, T. M. Millar and A. G. Kanaras, *Small*, 2012, **8**, 122–130.

85 M. P. Monopoli, D. Walczyk, A. Campbell, G. Elia, I. Lynch, F. Baldelli Bombelli and K. A. Dawson, *Journal of the American Chemical Society*, 2011, **133**, 2525–2534.

86 E. Casals, T. Pfaller, A. Duschl, G. J. Oostingh and V. Puntes, *ACS Nano*, 2010, **4**, 3623–3632.

87 H. Whitwell, R.-M. Mackay, C. Elgy, C. Morgan, M. Griffiths, H. Clark, P. Skipp and J. Madsen, *Nanotoxicology*, 2016, **10**, 1385–1394.

88 X. Cheng, X. Tian, A. Wu, J. Li, J. Tian, Y. Chong, Z. Chai, Y. Zhao, C. Chen and C. Ge, *ACS Applied Materials & Interfaces*, 2015, **7**, 20568–20575.

89 C. C. Fleischer and C. K. Payne, *Accounts of Chemical Research*, 2014, **47**, 2651–2659.

90 C. D. Walkey and W. C. W. Chan, *Chem. Soc. Rev.*, 2012, **41**, 2780–2799.

91 C. D. Walkey, J. B. Olsen, F. Song, R. Liu, H. Guo, D. W. H. Olsen, Y. Cohen, A. Emili and W. C. W. Chan, *ACS Nano*, 2014, **8**, 2439–2455.

92 K. Choi, J. E. Riviere and N. A. Monteiro-Riviere, *Nanotoxicology*, 2017, **11**, 64–75.

93 P. R. Leroueil, S. Hong, A. Mecke, J. R. Baker, B. G. Orr and M. M. Banaszak Holl, *Acc. Chem. Res.*, 2007, **40**, 335–342.

94 A. Stojiljković, K. Kuehni-Boghenbor, V. Gaschen, G. Schüpbach, M. Mevissen, C. Kinnear, A.-M. Möller and M. H. Stoffel, *Nanoscale*, 2016, **8**, 16650–16661.

95 L. A. Austin, B. Kang and M. A. El-Sayed, *Nano Today*, 2015, **10**, 542–558.

96 J. W. Kang, P. T. C. So, R. R. Dasari and D.-K. Lim, *Nano Letters*, 2015, **15**, 1766–1772.

97 V. T. Cong, N. H. Ly, S. J. Son, J. Min and S.-W. Joo, *Chem. Commun.*, 2017, **53**, 5009–5012.

98 A. Verma and F. Stellacci, *Small*, 2010, **6**, 12–21.

99 J. M. de la Fuente and C. C. Berry, *Bioconjug. Chem.*, 2005, **16**, 1176–1180.

100 A. G. Tkachenko, H. Xie, D. Coleman, W. Glomm, J. Ryan, M. F. Anderson, S. Franzen and D. L. Feldheim, *Journal of the American Chemical Society*, 2003, **125**, 4700–4701.

101 X.-S. Zheng, C. Zong, X. Wang and B. Ren, *Analytical Chemistry*, 2019, **91**, 8383–8389.

102 M. Babič, D. Horák, M. Trchová, P. Jendelová, K. Glogarová, P. Lesný, V. Herynek, M. Hájek and E. Syková, *Bioconjugate Chemistry*, 2008, **19**, 740–750.

103 L. Y. T. Chou, K. Ming and W. C. W. Chan, *Chem. Soc. Rev.*, 2011, **40**, 233–245.

104 R. Deng, H. Qu, L. Liang, J. Zhang, B. Zhang, D. Huang, S. Xu, C. Liang and W. Xu, *Analytical Chemistry*, 2017, **89**, 2844–2851.

105 Q. Zhang, J. Li, P. Tang, X. Lu, J. Tian and L. Zhong, *Nanomaterials*, 2019, **9**, 1373.

106 M. A. Herrero, F. M. Toma, K. T. Al-Jamal, K. Kostarelos, A. Bianco, T. Da Ros, F. Bano, L. Casalis, G. Scoles and M. Prato, *Journal of the American Chemical Society*, 2009, **131**, 9843–9848.

107 D. Chatterjee, A. Rufaihah and Y. Zhang, *Biomaterials*, 2008, **29**, 937–943.

108 G. J. Lutz, S. R. Sirsi and J. H. Williams, in *Gene Therapy Protocols: Production and In Vivo Applications of Gene Transfer Vectors*, ed. J. M. L. Doux, Humana Press, Totowa, NJ, 2008, pp. 141–150.

109 W. T. Al-Jamal, K. T. Al-Jamal, P. H. Bomans, P. M. Frederik and K. Kostarelos, *Small*, 2008, **4**, 1406–1415.

110 W. T. Al-Jamal, K. T. Al-Jamal, B. Tian, L. Lacerda, P. H. Bomans, P. M. Frederik and K. Kostarelos, *ACS Nano*, 2008, **2**, 408–418.

111 W.-K. Rhim, J.-S. Kim and J.-M. Nam, *Small*, 2008, **4**, 1651–1655.

112 V. P. Torchilin, *Advanced Drug Delivery Reviews*, 2008, **60**, 548–558.

113 Ž. Krpetić, S. Saleemi, I. A. Prior, V. Sée, R. Qureshi and M. Brust, *ACS Nano*, 2011, **5**, 5195–5201.

114 N. Todorova, C. Chiappini, M. Mager, B. Simona, I. I. Patel, M. M. Stevens and I. Yarovsky, *Nano Letters*, 2014, **14**, 5229–5237.

115 C. Ciobanasu, J. P. Siebrasse and U. Kubitscheck, *Biophysical Journal*, 2010, **99**, 153–162.

116 R. Fischer, M. Fotin-Mleczek, H. Hufnagel and R. Brock, *ChemBioChem*, 2005, **6**, 2126–2142.

117 S. V. Boddapati, G. G. M. D’Souza, S. Erdogan, V. P. Torchilin and V. Weissig, *Nano Letters*, 2008, **8**, 2559–2563.

118 H. J. Shin, J. H. Lee, Y. D. Kim, I. Shin, T. Sim and D.-K. Lim, *ACS Omega*, 2019, **4**, 8188–8195.

119 H. Ba, J. Rodríguez-Fernández, F. D. Stefani and J. Feldmann, *Nano Letters*, 2010, **10**, 3006–3012.

120 A. Huefner, W.-L. Kuan, R. A. Barker and S. Mahajan, *Nano Letters*, 2013, **13**, 2463–2470.

121 Y. Ozaki, K. Kneipp and R. Aroca, Eds., *Frontiers of Surface-Enhanced Raman Scattering: Single Nanoparticles and Single Cells*, John Wiley & Sons, Ltd, Chichester, UK, 2014.

122 A. M. Alkilany and C. J. Murphy, *Journal of Nanoparticle Research*, 2010, **12**, 2313–2333.

123 C. J. Murphy, A. M. Gole, J. W. Stone, P. N. Sisco, A. M. Alkilany, E. C. Goldsmith and S. C. Baxter, *Accounts of Chemical Research*, 2008, **41**, 1721–1730.

124 R. Sakhtianchi, R. F. Minchin, K.-B. Lee, A. M. Alkilany, V. Serpooshan and M. Mahmoudi, *Advances in Colloid and Interface Science*, 2013, **201–202**, 18–29.

125 Y.-P. Jia, B.-Y. Ma, X.-W. Wei and Z.-Y. Qian, *Chinese Chemical Letters*, 2017, **28**, 691–702.

126 S. Shin, I. Song and S. Um, *Nanomaterials*, 2015, **5**, 1351–1365.

127 Y. Pan, S. Neuss, A. Leifert, M. Fischler, F. Wen, U. Simon, G. Schmid, W. Brandau and W. Jahnen-Dechent, *Small*, 2007, **3**, 1941–1949.

128 Y. Pan, A. Leifert, D. Ruau, S. Neuss, J. Bornemann, G. Schmid, W. Brandau, U. Simon and W. Jahnen-Dechent, *Small*, 2009, **5**, 2067–2076.

129 C. M. Goodman, C. D. McCusker, T. Yilmaz and V. M. Rotello, *Bioconjugate Chemistry*, 2004, **15**, 897–900.

130 P. Khanna, C. Ong, B. Bay and G. Baeg, *Nanomaterials*, 2015, **5**, 1163–1180.

131 E. Hutter, S. Boridy, S. Labrecque, M. Lalancette-Hébert, J. Kriz, F. M. Winnik and D. Maysinger, *ACS Nano*, 2010, **4**, 2595–2606.

132 T. Niidome, Y. Akiyama, M. Yamagata, T. Kawano, T. Mori, Y. Niidome and Y. Katayama, *Journal of Biomaterials Science, Polymer Edition*, 2009, **20**, 1203–1215.

133 A. M. Alkilany, P. K. Nagaria, C. R. Hexel, T. J. Shaw, C. J. Murphy and M. D. Wyatt, *Small*, 2009, **5**, 701–708.

134 A. P. Leonov, J. Zheng, J. D. Clogston, S. T. Stern, A. K. Patri and A. Wei, *ACS Nano*, 2008, **2**, 2481–2488.

135 I. Fratoddi, I. Venditti, C. Cametti and M. V. Russo, *Toxicol. Res.*, 2015, **4**, 796–800.

136 I. R. Nabiev, H. Morjani and M. Manfait, *European Biophysics Journal*, , DOI:10.1007/BF00183320.

137 Y. S. Huh, A. J. Chung and D. Erickson, *Microfluidics and Nanofluidics*, 2009, **6**, 285–297.

138 C. A. R. Auchinvole, P. Richardson, C. McGuinnes, V. Mallikarjun, K. Donaldson, H. McNab and C. J. Campbell, *ACS Nano*, 2012, **6**, 888–896.

139 A. Huefner, W.-L. Kuan, K. H. Müller, J. N. Skepper, R. A. Barker and S. Mahajan, *ACS Nano*, 2015, **10**, 307–316.

140 J. Ando, K. Fujita, N. I. Smith and S. Kawata, *Nano Letters*, 2011, **11**, 5344–5348.

141 J. Ando, T. Yano, K. Fujita and S. Kawata, *Physical Chemistry Chemical Physics*, 2013, **15**, 13713.

142 K. A. Hollywood, I. T. Shadi and R. Goodacre, *The Journal of Physical Chemistry C*, 2010, **114**, 7308–7313.

143 I. A. Larmour and D. Graham, *The Analyst*, 2011, **136**, 3831.

144 V. Živanović, S. Seifert, D. Drescher, P. Schrade, S. Werner, P. Guttmann, G. P. Szekeres, S. Bachmann, G. Schneider, C. Arenz and J. Kneipp, *ACS Nano*, 2019, **13**, 9363–9375.

145 M. F. Escoriza, J. M. VanBriesen, S. Stewart and J. Maier, *Applied Spectroscopy*, 2007, **61**, 812–823.

146 B. Kang, L. A. Austin and M. A. El-Sayed, *Nano Letters*, 2012, **12**, 5369–5375.

147 Y. H. Ong, M. Lim and Q. Liu, *Optics Express*, 2012, **20**, 25041.

148 P. Ma, L. Xu, L. Wang, N. Chen, X. Zhang, H. Chen and J. Li, *Applied Sciences*, 2019, **9**, 3990.

149 Ö. F. Karataş, E. Sezgin, Ö. Aydın and M. Çulha, *Colloids and Surfaces B: Biointerfaces*, 2009, **71**, 315–318.

150 B. Kang, M. M. Afifi, L. A. Austin and M. A. El-Sayed, *ACS Nano*, 2013, **7**, 7420–7427.

151 K. Ock, W. I. Jeon, E. O. Ganbold, M. Kim, J. Park, J. H. Seo, K. Cho, S.-W. Joo and S. Y. Lee, *Analytical Chemistry*, 2012, **84**, 2172–2178.

152 J. Yang, Z. Wang, S. Zong, H. Chen, R. Zhang and Y. Cui, *Biosensors and Bioelectronics*, 2014, **51**, 82–89.

153 T. Santiago, R. DeVaux, K. Kurzatkowska, R. Espinal, J. I. Herschkowitz and M. Hepel, *International Journal of Nanomedicine*, 2017, **Volume 12**, 7763–7776.

154 J. Kim, S. H. Nam, D.-K. Lim and Y. D. Suh, *Nanoscale*, , DOI:10.1039/C9NR05159G.

155 J. Taylor, A. Huefner, J. Wingfield and S. Mahajan, in *Plasmonics in Biology and Chemistry*, Pan Stanford, 1st edn., 2019, pp. 233–276.

156 D. Uzunoglu, M. Altunbek, G. Kuku and M. Culha, in *Single-Cell Omics*, Elsevier, 2019, pp. 153–177.

157 R. Peng, Y. Si, T. Deng, J. Zheng, J. Li, R. Yang and W. Tan, *Chem Commun*, 2016, **52**, 8553–8556.

158 W. Wang, L. Zhang, L. Li and Y. Tian, *Anal. Chem.*, 2016, **88**, 9518–9523.

159 C. Wei, X. Liu, Y. Gao, Y. Wu, X. Guo, Y. Ying, Y. Wen and H. Yang, *Analytical Chemistry*, 2018, **90**, 11333–11339.

160 C. E. Talley, L. Jusinski, C. W. Hollars, S. M. Lane and T. Huser, *Analytical Chemistry*, 2004, **76**, 7064–7068.

161 L. E. Jamieson, A. Jaworska, J. Jiang, M. Baranska, D. J. Harrison and C. J. Campbell, *The Analyst*, 2015, **140**, 2330–2335.

162 A. Williams, K. J. Flynn, Z. Xia and P. R. Dunstan, *J. Raman Spectrosc.*, 2016, **47**, 819–827.

163 S. P. Mulvaney, M. D. Musick, C. D. Keating and M. J. Natan, *Langmuir*, 2003, **19**, 4784–4790.

164 J. F. Li, Y. F. Huang, Y. Ding, Z. L. Yang, S. B. Li, X. S. Zhou, F. R. Fan, W. Zhang, Z. Y. Zhou, D. Y. Wu, B. Ren, Z. L. Wang and Z. Q. Tian, *Nature*, 2010, **464**, 392–395.

165 X.-D. Tian, B.-J. Liu, J.-F. Li, Z.-L. Yang, B. Ren and Z.-Q. Tian, *Journal of Raman Spectroscopy*, 2013, **44**, 994–998.

166 S. Moreton, K. Faulds, N. C. Shand, M. A. Bedics, M. R. Detty and D. Graham, *Nanoscale*, 2015, **7**, 6075–6082.

167 Y. Chen, X. Bai, L. Su, Z. Du, A. Shen, A. Materny and J. Hu, *Scientific Reports*, 2016, **6**, 19173.

168 R. Stevenson, S. McAughtrie, L. Senior, R. J. Stokes, H. McGachy, L. Tetley, P. Nativo, J. M. Brewer, J. Alexander, K. Faulds and D. Graham, *The Analyst*, 2013, **138**, 6331.

169 Y. Cao, D.-W. Li, L.-J. Zhao, X.-Y. Liu, X.-M. Cao and Y.-T. Long, *Analytical Chemistry*, 2015, **87**, 9696–9701.

170 Q. Li, Q. Gao and G. Zhang, *Biomedical Optics Express*, 2014, **5**, 2435.

171 J. Li, Z. Skeete, S. Shan, S. Yan, K. Kurzatkowska, W. Zhao, Q. M. Ngo, P. Holubovska, J. Luo, M. Hepel and C.-J. Zhong, *Analytical Chemistry*, 2015, **87**, 10698–10702.

172 L. Tang, J. Casas and M. Venkataramasubramani, *Analytical Chemistry*, 2013, **85**, 1431–1439.

173 L. Wu and X. Qu, *Chem. Soc. Rev.*, 2015, **44**, 2963–2997.

174 I. Freitag, C. Matthäus, A. Csaki, J. H. Clement, D. Cialla-May, K. Weber, C. Krafft and J. Popp, *Journal of Biomedical Optics*, 2015, **20**, 055002.

175 Z. A. Nima, M. Mahmood, Y. Xu, T. Mustafa, F. Watanabe, D. A. Nedosekin, M. A. Juratli, T. Fahmi, E. I. Galanzha, J. P. Nolan, A. G. Basnakian, V. P. Zharov and A. S. Biris, *Scientific Reports*, , DOI:10.1038/srep04752.

176 C. M. MacLaughlin, N. Mullaithilaga, G. Yang, S. Y. Ip, C. Wang and G. C. Walker, *Langmuir*, 2013, **29**, 1908–1919.

177 M. K. Gregas, J. P. Scaffidi, B. Lauly and T. Vo-Dinh, *Applied Spectroscopy*, 2010, **64**, 858–866.

178 C. Y. Song, B. Y. Yang, W. Q. Chen, Y. X. Dou, Y. J. Yang, N. Zhou and L. H. Wang, *J. Mater. Chem. B*, 2016, **4**, 7112–7118.

179 L. Rodríguez-Lorenzo, Z. Krpetic, S. Barbosa, R. A. Alvarez-Puebla, L. M. Liz-Marzán, I. A. Prior and M. Brust, *Integrative Biology*, 2011, **3**, 922.

180 M. Ardini, J.-A. Huang, C. S. Sánchez, M. Z. Mousavi, V. Caprettini, N. Maccaferri, G. Melle, G. Bruno, L. Pasquale, D. Garoli and F. De Angelis, *Scientific Reports*, , DOI:10.1038/s41598-018-31165-3.

181 L. Liu, Y. Tang, S. Dai, F. Kleitz and S. Z. Qiao, *Nanoscale*, 2016, **8**, 12803–12811.

182 J. Zhang, X. Ma and Z. Wang, *Analytical Chemistry*, , DOI:10.1021/acs.analchem.9b00480.

183 J. Huang, C. Zong, H. Shen, Y. Cao, B. Ren and Z. Zhang, *Nanoscale*, 2013, **5**, 10591.

184 J. Song, J. Zhou and H. Duan, *Journal of the American Chemical Society*, 2012, **134**, 13458–13469.

185 C. Liu, C. Chen, S. Li, H. Dong, W. Dai, T. Xu, Y. Liu, F. Yang and X. Zhang, *Analytical Chemistry*, 2018, **90**, 10591–10599.

186 M. Schütz, C. I. Müller, M. Salehi, C. Lambert and S. Schlücker, *Journal of Biophotonics*, 2011, **4**, 453–463.

187 A. Matschulat, D. Drescher and J. Kneipp, *ACS Nano*, 2010, **4**, 3259–3269.

188 J. A. Dougan and K. Faulds, *The Analyst*, 2012, **137**, 545–554.

189 S. Schlücker, *ChemPhysChem*, 2009, **10**, 1344–1354.

190 D.-K. Lim, K.-S. Jeon, J.-H. Hwang, H. Kim, S. Kwon, Y. D. Suh and J.-M. Nam, *Nature Nanotechnology*, 2011, **6**, 452–460.

191 P. Zhang, L. Wang, Y. Fang, D. Zheng, T. Lin and H. Wang, *Molecules*, 2019, **24**, 2947.

192 J. C. Fraire, S. Stremersch, D. Brouckaert, T. Monteyne, T. De Beer, P. Wuytens, R. De Rycke, A. G. Skirtach, K. Raemdonck, S. C. De Smedt and K. Braeckmans, *ACS Applied Materials & Interfaces*, , DOI:10.1021/acsami.9b11473.

193 S. A. Grigoryev, Y. A. Bulynko and E. Y. Popova, *Chromosome Research*, 2006, **14**, 53–69.

194 T. Büchner, D. Drescher, H. Traub, P. Schrade, S. Bachmann, N. Jakubowski and J. Kneipp, *Analytical and Bioanalytical Chemistry*, 2014, **406**, 7003–7014.

195 Y. Zhuang, D. Wang, C. Yin, H. Deng, M. Sun, L. He, Y. Su and X. Zhu, *Science China Chemistry*, 2016, **59**, 1600–1608.

196 Md. K. Hossain, H.-Y. Cho, K.-J. Kim and J.-W. Choi, *Biosensors and Bioelectronics*, 2015, **71**, 300–305.

197 H. Cao, Y. Yang, X. Chen and Z. Shao, *Nanoscale*, 2016, **8**, 6754–6760.

198 F. Tian, J. Conde, C. Bao, Y. Chen, J. Curtin and D. Cui, *Biomaterials*, 2016, **106**, 87–97.

199 X. Zhang, H. Yin, J. M. Cooper and S. J. Haswell, *Analytical and Bioanalytical Chemistry*, 2008, **390**, 833–840.

200 N. Osna, K. Elliott and M. M. Khan, *International Immunopharmacology*, 2001, **1**, 135–145.

201 J. Yang, Y. Cui, S. Zong, R. Zhang, C. Song and Z. Wang, *Molecular Pharmaceutics*, 2012, **9**, 842–849.

202 R. Zhang, Y. Zhang, Z. C. Dong, S. Jiang, C. Zhang, L. G. Chen, L. Zhang, Y. Liao, J. Aizpurua, Y. Luo, J. L. Yang and J. G. Hou, *Nature*, 2013, **498**, 82–86.

203 Y. Chen, X. Bai, L. Su, Z. Du, A. Shen, A. Materny and J. Hu, *Scientific Reports*, 2016, **6**, 19173.

204 I. I. Patel, C. Steuwe, S. Reichelt and S. Mahajan, *Journal of Optics*, 2013, **15**, 094006.

205 A. H. Hill and D. Fu, *Analytical Chemistry*, 2019, **91**, 9333–9342.

206 T. Meyer, M. Chemnitz, M. Baumgartl, T. Gottschall, T. Pascher, C. Matthäus, B. F. M. Romeike, B. R. Brehm, J. Limpert, A. Tünnermann, M. Schmitt, B. Dietzek and J. Popp, *Analytical Chemistry*, 2013, **85**, 6703–6715.

207 F. B. Legesse, A. Medyukhina, S. Heuke and J. Popp, *Comput Med Imaging Graph*, 2015, **43**, 36–43.

208 B. F. M. Romeike, T. Meyer, R. Reichart, R. Kalff, I. Petersen, B. Dietzek and J. Popp, *Clin Neurol Neurosurg*, 2015, **131**, 42–46.

209 R. Galli, O. Uckermann, A. Temme, E. Leipnitz, M. Meinhardt, E. Koch, G. Schackert, G. Steiner and M. Kirsch, *Journal of Biophotonics*, 2017, **10**, 404–414.

210 M. Ji, S. Lewis, S. Camelo-Piragua, S. H. Ramkissoon, M. Snuderl, S. Venneti, A. Fisher-Hubbard, M. Garrard, D. Fu, A. C. Wang, J. A. Heth, C. O. Maher, N. Sanai, T. D. Johnson, C. W. Freudiger, O. Sagher, X. S. Xie and D. A. Orringer, *Science Translational Medicine*, 2015, **7**, 309ra163-309ra163.

211 D. Fu, F.-K. Lu, X. Zhang, C. Freudiger, D. R. Pernik, G. Holtom and X. S. Xie, *Journal of the American Chemical Society*, 2012, **134**, 3623–3626.

212 A. Folick, W. Min and M. C. Wang, *Current Opinion in Genetics & Development*, 2011, **21**, 585–590.

213 M. C. Wang, W. Min, C. W. Freudiger, G. Ruvkun and X. S. Xie, *Nature Methods*, 2011, **8**, 135–138.

214 L. Shi, C. Zheng, Y. Shen, Z. Chen, E. S. Silveira, L. Zhang, M. Wei, C. Liu, C. de Sena-Tomas, K. Targoff and W. Min, *Nature Communications*, , DOI:10.1038/s41467-018-05401-3.

215 J.-X. Cheng, Y. K. Jia, G. Zheng and X. S. Xie, *Biophys. J.*, 2002, **83**, 502–509.

216 J. Cheng, A. Volkmer, L. D. Book and X. S. Xie, *The Journal of Physical Chemistry B*, 2002, **106**, 8493–8498.

217 X. Nan, J.-X. Cheng and X. S. Xie, *Journal of Lipid Research*, 2003, **44**, 2202–2208.

218 X. Nan, E. O. Potma and X. S. Xie, *Biophysical Journal*, 2006, **91**, 728–735.

219 C. Di Napoli, I. Pope, F. Masia, P. Watson, W. Langbein and P. Borri, *Biomedical Optics Express*, 2014, **5**, 1378.

220 J. P. Smus, C. C. Moura, E. McMorrow, R. S. Tare, R. O. C. Oreffo and S. Mahajan, *Chem. Sci.*, 2015, **6**, 7089–7096.

221 C. Di Napoli, I. Pope, F. Masia, W. Langbein, P. Watson and P. Borri, *Analytical Chemistry*, 2016, **88**, 3677–3685.

222 R. Mouras, P. Bagnaninchi, A. Downes and A. Elfick, *Journal of Raman Spectroscopy*, 2013, **44**, 1373–1378.

223 A. D. Hofemeier, H. Hachmeister, C. Pilger, M. Schürmann, J. F. W. Greiner, L. Nolte, H. Sudhoff, C. Kaltschmidt, T. Huser and B. Kaltschmidt, *Sci Rep*, 2016, **6**, 26716.

224 J. Jasensky, A. P. Boughton, A. Khmaladze, J. Ding, C. Zhang, J. E. Swain, G. W. Smith, Z. Chen and G. D. Smith, *The Analyst*, 2016, **141**, 4694–4706.

225 F.-K. Lu, S. Basu, V. Igras, M. P. Hoang, M. Ji, D. Fu, G. R. Holtom, V. A. Neel, C. W. Freudiger, D. E. Fisher and X. S. Xie, *Proceedings of the National Academy of Sciences*, 2015, **112**, 11624–11629.

226 D. Fu, W. Yang and X. S. Xie, *Journal of the American Chemical Society*, 2017, **139**, 583–586.

227 L. Zhang and W. Min, *Journal of Biomedical Optics*, 2017, **22**, 1.

228 Y. Shen, F. Xu, L. Wei, F. Hu and W. Min, *Angewandte Chemie International Edition*, 2014, **53**, 5596–5599.

229 H. J. Lee and J.-X. Cheng, *Methods*, 2017, **128**, 119–128.

230 K. T. Schiessl, F. Hu, J. Jo, S. Z. Nazia, B. Wang, A. Price-Whelan, W. Min and L. E. P. Dietrich, *Nature Communications*, , DOI:10.1038/s41467-019-08733-w.

231 C. Zeng, F. Hu, R. Long and W. Min, *The Analyst*, 2018, **143**, 4844–4848.

232 W. J. Tipping, M. Lee, A. Serrels, V. G. Brunton and A. N. Hulme, *Chemical Science*, 2017, **8**, 5606–5615.

233 H. J. Lee, W. Zhang, D. Zhang, Y. Yang, B. Liu, E. L. Barker, K. K. Buhman, L. V. Slipchenko, M. Dai and J.-X. Cheng, *Scientific Reports*, , DOI:10.1038/srep07930.

234 L. Wei and W. Min, *The Journal of Physical Chemistry Letters*, 2018, **9**, 4294–4301.

235 Y. Suzuki, K. Kobayashi, Y. Wakisaka, D. Deng, S. Tanaka, C.-J. Huang, C. Lei, C.-W. Sun, H. Liu, Y. Fujiwaki, S. Lee, A. Isozaki, Y. Kasai, T. Hayakawa, S. Sakuma, F. Arai, K. Koizumi, H. Tezuka,

M. Inaba, K. Hiraki, T. Ito, M. Hase, S. Matsusaka, K. Shiba, K. Suga, M. Nishikawa, M. Jona, Y. Yatomi, Y. Yalikun, Y. Tanaka, T. Sugimura, N. Nitta, K. Goda and Y. Ozeki, *Proceedings of the National Academy of Sciences*, 2019, **116**, 15842–15848.

236 R. Mouras, G. Rischitor, A. Downes, D. Salter and A. Elfick, *Journal of Raman Spectroscopy*, 2010, **41**, 848–852.

237 N. Darville, J. Saarinen, A. Isomäki, L. Khriachtchev, D. Cleeren, P. Sterkens, M. van Heerden, P. Annaert, L. Peltonen, H. A. Santos, C. J. Strachan and G. Van den Mooter, *European Journal of Pharmaceutics and Biopharmaceutics*, 2015, **96**, 338–348.

238 Y. Tian, Y. Kong, X. Li, J. Wu, A. C.-T. Ko and M. Xing, *Colloids and Surfaces B: Biointerfaces*, 2015, **134**, 147–155.

239 H. J. Johnston, R. Mouras, D. M. Brown, A. Elfick and V. Stone, *Nanotechnology*, 2015, **26**, 505102.

240 J. Saarinen, E. Sözeri, S. J. Fraser-Miller, L. Peltonen, H. A. Santos, A. Isomäki and C. J. Strachan, *Int J Pharm*, 2017, **523**, 270–280.

241 C. Steuwe, I. I. Patel, M. Ul-Hasan, A. Schreiner, J. Boren, K. M. Brindle, S. Reichelt and S. Mahajan, *Journal of Biophotonics*, 2014, **7**, 906–913.

242 N. L. Garrett, A. Lalatsa, D. Begley, L. Mihoreanu, I. F. Uchegbu, A. G. Schätzlein and J. Moger, *Journal of Raman Spectroscopy*, 2012, **43**, 681–688.

243 M. Okuno, H. Kano, K. Fujii, K. Bito, S. Naito, P. Leproux, V. Couderc and H. Hamaguchi, *PLoS ONE*, 2014, **9**, e93401.

244 L. Zhang, S. Shen, Z. Liu and M. Ji, *Advanced Biosystems*, 2017, **1**, 1700013.

245 F. Hu, S. D. Brucks, T. H. Lambert, L. M. Campos and W. Min, *Chemical Communications*, 2017, **53**, 6187–6190.

246 G. Bergner, C. R. Albert, M. Schiller, G. Bringmann, T. Schirmeister, B. Dietzek, S. Niebling, S. Schlücker and J. Popp, *The Analyst*, 2011, **136**, 3686.

247 S. You, Y. Liu, Z. Arp, Y. Zhao, E. J. Chaney, M. Marjanovic and S. A. Boppart, *Journal of Biomedical Optics*, 2017, **22**, 070502.

248 M. M. Gaschler, F. Hu, H. Feng, A. Linkermann, W. Min and B. R. Stockwell, *ACS Chemical Biology*, 2018, **13**, 1013–1020.

249 S. Bandyopadhyay, J. Li, E. Traer, J. W. Tyner, A. Zhou, S. T. Oh and J.-X. Cheng, *PLOS ONE*, 2017, **12**, e0179558.

250 D. Fu, J. Zhou, W. S. Zhu, P. W. Manley, Y. K. Wang, T. Hood, A. Wylie and X. S. Xie, *Nature Chemistry*, 2014, **6**, 614–622.

251 J. Kovalevich and D. Langford, in *Neuronal Cell Culture*, eds. S. Amini and M. K. White, Humana Press, Totowa, NJ, 2013, vol. 1078, pp. 9–21.

252 H. Abramczyk, J. Surmacki, M. Kopeć, A. K. Olejnik, K. Lubecka-Pietruszewska and K. Fabianowska-Majewska, *The Analyst*, 2015, **140**, 2224–2235.

253 Y.-T. Cheung, W. K.-W. Lau, M.-S. Yu, C. S.-W. Lai, S.-C. Yeung, K.-F. So and R. C.-C. Chang, *NeuroToxicology*, 2009, **30**, 127–135.

254 J. W. Chan, D. S. Taylor and D. L. Thompson, *Biopolymers*, 2009, **91**, 132–139.

255 T. A. Pologruto, B. L. Sabatini and K. Svoboda, *BioMedical Engineering OnLine*, 2003, **2**, 13.

256 J. Trevisan, P. P. Angelov, A. D. Scott, P. L. Carmichael and F. L. Martin, *Bioinformatics*, 2013, **29**, 1095–1097.

257 I. T. Jolliffe and J. Cadima, *Philosophical Transactions of the Royal Society A: Mathematical, Physical and Engineering Sciences*, 2016, **374**, 20150202.

258 S. N. Kalkanis, R. E. Kast, M. L. Rosenblum, T. Mikkelsen, S. M. Yurgelevic, K. M. Nelson, A. Raghunathan, L. M. Poisson and G. W. Auner, *Journal of Neuro-Oncology*, 2014, **116**, 477–485.

259 A. Huefner, W.-L. Kuan, K. H. Müller, J. N. Skepper, R. A. Barker and S. Mahajan, *ACS Nano*, 2015, **10**, 307–316.

260 M. Mathlouthi, A.-M. Seuvre and J. L. Koenig, *Carbohydrate Research*, 1984, **131**, 1–15.

261 B. Giese and D. McNaughton, *The Journal of Physical Chemistry B*, 2002, **106**, 101–112.

262 F. Madzharova, Z. Heiner, M. Gühlke and J. Kneipp, *The Journal of Physical Chemistry C*, 2016, **120**, 15415–15423.

263 B. Kang, L. A. Austin and M. A. El-Sayed, *ACS Nano*, 2014, **8**, 4883–4892.

264 G. Kuku, M. Saricam, F. Akhatova, A. Danilushkina, R. Fakhrullin and M. Culha, *Analytical Chemistry*, , DOI:10.1021/acs.analchem.6b02917.

265 J. Song, J. Zhou and H. Duan, *Journal of the American Chemical Society*, 2012, **134**, 13458–13469.

266 M. P. Monopoli, A. S. Pitek, I. Lynch and K. A. Dawson, *Methods Mol. Biol.*, 2013, **1025**, 137–155.

267 P. I. T. Thomson and C. J. Campbell, in *Nanoscale Sensors*, eds. S. Li, J. Wu, Z. M. Wang and Y. Jiang, Springer International Publishing, Cham, 2013, vol. 19, pp. 35–54.

268 J. S. Gebauer, M. Malissek, S. Simon, S. K. Knauer, M. Maskos, R. H. Stauber, W. Peukert and L. Treuel, *Langmuir*, 2012, **28**, 9673–9679.

269 M. Lundqvist, J. Stigler, T. Cedervall, T. Berggård, M. B. Flanagan, I. Lynch, G. Elia and K. Dawson, *ACS Nano*, 2011, **5**, 7503–7509.

270 M. Mahmoudi, J. Meng, X. Xue, X. J. Liang, M. Rahman, C. Pfeiffer, R. Hartmann, P. R. Gil, B. Pelaz, W. J. Parak, P. del Pino, S. Carregal-Romero, A. G. Kanaras and S. Tamil Selvan, *Biotechnology Advances*, 2014, **32**, 679–692.

271 S. J. Soenen, P. Rivera-Gil, J.-M. Montenegro, W. J. Parak, S. C. De Smedt and K. Braeckmans, *Nano Today*, 2011, **6**, 446–465.

272 M. A. Vetten, N. Tlotleng, D. Tanner Rascher, A. Skepu, F. K. Keter, K. Boodhia, L.-A. Koekemoer, C. Andraos, R. Tshikhudo and M. Gulumian, *Particle and Fibre Toxicology*, 2013, **10**, 50.

273 E. Birben, U. M. Sahiner, C. Sackesen, S. Erzurum and O. Kalayci, *World Allergy Organization Journal*, 2012, **5**, 9–19.

274 B. Halliwell, *Biochemical Society Transactions*, 2007, **35**, 1147–1150.

275 J. J. Li, L. Zou, D. Hartono, C.-N. Ong, B.-H. Bay and L.-Y. Lanry Yung, *Advanced Materials*, 2008, **20**, 138–142.

276 A. Avalos, A. I. Haza, D. Mateo and P. Morales, *Journal of Applied Toxicology*, 2014, **34**, 413–423.

277 N. Singh, B. Manshian, G. J. S. Jenkins, S. M. Griffiths, P. M. Williams, T. G. G. Maffeis, C. J. Wright and S. H. Doak, *Biomaterials*, 2009, **30**, 3891–3914.

278 D. Ali, S. Alkahtani, M. A. Al Gurabi and S. Alarifi, *OncoTargets and Therapy*, 2015, 295.

279 T. Finkel and N. J. Holbrook, *Nature*, 2000, **408**, 239–247.

280 M. Schieber and N. S. Chandel, *Current Biology*, 2014, **24**, R453–R462.

281 J. Jiang, C. Auchinvole, K. Fisher and C. J. Campbell, *Nanoscale*, 2014, **6**, 12104–12110.

282 A. Shamsaie, J. Heim, A. A. Yanik and J. Irudayaraj, *Chemical Physics Letters*, 2008, **461**, 131–135.

283 A. Huefner, D. Septiadi, B. D. Wilts, I. I. Patel, W.-L. Kuan, A. Fragniere, R. A. Barker and S. Mahajan, *Methods*, 2014, **68**, 354–363.

284 Z. Movasaghi, S. Rehman and I. U. Rehman, *Applied Spectroscopy Reviews*, 2007, **42**, 493–541.

285 R. Malini, K. Venkatakrishna, J. Kurien, K. M. Pai, L. Rao, V. B. Kartha and C. M. Krishna, *Biopolymers*, 2006, **81**, 179–193.

286 R. Singh, R. J. Mailloux, S. Puiseux-Dao and V. D. Appanna, *Journal of Bacteriology*, 2007, **189**, 6665–6675.

287 O. Kurnasov, V. Goral, K. Colabroy, S. Gerdes, S. Anantha, A. Osterman and T. P. Begley, *Chemistry & Biology*, 2003, **10**, 1195–1204.

288 F. Sahm, I. Oezen, C. A. Opitz, B. Radlwimmer, A. von Deimling, T. Ahrendt, S. Adams, H. B. Bode, G. J. Guillemin, W. Wick and M. Platten, *Cancer Research*, 2013, **73**, 3225–3234.

289 L. Liu, Y. Tang, S. Dai, F. Kleitz and S. Z. Qiao, *Nanoscale*, 2016, **8**, 12803–12811.

290 Y. Zhuang, D. Wang, C. Yin, H. Deng, M. Sun, L. He, Y. Su and X. Zhu, *Science China Chemistry*, 2016, **59**, 1600–1608.

291 S.-S. Li, Q.-Y. Guan, G. Meng, X.-F. Chang, J.-W. Wei, P. Wang, B. Kang, J.-J. Xu and H.-Y. Chen, *Scientific Reports*, , DOI:10.1038/s41598-017-02510-9.

292 M. Altunbek, D. Çetin, Z. Suludere and M. Çulha, *Talanta*, 2019, **191**, 390–399.

293 J. Yang, Y. Cui, S. Zong, R. Zhang, C. Song and Z. Wang, *Molecular Pharmaceutics*, 2012, **9**, 842–849.

294 B. D. Chithrani, J. Stewart, C. Allen and D. A. Jaffray, *Nanomedicine: Nanotechnology, Biology and Medicine*, 2009, **5**, 118–127.

295 L. Urbanelli, A. Magini, A. Polchi, M. Polidoro and C. Emiliani, *Recent Pat CNS Drug Discov*, 2011, **6**, 1–19.

296 G. Parenti, *International Journal of Molecular Medicine*, , DOI:10.3892/ijmm.2012.1187.

297 S. Bolte and F. P. Cordelières, *J Microsc*, 2006, **224**, 213–232.

298 M. Aioub and M. A. El-Sayed, *Journal of the American Chemical Society*, 2016, **138**, 1258–1264.

299 P. H. C. Eilers, *Analytical Chemistry*, 2003, **75**, 3631–3636.

300 J. Adler and I. Parmryd, *Cytometry Part A*, 2010, **77A**, 733–742.

301 V. Zinchuk, O. Zinchuk and T. Okada, *ACTA HISTOCHEMICA ET CYTOCHEMICA*, 2007, **40**, 101–111.

302 E. M. M. Manders, F. J. Verbeek and J. A. Aten, *Journal of Microscopy*, 1993, **169**, 375–382.

303 S. V. Costes, D. Daelemans, E. H. Cho, Z. Dobbin, G. Pavlakis and S. Lockett, *Biophysical Journal*, 2004, **86**, 3993–4003.

304 Z. Chu, Y. Huang, Q. Tao and Q. Li, *Nanoscale*, 2011, **3**, 3291.

305 A. Huefner, W.-L. Kuan, R. A. Barker and S. Mahajan, *Nano Letters*, 2013, **13**, 2463–2470.

306 A. Albanese and W. C. W. Chan, *ACS Nano*, 2011, **5**, 5478–5489.

307 X.-M. Qian and S. M. Nie, *Chemical Society Reviews*, 2008, **37**, 912.

308 L. Tian, N. Gandra and S. Singamaneni, *ACS Nano*, 2013, **7**, 4252–4260.

309 S. A. Jensen, E. S. Day, C. H. Ko, L. A. Hurley, J. P. Luciano, F. M. Kouri, T. J. Merkel, A. J. Luthi, P. C. Patel, J. I. Cutler, W. L. Daniel, A. W. Scott, M. W. Rotz, T. J. Meade, D. A. Giljohann, C. A. Mirkin and A. H. Stegh, *Science Translational Medicine*, 2013, **5**, 209ra152-209ra152.

310 C. R. Patra, R. Bhattacharya, E. Wang, A. Katarya, J. S. Lau, S. Dutta, M. Muders, S. Wang, S. A. Buhrow, S. L. Safgren, M. J. Yaszemski, J. M. Reid, M. M. Ames, P. Mukherjee and D. Mukhopadhyay, *Cancer Res.*, 2008, **68**, 1970–1978.

311 M. Y. Spivak, R. V. Bubnov, I. M. Yemets, L. M. Lazarenko, N. O. Tymoshok and Z. R. Ulberg, *EPMA J*, 2013, **4**, 20.

312 W.-H. Chen, J.-X. Chen, H. Cheng, C.-S. Chen, J. Yang, X.-D. Xu, Y. Wang, R.-X. Zhuo and X.-Z. Zhang, *Chemical Communications*, 2013, **49**, 6403.

313 C. S. Y. Wong, I. Robinson, M. A. Ochsenkühn, J. Arlt, W. J. Hossack and J. Crain, *Biomedical Optics Express*, 2011, **2**, 2504.

314 M. Paar, C. Jungst, N. A. Steiner, C. Magnes, F. Sinner, D. Kolb, A. Lass, R. Zimmermann, A. Zumbusch, S. D. Kohlwein and H. Wolinski, *Journal of Biological Chemistry*, 2012, **287**, 11164–11173.

315 J. A. Olzmann and P. Carvalho, *Nature Reviews Molecular Cell Biology*, 2019, **20**, 137–155.

316 Y. Guo, K. R. Cordes, R. V. Farese and T. C. Walther, *Journal of Cell Science*, 2009, **122**, 749–752.

317 P. Shyu, X. F. A. Wong, K. Crasta and G. Thibault, *Bioscience Reports*, 2018, **38**, BSR20180764.

318 C. Nieva, M. Marro, N. Santana-Codina, S. Rao, D. Petrov and A. Sierra, *PLoS ONE*, 2012, **7**, e46456.

319 L. Magtanong, P. J. Ko and S. J. Dixon, *Cell Death & Differentiation*, 2016, **23**, 1099–1109.

320 J. Boren and K. M. Brindle, *Cell Death & Differentiation*, 2012, **19**, 1561–1570.

321 M. S. Larsen, C. W. Yde, I. J. Christensen and A. E. Lykkesfeldt, *International Journal of Oncology*, 2012, **41**, 1863–1870.

322 S. Al-Bahlani, B. Al-Dhahli, K. Al-Adawi, A. Al-Nabhani and M. Al-Kindi, *BioMed Research International*, 2017, **2017**, 1–13.

323 M. D. Hall, K. A. Telma, K.-E. Chang, T. D. Lee, J. P. Madigan, J. R. Lloyd, I. S. Goldlust, J. D. Hoeschele and M. M. Gottesman, *Cancer Research*, 2014, **74**, 3913–3922.

324 S. Koljenović, T. B. Schut, A. Vincent, J. M. Kros and G. J. Puppels, *Analytical Chemistry*, 2005, **77**, 7958–7965.

325 S. Hayashi, S. Takimoto and T. Hashimoto, eds. A. Periasamy and P. T. C. So, San Jose, CA, 2007, p. 644208.

326 A. V. Shubin, I. V. Demidyuk, A. A. Komissarov, L. M. Rafieva and S. V. Kostrov, *Oncotarget*, , DOI:10.18632/oncotarget.10150.

327 T. Henics and D. N. Wheatley, *Biol. Cell*, 1999, **91**, 485–498.

328 T. Aki, A. Nara and K. Uemura, *Cell Biology and Toxicology*, 2012, **28**, 125–131.

329 W. A. Maltese and J. H. Overmeyer, *The American Journal of Pathology*, 2014, **184**, 1630–1642.

330 S. Wang, M. He, L. Li, Z. Liang, Z. Zou and A. Tao, *Journal of Breast Cancer*, 2016, **19**, 231.

331 G. F. de Sousa, S. R. Wlodarczyk and G. Monteiro, *Brazilian Journal of Pharmaceutical Sciences*, 2014, **50**, 693–701.

332 A. Tyagi, C. Agarwal, D. Chan and R. Agarwal, *Oncology Reports*, , DOI:10.3892/or.11.2.493.

333 C. W. Yde, M. Gyrd-Hansen, A. E. Lykkesfeldt, O.-G. Issinger and J. Stenvang, *Molecular Cancer Therapeutics*, 2007, **6**, 1869–1876.

334 S. A. Mirmalek, M. A. Azizi, E. Jangholi, S. Yadollah-Damavandi, M. A. Javidi, Y. Parsa, T. Parsa, S. A. Salimi-Tabatabaee, H. Ghasemzadeh kolagar and R. Alizadeh-Navaei, *Cancer Cell International*, , DOI:10.1186/s12935-016-0279-4.

335 C. W. Freudiger, W. Min, B. G. Saar, S. Lu, G. R. Holtom, C. He, J. C. Tsai, J. X. Kang and X. S. Xie, *Science*, 2008, **322**, 1857–1861.

336 D. Zhang, P. Wang, M. N. Slipchenko and J.-X. Cheng, *Accounts of Chemical Research*, 2014, **47**, 2282–2290.

337 Y. Yu, P. V. Ramachandran and M. C. Wang, *Biochimica et Biophysica Acta (BBA) - Molecular and Cell Biology of Lipids*, 2014, **1841**, 1120–1129.

338 J. Mansfield, J. Moger, E. Green, C. Moger and C. P. Winlove, *Journal of Biophotonics*, 2013, n/a-n/a.

339 J. Li and J.-X. Cheng, *Scientific Reports*, , DOI:10.1038/srep06807.

340 L. Wei, Y. Yu, Y. Shen, M. C. Wang and W. Min, *Proceedings of the National Academy of Sciences*, 2013, **110**, 11226–11231.

341 W. J. Tipping, M. Lee, A. Serrels, V. G. Brunton and A. N. Hulme, *Chemical Society Reviews*, 2016, **45**, 2075–2089.

342 A. Khmaladze, J. Jasensky, E. Price, C. Zhang, A. Boughton, X. Han, E. Seeley, X. Liu, M. M. Banaszak Holl and Z. Chen, *Appl Spectrosc*, 2014, **68**, 1116–1122.

343 T. Bocklitz, T. Meyer, M. Schmitt, I. Rimke, F. Hoffmann, F. von Eggeling, G. Ernst, O. Guntinas-Lichius and J. Popp, *APL Photonics*, 2018, **3**, 092404.

344 F. Masia, A. Karuna, P. Borri and W. Langbein, *Journal of Raman Spectroscopy*, 2015, **46**, 727–734.

345 C. Jüngst, M. Klein and A. Zumbusch, *Journal of Lipid Research*, 2013, **54**, 3419–3429.

346 P. Wang, M. N. Slipchenko, B. Zhou, R. Pinal and J.-X. Cheng, *IEEE Journal of Selected Topics in Quantum Electronics*, 2012, **18**, 384–388.

347 K. Bae, W. Zheng, K. Lin, S. W. Lim, Y. K. Chong, C. Tang, N. K. King, C. B. Ti Ang and Z. Huang, *Analytical Chemistry*, 2018, **90**, 10249–10255.